The Dissertation Committee for Jinbo Chen Certifies that this is the approved version of the following dissertation:

Deterministic and Probabilistic Analyses of Offshore Pile Systems

Committee:

Robert B. Gilbert, Supervisor

Lance Manuel

Loukas F. Kallivokas

Brady Cox

James Don Murff

Deterministic and Probabilistic Analyses of Offshore Pile Systems

by

Jinbo Chen, B.E.; M.E.

Dissertation

Presented to the Faculty of the Graduate School of

The University of Texas at Austin

in Partial Fulfillment

of the Requirements

for the Degree of

Doctor of Philosophy

The University of Texas at Austin
August 2016

Dedication

This dissertation is dedicated to my wife,

Feiyuan Li,

who has sacrificed so much in supporting my research,

to my little sweet baby,

Scarlett Cici Chen,

who has brought so much happiness into my life,

and to my parents,

Xiujuan Wang and Caiyao Chen,

who are always supportive in every decision I have made.

Acknowledgements

I would like to express my deep appreciation and gratitude to my advisor, Dr. Robert B. Gilbert, for the patient guidance and mentorship provided to me since 2011 when I was a Research Engineer at the National University of Singapore. I have benefitted tremendously from Dr. Gilbert's knowledge, wisdom, and independent thinking. Without his inspiring supervision, constant help, and positive encouragement, this dissertation would not have been possible.

I would also like to acknowledge all my dissertation committee members, Dr. Lance Manuel, Dr. Loukas Kallivokas, Dr. Brady Cox, and Dr. James Don Murff, for the valuable discussion and comments on my research, and the inspiring suggestions to my research.

Special thinks go to Dr. Murff, Dr. Peter W. Marshall, Dr. Jorge Forristall, and Dr. J.Y. Chen. Dr. Murff has been providing guidance to me since 2011 when I was in Singapore. His experience and expertise in the plastic theory and offshore foundations have greatly broadened my knowledge of the offshore industry. Besides, Dr. Murff contributed to my two journal papers from which I greatly improved my technical writing.

I worked with Dr. Marshall for three years (from 2010 to 2013) at the National University of Singapore. His pioneering work on the two-plastic-hinge failure mechanism for offshore piles and the reliability of offshore structures have greatly helped me in completing my dissertation. In addition, Dr. Marshall's comments to the API RP 2A-LRFD project are valuable, especially on the uncertainties in beam-columns and tubular joints.

Dr. Forristall provided guidance to me through emails, on the wave and wave force modeling, especially on the uncertainty in the hindcast model. Without his knowledge and guidance, the wave uncertainty modeling in my dissertation would not have been possible.

Dr. J.Y. Chen provided the necessary platform information which greatly saved my time in compiling the platform database. His knowledge in both offshore geotechnical and structural engineering greatly helped me.

I would also like to thank all the other faculty members in Geotechnical Engineering at UT. Dr. Rathje's inspiring course, Geotechnical Earthquake Engineering, synthesized my geotechnical expertise and knowledge of dynamics. Dr. Zornberg's expertise in the geo-environmental area brought my knowledge to a higher level. Dr. Stokoe and Dr. El Mohtar provided valuable assistance in completing my TA assignment.

I would also like to thank my previous supervisors Dr. Y.S. Choo and Dr. Y.K. Chow at the National University of Singapore. Dr. Choo and Dr. Chow introduced me the offshore geotechnical engineering and recommended that I pursue my Ph.D. here at The University of Texas at Austin. I would not participate in the offshore industry without their guidance.

I would also like to thank my classmates, colleagues, and friends at UT. It would be difficult to acknowledge everyone who has in some way or another contributed to my study; however, I still would like to mention the following persons who greatly helped me: Mr. Asitha Senanayake, Ms. Hande Gerkus, Ms. Julia Roberts, Dr. Ali Helwa, Dr. Eugenio Iturriaga, Dr. Wing Shun Kwan, Ms. Ying Lai, Dr. Yubing Wang,

Dr. Farnyuh Menq, Mr. Andrew Keene, Mr. Joseph Cibor, Ms. Leslie McCroddan, Ms. Sherian Williams, Ms. Velma Vela, Mr. Federico Castro, Mr. Danny Quiroz.

I also would like to acknowledge the Bureau of Safety and Environmental Enforcement (BSEE, former MMS) and the American Petroleum Institute (API) for providing financial support through the Offshore Technology Research Center for the projects upon which this dissertation is partially based. I would also like to thank Cibor Inc. for providing financial support through the drilled shaft group efficiency project, and Dr. Albert Ku in Energo Engineering for many fruitful discussions on the API project. However, the views and opinions contained in this dissertation are those of the author alone and do not necessarily reflect those of any of the sponsors or other contributors.

Last but not least, I would like to thank my wife, Feiyuan Li, who has been and is continuously supportive to my research. Without her support, I would not have been able to finish my Ph.D. research.

Deterministic and Probabilistic Analyses of Offshore Pile Systems

Jinbo Chen, Ph.D.

The University of Texas at Austin, 2016

Supervisor: Robert B. Gilbert

The offshore pile system capacity and the pile capacity model biases are important aspects in the assessment of existing offshore platforms and in the performance reliability that is achieved using the state of practice. The objectives of this research are to improve understanding of the pile system behavior, to calibrate the pile system capacity model bias factors, and to evaluate the reliabilities of offshore pile systems.

A simplified single pile failure surface in terms of three dimensional pile head loads is proposed based on the analytical lower and upper solutions, and is verified through finite element analyses. Numerical lower and upper bound models are then proposed for the ultimate capacity of a pile system, and are shown to be efficient and be effective in considering global torsion and out-of-plane failures. The evidence from the survival of offshore platforms indicates that (1) well conductors should be included in assessing the pile system ultimate capacity; (2) static p-y curves should be used which increases the pile system lateral capacity by 10 to 20%; (3) the mean value of the steel yield strength should be used; (4) jacket leg stubs should be included; and (5) site-specific geotechnical information is important.

The model bias factors in the API load and resistance design recipe are calibrated through Bayes' Theorem based on the predicted and observed performance of eighteen offshore platforms in recent Gulf of Mexico hurricanes. The API load and

resistance design recipe is calibrated to be close to unbiased for predicting the jacket system performance; be slightly conservative for predicting a foundation overturning failure in clay; and be conservative for predicting a lateral failure in clay and a foundation overturning failure in sand.

The reliability of a pile system is shown to be insensitive to water depths and locations in the Gulf of Mexico, but depends on the pile layout, number of piles, loading direction, and expected failure mode. The pile system redundancy (a measure of capacity beyond failure of the first element) and robustness (a measure of capacity when the system is damaged) depend on the failure mode, pile geometry and layout, and loading directions. In general, the 8-leg pile system is more redundant and more robust than the 3-leg and 4-leg pile systems. The complexity (a measure of the how well the most critically-loaded element represents all elements) depends on the pile layout, the expected failure mode of a single pile and the pile capacity uncertainty. The complexity is generally small, indicating that the failure probability of the most critically-loaded pile is representative of the failure probabilities for all piles.

Table of Contents

List of Tables

List of Figures

1 Introduction

1.1 Brief description of fixed offshore platforms

Fixed offshore platforms, conventionally called offshore jackets, are usually used for producing offshore oil and gas in relatively shallow water depth (e.g., water depth less than 1500 ft). Typically, an offshore jacket consists of a deck which supports oil producing and processing equipment, a jacket structure which is typically made up of tubular members, and a pile foundation (see Figure 1.1). The pile is usually installed through the jacket leg, and the annulus between the pile and the jacket leg may be grouted to prevent corrosion and/or to increase the structural integrity. Typically, well conductors will be installed which are not designed to resist any vertical loads; however, well conductors can attract wave loads as well as provide lateral resistance to the foundation capacity. The deck is usually supported by deck legs, and the distance between the bottom of the deck and the mean sea level should be designed to prevent wave hitting the deck, i.e., to avoid wave-in-deck loads in design.

The loads on the jacket platform include gravity and environmental loads. The gravity loads consists of the jacket structure and equipment dead load (buoyancy should be considered), and the live load on the deck. The environmental loads typically consists of wave and current loads, and wind loads. For jacket platforms, the wind load is usually less than 15% of the total environmental loads. In arctic region, loads caused by ice will typically be considered, and in locations with potential submarine slides, mudslide loads will also be considered.

The common failure mechanisms for an offshore jacket are the deck failure, the jacket structure failure, and the pile foundation failure. All these failure mechanisms

have been observed in the Gulf of Mexico in recent hurricanes. The deck failure is primarily caused by the wave-in-deck load while the jacket structure may remain intact as can be seen from Figure 1.2 after Energo Engineering (2007). The jacket structure failure can be initiated by local and/or global buckling of legs, joint damages, diagonal and brace damages (Energo Engineering, 2007). A comparison of the jacket before the storm and after the storm is shown in Figure 1.3 after ABS (2004). Pile foundation failures have rarely been reported or documented. The first comprehensively documented pile foundation failure case was reported by Chen *et al.* (2013). This failed pile foundation has three piles and the failure was initiated by the pull out of the pile loaded in tension as shown in Figure 1.4 (Energo Engineering, 2010).

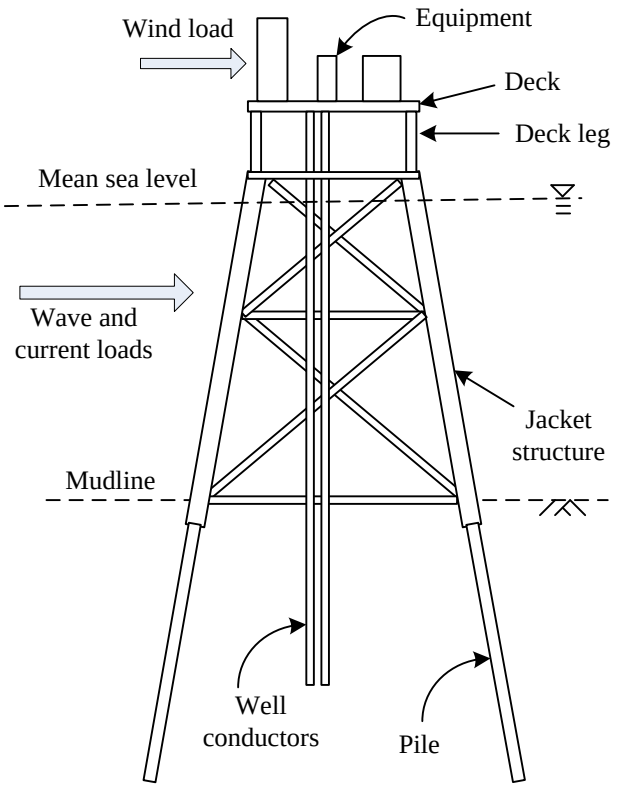

Figure 1.1 Brief description of fixed offshore platform

Figure 1.2 Deck failure

(a) Before storm

Figure 1.3 continues next page

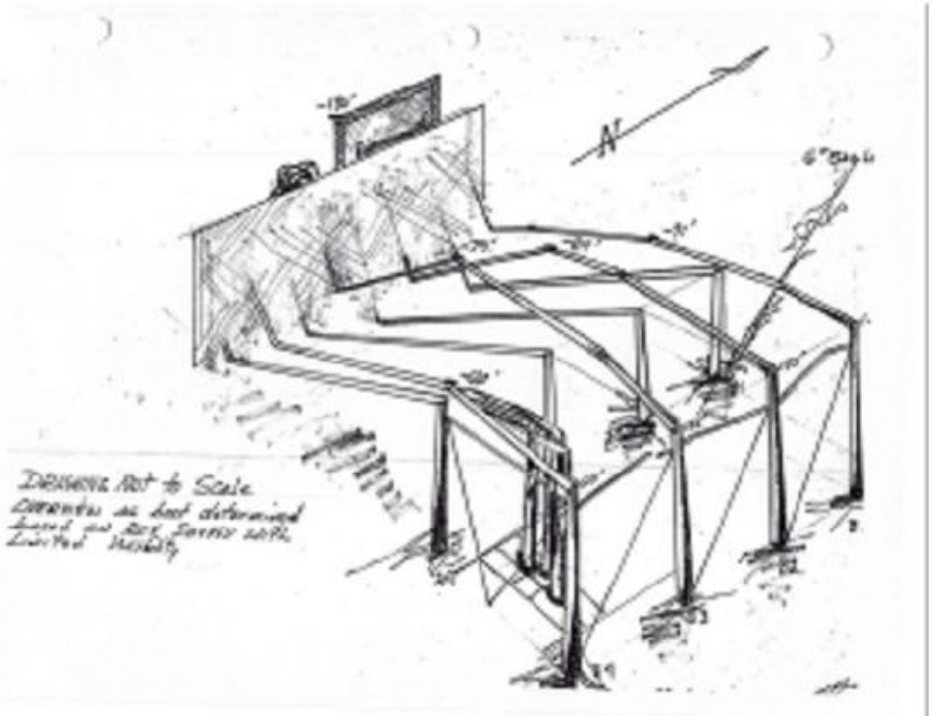

(b) After storm

Figure 1.3 Jacket failure

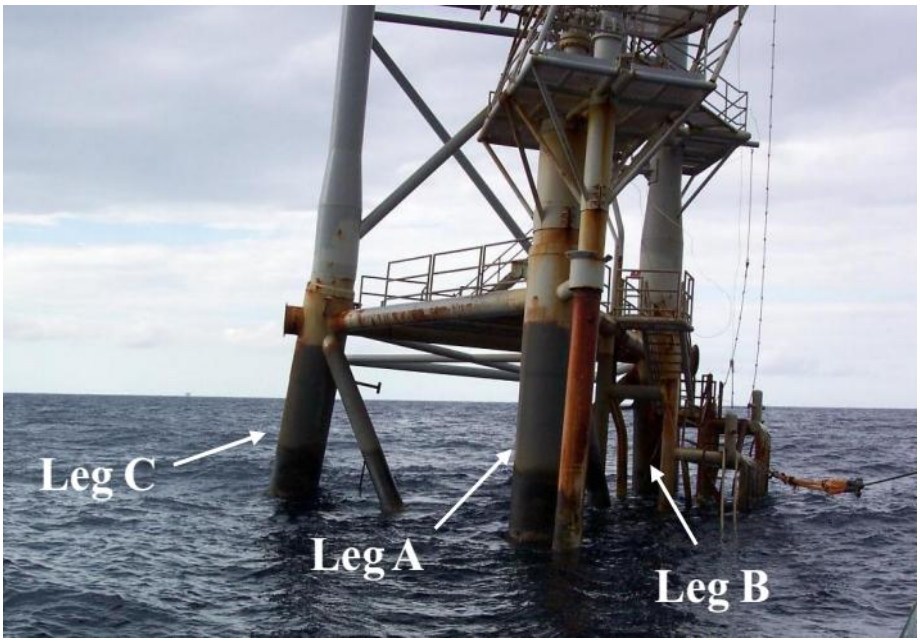

Figure 1.4 Pile foundation failure

1.2 Offshore pile system capacity

Current offshore pile foundation designs in the Gulf of Mexico generally follow American Petroleum Institute (API) guidelines (API RP 2GEO, 2011). The pile embedment length is determined by the extreme axial load on the most heavily loaded pile in the system with a specified factor of safety (FS), e.g., FS=1.5 (Murff and Wesselink, 1986, Murff, 2000). For the lateral loading effect, the ultimate lateral capacity of a long offshore pile is not usually considered specifically because the design requirements are based on limiting the stress in the pile wall to allowable values (Murff, 2012, Murff, 2000). These design methods do not explicitly take the pile foundation system capacity into account.

Nevertheless, the offshore pile foundation system capacity is an important aspect of the requalification of existing offshore platforms for life extension, and of the evaluation the redundancy and the reliability of offshore pile foundation design methods. The determination of the pile foundation design in practice is usually conducted such that the interaction of piles and soils is modeled as a beam on nonlinear springs. The soils are represented by a series of discrete, de-coupled, nonlinear axial and lateral springs. This type of analysis is much simpler than the full three dimensional (3D) finite element (FE) analyses, which adopts nonlinear constitutive models for the soil continuum and the pile-soil interface. However, commercial software is often required to model the platform and the pile system, and it is still relatively expensive to get the ultimate capacity, which is not routinely checked at the design stage. Simplified plastic limit analysis based on the upper bound theorem has been investigated extensively in terms of global base shear and overturning moment that cause the complete collapse of the pile system in the limiting case (Murff and Wesselink, 1986, Tang and Gilbert, 1992, Murff, 2000, Chen *et al.*,

2010, Gilbert *et al.*, 2010). This method assumes the jacket structure is perfectly rigid and the piles are long enough to form a two-plastic-hinge failure mechanism. It considers the complex pile layout, the variations of pile cross-sectional properties and soil conditions. This planar upper bound approach was used comprehensively in two API sponsored projects in evaluating the system reliability of offshore pile foundations (Tang and Gilbert, 1992) and in the assessment of performance of offshore pile foundations in recent Gulf of Mexico hurricanes (Gilbert *et al.*, 2010, Chen *et al.*, 2010).

In comparison to the upper bound method, little work has thus far been presented in determining the lower bound capacity (i.e., a conservative result) of an offshore pile foundation system. Besides, under general loading conditions, for a single pile, due to the displacement and rotation imposed by the offshore jacket structure, an out-of-plane moment may be induced by the asymmetric loading (e.g., torsion or the loading direction deviates from the symmetric axis). For a pile foundation system, due to the asymmetry of the pile system (e.g., the layout of piles is asymmetric or piles differ in diameter and length), an out-of-plane failure may occur (i.e., failure occurs in directions different from the loading direction). Hence, a lower solution will be preferred in order to provide a conservative estimate of the pile system capacity, and limit analysis needs to be extended in order to consider torsion effects and out-of-plane failures.

Murff (1999) adjusted the constrained system failure load obtained from the planar upper bound analysis to consider out-of-plane failures by comparing the components of the constrained failure load in other out-of-plane directions with the constrained failure load obtained in that out-of-plane direction; however, failure loads in directions other than the loading direction under consideration need to be established,

and torsion was not included in the analysis. Although Tang and Gilbert (1992) extended the model to incorporate the global torsion on the jacket, the overturning failure analysis of a platform is still restricted to a single plane and the method becomes complex and time-consuming to use, and the advantage of simplicity inherent in limit analysis begins to be lost.

Therefore, the limitations in the planar upper bound pile system model and the relation between the pile system capacity and the current component-based design motivates this study. In addition, the pile system capacity can be used to assess whether there is excessive conservatism in the current API pile design method.

1.3 Offshore pile uncertainty

Both aleatory and epistemic uncertainties exist in the predicted pile capacities. The aleatory variability of the pile foundation accounts for variations between piles due to variations in local and depth-averaged soil properties and in installation effects. The epistemic variability comes from limited data in the pile load testing databases, small scale load tests, and different loading conditions (Chen *et al.*, 2013, Lacasse *et al.*, 2013, Tang, 1988). The evaluation of the model biases for the API method is generally based on the pile load testing databases, accumulated industry experience and the observed pile performance in hurricanes.

From pile load testing databases, Tang (1988) concluded that the overall bias for the pile axial capacity in clay ranged from 1.3 to 3.7 and the corresponding coefficient of variation (c.o.v.) ranged from 0.32 to 0.53 based on the pile load testing database of Olsen (1984). Based on an update of a similar database, Lacasse and Nadim (1996) recommended the pile axial capacity bias to be 1.0 to 1.2 and 1.1 to 1.3 in clay and in medium to dense sand, respectively, for the API RP 2A-WSD (20^{th} edition). Lacasse

et al. (2013) further updated these biases to be respectively 1.07 to 1.1 and 1.58 for piles in clay and piles in sand, and the corresponding c.o.v. values were estimated to be respectively 0.27 to 0.32 and 0.61 for piles in clay and in sand based on the NGI and Imperial College databases. For laterally loaded piles, based on the test data reported by O'Neill and Murchison (1983), O'Neill and Gazioglu (1984), Tang and Gilbert (1990) found that the API soft clay p-y curves respectively overestimated by 12% and underestimated by 62% the pile head displacement for fixed head and free head piles; the API sand p-y curves overestimated the pile head displacement by 32%.

From accumulated industry experience, Moses (1986) found that the axial reliability of a pile foundation would be lower than that of a structural member if the mean and the c.o.v. of the bias are assumed to be 1.0 and 0.2, respectively. Moses (1986) further concluded that the suggestion of Bea (1983) that a bias in the range of 2.0 to 3.0, and a c.o.v. in the range of 0.4 to 0.6, was consistent with the reliabilities of structural members and would be expected from the accumulated pile foundation design experience. Hamilton and Murff (1988) inferred that an axial capacity bias of 1.5 to 3.0 would be required to reach a reasonable upper bound failure probability (on the order of 0.001) of pile foundations in 20 years. Hamilton and Murff (1992) suggested to use a bias of 1.3 and a c.o.v. of 0.3 for piles in clay and a bias of 1.2 and c.o.v. of 0.4 for piles in sand, which was consistent with the expert survey result presented by Lacasse and Goulois (1989).

From the observed pile performance in hurricanes, an inferred bias was around 2.0 for 8-leg systems, and around 3.0 for single pile systems in the Bay of Campeche (Bea *et al.*, 1999). The Bayesian calibrated model biases were around 1.3 and 1.5 for the lateral and overturning capacities of pile systems, respectively, in the Gulf of Mexico (ABS, 2004, Aggarwal *et al.*, 1996, Energo Engineering, 2005).

Limitations exist in the model bias estimated from pile load testing databases since the vast majority of available data correspond to small-scale piles with axial capacities that are smaller by ten times or more than the axial capacities for piles used in offshore platforms (Chen *et al.*, 2013), and the loading condition in the actual storms will generally be different from that in the load testing (e.g., rapid loading and cyclic degradation effects). The inferred bias from accumulated industry experience also subjects to shortcomings that: (i) some platforms may not be loaded beyond the design capacity; hence the survival of the platform is expected; (ii) for platforms destroyed in hurricanes but without detailed underwater investigations after hurricanes, it may be difficult to confirm whether the failure was initiated from the jacket structure or the pile foundation.

Therefore, a reliability-based design approach, which implicitly and/or explicitly considers the uncertainty in the pile capacities, motivates this study. In addition, the incorporation of pile system behavior makes the reliability-based design more rational.

1.4 Research objectives

The objectives of this dissertation are summarized as follows:

1. Extend the existing planar pile system capacity analysis to 3D loading conditions in order to improve understanding of how pile systems perform under a wide range of 3D loading conditions.
2. Relate the current component-based design to the pile system behavior, i.e., the relation between the component failure load and the pile system ultimate capacity.
3. Calibrate the API pile design method based on actual pile systems in Gulf of Mexico hurricanes.

4. Evaluate the offshore pile system reliability and provide a basis for the load and resistance factor design format.

1.5 Research Methodologies

The specific methodologies in the current study can be summarized as follows:

1. Upper and lower bound analyses of a single pile under 3D head loads will be carried out. Analytical bounding solutions will be derived and an approximate single pile failure surface in terms of pile head loads will be proposed. Verification of the proposed single pile failure surface will be conducted.
2. Upper and lower bound analyses of a pile system under 3D conditions will be carried out. The detailed procedure for constructing a lower bound solution will be given based on the elastic compensation method and the linear matching method. The derivation of an upper bound solution will be given.
3. The model biases in the API load and resistance recipes will be calibrated based on the analytically predicted and actually observed offshore platform performance in recent Gulf of Mexico hurricanes. Eighteen platforms will be compiled. Both the wave-by-wave approach and the sea state approach will be investigated.
4. The redundancy and robustness of a pile system will be analyzed deterministically and probabilistically. Reliability analysis will be conducted both for generic and case study offshore pile systems using the first order reliability method.

1.6 Outline of the dissertation

This dissertation consists of eight chapters. Chapter 1 reviews the previous studies on the offshore pile system capacity and reliability, and lists the motivations, objectives, and methodologies for this dissertation.

Chapter 2 and the associated appendices present the derivation of the failure surface of a single pile under 3D head load based on the plastic bounding theorems. The verification of the proposed single pile failure surface is also provided.

Chapter 3 proposes upper and lower bound methods for predicting the pile system capacity based on the failure surface derived in Chapter 2.

Chapter 4 presents the applications of the proposed pile system capacity model in the assessment of offshore pile foundations.

Chapter 5 presents the deterministic redundancy and robustness analyses of three case study offshore pile systems.

Chapter 6 constructs the Bayesian framework for calibrating the model bias factors in the API load and resistance recopies based on observed offshore platforms performance in recent Gulf of Mexico hurricanes.

Chapter 7 presents reliability analyses of generic and case study offshore pile systems. The pile system redundancy and robustness are examined in a probabilistic framework.

Chapter 8 summarizes the conclusions of the dissertation. Related future work is also recommended.

2 Limit Analysis of Single Piles[1]

This chapter aims to propose a simplified single pile failure surface in terms of 3D loads at the pile head based on plastic limit bounding theorems. Analytical upper and lower bound solutions for a single pile under 3D loading will be derived, and the proposed simplified failure surface will be verified by case studies using detailed FE and optimized upper bound analyses.

2.1 Plastic limit theorems

According to Martin (1975), the plastic bounding theorems (i.e., the upper and lower bound theorems) bracketing the ultimate capacity of a rigid-perfect-plastic system under small deformations are stated as follows. Upper bound theorem: the load determined by equating the external work rate and the internal energy dissipation rate associated with a pertinent, kinematically admissible field constitutes an upper bound of the actual collapse load. Lower bound theorem: the load obtained from a pertinent, statically admissible field that nowhere violates the yield condition constitutes a lower bound of the actual collapse load. In the current study, analysis is carried out using work conjugate loads and displacements, so that the ultimate capacity is bracketed by application of the limit theorems in load space (Martin, 1975). The following presentations are primarily based on Chen *et al.* (2015) and Chen *et al.* (2016).

2.2 Single pile representation

For the problem under consideration, focus is restricted to typical long offshore steel pipe piles where the lateral failure mechanism involves the formation of a plastic

[1] Part of the derivations in this chapter comes from Chen, J. B., Gilbert, R. B., Choo, Y. S., Marshall, P. W. and Murff, J. D. (2015) Two dimensional lower bound analysis of offshore pile foundation systems, *INT J NUMER ANAL MET, doi: 10.1002/nag.2488.* The author of this dissertation is the first and corresponding author of the cited paper, and completed the derivation and implementation of the proposed algorithm in the paper.

hinge some depth below the mudline (Marshall and Bea, 1976, Murff, 1987). Throughout the report, a beam-column on nonlinear spring model is used to represent the pile-soil interaction, with the soil resistance taken to follow the recommendations of API RP 2GEO (2011).

Referring to the directions parallel and perpendicular to the pile axis as shown in Figure 2.1, a free-head steel pipe pile is subjected to the axial load *V*, the lateral load *F* and the moment loads M_x and M_y respectively in the x and y directions at the pile head *a*. The z-axis is along the pile axis, and downward is defined as positive. A right-hand coordinate system is used for defining the direction of moment loads. The pile fails axially when *V* equals the axial capacity of the pile V_m, which is the minimum of the structural and geotechnical axial capacities of the pile. The pile fails laterally when a plastic hinge forms in the pile cross-section at *b*, which is some distance l_{ab} below the pile head *a* (depending on the magnitude of M_x and M_y, a plastic hinge can also occur at *a*, which is true for typical fixed-head offshore piles).

Throughout this dissertation, the single pile cross-sectional torsional resistance is neglected nor the reduction of the pile cross-section capacity due to torsion is considered. The exclusion of torsion on a single pile is primarily for simplicity but is based on the following reasons: (i) global torsion on an offshore jacket is typically small and the jacket structure usually will not be designed to resist significant torsion; (ii) even global torsion is relatively significant, global torsion will mainly be resisted by the horizontal resistance on the pile head, and the single pile cross-sectional torsional resistance is usually small due to the small single pile diameter. However, if the single pile diameter and global torsion on the jacket are large enough to affect the pile system behavior, the following analyses should be modified, i.e., to incorporate

torsional resistance of soils and the reduction of the pile cross-sectional capacity due to torsion.

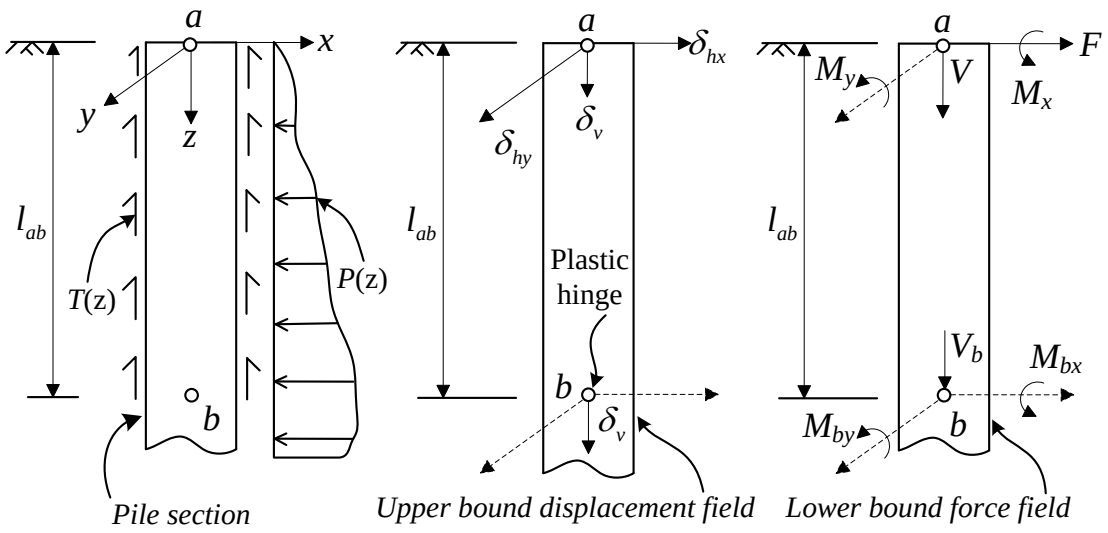

Figure 2.1 Single pile representation

2.3 3D upper bound analysis of single piles

If the pile geometry, the steel properties and the soil resistance vary smoothly along with pile length, an analytical upper bound solution for the lateral capacity of single piles under 3D head loads is shown in Equation 2.1 (derivation is given in Appendix I).

$$F = \frac{1}{\cos(\varphi)}\left[\int_0^{l_{ab}} P(z)dz + \frac{\pi M_{pb} T(l_{ab})}{2V_{pb}} \sin\left(\frac{\pi V_b}{2V_{pb}}\right)\right] \qquad 2.1\ (a)$$

where l_{ab} is determined as follows

$$\int_0^{l_{ab}} P(z)zdz = M_{pb}\cos\left(\frac{\pi}{2}\frac{V_b}{V_{pb}}\right) - \frac{\pi M_{pb} T(l_{ab}) l_{ab}}{2V_{pb}} \sin\left(\frac{\pi}{2}\frac{V_b}{V_{pb}}\right) + M\sin(\theta - \varphi) \qquad 2.1\ (b)$$

$$V_b = V - \int_0^{l_{ab}} T(z)\,dz \qquad \text{2.1 (c)}$$

$$\varphi = \begin{cases} \chi \dfrac{\pi}{4}\cos(\theta), & 0 \le \theta < \pi \\ \dfrac{1+\chi^2}{2}\sin^{-1}\left[\chi\cos(\theta)\right], & \pi \le \theta < 2\pi \end{cases} \qquad \text{2.1 (d)}$$

$$\chi = \sqrt{M_x^2 + M_y^2}\left[M_{pa}\cos\left(\frac{\pi V}{2V_{pa}}\right)\right]^{-1} \qquad \text{2.1 (e)}$$

where M_p and V_p are the pile cross-sectional plastic moment capacity (pure bending) and steel yield capacity (pure axial loading), respectively. The subscript '*a*' and '*b*' respectively indicate the positions are at *a* and *b*. V_b is the axial load acting on the pile at *b*. $M = \sqrt{M_x^2 + M_y^2}$ is the moment acting on the pile head. θ is the angle between the direction of *M* and *F*. The sign of θ is defined following the right-hand coordinate system. z is the depth of a specific point under consideration from *a*. $T(z)$ and $P(z)$ are the unit axial and lateral resistance of the soil surrounding the pile, respectively.

Theoretically, Equation 2.1 (a) may not give the best upper bound solution for $\theta \neq \pm 90^0$. As can be seen from Appendix I, φ represents the angle between the direction of the plastic lateral virtual velocity and the direction of *F*. The optimized upper bound solution should be obtained by minimizing the solution with respect to φ, which depends on the magnitude of *F*, the magnitude and the direction of *M* at the pile head. However, *F* is unknown as a prior. Thus it is difficult to obtain an explicit expression for φ to give an optimized upper bound solution. Based on parametric studies, Equation 2.1 (d) can give satisfactory result when compared to the optimized upper bound solution.

2.4 3D lower bound analysis of single piles

With the same assumptions made in the 3D upper bound analysis of a single pile, the lower bound lateral failure load *F* for piles subjected to 3D head loads is given in Equation 2.2 (derivation is given in Appendix I).

$$F = \int_0^{l_{ab}} P(z)dz \qquad 2.2\ (a)$$

where l_{ab} is determined as follows

$$\int_0^{l_{ab}} P(z)zdz = M\sin(\theta) + \sqrt{\left[M_{pb}\cos\left(\frac{\pi}{2}\frac{V_b}{V_{pb}}\right)\right]^2 - \left[M\cos(\theta)\right]^2} \qquad 2.2\ (b)$$

$$V_b = V - \int_0^{l_{ab}} T(z)\,dz \qquad 2.2\ (c)$$

In general, the lower bound lateral failure load in Equation 2.2 will not coincide with the true solution since the shaft friction of the soil between *a* and *b* is neglected in determining Equation 2.2 as shown in Appendix I. This assumption is based on the fact that typically the shaft friction of the soil above the lower plastic hinge is small relative to the overall axial capacity. Further, the derivation (see Appendix I) assumes the direction of lateral resistance of the soil is aligned with the direction of *F*. This assumption deviates from the actual situation when an out-of-plane moment is present. Thus the solution from Equation 2.2 is expected to be slightly smaller than the true solution when $\theta \neq \pm 90^0$.

2.5 Special case: in-plane loading

For piles subjected to in-plane loading, i.e., $\theta = \pm 90^0$ or M=0, Equation 2.1 and 2.2 degenerate to the same equation as follows:

$$F = \int_0^{l_{ab}} P(z)dz + \frac{\pi M_{pb} T(l_{ab})}{2V_{pb}} \sin\left(\frac{\pi}{2}\frac{V_b}{V_{pb}}\right) \qquad 2.3\ (a)$$

where l_{ab} is determined as follows

$$\int_0^{l_{ab}} P(z)zdz = M + M_{pb}\cos\left(\frac{\pi}{2}\frac{V_b}{V_{pb}}\right) - \frac{\pi M_{pb} T(l_{ab}) l_{ab}}{2V_{pb}} \sin\left(\frac{\pi}{2}\frac{V_b}{V_{pb}}\right) \qquad 2.3\ (b)$$

$$V_b = V - \int_0^{l_{ab}} T(z)\,dz \qquad 2.3\ (c)$$

Note that the shaft friction within l_{ab} has not been neglected in the lower bound analysis in arriving Equation 2.3. Hence, Equation 2.3 gives the exact solution for a single pile subjected to in-plane loading.

2.6 Approximate lower bound failure surface

If the pile geometry and the steel properties remain the same within the range of l_{ab}, and $P(z)$ can be expressed as $P(z) = kz^n$ (where k and n are resistance fitting parameters), Equation 2.2 can be solved analytically as follows

$$\frac{|F|}{F_m} = \left[\frac{\chi\sin(\theta) + \sqrt{1-\chi^2\cos^2(\theta)}}{2}\cos\left(\frac{\pi}{2}\frac{V}{V_{pa}}\right)\right]^{\frac{n+1}{n+2}} \qquad 2.4\ (a)$$

$$F_m = \frac{(n+2)^{n+1/n+2}}{n+1} k^{1/n+2} \left(2M_{pa}\right)^{n+1/n+2} \qquad 2.4\text{ (b)}$$

$$l_{ab} = \left\{ \frac{n+2}{k} \left[\chi \sin(\theta) + \sqrt{1-\chi^2 \cos^2(\theta)} \right] M_{pa} \cos\left(\frac{\pi}{2} \frac{V}{V_{pa}} \right) \right\}^{1/n+2} \qquad 2.4\text{ (c)}$$

where F_m is the maximum ultimate lateral capacity of a fixed-head pile under in-plane loading (i.e., $V = 0$, $\chi = 1$ and $\theta = 90^0$). It is noted that χ represents the ratio of the magnitude of the pile head moment to the yield moment of the pile head cross-section as shown in Equation 2.1 (e). Thus χ is in the range of $0 \sim 1$. A plastic hinge occurs at the pile head when $\chi = 1$. For $\theta = \pm 90^0$ or $\chi = 0$, Equation 2.4 degenerates to the one in the planar condition. Hence, fixed-head and free-head piles under in-plane loading correspond to the situation with $\left(\chi = 1,\ \theta = 90^0\right)$ and $\theta = -90^0$, respectively. Similarly, the normalized pile lateral capacity from the upper bound solution (Equation 2.1) can be determined as

$$\frac{|F|}{F_m} = \frac{1}{\cos(\varphi)} \left[\frac{1 + \chi \sin(\theta - \varphi)}{2} \cos\left(\frac{\pi}{2} \frac{V}{V_{pa}} \right) \right]^{\frac{n+1}{n+2}} \qquad 2.5$$

In general, Equation 2.1, 2.2 and 2.3 can only be solved numerically since the pile geometry and/or the steel properties usually vary along the pile length. If F_m is determined correctly, it is found that the lateral capacity can be well approximated in a form similar to Equation 2.4 (a) and 2.5. Thus a lateral capacity fitting parameter α is introduced to reflect the effects of the variations of the pile geometry, the steel yield stress, and the soil resistance on the calculated lateral failure load. The failure surface of a single pile is shown in Equation 2.6, where Equation 2.6 (a) and 2.6 (d)

respectively specify the failure criteria of the pile cross-section and the failure in the axial direction.

$$\chi = \frac{|M|}{M_{pa}\cos\left[\pi V \big/ \left(2V_{pa}\right)\right]} \le 1 \qquad \text{2.6 (a)}$$

$$\frac{|F|}{F_m} \le \begin{cases} \dfrac{1}{\cos(\varphi)}\left[\dfrac{1+\chi\sin(\theta-\varphi)}{2}\cos\left(\dfrac{\pi}{2}\dfrac{V}{V_{pa}}\right)\right]^{\alpha}, & \text{Upper bound, 3D loading} \\ \left[\dfrac{\chi\sin(\theta)+\sqrt{1-\chi^2\cos^2(\theta)}}{2}\cos\left(\dfrac{\pi}{2}\dfrac{V}{V_{pa}}\right)\right]^{\alpha}, & \text{Lower bound, 3D loading} \end{cases} \qquad \text{2.6 (b)}$$

$$\frac{|F|}{F_m} \le \left[\frac{1\pm\chi}{2}\cos\left(\frac{\pi}{2}\frac{V}{V_{pa}}\right)\right]^{\alpha} \qquad \text{Upper \& lower bound, In-plane loading} \qquad \text{2.6 (c)}$$

$$\frac{|V|}{V_m} \le 1 \qquad \text{2.6 (d)}$$

where φ is given in Equation 2.1 (d).

A comparison of the 3D upper and lower bound solutions from Equation 2.6 (b) is shown in Figure 2.2 to 2.4. As shown, the agreement between the approximate upper and lower bound solutions is satisfactory. Since both the approximate upper and lower bound single pile failure surfaces involve a fitting parameter α which needs to be calibrated with actual piles to account for the variation of the pile and/or soil properties with depth, the upper bound solution is presented here only for the completeness of limit analysis, and is not used in the pile system analysis in this study.

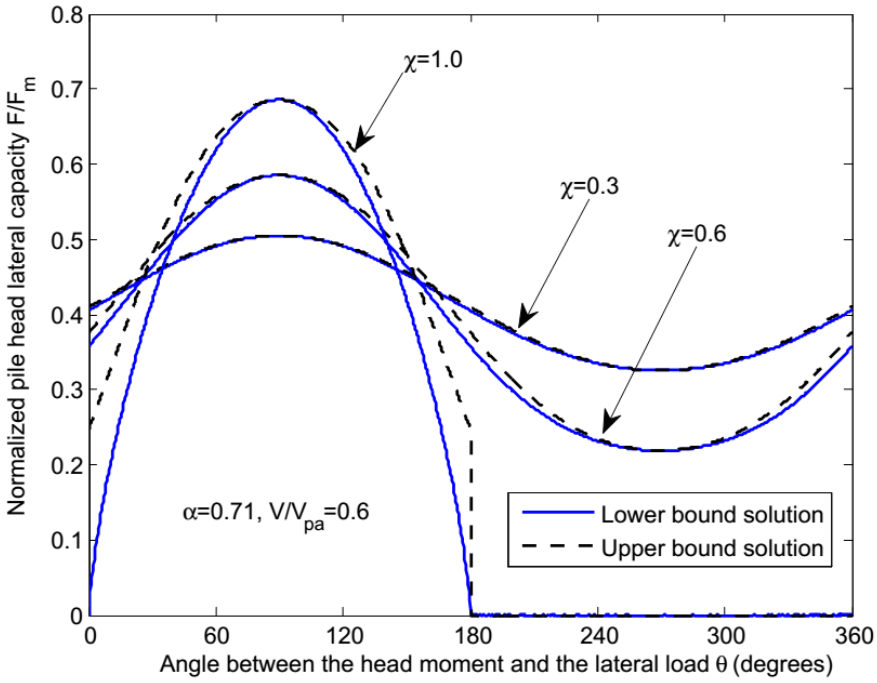

Figure 2.2 Variation of normalized lateral capacity with θ

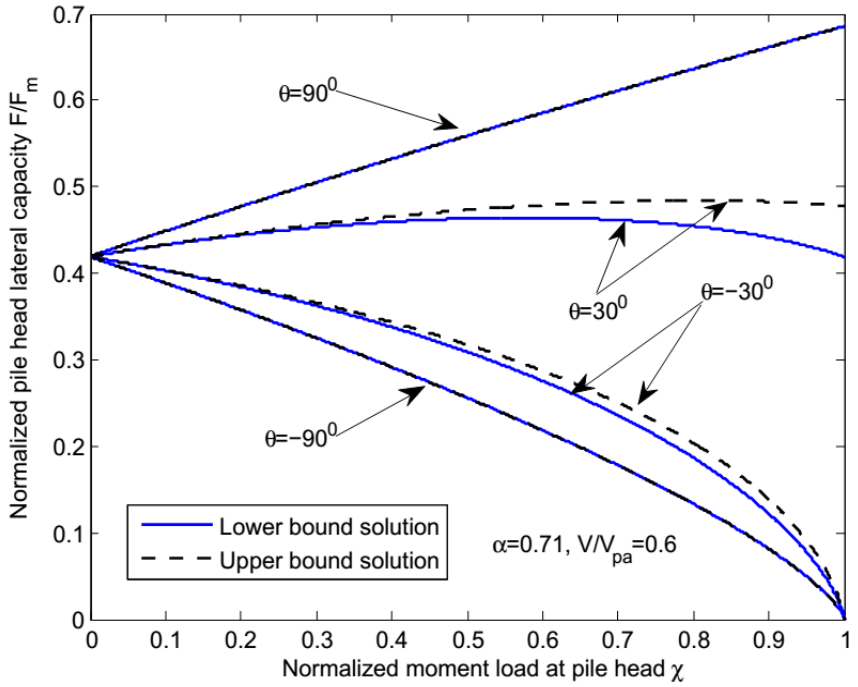

Figure 2.3 Variation of normalized lateral capacity with χ

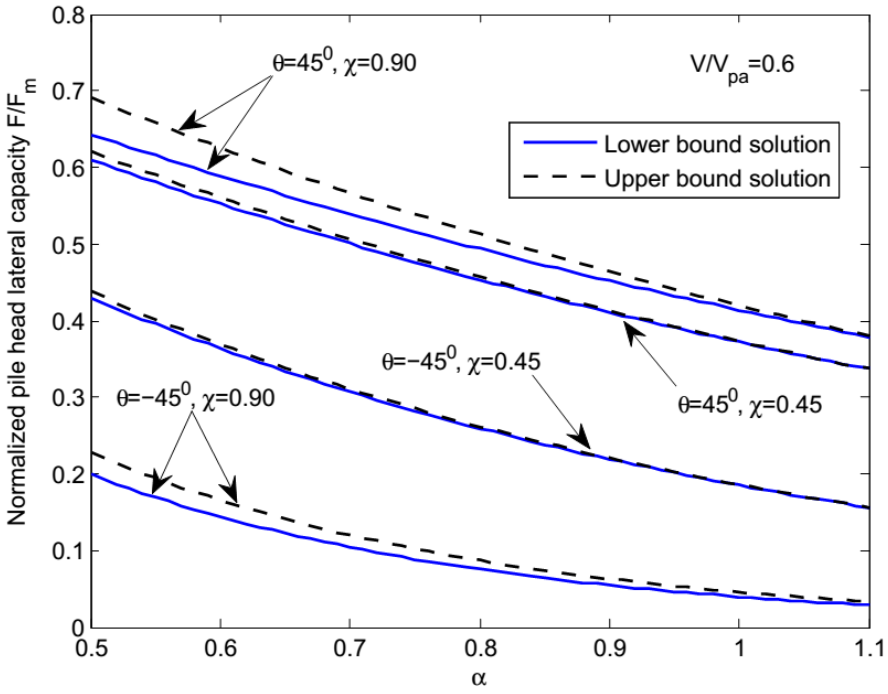

Figure 2.4 Variation of normalized lateral capacity with α

2.7 FE analysis for failure surface verification-in-plane loading

To verify the above approximate solution under in-plane loading, a detailed analysis is carried out on the pile foundation of a platform in the Gulf of Mexico that failed in 2008 (Chen *et al.*, 2013). The vertical pile, which has the largest lateral capacity among the piles in that platform, is considered here. The embedment length and the outer diameter of the pile are respectively 265 ft and 48 in. The wall thickness for the top 50 ft of the pile (below the mudline) is 1.75 in, and decreases to 1.25 in at the pile tip. The nominal yield stress of the pile steel is 36 ksi. The site-specific soil boring indicates that the soil strata are classified as very soft clay for the top 11 ft, underlain by soft to hard clay.

The pile geotechnical capacity in compression V_m is calculated to be 6250 kips. The pile head is assumed to be fixed against rotation and static p-y curves are used in the verification. Figure 2.5 shows the ultimate unit lateral resistance of the soil

calculated following the API guidelines (API RP 2GEO, 2011), and three linearly fitted resistance profiles for the top 60 ft below the mudline. Following the approximate solution in Equation 2.4, neglecting the shaft friction and using the linearized lateral resistance, H_m is determined to be 840 kips, 760 kips and 794 kips for fitted lateral resistance 1, 2 and 3, respectively. The corresponding lower plastic hinge forms respectively at about 40.0 ft, 44.3 ft and 42.7 ft from the pile head. The exact numerical solution of Equation 2.3 gives H_m of 782 kips with the lower plastic hinge about 41.0 ft below the pile head. Therefore, neglecting the shaft friction and linearizing the soil lateral resistance can give a good approximation to the pile lateral capacity.

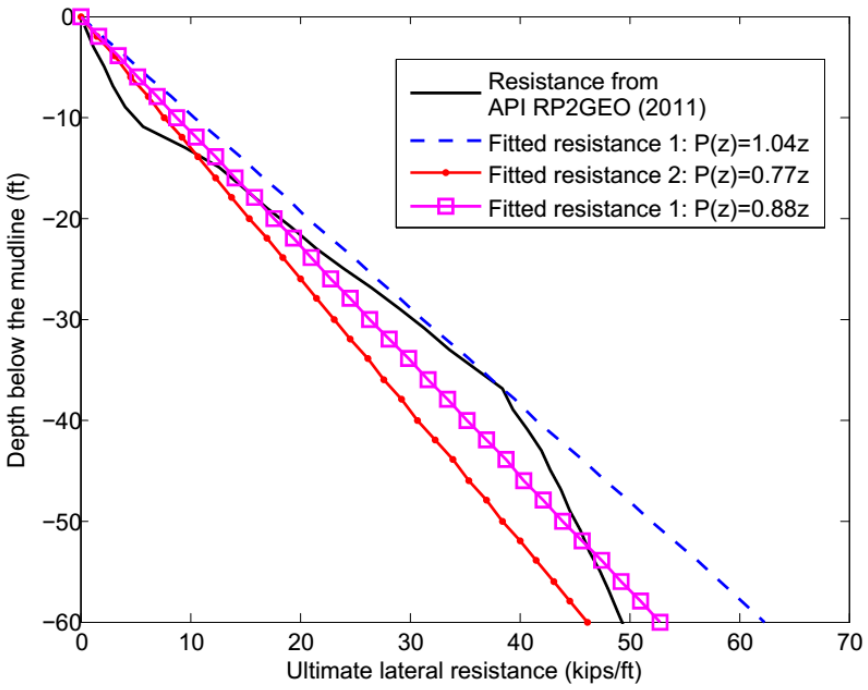

Figure 2.5 Linearization of unit lateral resistance of soil

For this case, above the lower plastic hinge, the pile properties remain the same and the linearization of the soil lateral resistance approximates well the pile lateral capacity, hence α is expected to be around 0.67 according to Equation 2.4 (i.e., n=1).

The best-fit value of α is determined to be about 0.70 by fitting the failure surface obtained from the exact solution of Equation 2.5 by varying the applied axial load at the pile head. As shown in Figure 2.6, both the upper bound approach of Murff (1987) and the FE analysis are adopted to verify Equation 2.5. The bending moment-thrust-curvature relation of the steel pipe cross-section follows Chen and Han (1985). As the pile under lateral loading exhibits ductile behavior, the ultimate capacity is determined at the lateral displacement of 1.5 diameters of the pile, where the load-displacement curve almost reaches a plateau. The $P-\Delta$ effect is excluded from the FE analysis in order to be consistent with limit analysis, although the lateral displacement is large. Taking account of the different resolutions in each method, Equation 2.5 is in good agreement with the above two methods.

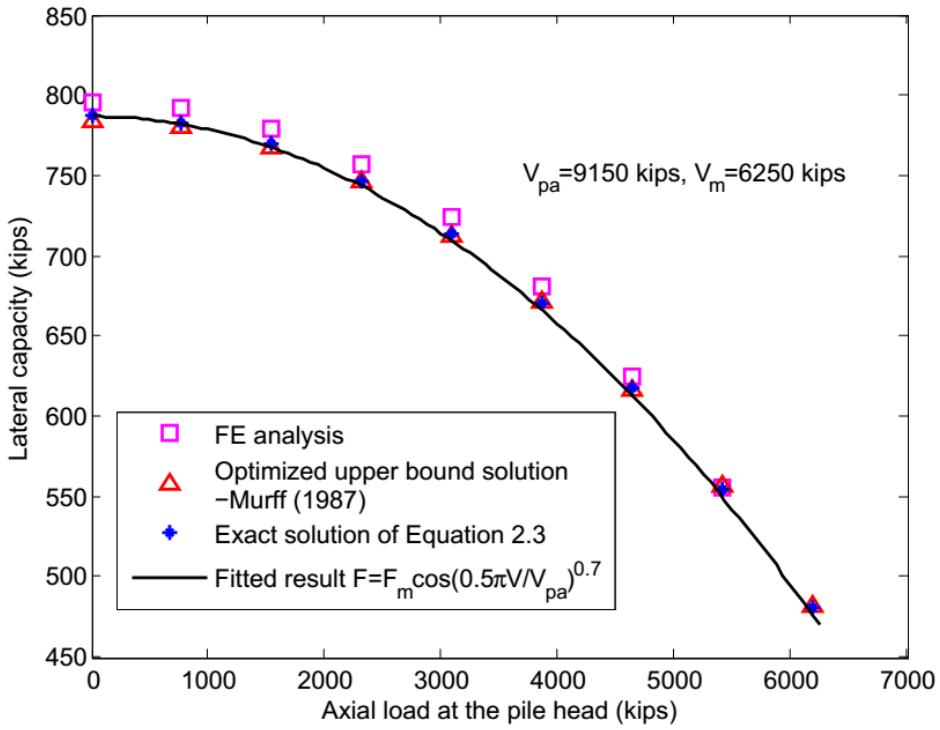

Figure 2.6 Verification of approximated single pile failure surface

Table 2.1 summarizes the best fitted α for 16 piles from 13 offshore platforms in a database of platforms that were loaded in hurricanes (Chen *et al.*, 2010) assuming both fixed-head and free-head conditions (no moment at the pile head). The platform

number in Table 2.1 remains the same as the original platform database in order for easy reference. 12 soil profiles from available soil borings are used in the prediction. Each pile differs in the geometry and capacity. Only piles under compressive loading are considered as α will be the same for both the compressive and tensile cases from limit analysis.

For the fixed-head condition, the fitted value of α ranges from 0.5 to 1.1 with a mean value of 0.71, and a c.o.v. of 0.19. For the free-head condition, α ranges from 0.6 to 0.9 with an average of 0.70 and a c.o.v. of 0.12. As can be seen from Equation 2.3, the lateral capacity depends on the pile properties at the lower plastic hinge *b* (see Figure 2.1), while the approximate failure surface in Equation 2.6 uses the reference pile properties at the pile head *a* (see Figure 2.1). Therefore, α will increase if the pile wall thickness and/or steel yield stress decrease in the section between *a* and *b*. Based on the case study, if the pile properties remain constant, and the soil type is clay for the top 15 to 20 diameters below *a*, the fitted value of α will be close to 0.7 since the linearization of the ultimate unit lateral resistance is a good approximation to that in the API guidelines (API RP 2GEO, 2011). If there is a reduction of pile wall thickness in the top 10 diameters, a typical α will be around 0.8; whereas if the pile wall thickness increases in that region, a typical α will be close to 0.6. Furthermore, for piles having large values of V_m/V_{pa}, α is expected to be around 0.7 since the wall thickness of that pile is not likely to decrease significantly within l_{ab} in practice. For Platform 1, significant reduction of wall thickness (from 1.5 in to 0.75 in) occurs in the top 15 diameters, which results in a relatively large α value of 1.1. For Platform 2, the actual lower plastic hinge is below the position determined by Equation 2.4 (c), and occurs in the pile section where there is a sudden reduction of the pile wall thickness. The reduced wall thickness reduces the pile lateral capacity, while the

increased depth of the lower plastic hinge potentially compensates for this negative effect. This case gives the lowest value of $\alpha = 0.5$ among the cases studied.

For the free-head condition, l_{ab} will be smaller (see Equation 2.4 (c)), so that the soil and the pile properties in that section experience less variation. Therefore, α is expected to be closer to 0.70 and have less variation when compared to that for the fixed-head condition.

Figure 2.7 shows the exact pile lateral capacity calculated for 16 piles. As can be seen, the pile lateral capacity is not sensitive to the value of α, especially in the fixed-head condition. In general, α may depend on the moment at *a* due to the variation of pile geometry within l_{ab}. However, if α is close to 0.7 in the fixed-head condition, α will largely be independent of the moment at *a* based on the above discussion and Table 2.1.

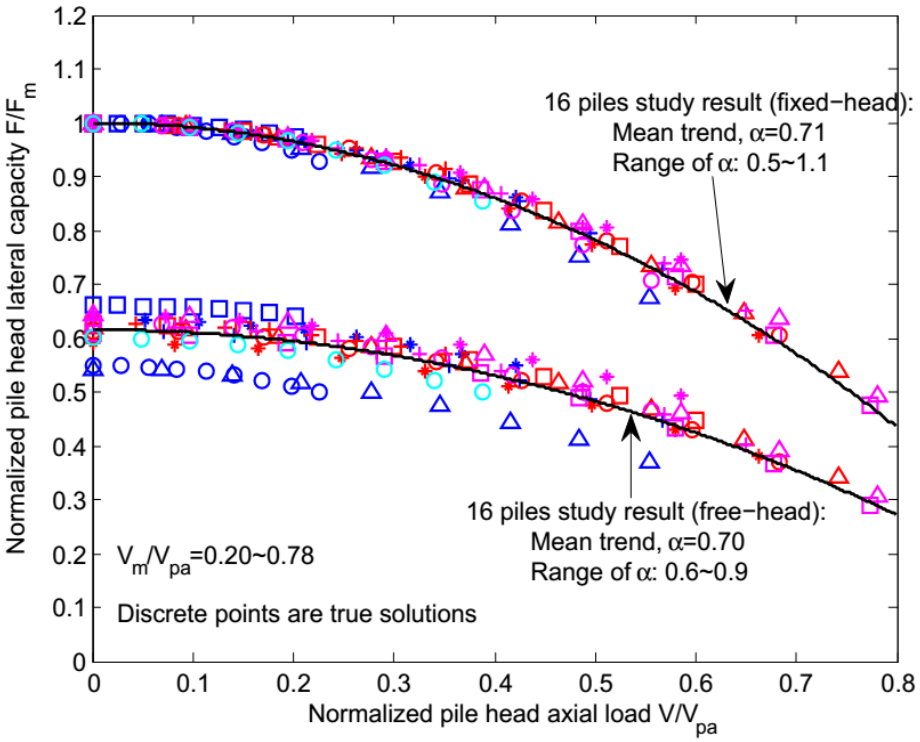

Figure 2.7 Exact lateral capacity of 16 piles

Table 2.1 Summary of $\aleph$ from 16 piles

Platform No.	Pile length (ft)	Pile diameter (ft)	Wall thickness (top 20 diameters) (*in*)	Steel yield stress (ksi)	Soil type (top 20 diameters)	V_m (*kips*)	H_m (*kips*)	α (fixed head)	α (free head)
1	139	2.75	1.5-0.75	36	Clay	1205	239	1.10	0.90
2	140	3.00	1.75	36		1363	352	0.50	0.60
8	274	4.00	2-1.75	36	Clay-Sand	5763	881	0.88	0.88
9	120	2.50	1	36	Sand-Clay-Sand	1378	284	0.65	0.65
10	220	4.00	1.5-1.25	36	Clay	4469	710	0.70	0.70
	265	4.00	1.75-1.5	36		6246	782	0.70	0.70
11	239	3.50	1.75-1.5	36	Sand-Clay-Sand	4775	656	0.67	0.67
	309	3.50	2-1.75	36		6710	714	0.67	0.67
12	255	4.00	1.5-1.375	36	Clay-Sand-Clay	5224	576	0.74	0.74
22	290	3.50	1.75-1.875	50	Clay	3877	655	0.58	0.67
25	169	3.00	1.625-1.25-0.875	36	Clay-Sand-Clay	3515	578	0.78	0.68
27	264	4.00	1.25-1	36	Clay	5117	612	0.70	0.70
	281	5.00	1.5-1.25-1	36		7741	951	0.64	0.64
29	140	3.50	1.25-1.375-1.25	36	Clay	3368	393	0.60	0.63
30	205	4.00	1.75	36	Clay	5944	574	0.68	0.68
31	180	3.50	2-1.75	36	Clay	3510	603	0.76	0.76

2.8 Upper bound and FE analyses for failure surface verification-3D loading

In this study, the numerical searching for the optimized upper bound solution is essentially the same as the method proposed by Murff (1987), in which the upper bound lateral failure load is obtained by equating the input work rate to the energy dissipation rate and is optimized by considering different combinations of failure mechanism controlling variables. The only difference between the 2D and 3D analyses for single piles is that the out-of-plane virtual angular velocity caused by the out-of-plane moment needs to be accounted for in the energy balancing equation in the 3D analysis.

To verify the proposed lower bound failure surface, selected piles from a database of platforms that were loaded in hurricanes (Chen *et al.*, 2010) under various loading situations are studied. The value of α for each pile is from Table 2.1. Figure 2.8 and 2.9 show the comparison of the pile lateral capacity obtained from various methods. The platform numbers in Figure 2.8 and 2.9 remain the same as those in Table 2.1. Figure 2.8 shows the variation of the pile lateral capacity with the moment direction at the pile head. The magnitude of the moment remains constant (i.e., $\chi = 0.6$). The design axial load is applied at the pile head (i.e., $V_m/V = 1.5$). As can be seen, good agreement is obtained among the above three methods. Figure 2.9 shows the variation of the pile lateral capacity with the moment magnitude for $\theta = -45^0$ ($V_m/V = 1.5$). Excellent agreement is obtained among the proposed lower bound failure surface, the upper bound and FE results for the piles from Platform 9 and 10. For the pile from Platform 2, the proposed failure surface gives slightly lower lateral capacity than the optimized upper bound result. For this pile, the value of α depends on the pile head

moment and is in the range of 0.5~0.6 as shown in Table 2.1. A larger value of α (i.e., $\alpha = 0.6$) is used in the comparison in Figure 2.9. Thus it is expected the proposed failure surface gives lower capacity than that from the optimized upper bound method. Hence, the good agreement among the above three methods validates the proposed failure surface.

Generally the agreement between the proposed failure surface and the optimized upper solutions depends on the variation of pile cross-sectional properties. The best agreement is observed when the pile cross-sectional properties are uniform above the lower plastic hinge. In this case, the fitted value of α will be close to 0.7 and approximately independent of the moment at the pile head since the linearization of the ultimate unit lateral resistance is a good approximation to that in the API guidelines. If α depends on the moment at the pile head, whereas a larger value of α is suggested to be used in the proposed failure surface, deviations from the exact solution are therefore expected. However, based on the current case studies, the deviation between the proposed lower bound failure surface and the optimized upper bound solution for a single pile is generally less than 10%.

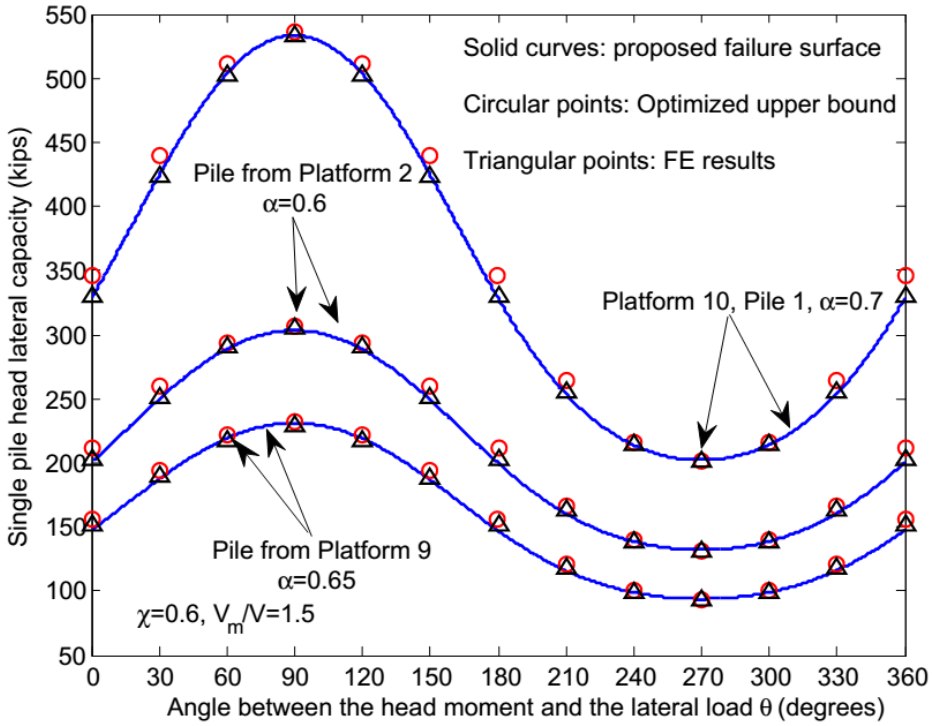

Figure 2.8 Variation of lateral capacity with moment direction

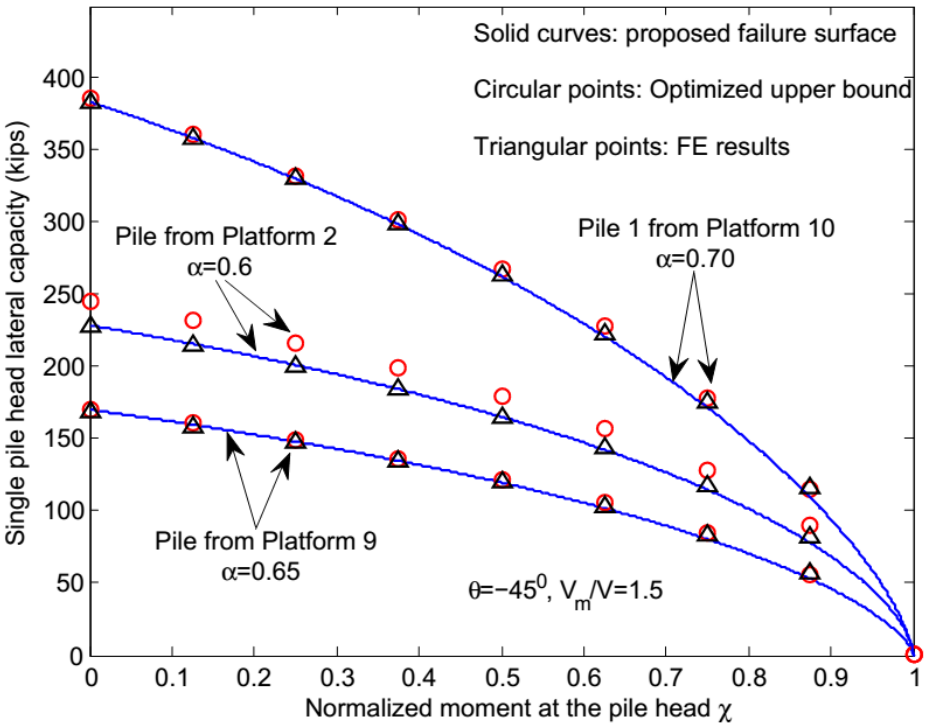

Figure 2.9 Variation of lateral capacity with moment magnitude

2.9 Conclusions

This chapter and the associated appendices derive the analytical upper and lower bound solutions for a long steel pipe pile subjected to head loading under general soil and pile geometry conditions. For in-plane loading, the two analytical bounding solutions coincide, provding in the exact lateral capacity of a single pile. For three dimensional loading, the two analytical bounding solutions are close. A failure surface for a single pile in terms of pile head loads is then proposed based on the lower bound solution by introducing a fitting parameter α, which has a mean of about 0.7 from the analyses of 16 actual offshore piles. The proposed single pile failure surface is verified by the close agreement with the results from optimized upper bound and FE analyses in a set of case studies.

3 Limit Analysis of Pile Systems

This chapter aims to propose plastic limit solutions for the pile system capacity under general 3D loading. The procedure for constructing a lower bound solution to the pile system capacity will be described based on the simplified single pile failure surface. The upper bound solution will be derived based on the failure mechanism determined from the lower bound solution. A discussion on the proposed lower and upper bound solutions for the pile system capacity will also be provided.

3.1 Pile system representation

The jacket structure is assumed to be rigid as shown in Figure 3.1. In the jacket global coordinate system as defined in Figure 3.1, the jacket structure is subjected to 3D loads and allows for six degrees of freedom. $\mathbf{P}_c$ represents a set of constant gravity loads. $\lambda\tilde{\mathbf{p}}$ represents the environmental loads, where $\tilde{\mathbf{p}}$ is a unit load vector specifying the direction and location of the load and λ is a positive load multiplier. Thus proportional loading is assumed for environmental loading, and the ultimate capacity of the pile system can be expressed through the single load multiplier λ. Note that $\mathbf{P}_c$ and $\tilde{\mathbf{p}}$ both have six components (three force components and three moment components) and are indicated by bold typeface. The following presentations are primarily based on Chen *et al.* (2015) and Chen *et al.* (2016).

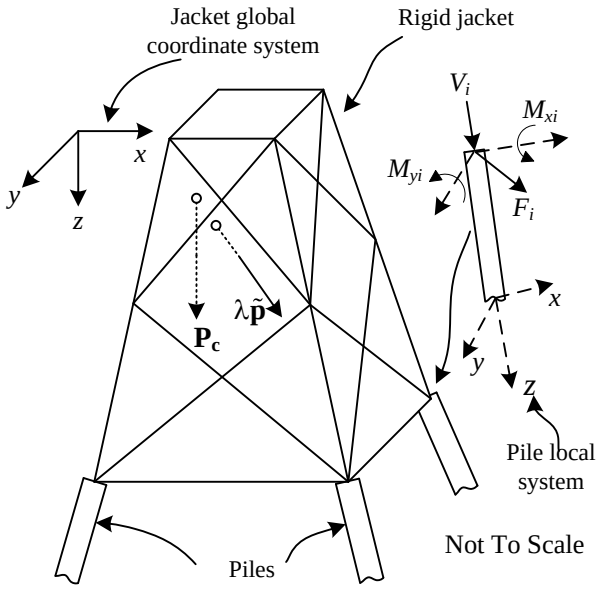

Figure 3.1 Representation of simplified model

3.2 3D lower bound analysis of pile systems

Using Prager's generalized stress concept, the lower bound analysis is conducted in load space. Each pile is treated as a macro-element with a yield surface defined by the proposed single pile failure surface, i.e., Equation 2.6 from the lower bound analysis of single piles, in terms of the pile head loads (V_i, F_i, M_i) in the pile local system, where the subscript '*i*' indicates the *ith* macro-element as will be used throughout this study. The pile local coordinate system is defined to be the same as that in the single pile analysis: *z*-axis is along the pile axis, *x* and *y* directions are the two orthogonal lateral directions, a right-hand coordinate system is used as shown in Figure 3.1. The lower bound analysis is then equivalent to finding an optimized lower bound load multiplier λ_{low}, subjected to the restriction that $\mathbf{P_c} + \lambda_{low}\tilde{\mathbf{p}}$ are in equilibrium with all the pile head loads (V_i, F_i, M_i),which do not violate the yield surface defined in Equation 2.6.

Each macro-element is assumed to have linearly elastic axial and lateral stiffnesses (respectively k_{Ai} and k_{Li}, which are defined in the pile local coordinate system) but no rotational stiffness. It is convenient to determine $\left(V_i, F_i, M_i\right)$ for given $\mathbf{P_c} + \lambda\tilde{\mathbf{p}}$ from the elastic analysis by constructing a 6 by 6 global stiffness matrix. The effect of pile batter is taken into account in constructing the global stiffness matrix. $M_i = 0$ in the elastic analysis since no rotational stiffness is assigned to the macro-element. The obtained loads are scaled to satisfy the yield condition of the macro-element. The lower bound solution is then optimized using the elastic compensation method and the linear matching method where the stiffnesses of each macro-element are adjusted systematically. The proposed iterative procedure is described as follows:

(1) Determine $\left(V_i^j, F_i^j, M_i^j = 0\right)$ on each macro-element at the *jth* iteration for given loads $\left(\mathbf{P_c} + \xi_{\min}^{j-1}\lambda\tilde{\mathbf{p}} - \mathbf{P_u}^{j-1}\right)\Big/\xi_{\min}^{j-1}$ applied on the jacket, where the superscript '*j*' indicates the *jth* iteration; ξ is a scaling factor and the subscript 'min' indicates the minimum scaling factor among all the macro-elements. $\mathbf{P_u}$ is the unbalanced loads and will be discussed in detail later (to start the iteration, $\xi_{\min}^0$ is set to 1 and $\mathbf{P_u}^0$ is set to $\mathbf{0}$).

(2) Linearly scale $\left(V_i^j, F_i^j, M_i^j = 0\right)$ such that $\left(\xi_i^j V_i^j, \xi_i^j F_i^j\right)$ will be exactly on the yield surface. ξ_i^j cannot be determined without the specification of χ_i^j. There are three sub-steps to determine ξ_i^j and χ_i^j. In the first sub-step, for the *ith* macro-element, assign a value for χ_i^j that maximizes ξ_i^j. If $\left(\xi_i^j V_i^j, \xi_i^j F_i^j\right)$ will lie on the curved part of the yield surface for $\chi_i^j = 1.0$ and $\theta_i^j = 90^o$, then χ_i^j should be set to 1.0 and θ_i^j to 90^o in order to maximize the yield surface as can be seen from

Equation 2.6; otherwise, $\left(\xi_i^j V_i^j, \xi_i^j F_i^j\right)$ will lie on the vertical portion of the yield surface and the maximum ξ_i^j can be determined to be $\xi_i^j = V_{mi} / V_i^j$ since the axial failure governs the maximum ξ_i^j as can be seen from Figure 3.2. However, in this case, χ_i^j cannot be determined uniquely from Equation 2.6 (b) (lower bound solution) since the yield surface depends both on the magnitude and direction of the moment. In the general case, an out-of-plane failure may occur. Hence, χ_i^j and θ_i^j are determined by maximizing $M_{ix}^j \phi_{ix}^j + M_{iy}^j \phi_{iy}^j$, subjected to the restriction that the resulting ξ_i^j is not smaller than V_{mi} / V_i^j, where *x* and *y* respectively represent the components in the local *x* and *y* direction; ϕ_i^j is the head rotation of the *ith* macro-element in the local coordinate system at the *jth* iteration and ϕ_i^j is available from the elastic solution. Thus no additional effort is required to evaluate ϕ_i^j. The reason for the above algorithm is that in the limiting case, the displacement field generated from the elastic analysis can be treated as a plastic displacement field (Ponter and Carter, 1997). Thus maximizing $M_{ix}^j \phi_{ix}^j + M_{iy}^j \phi_{iy}^j$ is equivalent to maximizing the internal energy dissipation rate, which tends to maximize the lower bound failure load. In the second sub-step, let $\xi_{\min}^j = \min_{all\ i}\left(\xi_i^j\right)$. Scale the linearly elastic system using the scaling factor $\xi_{\min}^j$, the loads on each macro-element will be $\left(\xi_{\min}^j V_i^j, \xi_{\min}^j F_i^j\right)$. Thus $\left(\xi_{\min}^j V_i^j, \xi_{\min}^j F_i^j\right)$ will lie within the yield surface except for the *ith* macro-element with $\xi_i^j = \xi_{\min}^j$, which will lie exactly on the yield surface. In the third sub-step, recalculate χ_i^j and θ_i^j for the macro-elements with $\xi_i^j \neq \xi_{\min}^j$ by maximizing $M_{ix}^j \phi_{ix}^j + M_{iy}^j \phi_{iy}^j$ with the restriction that the resulting scaling factor of that macro-element is not smaller than $\xi_{\min}^j$.

After the above three sub-steps, all the macro-elements will lie on the yield surface while $\xi_{\min}^{j}$ is maximized, and the resulting χ_i^j and θ_i^j yield maximum internal energy dissipation rates in that iteration.

(3) With the obtained χ_i^j and θ_i^j, the bending moment on the *ith* macro-elements in the corresponding local system is determined from Equation 2.1 (e) as follows

$$M_{ix}^{j} = \chi_i^j M_{pai} \cos\left(\frac{\pi}{2}\frac{\xi_{\min}^{j} V_i^j}{V_{pai}}\right)\cos\left(\theta_i^j + \varphi_i^j\right) \qquad 3.1\ (a)$$

$$M_{iy}^{j} = \chi_i^j M_{pai} \cos\left(\frac{\pi}{2}\frac{\xi_{\min}^{j} V_i^j}{V_{pai}}\right)\sin\left(\theta_i^j + \varphi_i^j\right) \qquad 3.2\ (b)$$

where φ_i is the angle between the *x*-axis and the direction of the lateral load in the *ith* macro-element local system, which is determined from the elastic analysis. Considering the assigned bending moments on the macro-elements, $\left(\xi_{\min}^{j} V_i^j, \xi_{\min}^{j} F_i^j, M_i^j\right)$ are in equilibrium with $\xi_{\min}^{j}\left(\mathbf{P_c} + \xi_{\min}^{j-1}\lambda\tilde{\mathbf{p}} - \mathbf{P_u}^{j-1}\right)\Big/\xi_{\min}^{j-1} + \mathbf{P_u}^{j}$. Thus $\mathbf{P_u}$ represents the unbalanced loads (global overturning moment and torsion if piles are battered) in the jacket global system, which results from the sum of the assigned bending moment on each macro-element in the local system. Hence, $\mathbf{P_u}^{j}$ is determined from Equation 3.1 and 3.2 as follows (presented in a vector form in order to be consistent):

$$\mathbf{P_u}^{j} = \sum_{all\ i}\left\{\mathbf{B}_i^{-1}\left[0, 0, 0, M_{ix}^{j}, M_{iy}^{j}, 0\right]^{T}\right\} \qquad 3.2$$

where $\mathbf{B}_i$ is the transformation matrix from the jacket global system to the *ith* pile local coordinate system. As can be seen from Figure 3.2, ξ_i^j represents an inverse measure of loads on the macro-element. Heavily (lightly) loaded macro-elements have smaller (larger) ξ_i^j, and the stiffnesses should be reduced (increased) in the

next iteration to simulate the load re-distribution of the plastic system. Therefore, the elastic compensation method is used so that the axial and lateral stiffnesses of each macro-element are respectively updated as $k_{Ai}^{j+1} = \xi_i^j k_{Ai}^j$ and $k_{Li}^{j+1} = \xi_i^j k_{Li}^j$. Then *(j+1)th* iteration starts with $\xi_{\min}^j$, $\mathbf{P}_{\mathbf{u}}^j$, k_{Ai}^{j+1} and k_{Li}^{j+1}.

The above process is repeated until convergence occurs (i.e., $\xi_{\min}^j \approx \xi_{\min}^{j-1}$, $\mathbf{P}_u^j \approx \mathbf{P}_u^{j-1}$). At this point, the loads on the macro-elements will be in equilibrium with $\xi_{\min}^j \left(\mathbf{P_c} + \xi_{\min}^{j-1}\lambda\tilde{\mathbf{p}} - \mathbf{P}_{\mathbf{u}}^{j-1}\right) \Big/ \xi_{\min}^{j-1} + \mathbf{P}_{\mathbf{u}}^j \approx \mathbf{P_c} + \xi_{\min}^j \lambda\tilde{\mathbf{p}}$. Therefore, the optimized lower bound solution is given by $\lambda_{low} = \xi_{\min}^j \lambda$.

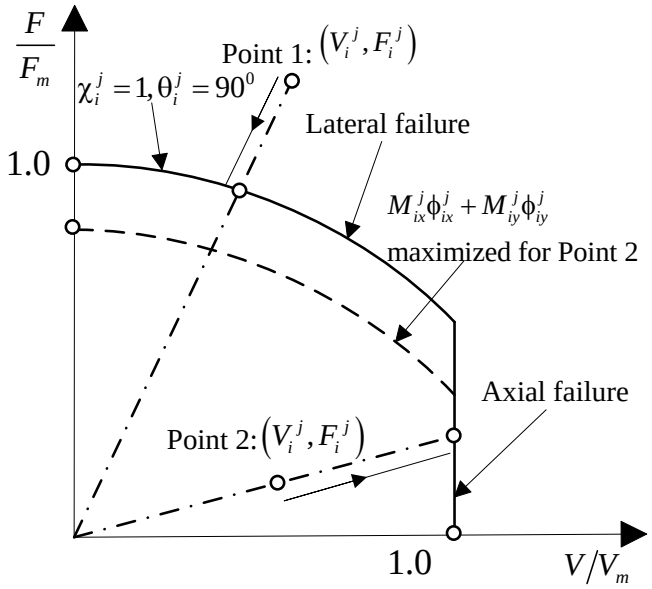

Figure 3.2 Determination of χ_i^j, ξ_i^j and θ_i^j

3.3 3D upper bound analysis of pile systems

As in the lower bound analysis, the upper bound analysis is equivalent to finding an optimized upper bound load multiplier λ_{upp} from the energy balancing equation for pertinent kinematically admissible virtual velocity fields. Since the jacket structure is

rigid, the plastic virtual velocity field of a pile system can be represented by the plastic virtual velocity vector of the jacket $\dot{\mathbf{\Delta}}$, which contains six degrees of freedom and is defined at the origin of the jacket global coordinate system as shown in Figure 3.1. The '$\cdot$' in $\dot{\mathbf{\Delta}}$ indicates the virtual velocity throughout this study. By equating the jacket input work rate to the pile system energy dissipation rate, the upper bound load multiplier λ_{upp} can be obtained as follows

$$\lambda_{upp} = \frac{\sum_{all\ i} \dot{D}_i - \mathbf{P_c} \bullet \dot{\mathbf{\Delta}}}{\tilde{\mathbf{p}} \bullet \dot{\mathbf{\Delta}}} \qquad 3.3$$

where $\dot{D}_i$ is the energy dissipation rate of the *ith* macro-element; The '$\bullet$' is the vector scalar product. Note that $\mathbf{P_c}$ and $\tilde{\mathbf{p}}$ are defined based on the same reference point with $\dot{\mathbf{\Delta}}$, i.e., the jacket origin in the global coordinate system. A detailed derivation of λ_{upp} is given in Appendix II.

$\dot{\mathbf{\Delta}}$ governs the plastic failure mechanism of the jacket pile system, and needs to be admissible such that: (1) $\tilde{\mathbf{p}} \bullet \dot{\mathbf{\Delta}} > 0$, so the input energy due to environmental loads is positive; (2) $\left(\sum_{all\ i} \dot{D}_i - \mathbf{P_c} \bullet \dot{\mathbf{\Delta}} \right) > 0$, so the pile system does not fail under the constant gravity loads $\mathbf{P_c}$. For a fixed $\dot{\mathbf{\Delta}}$ and hence a fixed failure mechanism, λ_{upp} is optimized by minimizing each $\dot{D}_i$, The minimization of $\dot{D}_i$ involves the determination of the plastic virtual axial velocity due to the yielding at the pile head and the location of the lower plastic hinge in each pile (Appendix II), which depends on the pile head virtual velocity that is compatible with $\dot{\mathbf{\Delta}}$. Theoretically, by considering every admissible failure mechanism (i.e., every admissible $\dot{\mathbf{\Delta}}$), the minimization of $\dot{D}_i$ can give the optimized λ_{upp} equaling the exact solution.

In general, the determination of $\dot{\boldsymbol{\Delta}}$ corresponding to the exact failure mechanism under 3D loading involves the optimization of five parameters ($\dot{\boldsymbol{\Delta}}$ has six degrees of freedom, and the relative values in each degree of freedom govern the failure mechanism). As the computational time of the upper bound method approximately increases geometrically with the number of optimizing parameters (if a grid search algorithm is used), it is expected that the general 3D upper bound method will be complex and inefficient, and the merits of limit analysis may begin to be lost.

The method to calculate λ_{upp} proposed here fully takes the advantage of the results from the elastic analysis as presented in the previous section. As discussed before, the elastic displacement field can be used to mimic the plastic displacement field in the limiting case. Thus the elastic displacement of the jacket obtained from each lower bound iteration represents a failure mechanism of the jacket, and the one corresponding to the converged optimized lower bound solution is expected to be close to the exact failure mechanism. If $\dot{\boldsymbol{\Delta}}$ in Equation 3.3 takes the value of the jacket elastic displacement corresponding to the converged optimized lower bound solution, the resulting λ_{upp} is expected to be close to the exact solution. This proposed method greatly improves the efficiency of the 3D upper bound method since the searching process of the jacket failure mechanism is avoided.

3.4 Special case: lower bound solution for in-plane loading

For the in-plane lower bound analysis, the procedure remains the same as in the 3D case. However, the global load vector on the jacket contains only three components (the vertical load, the horizontal load and the overturning moment) instead of six, and the global stiffness matrix is three-by-three instead of six-by-six. Another

simplification is that the determination of χ_i^j will be more straightforward. From Equation 2.6 (c), χ_i^j should be as large as possible to maximize the yield surface. However, from equilibrium considerations, χ_i^j should be as small as possible in order to reduce the driving overturning moment acting on the jacket. Three sub-steps are used to determine χ_i^j: first, for the *ith* macro-element, assign a value for χ_i^j (as small as possible) to maximize ξ_i^j. As can be seen from Figure 3.2, if $\left(\xi_i^j V_i^j, \xi_i^j F_i^j\right)$ always lies on the curve part of the yield surface for $-1 \le \chi_i^j \le 1$, then $\chi_i^j = 1$ in order to maximize the yield surface, and the lateral failure is expected. If for a certain value of χ_i^j, $\left(\xi_i^j V_i^j, \xi_i^j F_i^j\right)$ will lie on the vertical portion of the yield surface, then χ_i^j is determined such that $\left(\xi_i^j V_i^j, \xi_i^j F_i^j\right)$ lies on the corner of the yield surface, and the maximum ξ_i^j is determined to be $\xi_i^j = V_{mi} / V_i^j$. This represents axial failure. Any value larger than this χ_i^j will not increase ξ_i^j as the failure is governed by the axial failure ($\xi_i^j = V_{mi} / V_i^j$). Any value smaller than this χ_i^j leads to the lateral failure, and ξ_i^j is not maximized. Thus χ_i^j is determined from Equation 3.4 as follows:

$$\chi_i^j = \begin{cases} 1, & \text{if } \dfrac{F_i^j / F_{mi}}{V_i^j / V_{mi}} \ge \left[\cos\left(\dfrac{\pi}{2}\dfrac{V_{mi}}{V_{pai}}\right)\right]^{\alpha} \\ \dfrac{2\left[\left(F_i^j V_{mi}\right) / \left(F_{mi} V_i^j\right)\right]^{1/\alpha}}{\cos\left[\left(\pi V_{mi}\right) / \left(2 V_{pai}\right)\right]} - 1, & \text{if } \dfrac{F_i^j / F_{mi}}{V_i^j / V_{mi}} < \left[\cos\left(\dfrac{\pi}{2}\dfrac{V_{mi}}{V_{pai}}\right)\right]^{\alpha} \end{cases} \qquad 3.4$$

3.5 Special case: upper bound solution for in-plane loading

For the in-plane upper bound analysis, the procedure remains the same as in the 3D case. However, the global load vector on the jacket only contains three components as

in the in-plane lower bound analysis. Besides, all the virtual displacements are projected onto the plane under consideration.

3.6 Discussion on lower and upper bound methods

For the lower bound analysis, a rigorous proof for the convergence of the proposed procedure has not been established, nor has the convergence rate been evaluated. However, the strong convergent characteristic is observed in both 2D and 3D cases. Generally 10 to 20 iterations can give a result with sufficient accuracy. The iterations are efficient since the analysis is elastic. Generally the 3D analysis requires more computational time than the 2D case since the determination of χ_i^j and θ_i^j requires the maximization of $M_{ix}^j\phi_{ix}^j + M_{iy}^j\phi_{iy}^j$. Nevertheless, by using an elastic solution, minor additional effort is required to extend the planar analysis to the 3D case. By using the approximate yield surface at the pile head (Equation 2.6), the searching of the lower plastic hinge of each pile is avoided, which further improves the efficiency of the method.

The proposed lower bound method starts with an arbitrarily distributed initial axial and lateral stiffnesses of piles $\left(k_{Ai}^0, k_{Li}^0\right)$. According to Ponter and Carter (1997), the displacement field generated from the elastic analysis can be treated as the plastic displacement field in the limiting case since both of them are kinematically admissible and satisfy the displacement boundary conditions. Therefore, the linear matching method (Ponter *et al.*, 2000, Ponter and Carter, 1997) can be used to generate an initial distribution of pile axial and lateral stiffnesses as follows: starting with a specific initial distribution of $\left(k_{Ai}^0, k_{Li}^0\right)$, when a convergent solution is obtained at the *jth* iteration with $\left(k_{Ai}^j, k_{Li}^j\right)$, the axial and lateral loads on the macro-element are

calculated from the convergent elastic displacement field (treated as a plastic displacement field, and the associated flow rule is adopted) by solving Equation 3.5:

$$Y\left(V_i^{as}, F_i^{as}, \chi_i^j, \theta_i^j\right) = 0 \qquad 3.5\ (a)$$

$$\frac{\delta_{Ai}}{\delta_{Li}} = \frac{\partial Y}{\partial V_i^{as}} \Big/ \frac{\partial Y}{\partial F_i^{as}} \qquad 3.5\ (b)$$

where Y is the yield surface expressed in Equation 2.6 (b) (lower bound solution); the superscript '*as*' indicates the loads are calculated from the associated flow rule when a convergent solution is obtained at the *jth* iteration with $\left(k_{Ai}^j, k_{Li}^j\right)$; δ_A and δ_L respectively represent the axial and lateral displacements of the pile head from the elastic analysis when the convergence is achieved. A new initial distribution of stiffnesses is obtained as $k_{Ai}^0 = V_i^{as} / \delta_{Ai}$ and $k_{Li}^0 = F_i^{as} / \delta_{Li}$. Then the previous procedures in Section 3.2 can be repeated with the new $\left(k_{Ai}^0, k_{Li}^0\right)$ to get an updated convergent result. The reason for using the linear matching method to generate the new $\left(k_{Ai}^0, k_{Li}^0\right)$ is that if the obtained lower bound solution is close to the true solution, the displacement field from the elastic analysis is expected to be similar to the true plastic displacement field, and the loads on the macro-element from the lower bound solution will approximately obey the associated flow rule.

For the linear matching method, simplified yield surfaces can be used in Equation 3.5 (e.g., χ, θ and α are set equal to 1.0, 90^0 and 0.7, respectively) to generate the initial distribution of the axial and lateral stiffnesses because the optimization of the lower bound capacity is mainly governed by the systematic updates of stiffnesses and not their initial values. For the same reason, for the lower bound analysis, the linear matching method only improves the prediction accuracy slightly in the base shear-

overturning interaction region for complex pile systems (e.g., 8-leg platforms with piles differ in length), where different piles may exhibit different failure modes.

For the upper bound analysis, the approach of taking the elastic displacement field of the jacket corresponding to the converged optimized lower bound solution as a failure mechanism avoids the searching of the optimized failure mechanism of the jacket. Typically, the searching of the failure mechanism governs the computational time in the upper bound analysis of a pile system. Hence, the proposed method greatly improves the efficiency of a general 3D upper bound method for pile systems. Furthermore, the upper bound solution provides a criterion to check the accuracy of the proposed bounding methods by comparing the lower and upper bound solutions.

There are two issues of clarification in the proposed upper bound methods: (1) since the upper bound solution depends highly on the assumed failure mechanism (i.e., the elastic displacement of the jacket in this study), it is generally necessary to use the linear matching method to generate different axial and lateral stiffnesses in order to obtain a failure mechanism close to the exact one; and (2) the accuracy of the proposed upper bound depends both on the accuracy of the lower bound solution (because the elastic solution in the lower bound analysis gives the failure mechanism in the upper bound analysis) and the pile system layout. Since the proposed upper bound solution is not optimized against all the potential failure mechanisms, the obtained λ_{upp} may not be the exact one. This discrepancy is especially true for statically determinate systems, where the lower bound solution may be determined accurately independent of the assumed failure mechanism, while the upper bound solution may not be optimized. However, based on the current study, the difference between the two bounding solutions is generally within 10%, even for statically determinate systems.

Since each pile is modeled as a macro-element in the lower bound analysis with a yield surface given by Equation 2.6, piles are equivalent to shallow foundations if yield surfaces are constructed for shallow foundations in the lower bound analysis. Hence with minor changes on the determination of the moment on the macro-element depending on the specific yield surface, the lower bound method proposed here can be further extended to analyze the lower bound capacity of shallow foundation systems such as jack up rigs. Thus the limit analysis of offshore platform deep and shallow foundation systems can be synthesized. Although the analyses of single piles and pile systems presented in the current study are conducted on offshore steel pipe piles, the general analysis framework is the same for concrete pile systems for bridges if the concrete piles are designed to form plastic hinges in the ultimate condition. Hence, the lower and upper bound methods proposed here can be further extended to concrete pile systems for bridges.

3.7 Conclusions

This chapter presents lower and upper bound methods for predicting the pile system capacity. The lower bound solution employs the simplified single pile failure surface proposed in Chapter 2 and is based on an elastic analysis. Therefore, the two dimensional and three dimensional lower bound analyses of the pile system capacity can be synthesized. The upper bound solution employs the failure mechanism determined from the elastic solution in the lower bound analysis. The proposed bounding solutions are expected to be efficient because the lower bound solution is based on elastic analyses and the searching for the failure mechanism is avoided in the upper bound analysis. In addition, the proposed bounding solutions consider the global torsion on the jacket and the potential of an out-of-plane overturning failure since the failure of the pile system is not restricted to a specific vertical plane.

4 Offshore Pile System Assessment – Case Studies

This chapter aims to present the application of the proposed pile system capacity model in the offshore pile foundation assessment. Selected case study offshore pile systems will be analyzed. The effects of global torsion, out-of-plane failure, and strain softening in the pile axial capacity will be studied. Various factors affecting the pile system capacity will be addressed.

4.1 Pile system failure surface

Following the convention of offshore platform analyses, the ultimate load that a pile system can resist is expressed in terms of the global base shear, which is the horizontal force acting on a platform at the mudline. Hence, the failure surface of a pile system can be constructed in terms of the global base shear at the mudline and the global overturning moment at the mudline (Murff and Wesselink, 1986). In this study, the global load acting on the jacket can be expressed as $\mathbf{P}_c + \lambda\tilde{\mathbf{p}}$ as shown in Chapter 3. Thus the global overturning moment at the mudline is calculated as $\mathbf{h} \times \lambda\tilde{\mathbf{p}}$, where $\mathbf{h}$ is the moment arm vector, and "$\times$" represents the cross product. The above calculation implicitly assumes that the reference point at the mudline for defining the global overturning moment is on the line that passes the vector of $\mathbf{P}_c$.

For platforms in shallow water, the platform will usually fail in the horizontal translation, a so-called base shear failure. For deep water platforms, the failure mode is usually overturning. For intermediate water depths, the platform failure mode is a combined interaction of base shear and overturning, i.e., some of the piles fails by forming two plastic hinges, while others plunge-in or pull-out axially. Figure 4.1

shows a simple illustration of the different failure modes, and the corresponding region in the failure surface.

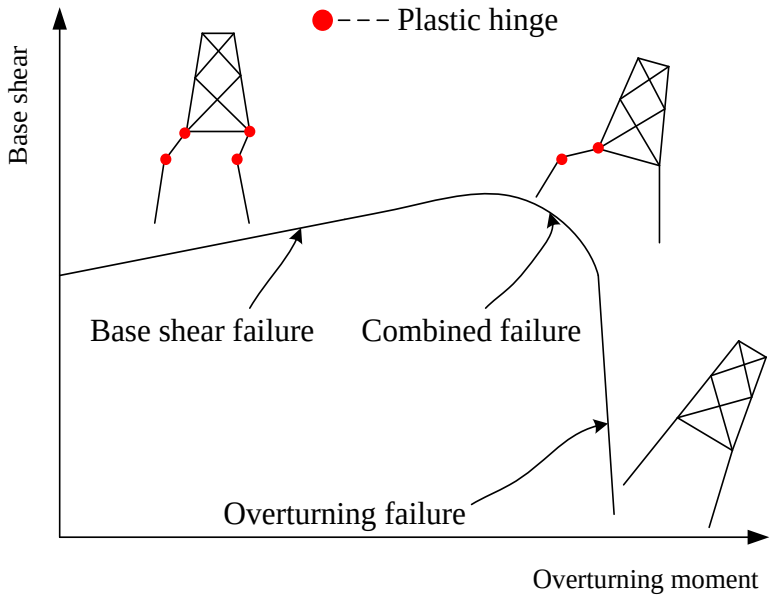

Figure 4.1 Illustration of different pile system failure modes

4.2 Platform 10

4.2.1 Description

The description of Platform 10 presented here follows Chen *et al.* (2010) and Chen *et al.* (2013). Platform 10 is a 3-leg jacket platform (tripod) located in about 360 ft of water depth offshore from the coast of Louisiana, USA. The platform is categorized as A-2. It was inspected after Hurricane Ike in 2008, and was found to leaned 4 degrees to the south-west corner of the platform. The failure of the platform was observed to be initiated by the pull-out of one of the piles loaded in tension. A plan view is shown in Figure 4.2. The piles are steel pipe piles, designated as Pile 1, 2 and 3 as shown in the figure. Pile 1 and 2 are the same and have two-way batter with a total angle of about 11.3^{o} (i.e., vertical to horizontal of 5:1 indicated as V5:H1 in Figure 4.2). Pile 3

is vertical and has the largest lateral capacity among the piles. The outer diameters of all the three piles are 4 ft, the wall thickness varies from 1.75 in to 1.0 in. The embedment depth of Pile 1, 2 and 3 are 215 ft, 215 ft and 265 ft, respectively.

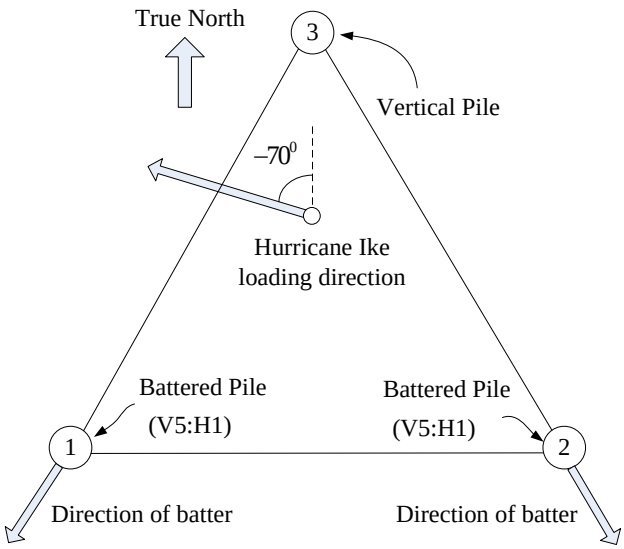

Figure 4.2 Plan view of Platform 10

The gravity load acting on the jacket is estimated to be about 3044 kips, with the loading point at about 23 ft south from Pile 3. Based on the hindcast data of Hurricane Ike (Chen *et al.*, 2010), the primary wave loading direction is about 290 degrees from True North. The environmental load is assumed to be in the horizontal direction with the loading center the same as that of the gravity load, and the moment arm of the horizontal environmental load in Hurricane Ike is about 296 ft above the mudline.

A site-specific soil boring was performed by Fugro-McClelland Marine Geoscience (FMMG) in 2001 at the location of Platform 10. According to FMMG (2001), the sampling and testing methods reflected the state-of-practice at the time of 2001. A soil boring was drilled to 348-ft below the mudline. Samples were obtained through 4.5 in drill pipe at 3 ft intervals to 50 ft penetration and at 10 ft intervals thereafter to the final boring depth. A 2.5 in outer diameter (OD) linear sampler was used to 17 ft

penetration. The remaining samples were taken using a 3 in OD thin-walled, Shelby tube sampler pushed into the soil with the weight of the drill pipe. The general soil strata are classified to be very soft clay for the top 11 ft, underlain by soft to hard clay. No sand layer is classified within the boring depth. The design undrained shear strength and submerged unit weight profiles are shown in Figure 4.3.

Table 4.1 summarizes the pile capacities based on different scenarios. For the lateral capacity, static p-y curves following API RP 2GEO (2011) are used.

Table 4.1 Pile capacities of Platform 10

Pile No.	M_{pa} (ft-kips)	V_{pa} (kips)	V_m compression (kips)			V_m tension (kips)			F_m (kips)
			Rigid	Flexible	Residual	Rigid	Flexible	Residual	
Pile 1 and 2	9736	7891	4339	3844	3552	4002	3620	3215	710
Pile 3	11212	9150	6250	5306	5081	5845	5148	4676	782

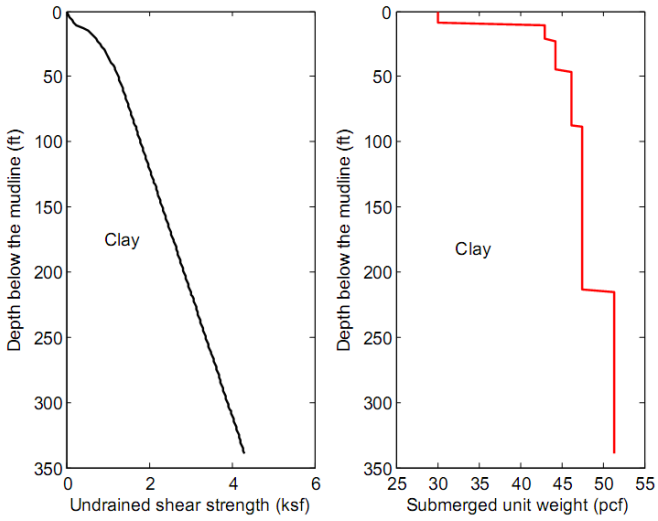

Figure 4.3 Design profile of undrained shear strength and submerged unit weight

4.2.2 FE, lower and upper bound methods comparison

Figure 4.4 shows the comparison of the failure load predicted by various methods for the horizontal loading direction of 290^o from True North. The peak axial capacity for rigid piles (indicated as "Rigid" in Table 4.1), which is obtained by summing up the peak shaft resistance and the peak end bearing capacity of soils, is used in limit analysis. For the FE analysis, the ultimate system capacity is determined at large displacement, where the load-displacement curve almost reaches a plateau; however the $P-\Delta$ effect is excluded in the FE analysis in order to be consistent with limit analysis. For this case, no softening is introduced in the soil resistance. As can be seen, the 3D lower bound solution agrees well with the result from the FE analysis. The difference between the 3D lower and upper bound solutions is within 5%. The 2D limit analysis (both the upper and lower bound analyses) over-predict the failure load in both the base shear and overturning regions. However, the reasons for the over-predictions are different. In the base shear failure region, the planar analysis neglects global torsion on the jacket. Platform 10 is asymmetric about the horizontal loading direction of 290^o, and the horizontal loading point deviates from the jacket center. Hence, the effect of global torsion for this platform is significant in the base shear region. As global torsion is resisted by the horizontal forces at the pile heads, neglecting global torsion will over-predict the failure load in the base shear region. In the overturning region, the resistance of the platform mainly comes from the axial capacities of piles. Thus the over-prediction of the planar analysis is a result of the restriction of the failure plane and the asymmetry of the platform and the loading. The planar upper bound method restricts the failure to the vertical plane parallel with the loading direction. Hence, the result is not optimized with respect to the out-of-plane rotation center when compared to the true solution. For the planar lower bound

method, equilibrium is only achieved in the loading direction plane, out-of-plane equilibrium is neglected.

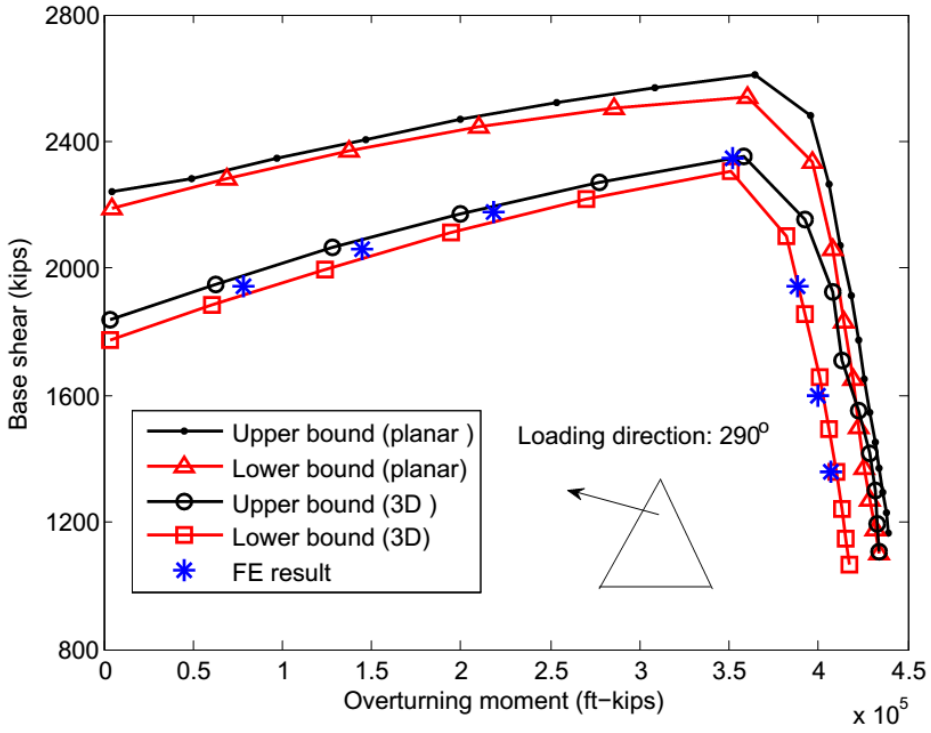

Figure 4.4 Foundation system capacity of Platform 10 (290°)

The comparison of the distributions of loads at failure from the lower bound (both 2D and 3D) and FE solutions are shown in Figure 4.5 to 4.7 for the loading direction of 290°. The distributions of loads obtained from the 3D lower bound method are in good agreement with those from the FE analysis as shown in Figure 4.5 (for pile head axial loads) and Figure 4.6 (for pile head horizontal loads in the loading direction), which demonstrates that the proposed 3D lower bound model can effectively capture the effects of global torsion and out-of-plane failures. For this 3-leg platform, the pile system is close to failure in overturning once one pile fails axially. The 2D lower bound model predicts two piles failing axially (Pile 1 and 2 as can be seen from Figure 4.5) in the ultimate condition since the failure is constrained to the vertical plane parallel with the loading direction. Hence, the 2D lower bound solution yields

larger system capacity when compared to that from the FE analysis in the overturning region as can be seen from Figure 4.6. In the base shear region, the horizontal load at the pile head in the loading direction is over-predicted by the 2D lower bound model for all the piles in the limiting case since global torsion is excluded. Hence, the system capacity is over-predicted by the 2D lower bound model in the base shear region as shown in Figure 4.4.

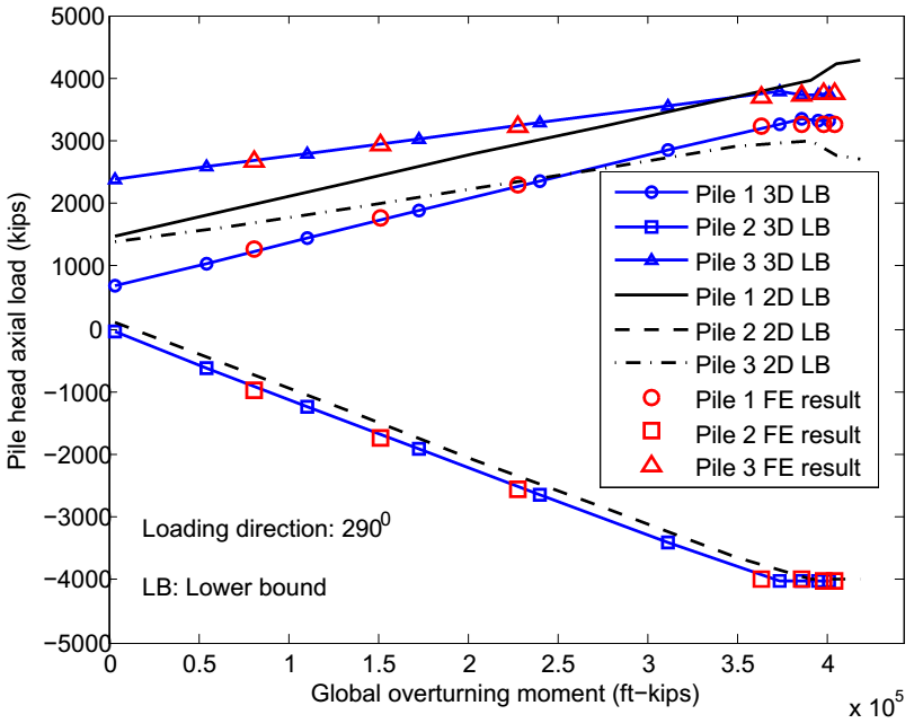

Figure 4.5 Comparison of axial load distribution (2D, 3D lower bound and FE)

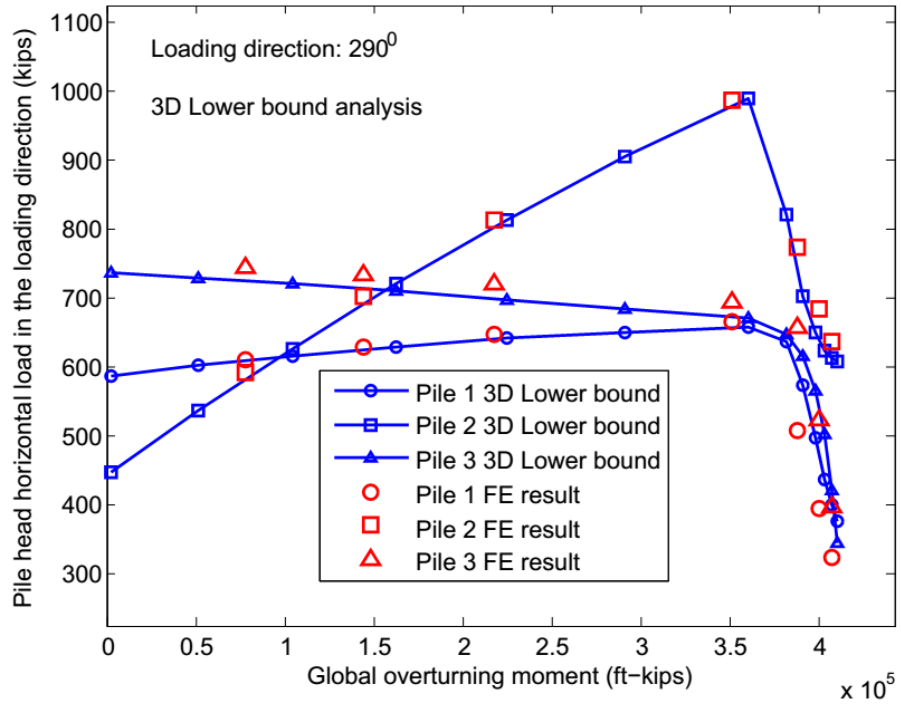

Figure 4.6 Comparison of horizontal load distribution (3D lower bound and FE)

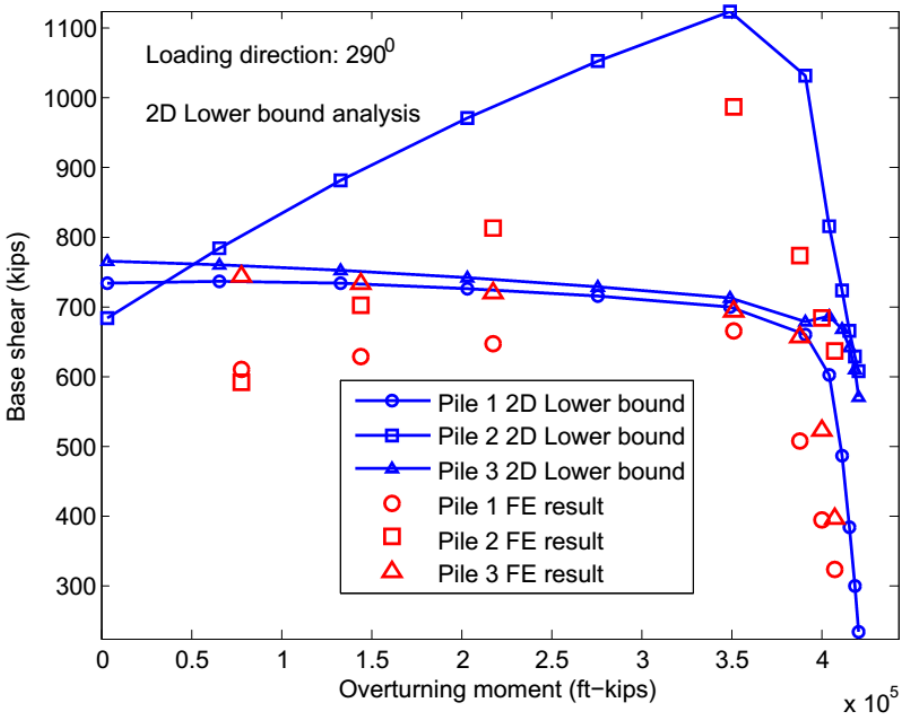

Figure 4.7 Comparison of horizontal load distribution (2D lower bound and FE)

4.2.3 Effect of global torsion

Figure 4.8 shows the effect of global torsion on the pile system capacity for loading 290^0 from True North. In the base case, a constant global torsional eccentricity is applied, i.e., the wave loading center is at 23 ft south of Pile 3 (Figure 4.2). Comparing to the base case (Figure 4.8(a)), the ultimate system capacity increases if no global torsional eccentricity is introduced for wave loading (i.e., the wave loading center coincides with the foundation center) for relatively small overturning moment arms; in the overturning failure region, the pile system capacity is independent of the torsional eccentricity because the overturning capacity is mainly controlled by the pile axial capacities; in the base shear-overturning interaction region, the pile system capacity without the torsional eccentricity is smaller than that with the constant eccentricity case. From the detailed FE analysis, the pile system tends to rotate in the clockwise direction for the wave direction of 290^o. For the case with a constant torsional eccentricity (i.e., the wave loading center is at 23 ft south of Pile 3) in 290^o, a counter clockwise torsional moment is caused by the wave load which tends to prevent the rotation of the pile system. Hence, the a higher system capacity is reached for the constant torsional eccentricity case.

The effect of the direction of global torsion on the pile system capacity is also shown in Figure 4.8 (b). A constant global torsional moment of 1.62×10^4 ft-kips, which is independent of the wave load (e.g., the wind load), is applied on the jacket. For the clockwise torsional moment, the pile system capacity is always smaller than that of the base case except in the overturning failure region. For the counter clockwise case, the pile system capacity is larger than that of the base case, except in the overturning failure region and the wave load moment arm is close to zero. The reason for the difference in the pile system capacity with different torsional moment

direction is the same to the constant torsional moment case that the counter torsional moment tends to balance the rotation caused by the wave load, and hence tends to increase the pile system capacity.

Therefore, the effect of global torsion depends highly on the torsional eccentricity, the pile layout and the expected failure mode of the pile system.

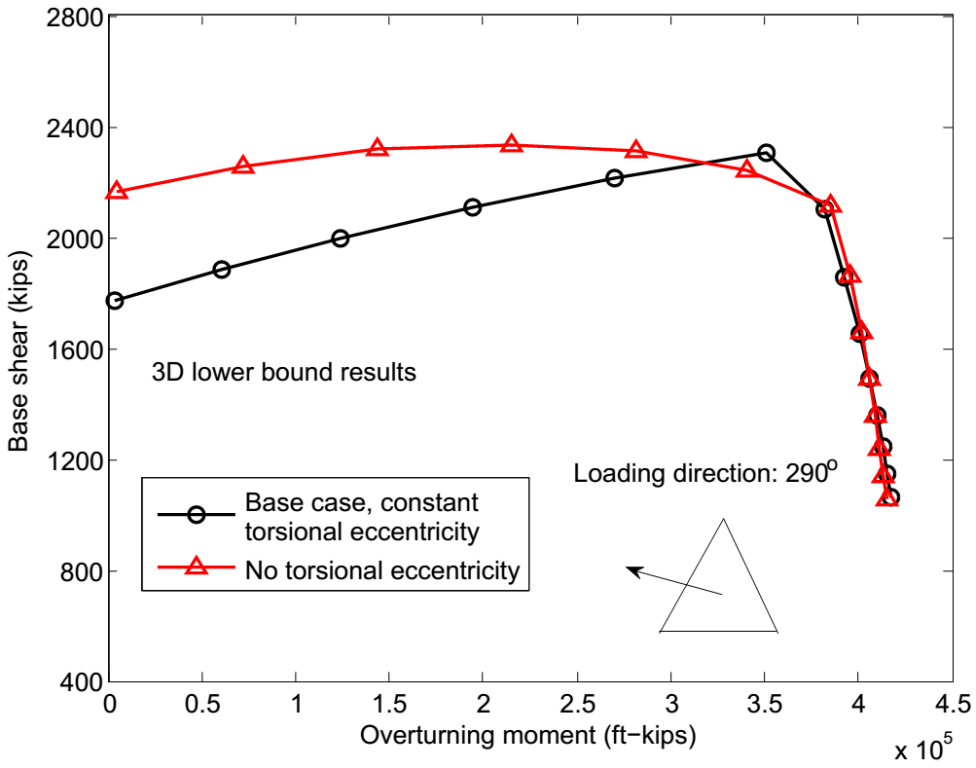

(a) Constant torsional eccentricity

Figure 4.8 continues next page

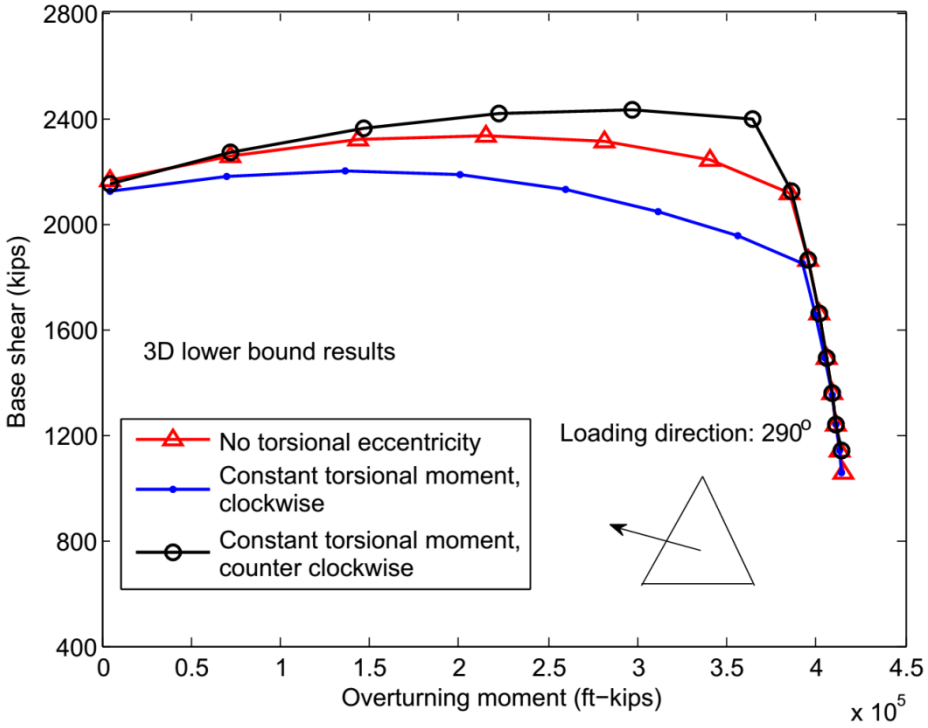

(b) Constant torsional moment

Figure 4.8 Effect of global torsion on pile system capacity

4.2.4 Effect of out-of-plane failures

Figure 4.9 shows the failure load of the foundation system for the loading direction of 225^0 from True North. The 2D bounding solutions restrict the failure of the pile system to the vertical plane parallel to the loading direction, i.e., the out-of-plane failure is prohibited. Since the platform is highly asymmetric (both platform geometry and the pile resistance) in 225^0, the 2D bounding solutions respectively over-predict the failure load by around 15% and 30% in the base shear and overturning regions when compared to the 3D bounding solutions. The extended method by Tang and Gilbert (1992) for incorporating global torsion is not a true 3D upper bound approach since the overturning rotation center is still restricted to the vertical plane parallel with the loading direction. Hence, the method of Tang and Gilbert (1992) predicts well in

the base shear region, but tends to coincide with the 2D upper bound method in the overturning region.

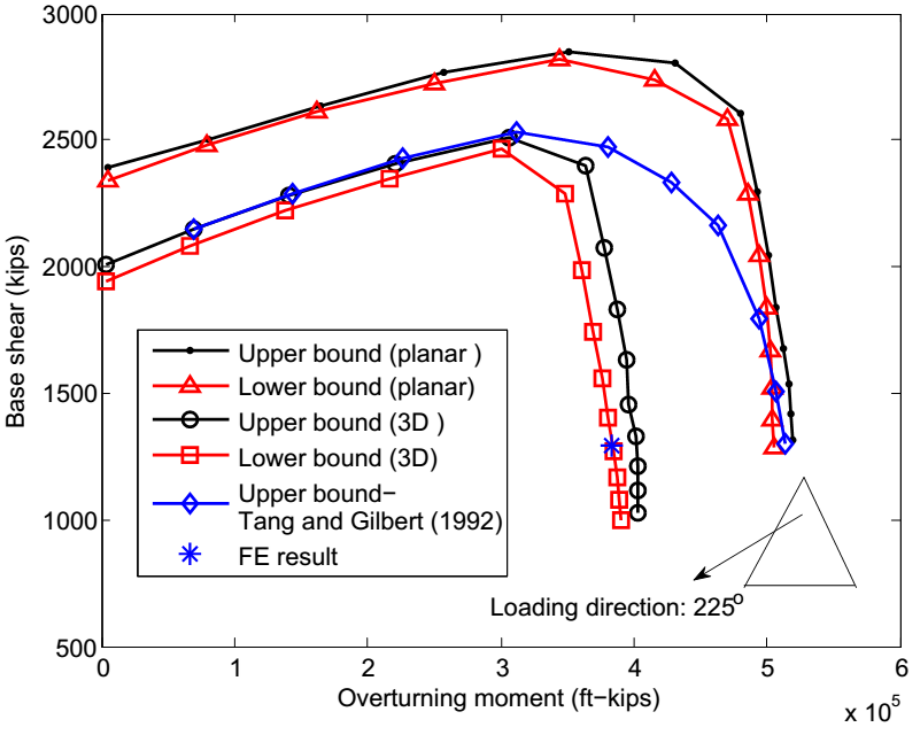

Figure 4.9 Effect of out-of-plane failure on pile system capacity

4.2.5 Effect of lower bound fitting parameter α

Figure 4.10 shows the system capacity predicted by the 3D lower bound method with different values of α (peak axial capacities of rigid piles are used). As shown, the predicted capacity is relatively insensitive to the value of α. The maximum increase of the failure load is less than 10% when α decreases from 0.9 to 0.5. Therefore, $\alpha = 0.7 \sim 0.8$ will be appropriate for preliminary studies, and it is always safe to use a slightly larger value of α in the lower bound analysis. Besides, with the proposed upper bound method, the accuracy of the two bounding solutions can always be checked.

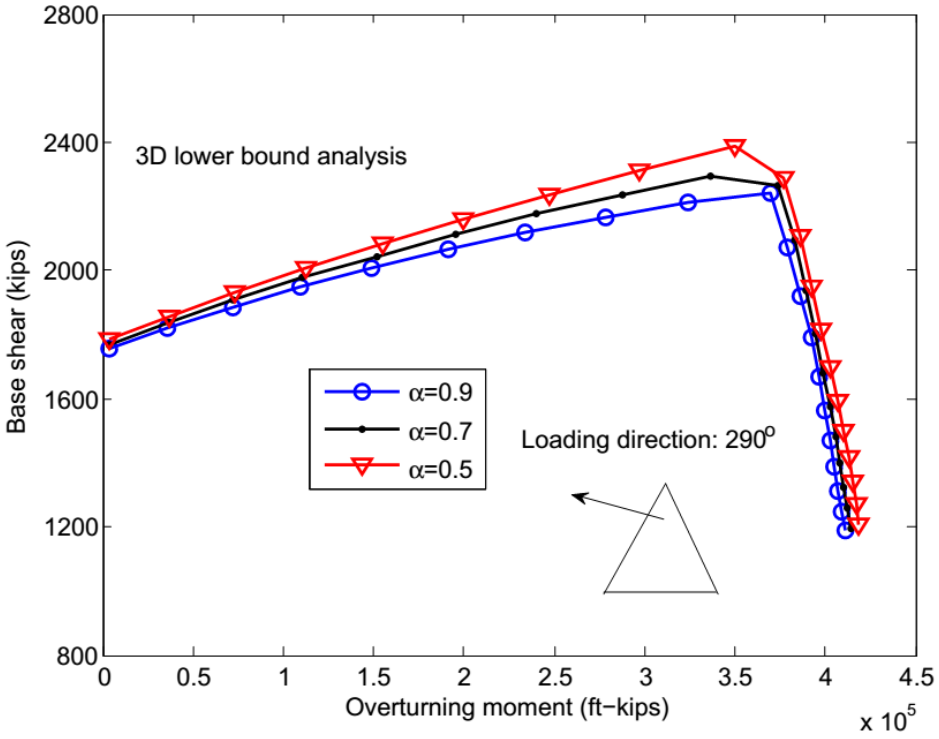

Figure 4.10 Effect of α on pile system capacity

4.2.6 Effect of strain softening

Plastic limit analysis assumes the materials under investigation are perfectly plastic. Thus strain-softening behavior of the material violates this basic assumption in limit analysis. Detailed FE analysis reveals the peak axial capacity of the actual piles (indicated as "Flexible" in Table 4.1) is about 10% lower than the capacity of rigid piles due to the strain-softening of the clay and the flexibility of the pile. The detailed nonlinear FE analysis, which considers the strain-softening of side resistance of soil and the $P-\Delta$ effect, is consistent with the expected maximum hindcast load in Hurricane Ike (see Figure 4.11). The 3D lower bound analysis using the actual axial capacity of flexible piles ("Flexible" in Table 4.1) over-predicts the expected maximum load in Hurricane Ike by about 5%; the lower bound analysis using the residual axial capacity (obtained by summing the residual side and full end bearing

resistance indicated as “Residual” in Table 4.1) under-predicts the expected maximum load by about 5%.

The plastic lower bound solution using the actual peak capacities of single piles over-predicts the actual system failure load for strain-softening soils. This over-prediction is because the lower bound solution gives the failure load in the limiting case where the applied global loads are fully redistributed among all the piles; however, for soils exhibiting strain-softening, the capacities of different piles in a pile system may not be mobilized simultaneously (i.e., when one pile reaches the peak capacity, the other piles may reach the post-peak capacity), which can result in a lower system capacity compared to the plastic lower bound solution. In reality, failure can also be defined based on the serviceability of the jacket which restricts the allowable displacement of the jacket. In those cases, even if the residual capacities of piles are used, the lower bound solution may still over-predict this serviceability load.

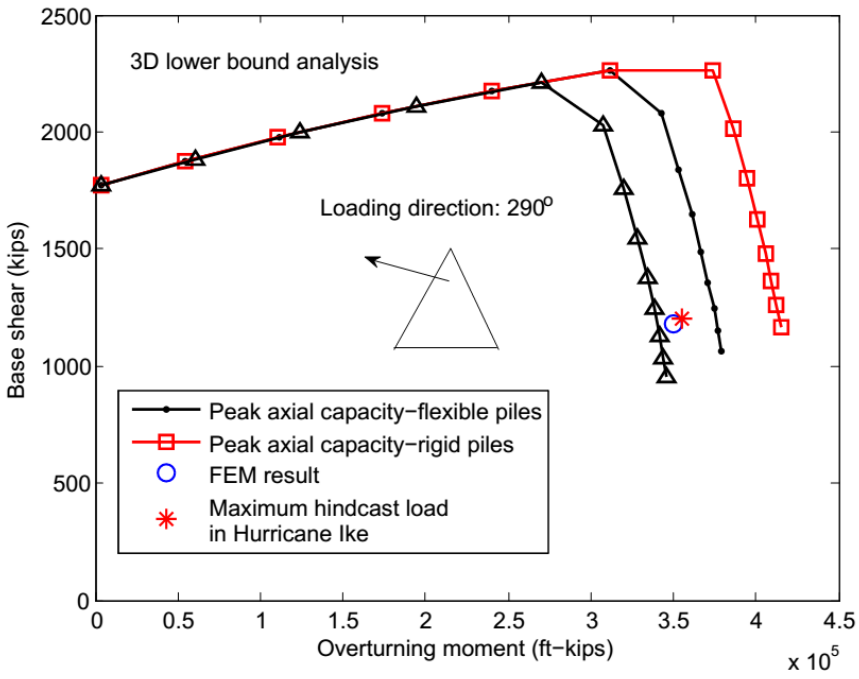

Figure 4.11 Effect of strain softening on pile system capacity

4.3 Platform 27

4.3.1 Description

Platform 27 (Chen *et al.*, 2010) is a 4-leg structure with two well conductors. The platform was installed in 2000 in the water depth of about 300 ft in the Gulf of Mexico. The platform is asymmetric with two of the piles battered in two directions, and two battered in one direction. A plan view of Platform 27 is shown in Figure 4.12.

The soil strata at the Platform 27 site are mainly classified to be clay. Very soft clay is present for the top 14 ft below the mudline, underlain by an 86 ft thick firm to stiff clay layer. A thin medium dense sand layer of about 15 ft is followed, below which the soil is very stiff clay. The double-batter piles are 264 ft long with the diameter of 48 inches. The single-batter piles are 281 ft with the diameter of 60 inches. The pile steel grade is A36 with the nominal yield strength of 36 ksi. The platform survived Hurricane Rita in 2005. The expected maximum wave height at the Platform 27 site about is 75 ft, while the design maximum wave height is 61ft (Chen *et al.*, 2010).

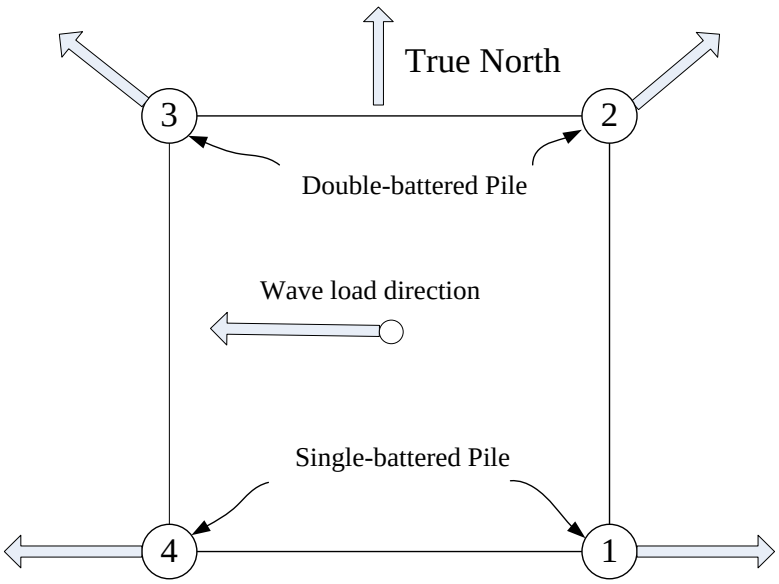

Figure 4.12 Plan view of Platform 27

4.3.2 Out-of-plane failures

Platform 27 was predicted to survive Hurricane Rita using cyclic p-y curves without the contribution of the well conductors based on a 2D upper bound model (Chen *et al.,* 2010). The primary wave load direction is in the end-on direction, i.e., 270^{o} from True North. The same result as Chen *et al.* (2010) is obtained using the 2D lower bound method proposed in this study as shown in Figure 4.13. The maximum hindcast wave load in Hurricane Rita is within the pile system failure surface obtained from the 2D analysis. Therefore, the platform is expected to survive based on the 2D analysis.

However, Platform 27 is highly asymmetric due to the different pile embedment depths and the different pile battered angles. Hence, the effect of out-of-plane failures may be significant. As shown in Figure 4.13, the transition between the pile system base shear failure and overturning failure is gradual from the 3D limit analysis, and the 2D result is about 20% higher than that from the 3D analysis under the Rita wave load path. The reason for the over-prediction in the 2D analysis is that the out-of-plane failure is excluded, i.e., Pile 3 (see Figure 4.12) will plunge into soil before the lateral capacities of all the piles are mobilized, and the pile system tends to rotate in the clockwise direction under the Rita wave load path.

From the 3D analysis, the maximum wave load from Hurricane Rita is about on the pile system failure surface which is based on cyclic p-y curves and excluding the contributions from the well conductors. However, Platform 27 survived Rita. Therefore, other factors must contribute to the survival of Platform 27.

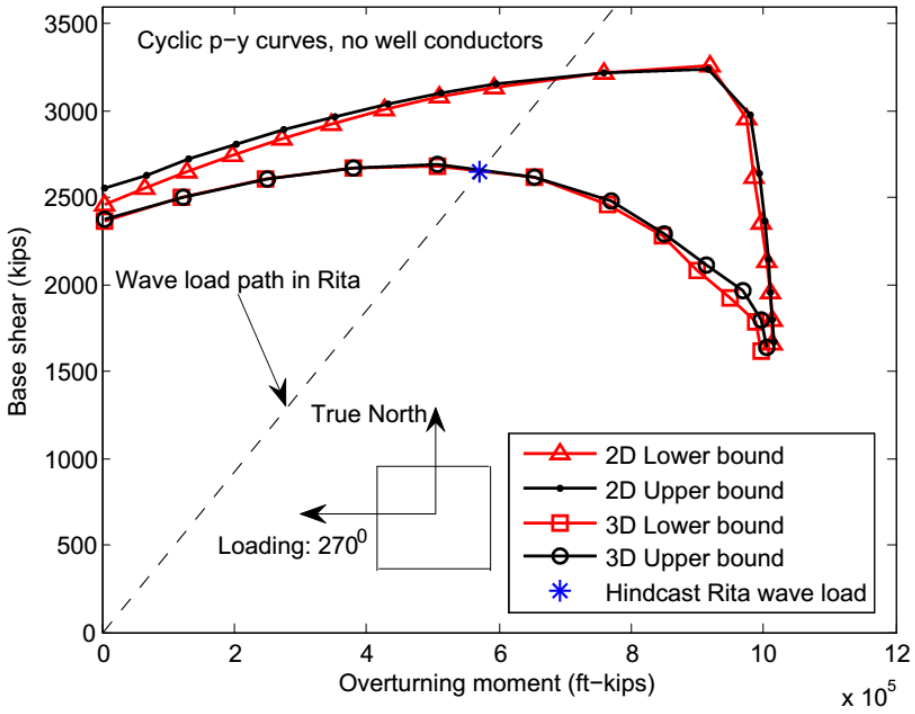

Figure 4.13 Comparison of 2D and 3D analyses (Platform 27)

4.3.3 Well conductors

Gilbert *et al.* (2010) and Gilbert *et al.* (2014) highlighted the importance of the contributions from the well conductors to the pile system capacity. However, the well conductors alone cannot explain the survival of Platform 27 since the maximum hindcast load exceeds the failure surface that takes the well conductors into account (Figure 4.14). Note that in Figure 4.14: (i) the base case refers to the pile system capacity obtained from using cyclic p-y curves, nominal yield strength, and without well conductors; (ii) detailed investigations into the hindcast data reveal that the primary wave direction deviated the end-on direction by about 15 degrees toward True North, i.e., the wave direction is about 285^{o} from True North which is used in the calculation.

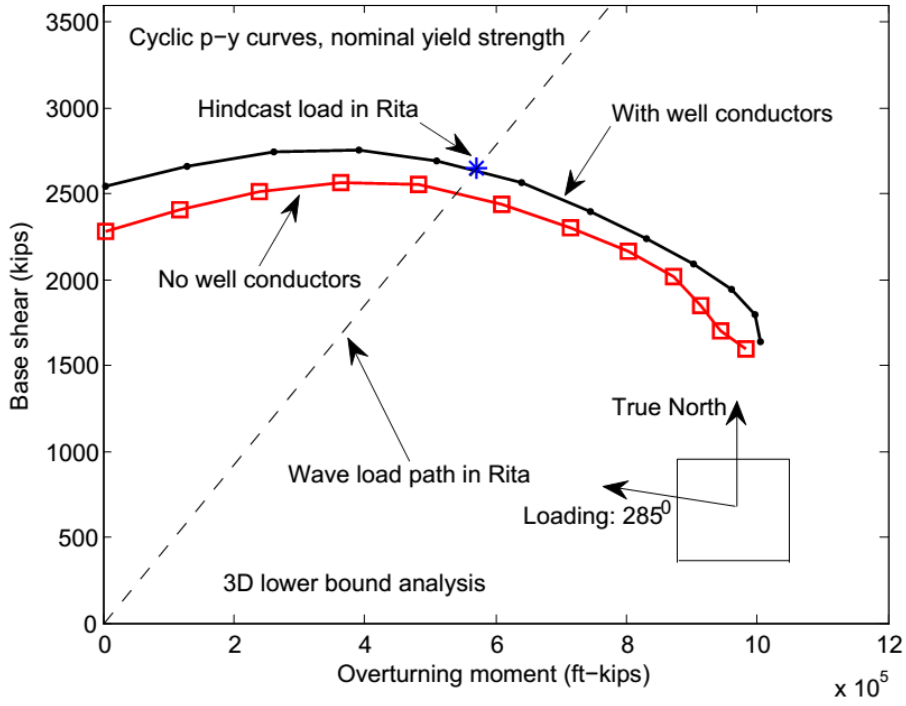

Figure 4.14 Effect of well conductors (Platform 27)

4.3.4 Static vs. cyclic p-y curves

Gilbert *et al.* (2010) and Gilbert *et al.* (2014) suggested the use of static p-y curves in the re-assessment of offshore pile foundations. This suggestion recognizes that (i) for the lateral failure under extreme random loads, piles will be pushed into soils that have not been degraded by cyclic loading (Murff *et al.*, 1993, Jeanjean, 2009), and the ultimate lateral capacity of the pile is not significantly affected by the previous cyclic loading (Senanayake *et al.*, 2015); (ii) the lateral bearing capacity factors in static p-y curves in the API guidelines for soft clays are underestimated and the magnitude of cyclic displacements in a storm is relatively small compared to that required to cause severe cyclic degradation (Hamilton and Murff, 1995).

The survival of Platform 27 can be explained by using static p-y curves (see Figure 4.15). As shown, the pile system capacity obtained from static p-y curves is larger than the hindcast load, and is about 20% higher than that from cyclic p-y curves in the

base shear region; in the overturning failure region, the effect of static p-y curves tends to be small since the system capacity will be mainly governed by the axial capacities of the piles.

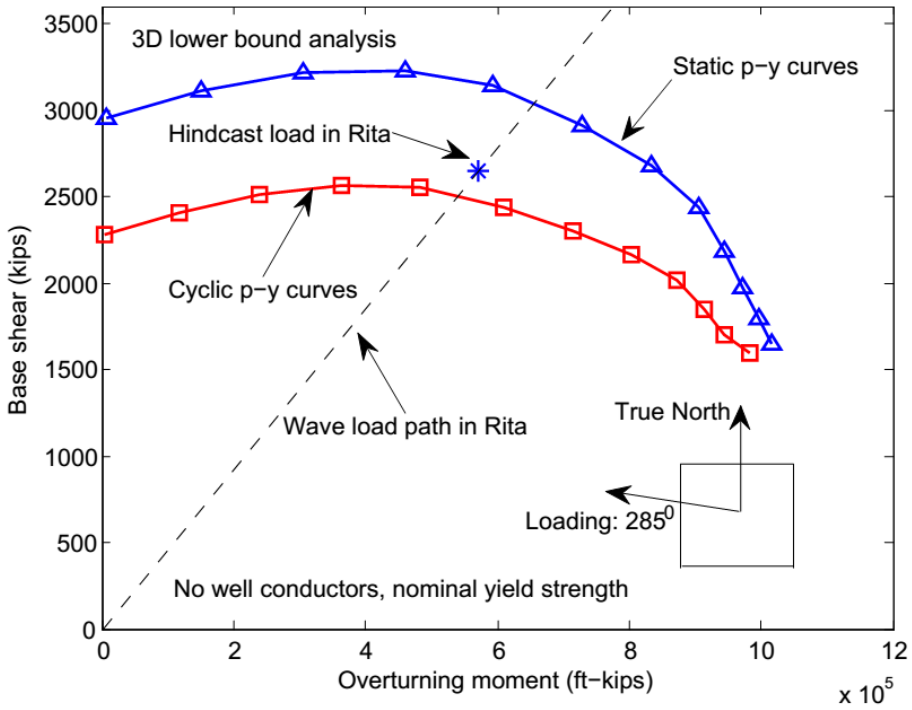

Figure 4.15 Effect of static p-y curves (Platform 27)

4.3.5 Mean vs. nominal yield strength

The nominal yield strength of 36 ksi of the A36 steel is increased by 15% to reflect the difference between the mean yield strength and the rapid loading effect (PMB Engineering, 1993, PMB Engineering, 1996, Chen *et al.*, 2010). Figure 4.16 shows the comparison of the pile system capacities obtained from nominal and mean yield strengths of the pile steel. As shown, both the base shear and overturning capacities of the pile system increase, and the survival of the platform can be explained by using the mean yield strength of the steel. Usually, the axial capacity of the pile will be governed by the geotechnical capacity of the pile. However, for Platform 27, the axial capacities of the four piles are limited by the pile structural yield capacities in the

cross-sections around 100 ft below the mudline. Therefore, using the mean yield strength increases the pile axial capacities, and consequently increases the overturning capacity of the pile system.

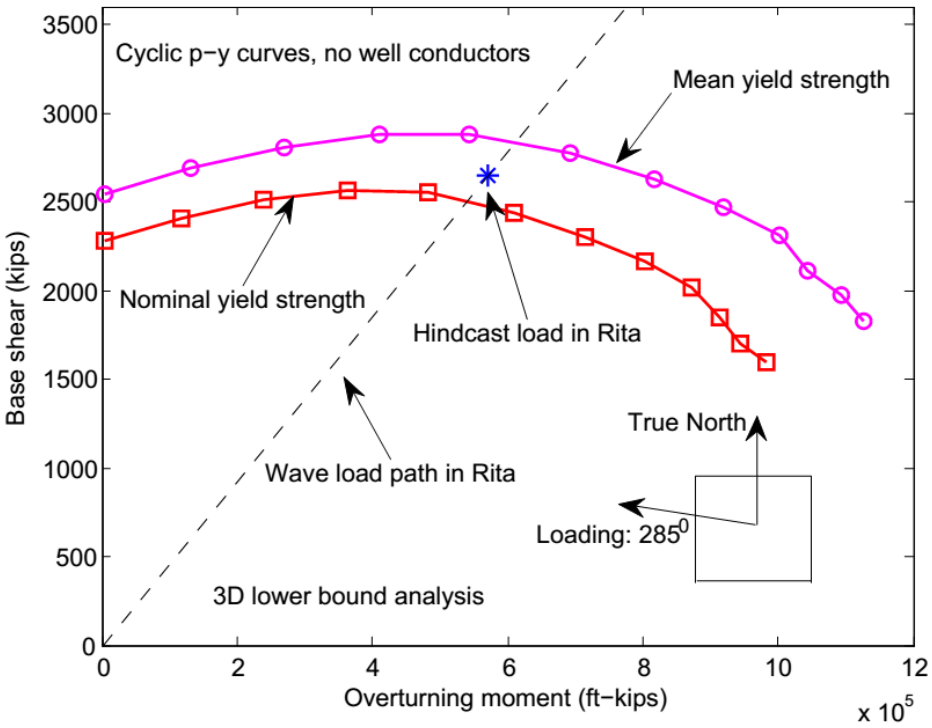

Figure 4.16 Effect of mean yield strength (Platform 27)

4.3.6 Combined effects

Considering the contribution of the well conductors, static p-y curves, and mean yield strength, the pile system capacity under the hindcast wave load path exceeds the maximum hindcast load by 35% (see Figure 4.17). Therefore, the survival of Platform 27 is expected.

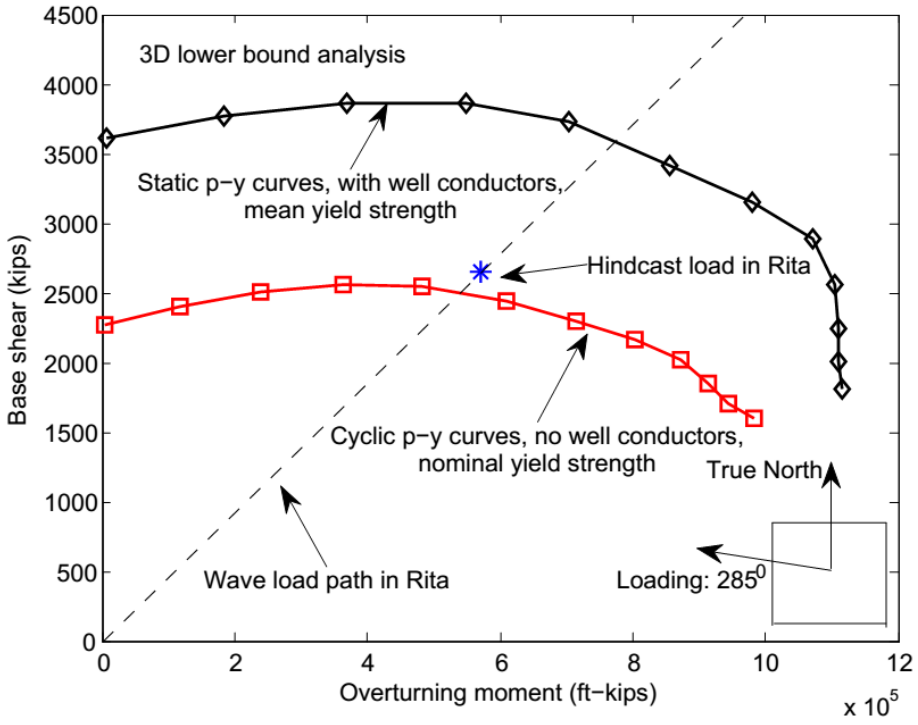

Figure 4.17 Combined effect of well conductors, static p-y curves, and mean yield strength (Platform 27)

4.4 Platform 1 and 2

4.4.1 Description

Platform 1 and 2 are located at the same site where the water depth is about 140 ft and survived Hurricane Katrina. Platform 1 was installed in 1965, while Platform 2 was installed in 1966. The two platforms are connected by a bridge. Platform 1 is an 8-leg structure with 20 well conductors, while Platform 2 is a 6-leg structure with 12 well conductors. The outer diameters of the piles of Platform 1 and 2 are 33 in and 36 in, respectively. A plan view of Platform 1 and 2 is shown in Figure 4.18. Following Chen *et al.* (2010), the soil properties used in the assessment are from an adjacent platform site about 0.3 miles away from the Platform 1 and 2 site. The top 80 ft below the mudline is soft clay, followed by interbedded sand and clay layers. All the piles

tipped at the loose sand layer with the sand internal friction angle of 25^0. The design soil profile is shown in Figure 4.19.

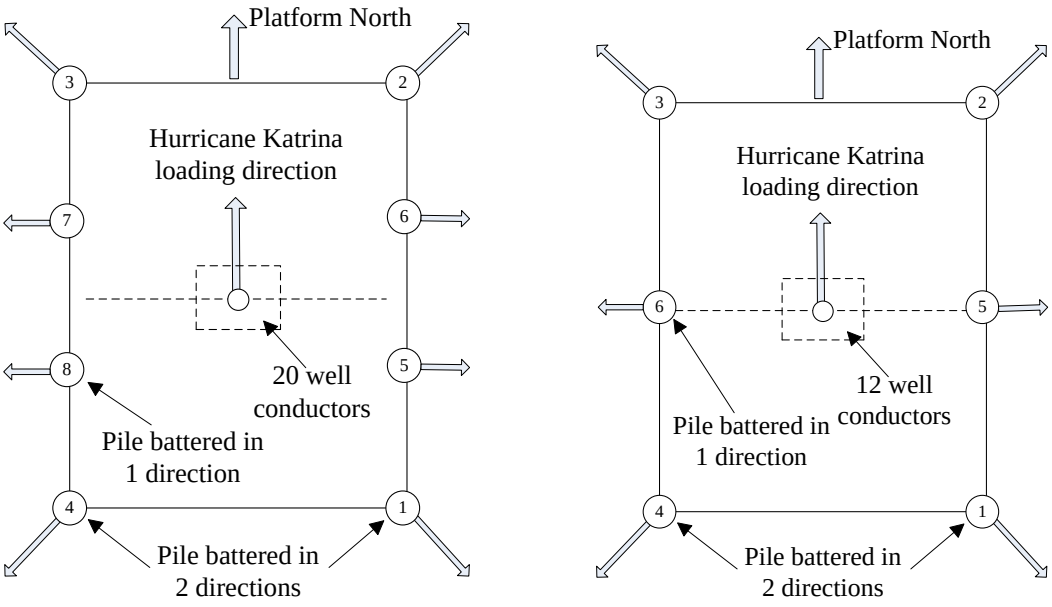

(a) Platform 1 (b) Platform 2

Figure 4.18 Plan view of Platform 1 and 2

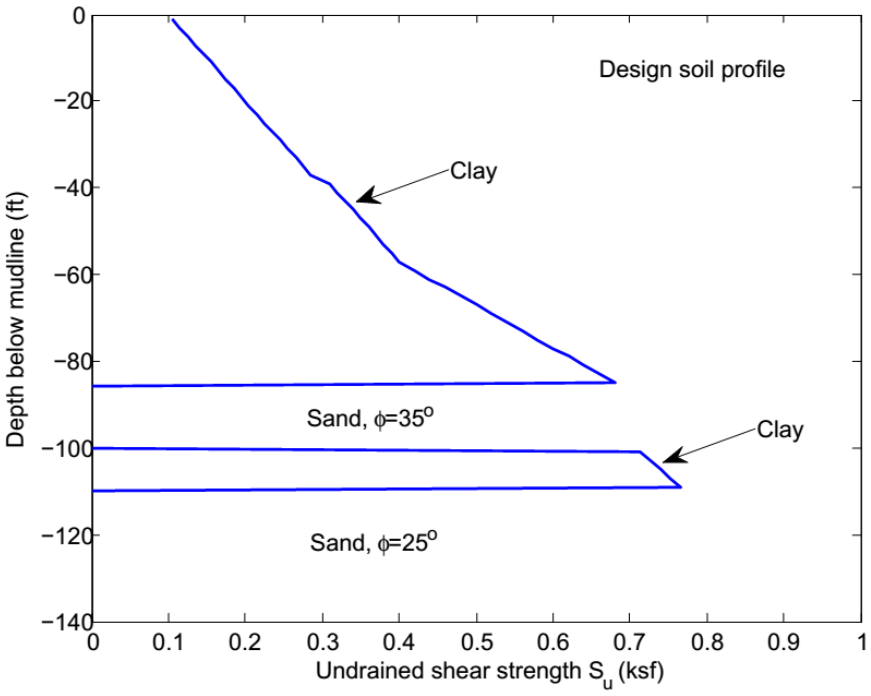

Figure 4.19 Design soil profile for Platform 1 and 2

4.4.2 Importance of site-specific geotechnical information

Chen *et al.* (2010) and Gilbert *et al.* (2010) analyzed Platform 1 and 2 based on a 2D upper bound model and highlighted the importance of the site-specific geotechnical information on the predicted pile system performance. Similar results are obtained using the proposed lower bound model. Both platforms are predicted to fail using static p-y curves, mean pile steel yield strength, and with the contributions of the well conductors (see Figure 4.20 and 21) based on the nearby geotechnical report that was obtained from a site 0.3 miles away from the Platform 1 and 2 site. However, Chen *et al.* (2010) and Gilbert *et al.* (2010) pointed out that the soil parameters may be highly underestimated due to (i) the soil from the nearby geotechnical report is complex and variable alluvial deposit with interbedded layers of clay and sand; (ii) the high uncertain alluvial deposit makes it difficult to extrapolate the soil parameters from 0.3 miles away to the Platform 1 and 2 site.

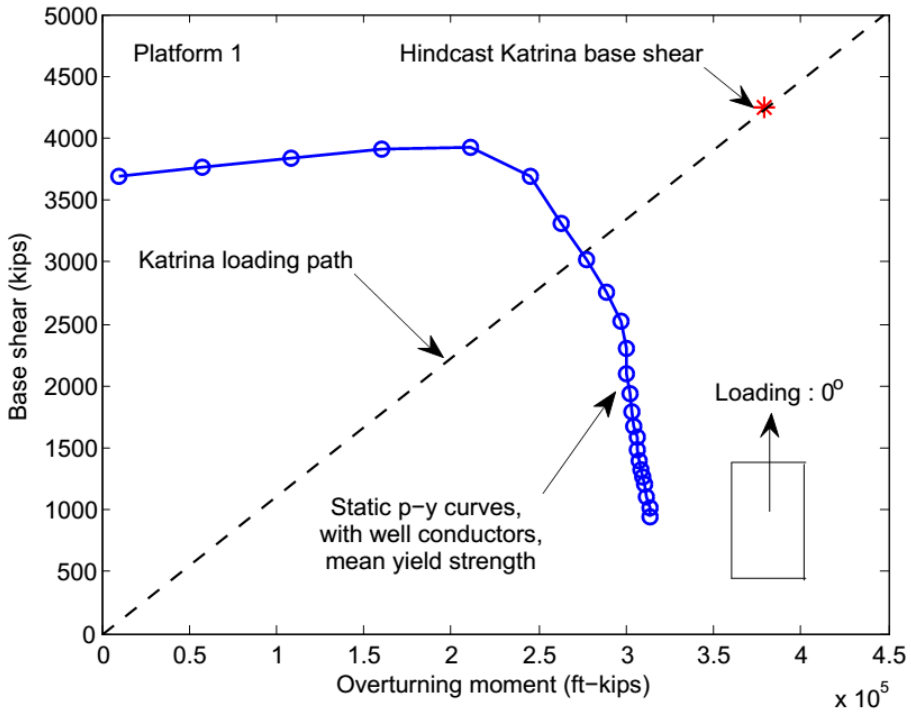

Figure 4.20 Platform 1 pile system capacity - nearby geotechnical information

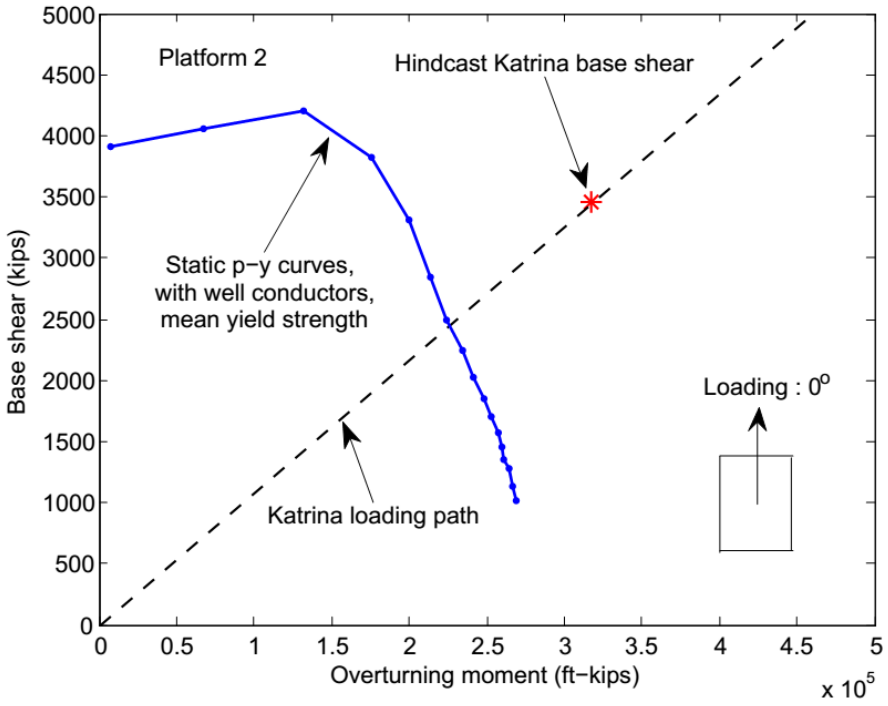

Figure 4.21 Platform 2 pile system capacity - nearby geotechnical information

Additional evidence is shown here to indicate that the soil strength parameters from the geotechnical report obtained from 0.3 miles away are not representative for the Platform 1 and 2 site. Figure 4.22 and 4.23 show the relation between the design axial load at the pile head and the design wave height (the wave force model is shown in Chapter 6, the current is neglected, and the design factor of safety is 1.5). The Glenn's design wave height criterion is also shown. Note that the Glenn's criterion gives the smallest design wave height in the 1960s (Bea, 1974). As can be seen, the axial capacities of the most heavily loaded piles from Platform 1 and 2 based on the nearby geotechnical report (labeled nearby soils in Figure 4.22 and 4.23) do not satisfy the Glenn's 25-year wave height. Hence, the interbedded clay and sand layers near the pile tip (110 ft below the mudline) are changed to dense sand with the internal friction angle of 35^0. The design axial capacities from the updated soils satisfy the Glenn's 50-year wave height in compression, but do not satisfy the Glenn's 25-year wave height in tension (see Figure 4.22 and 4.23). Since the design gravitational load in the 1960s

may be different from the one used in the current study, the internal friction angle of 35^0 reflects the current best estimate of the pile tip soil parameters.

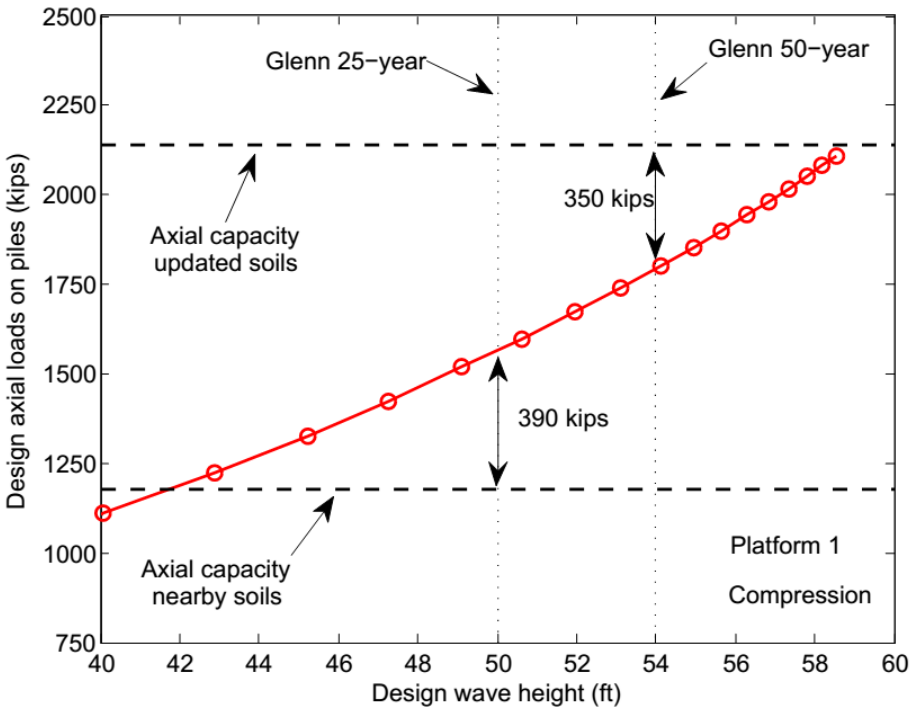

(a) Compression

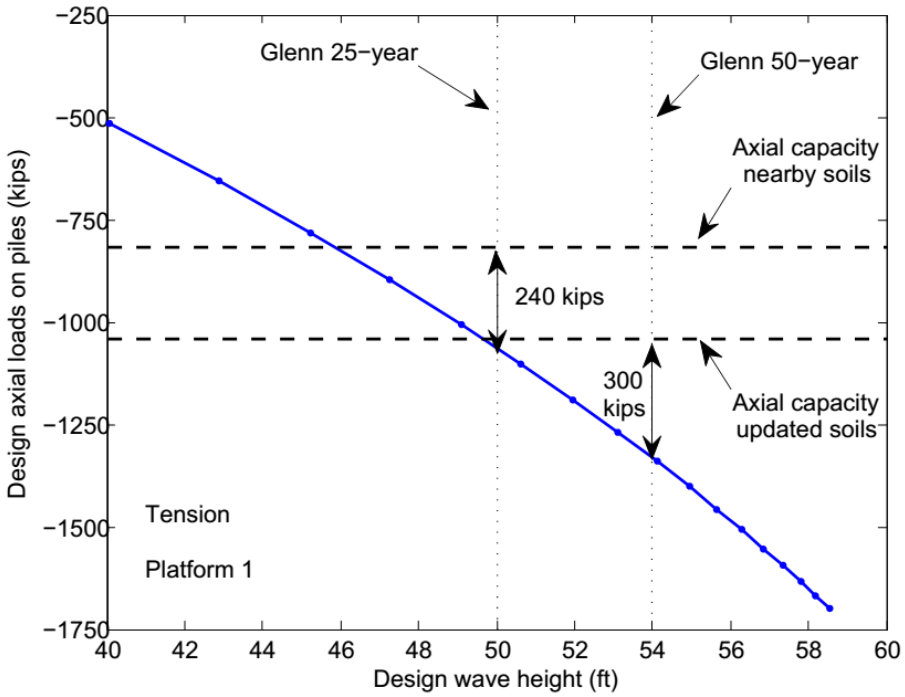

(b) Tension

Figure 4.22 Design axial load at pile head-Platform 1

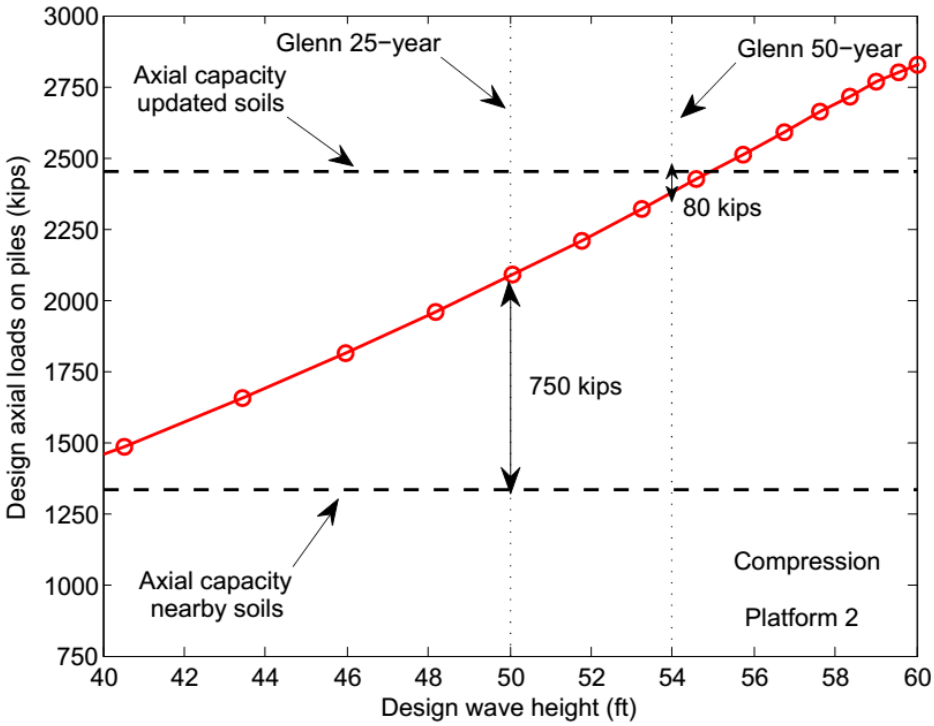

(a) Compression

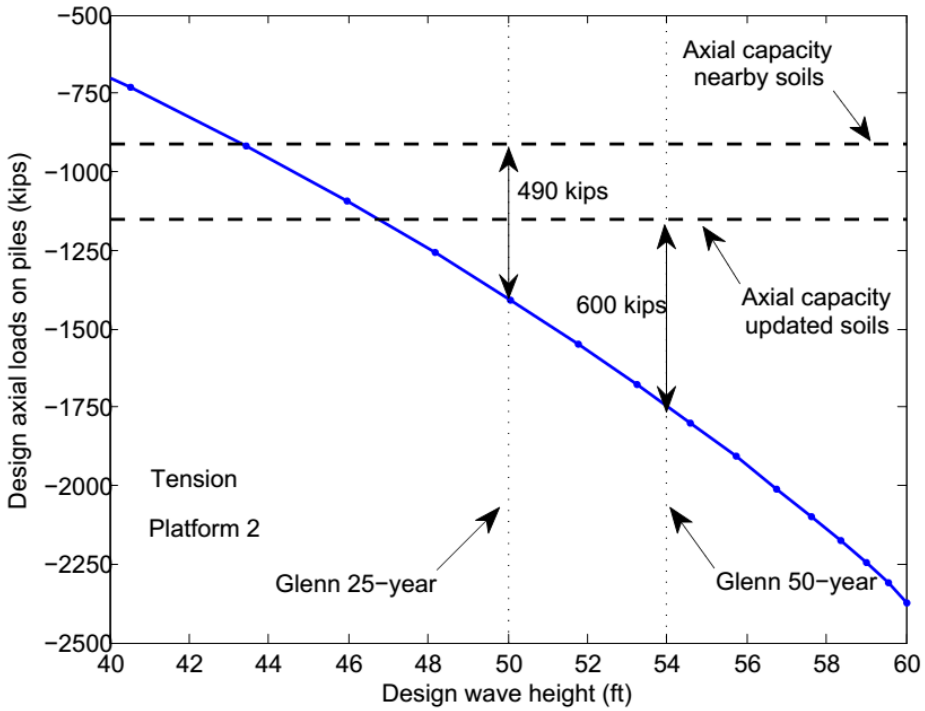

(b) Tension

Figure 4.23 Design axial load at pile head-Platform 2

From the nearby geotechnical report, the top 80 ft below the mudline is soft clay. Based on the finite element analysis with cyclic p-y curves which were used in design in the 1960s (Marshall, 2015), for Platform 1, the unfactored stress in the pile wall exceeds the steel nominal yield strength using the Glenn's 50-year wave height (see Figure 4.24); for Platform 2, the unfactored compressive and tensile stresses are respectively about 3% and 10% lower than the steel nominal yield strength using the Glenn's 50-year wave height (see Figure 4.25). Therefore, it is judged that the nearby soil report underestimates the undrained shear strength of the soft clay at the Platform 1 and 2 site. Hence, the undrained shear strength for the top 80 ft is increased by 50% in order to meet the Glenn's 50-year wave height as shown in Figure 4.24 and 4.25 for Platform 1 and 2, respectively.

Based on the above reasons, the soil strength parameters used in this study are updated as follows: the pile tip bearing sand layer is changed to dense sand with an internal friction angle of 35^{o}, the undrained shear strength of the top 80 ft clay layer is increased by 50%. Based on the updated soils parameters, the pile system capacity is re-estimated using the mean yield strength of the steel and static p-y curves. In addition, the contributions from the well conductors are included. Both platforms are re-estimated to survive Hurricane Katrina as shown in Figure 4.26 and 4.27.

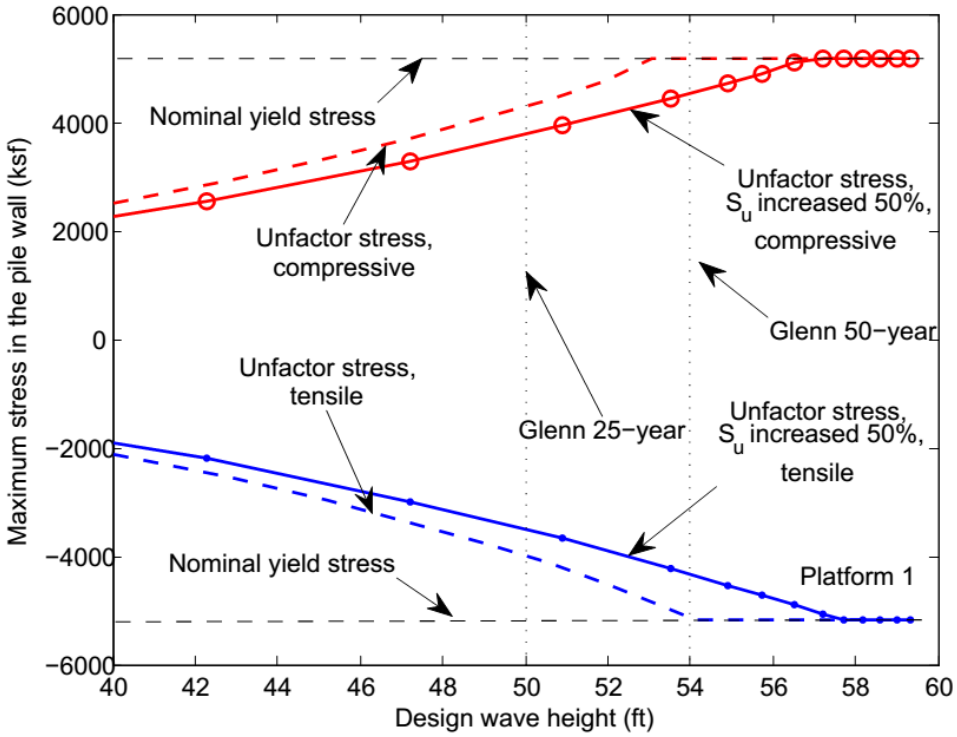

Figure 4.24 Design pile wall stress-Platform 1

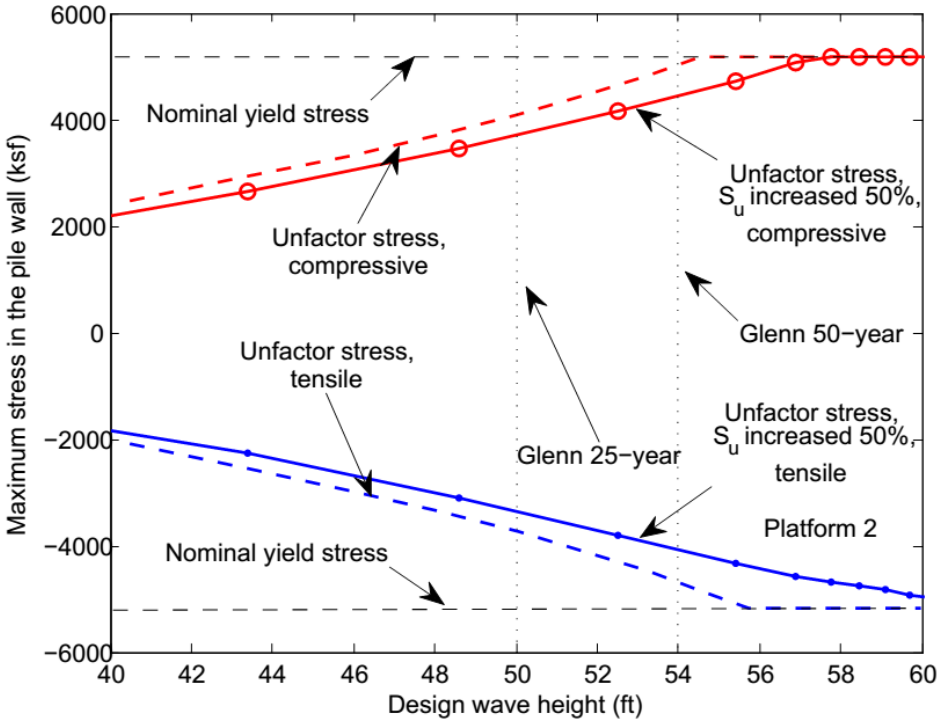

Figure 4.25 Design pile wall stress-Platform 2

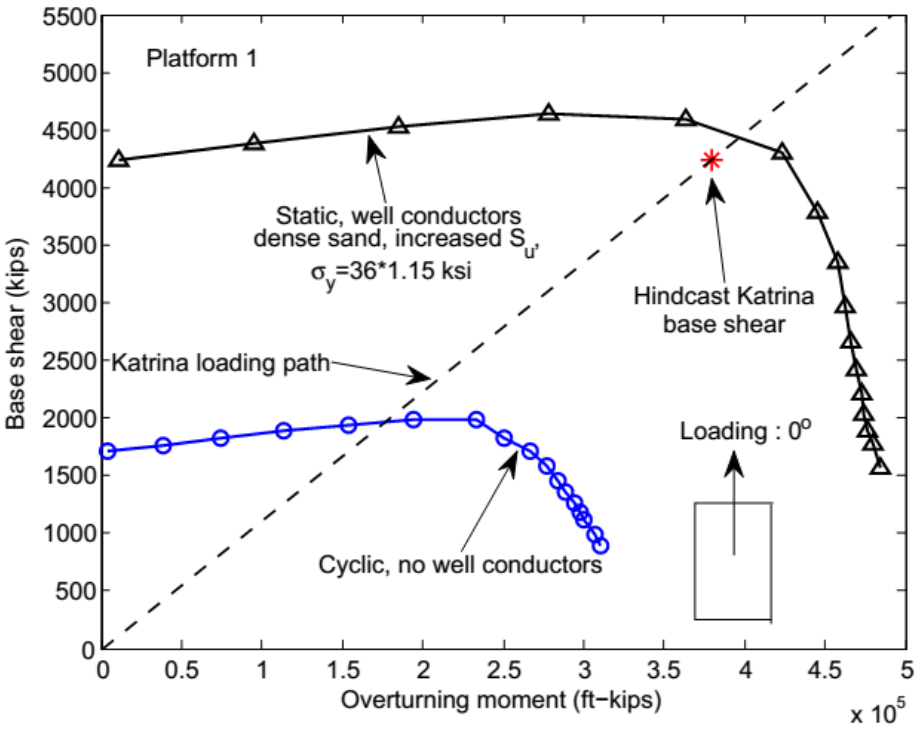

Figure 4.26 Failure surface of Platform 1

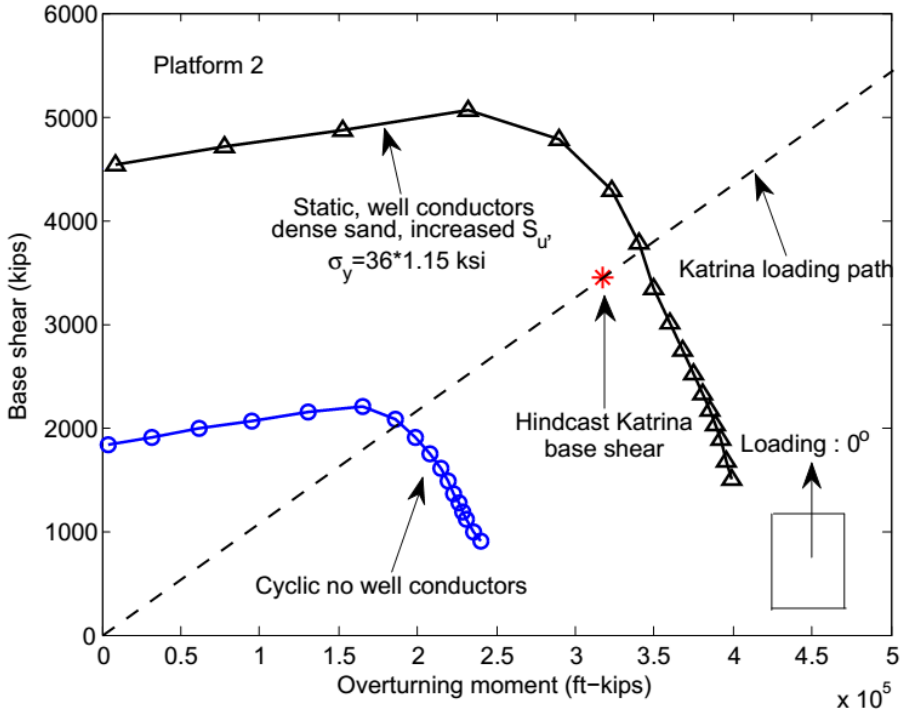

Figure 4.27 Failure surface of Platform 2

4.5 Confidential platform

The description of the platform is excluded due to the confidentiality requirement. The effect of the jacket leg stub on the pile system capacity is examined. The leg stub refers to the portion of the jacket leg that extends from the jacket bottom frame into the soil as shown in Figure 4.28.

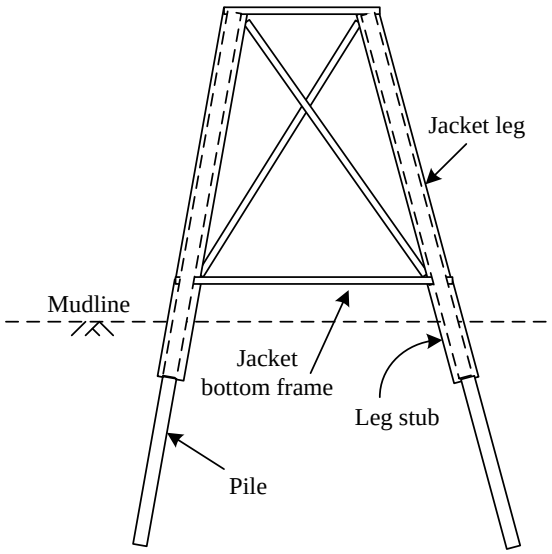

Figure 4.28 Example of jacket leg stub

Figure 4.29 shows the effect of the jacket leg stub and static p-y curves. The base case under consideration is the pile system capacity obtained using cyclic p-y curves and without the leg stub. The pile system capacities are normalized by the capacity in the base case, i.e., the base shear is normalized by the base shear capacity at the zero moment arm in the base case, the overturning moment is normalized by the maximum overturning moment capacity in the base case. In the base shear failure region, the pile system capacity increases by about 12% using static p-y curves compared to that using cyclic p-y curves; the pile system capacity increases by about 35% when the jacket leg stub is considered. In the overturning failure region, the effects of the jacket leg stub and p-y curves are small. Therefore, the effect of the jacket leg stub should be

taken into account in assessing the pile system capacity in the base shear failure region.

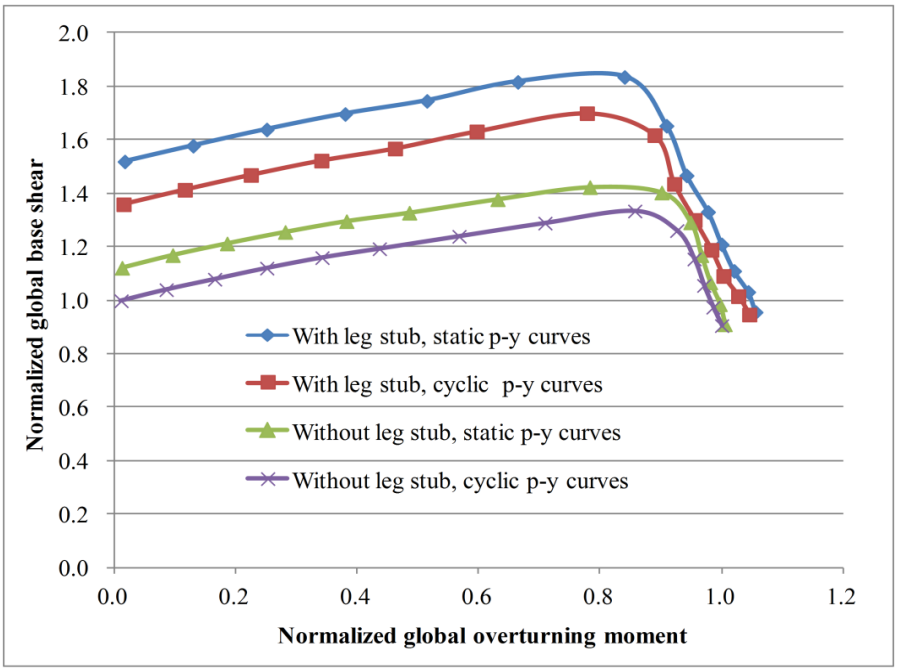

Figure 4.29 Effect of leg stub and static p-y curves

4.6 Conclusions

This chapter presents offshore pile system case studies with the proposed bounding methods. The close agreement between the limit analysis results and the finite element results validates the proposed bounding methods. The proposed lower bound method can effectively capture the effects of global torsion on the jacket and global out-of-plane failures. The evidence from the survival of offshore platforms indicates that (1) well conductors should be included in assessing the pile system ultimate capacity; (2) static p-y curves should be used in the assessment – the use of static p-y curves increases the pile system base shear capacity by about 10 to 20% and the actual performance in several case studies can only be explained if static p-y curves are assumed (the survival of Platform 27 can also be explained by using the steel mean

yield strength); (3) the mean value of the steel yield strength should be used to acknowledge the rapid loading effect and the difference between the mean value and nominal yield strength of the steel; (4) jacket leg stubs should be included because the jacket leg stub essentially increases the pile cross-sectional bending capacity; and (5) site-specific geotechnical information is important – when a soil boring at the platform site is not available, the soil conditions can at least be inferred approximately based on the design practice (e.g., the design wave height, the stress in the pile wall) at the time the platform was designed.

5 Pile System Redundancy and Robustness

This chapter aims to conduct deterministic studies on the pile system redundancy and robustness. A FE procedure for determining the loads causing the first damage and first failure in a pile system will be described. The redundancy and robustness of three case study pile systems will be determined.

5.1 Redundancy

For a pile system, the failure of a single pile does not necessarily cause the complete collapse of the pile system since the applied load can be re-distributed to less loaded piles in the system, i.e., the pile system has reserve capacity upon the first damage and/or first failure in a single pile. This reserve capacity is categorized as the pile system redundancy in the current study. While the current state of practice does not explicitly consider the pile system redundancy in design, it is an important aspect in the performance that is achieved using the state of practice.

Lloyd and Clawson (1984) pioneered the study on the overturning redundancy of an offshore pile system based on a deterministic elastic limit equilibrium approach. The redundancy was found to vary with the environmental-to-gravity load. Tang and Gilbert (1992) studied the redundancy of offshore pile systems probabilistically using an elastic approach in estimating the first failure load and an upper-bound plasticity approach in estimating the system capacity. The redundancy was found to depend on the pile system configuration, the failure mode and the loading direction.

5.1.1 First damage and first failure loads

The failure surface for a single long offshore steel pipe pile under 3D head loading (i.e., axial load *V*, lateral load *F* and moment *M*) from the lower bound solutions is shown in Equation 2.6 and is re-presented here:

$$\chi = \frac{|M|}{M_{pa}\cos\left[\pi V \big/ \left(2V_{pa}\right)\right]} \le 1 \qquad 5.1\ (a)$$

$$\frac{|F|}{F_m} \le \left[\frac{\chi\sin(\theta) + \sqrt{1-\chi^2\cos^2(\theta)}}{2}\cos\left(\frac{\pi}{2}\frac{V}{V_{pa}}\right)\right]^{\alpha} \qquad 5.1\ (b)$$

$$\frac{|V|}{V_m} \le 1 \qquad 5.1\ (c)$$

Two scenarios are considered for a single pile: (i) the pile is damaged axially or laterally, and (ii) the pile is failed axially or laterally. Following Chapter 2, Equation 5.1 (a), (b), and (c) respectively specify the bending failure of the pile head, the complete lateral and axial failures of the pile. If Equation 5.1 (a) is satisfied under lateral loading, a plastic hinge occurs at the pile head and the pile is damaged. If Equation 5.1 (b) or (c) is satisfied, the pile fails laterally or axially. Hence, it implicitly assumes that the damage in the axial direction is equivalent to axial failure.

The first damage/failure load of a pile system is expressed in terms of the global base shear force at the mudline. A FE program utilizing a beam-column on nonlinear, uncoupled springs model is implemented to determine the first damage/failure load. Therefore, the nonlinearities in the pile and soil are taken into account when the pile system approaches to the first single pile damage/failure load. The FE program is elastic based, but the stiffness of each pile will be updated through iterations

according to the bending moment-thrust-curvature relation of the pile cross sections and the nonlinear soil springs. The detailed procedure is described as follows:

First step: with assumed elastic stiffnesses for pile cross-sections and soil springs, determine the global base shear force on the platform causing the first damage/failure of the most critical pile and the corresponding displacements at the pile heads. This determination can be done through the elastic scaling and the damage/failure criteria specified in Equation 5.1.

Second step: in general, the bending moments and the associated curvatures, the deformations of soil springs and the associated resistance will not match the prescribed "true" relations of piles and soils. Hence, update the secant axial and bending stiffnesses of each pile cross-section and the secant axial and lateral stiffnesses of soil springs based on the displacement field obtained from the elastic analysis. These updated values are used as input for the next elastic analysis.

Third step: Iteratively repeat the first two steps until a converged solution is obtained. In this approach, the first damage/failure load can be determined and the possible load distribution before the first damage/failure can be assessed.

The above procedure implicitly neglects the geometric nonlinearity of the pile (i.e., the $P-\Delta$ effect) since Equation 5.1 is based on the lower bound theorem of limit analysis.

5.1.2 Pile system capacity

The pile system capacity is determined using the proposed 3D lower bound method in Chapter 3. As presented before, the proposed lower bound method is based on the single pile failure surface in Equation 5.1

5.1.3 Pile system redundancy

In this deterministic analysis, the pile system redundancy is measured by the deterministic system redundancy factor (DSRF) which is defined as the ratio of the global base shear causing complete failure of the pile system to that causing initial damage/failure of an individual pile.

5.1.4 Pile system redundancy case studies

Three offshore platforms in an API study for the API RP 2A-LRFD 2nd edition project are analyzed to examine the redundancy of different pile systems. These three platforms are termed Platform I, II, and III. Platform I is a 3-leg platform, Platform II is a 4-leg platform, while Platform III is a 8-leg platform.

5.1.4.1 Platform I

Platform I is the same platform (Platform 10) as that analyzed in Chapter 4. The 100-year environmental load (W_n) to the gravity load (G_n) ratio for each pile is shown in Figure 5.1 as a function of the loading direction (these loads refer to the axial loads on the pile head). Figure 5.2 to 5.4 show the interaction diagrams for the first damage, first failure, and ultimate system capacities in terms of the base shear and overturning moment for Platform I. The base shear is normalized by the pile system base shear capacity at zero moment. The overturning moment is normalized by the maximum overturning capacity of the pile system. As shown, the redundancy of the platform depends on the loading direction and the failure mechanism. Under the hindcast wave load path in Hurricane Ike, Platform I is expected to fail in overturning.

In the overturning failure region, the first damage and first failure loads of the platform coincide since the most critical pile fails axially (also see Equation 5.1 (c)),

and the pile system capacity is about 5% larger than the pile system first damage/failure load. Little redundancy is expected in the overturning region since Platform I is a 3-leg platform that if one pile fails axially, the pile system is close to global instability. The minor redundancy in the overturning region comes from the bending resistance of piles.

In the base shear region, there is large redundancy against the complete system failure after the first damage (i.e., forming one plastic hinge in the most critical pile). The pile system capacity is about 50 to 60% higher than the first damage load; however, the system capacity is only about 5% larger than the first failure load. In the loading direction of 180^{o}, the first failure load and the pile system capacity are almost identical. Therefore, the layout of the piles and the loading direction affect the redundancy of pile systems. The minor redundancy after first failure in the base shear region is due to that the pile cross-section is ductile that significant load re-distribution occurs when one pile approaches failure.

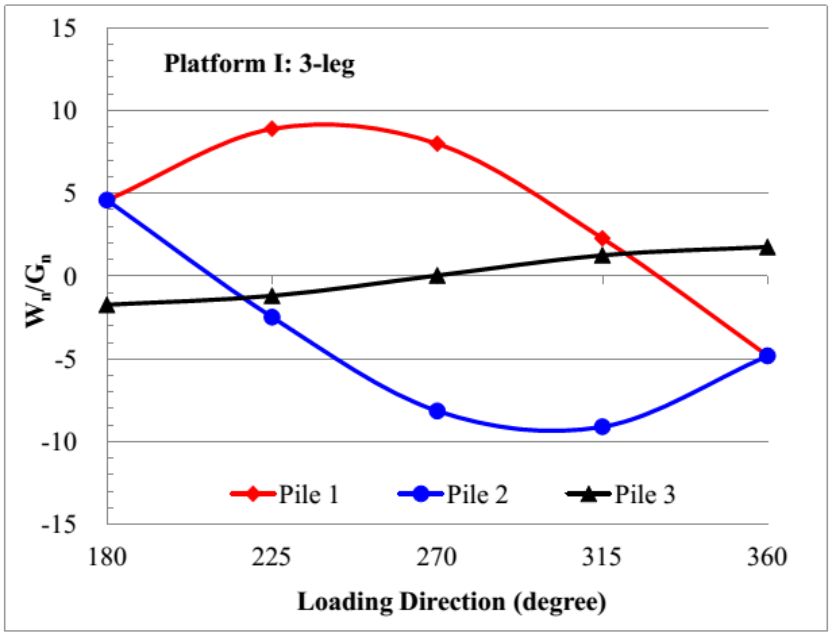

Figure 5.1 Variation of Wn/Gn with loading direction – Platform I

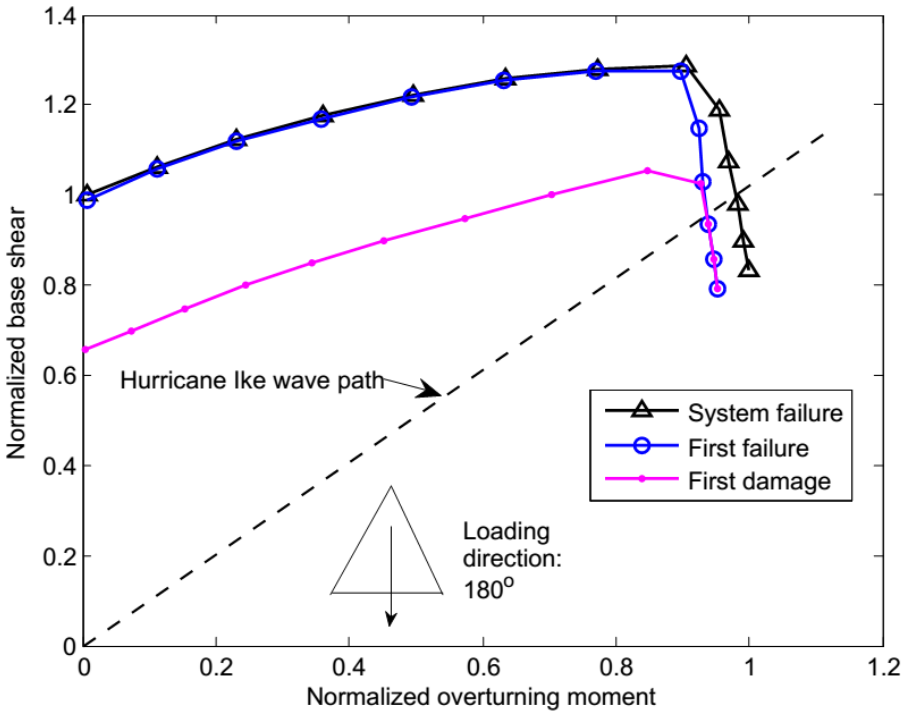

Figure 5.2 Interaction diagram for loading direction of 180°

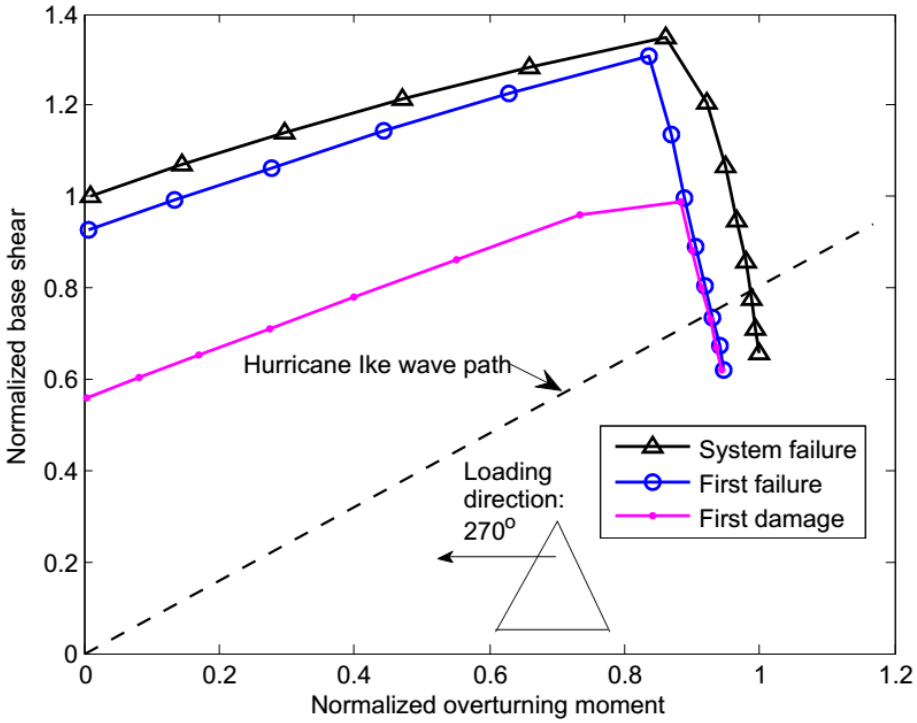

Figure 5.3 Interaction diagram for loading direction of 270°

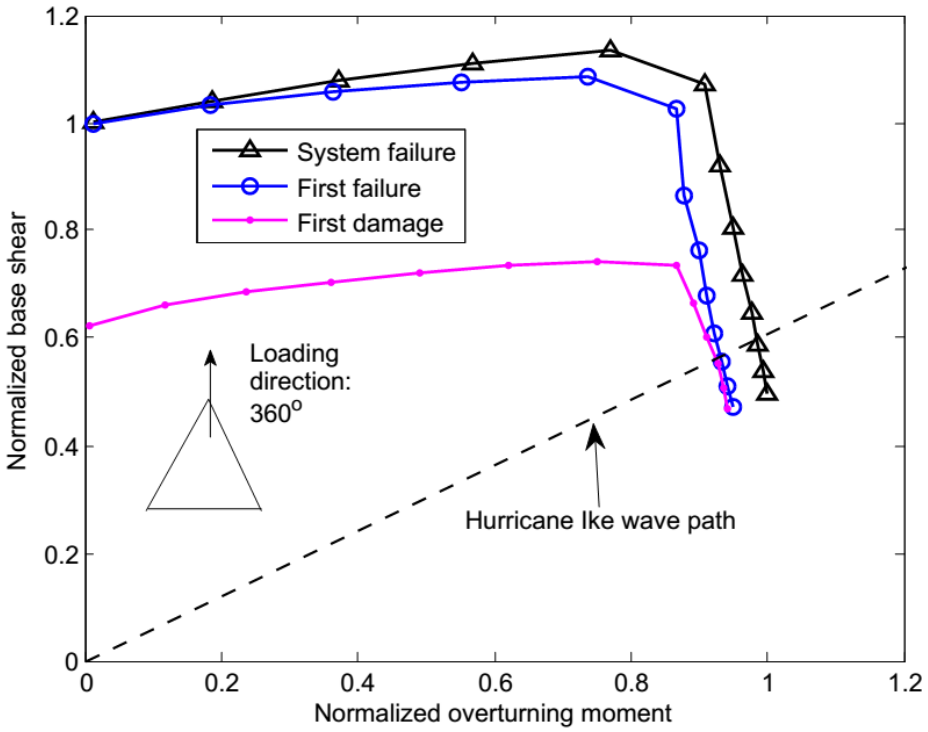

Figure 5.4 Interaction diagram for loading direction of 360°

5.1.4.2 Platform II

Platform II is described briefly due to the requirement of API. Platform II is a 4-pile platform with base orientation shown in Figure 5.5. The piles (1-4 in Figure 5.5) are steel pipe piles. Piles 1 and 2 have shorter penetrations than Piles 3 and 4. The soil stratigraphy is complex with interbedded clay and sand layers based on recent soil borings. A detailed study on the cyclic loading effect reveals that the pile axial capacity is almost the same as that from the API method when the cyclic degradation and the rapid loading effect are considered. Therefore, the single pile capacities are calculated following API RP 2GEO (2011). The value of W_n/G_n varies from about -2.0 (environmental load causes tensile axial load) to about 2.5 (environmental load causes compressive axial load) as shown in Figure 5.6.

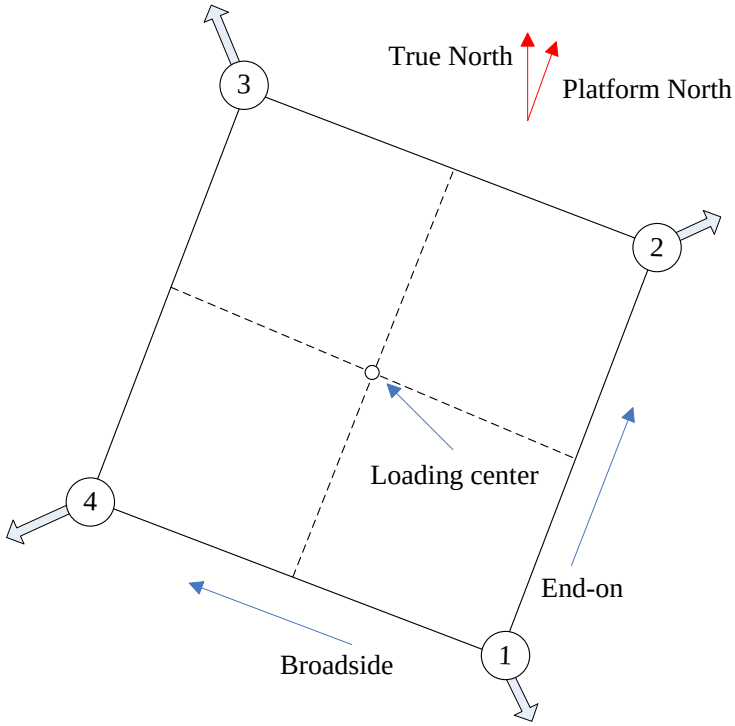

Figure 5.5 Plan view of Platform II

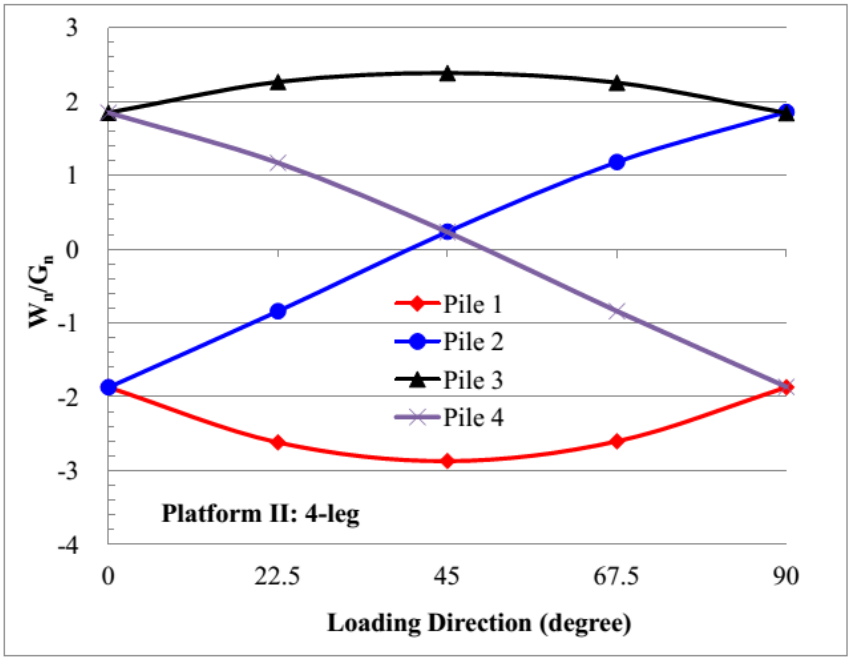

Figure 5.6 Variation of Wn/Gn with loading direction – Platform II

Figure 5.7 to 5.9 show the interaction diagrams for the first damage, first failure, and ultimate system capacities in terms of the normalized base shear and normalized overturning moment for Platform II. For the convenience of the presentation, the

broadside and end-on directions of Platform II shown in Figure 5.5 are respectively defined as 0^o and 90^o. As shown, the failure mode of Platform II depends highly on the loading direction due to the specific pile layout and the pile geometry of Platform II. For the loading direction of 0^o, the platform and loading are symmetric, the overturning moment capacity of the platform is relatively high. Therefore, the platform is expected to fail in the base shear region. For the loading direction of 90^o, the platform is asymmetric because Pile 1 and 2 are shorter than Pile 3 and 4. Therefore, Pile 2 tends to plunge into the soil for the loading direction of 90^o, which causes an out-of-plane failure and reduces the overturning capacity of the pile system. Hence, the platform is expected to fail in the base shear-overturning interaction region. For the loading direction of 180^o, the overturning capacity is minimum since Pile 1 and 2 are shorter than Pile 3 and 4, and the platform is expected to fail in overturning.

Similar to Platform I, the redundancy of Platform II is minor after the first failure in the overturning region, and after the first failure in the base shear region. The minor redundancy in the overturning region is due to the small number of piles in the pile system, while the minor redundancy after the first failure in the base shear region is because of the ductile behavior of the pile cross-section that load re-distribution occurs before the failure of the most critical pile. The redundancy after the fist damage is higher, and the DSRF is about 1.4 to 1.5 in the base shear failure region.

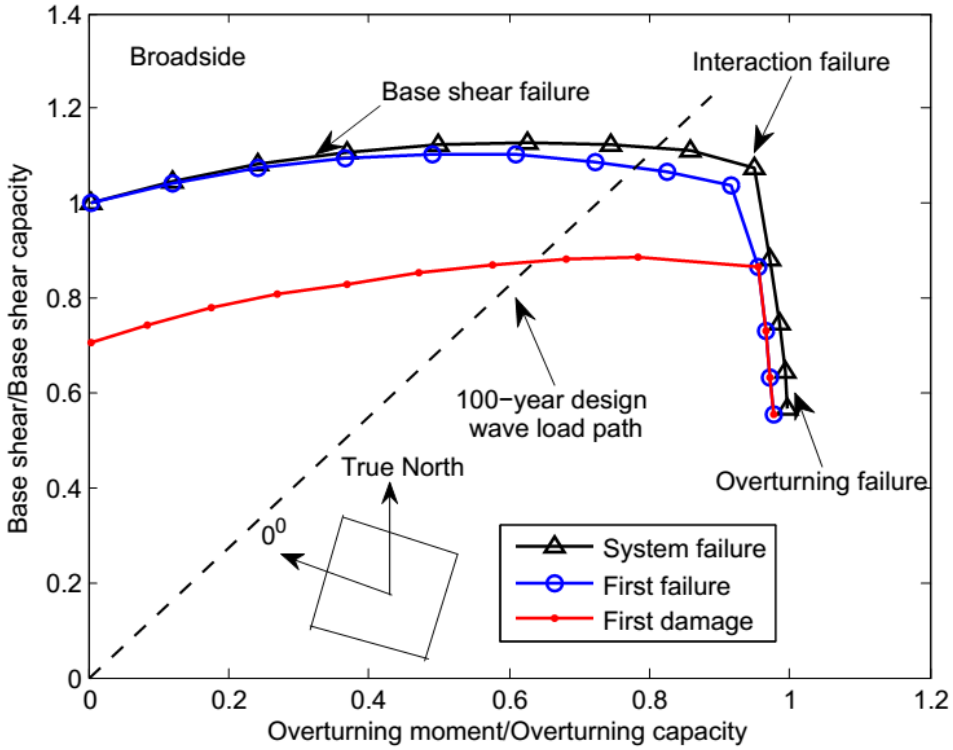

Figure 5.7 Interaction diagram for loading direction of 0^o

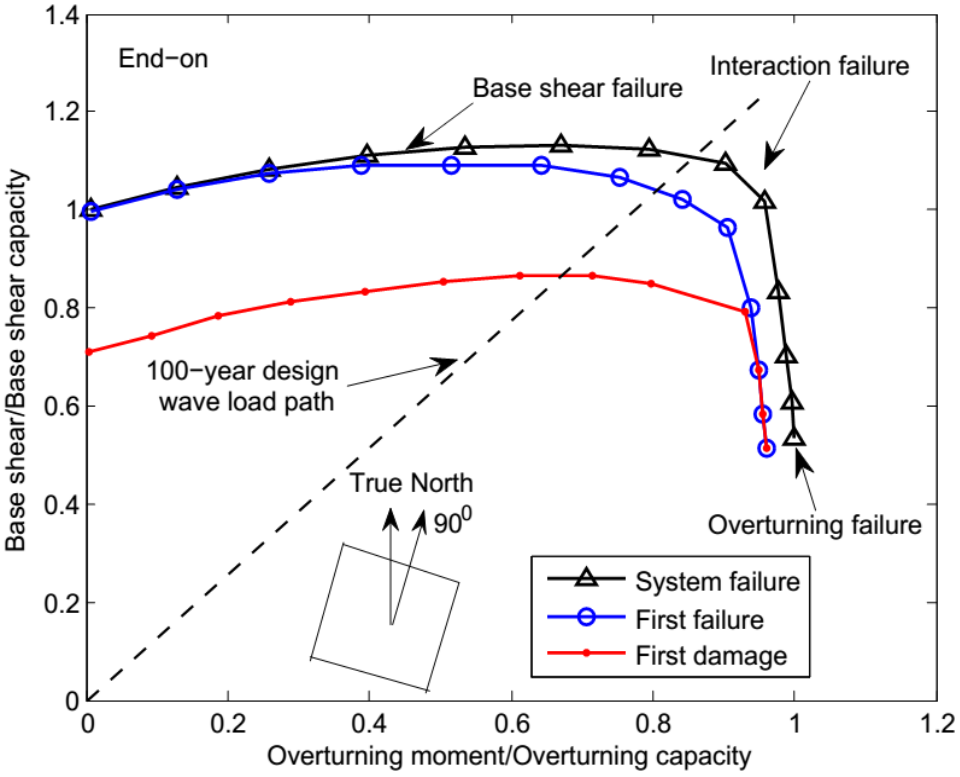

Figure 5.8 Interaction diagram for loading direction of 90^o

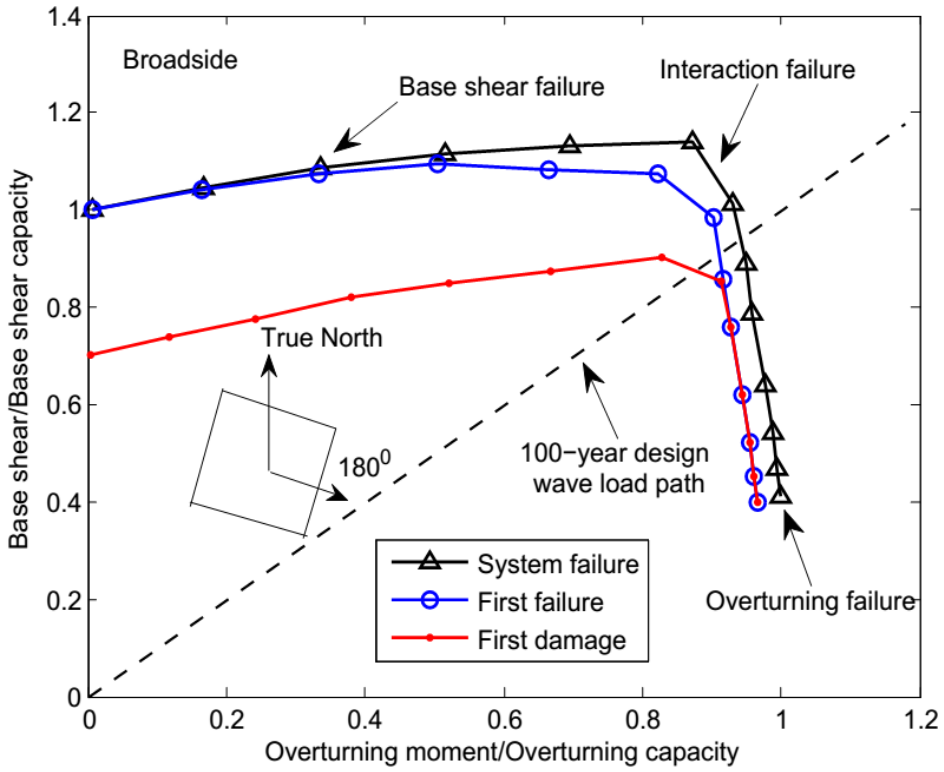

Figure 5.9 Interaction diagram for loading direction of 180^{o}

5.1.4.3 Platform III

Platform III is described briefly due to the requirement of API. Platform III is an 8-pile platform without conductors (Figure 5.10). The piles are steel pipe piles. All eight piles penetrated through the upper clay layer and tipped in the sand layer. The single pile capacities are calculated following API RP 2GEO (2011). The value of W_n/G_n varies from about -2.0 (environmental load causes tensile axial load) to about 2.5 (environmental load causes compressive axial load) as shown in Figure 5.11.

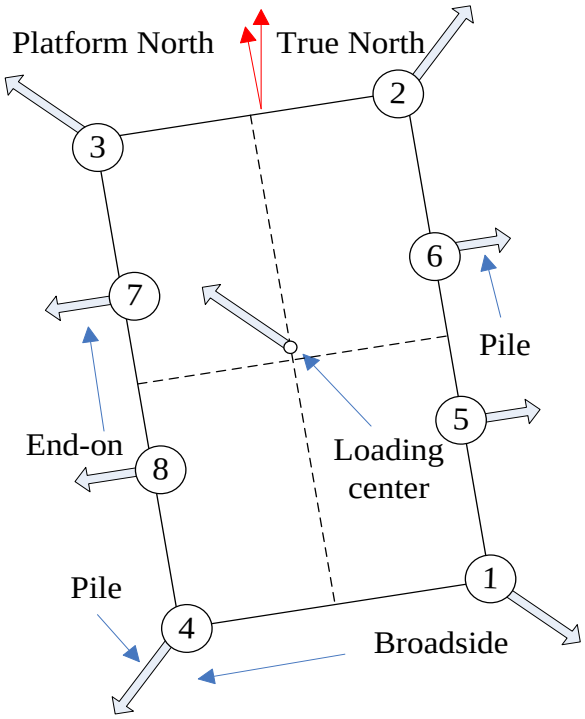

Figure 5.10 Plan view of Platform III

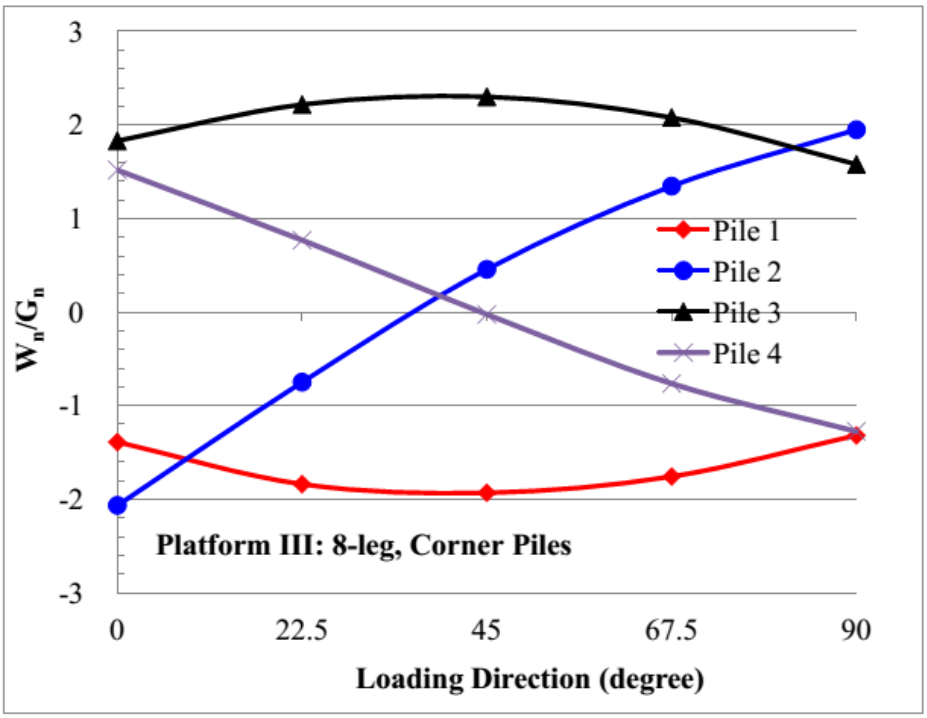

Figure 5.11 Variation of Wn/Gn with loading direction – Platform III

Figure 5.12 to 5.14 show the interaction diagrams for the first damage, first failure, and ultimate system capacities in terms of the normalized base shear and normalized

overturning moment for Platform III. As shown, Platform III is expected to fail in the base shear region in the broadside and end-on directions, but is expected to fail in the base shear-overturning interaction region in the diagonal direction.

In the base shear failure region, similar to Platform I and II, the redundancy is small when the most critical pile fails, but pile system capacity is about 40% higher than the first damage load. In the overturning region, the redundancy depends highly on the loading direction. In the broadside direction, the redundancy mainly comes from the bending resistance of the pile, and thus the redundancy is minor. In the end-on direction, the interior piles (Pile 5-8 in Figure 5.10) can still carry loads once the exterior pile fails. Hence, the redundancy is relatively larger, and the pile system capacity is about 15% greater than the first failure load. In the diagonal direction, the pile system capacity is about 25% greater than the first failure load.

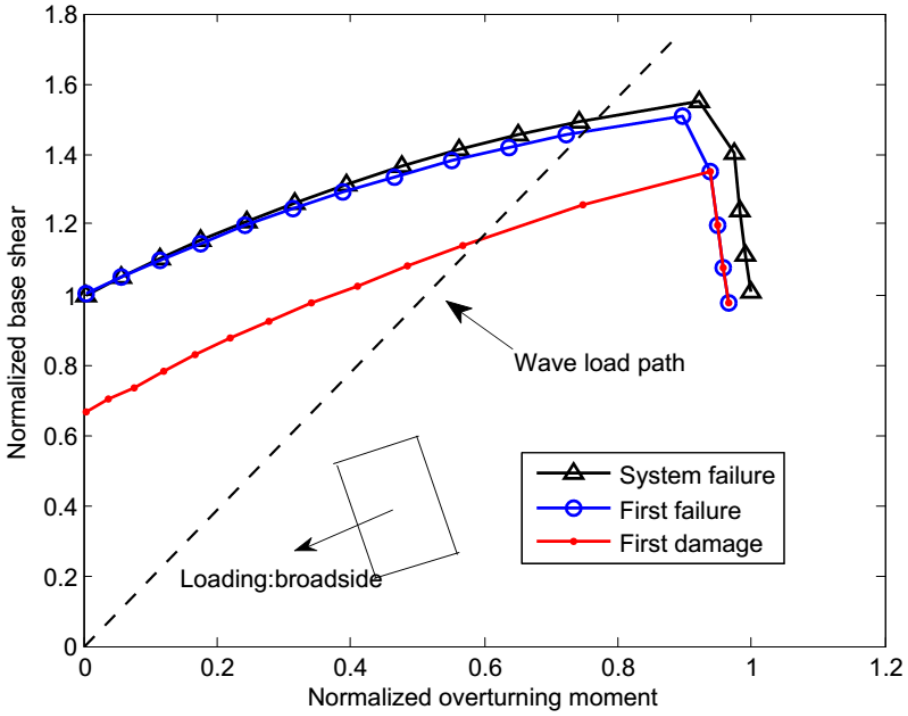

Figure 5.12 Interaction diagram for broadside direction

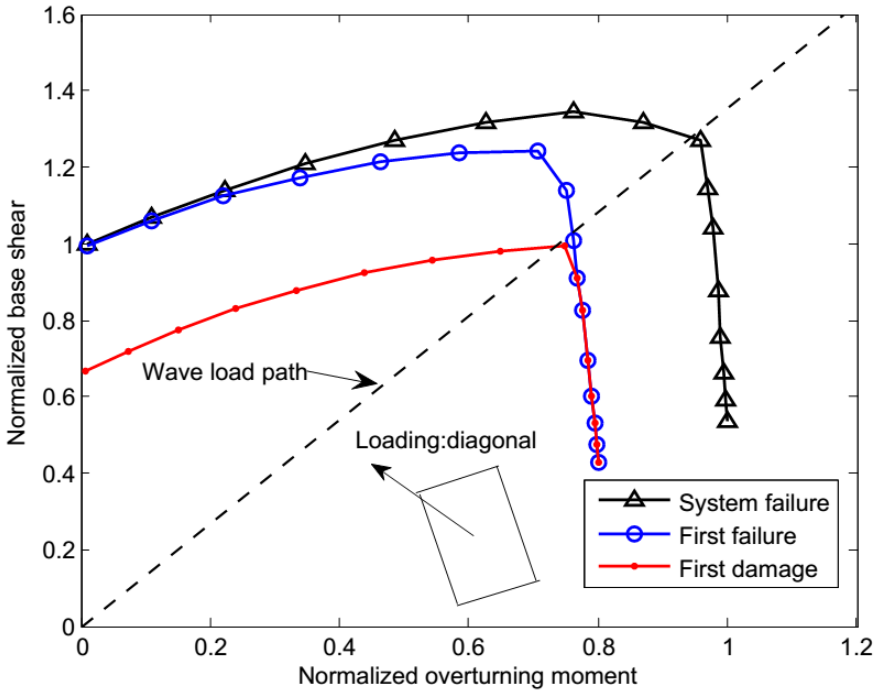

Figure 5.13 Interaction diagram for diagonal direction

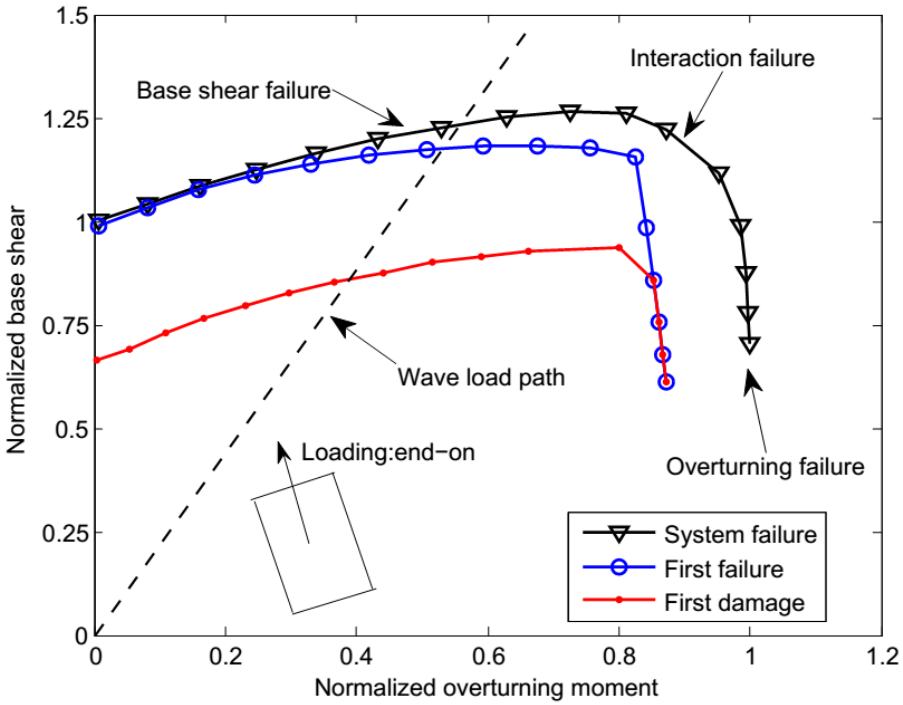

Figure 5.14 Interaction diagram for end-on direction

5.2 Robustness

Nordal *et al.* (1988) proposed the probabilistic system robustness, which is measured by the increase of the failure probability when selected members in the jacket frame are removed, i.e., to simulate selected members are damaged. For the pile foundation, the complete removal of one pile is believed to be unrealistic. Hence, from a deterministic aspect, the robustness of the pile system in this study measures the sensitivity of the pile system capacity to the capacity of the most critical pile in the foundation system (Chen *et al.*, 2013), and this definition of robustness is used in the deterministic robustness study. The sensitivity of the pile system capacity is determined by increasing and decreasing the capacity (both axial and lateral) of the most critical pile by 30%. The increasing and decreasing of the pile capacity by 30% approximately give the 90% and 70% confidence intervals of the pile capacity for a c.o.v. of 0.2 and 0.3 for the pile capacity, respectively.

Figure 5.15 to 5.17 show the comparison of the foundation robustness of the three platforms (Platform I, II, and III in Section 5.1.4) under different loading directions. The global base shear is normalized by the sum of the maximum single pile lateral capacities (F_m) of all the piles in the foundation system, while the global overturning moment is normalized by the maximum overturning capacity in the base case.

For all the three platforms, the system capacity is less sensitive in the base shear region than that in the overturning region. Hence, the pile system is more robust in the base shear region than in the overturning region. In the base shear region, the sensitivity of the system capacity is roughly inversely proportional to the number of piles, and is insensitive to the loading directions and torsional loading. In the

overturning region, the sensitivity decreases with the number of piles. Therefore, Platform III (8-pile) is more robust than Platform I (3-pile).

Depending on the specific layout of the piles, the robustness of the same pile system can be different under different loading directions. For Platform I, under the loading directions of 225^o and 290^o, Pile 1 (under compression) and Pile 2 (under tension) (see Figure 4.1) are the most critical pile, respectively. As can be seen from Figure 5.15 and 5.16, the change of the pile system capacity is almost the same as the change of the axial capacities of those two piles in the overturning region. However, for the 360^o direction, Pile 3 (under compression) is the most critical pile, and 30 % change of the axial capacity of Pile 3 results in about 50% change of the system capacity. Hence, for Platform I, the robustness in the 360^o is less than that in the 225^o and 290^o in the overturning region. The reason for this difference is that the location of the gravity load is close to Pile 3, and thus Pile 3 carries a large part of the gravity load.

For Platform II, the system is more robust in the broadside direction than that in the end-on direction in the overturning region (The broadside and end-on directions are shown in Figure 5.5). In the broadside direction, the foundation is symmetric, while in the end-on direction, out-of-plane failure of the pile system occurs that Pile 2 plunges into the soil since Pile 2 is shorter than Pile 3 (both of the two piles are under compression). Therefore, the pile system capacity in the end-on direction is sensitive to the shorter pile (Pile 2). This finding highlights the importance of symmetry in the system robustness. For Platform III, the pile system capacity is not sensitive to the loading direction in the overturning region.

For all the three pile systems, the pile system capacity is less sensitive to the single pile capacity in the base shear failure region than that in the overturning failure region. Therefore, in general, the pile system is more robust in the base shear failure region than that in the overturning failure region.

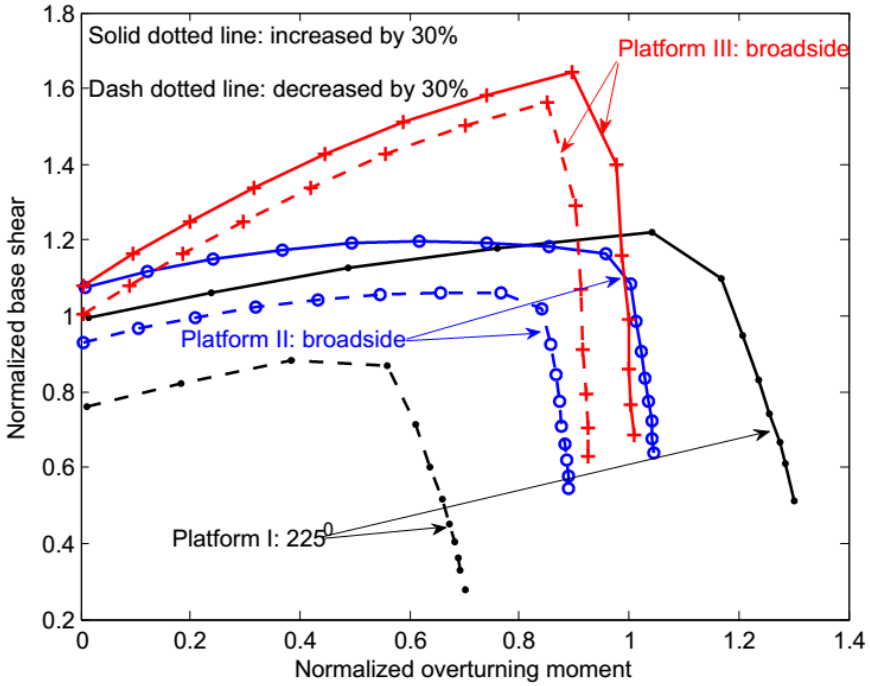

Figure 5.15 Comparison of pile system robustness - broadside

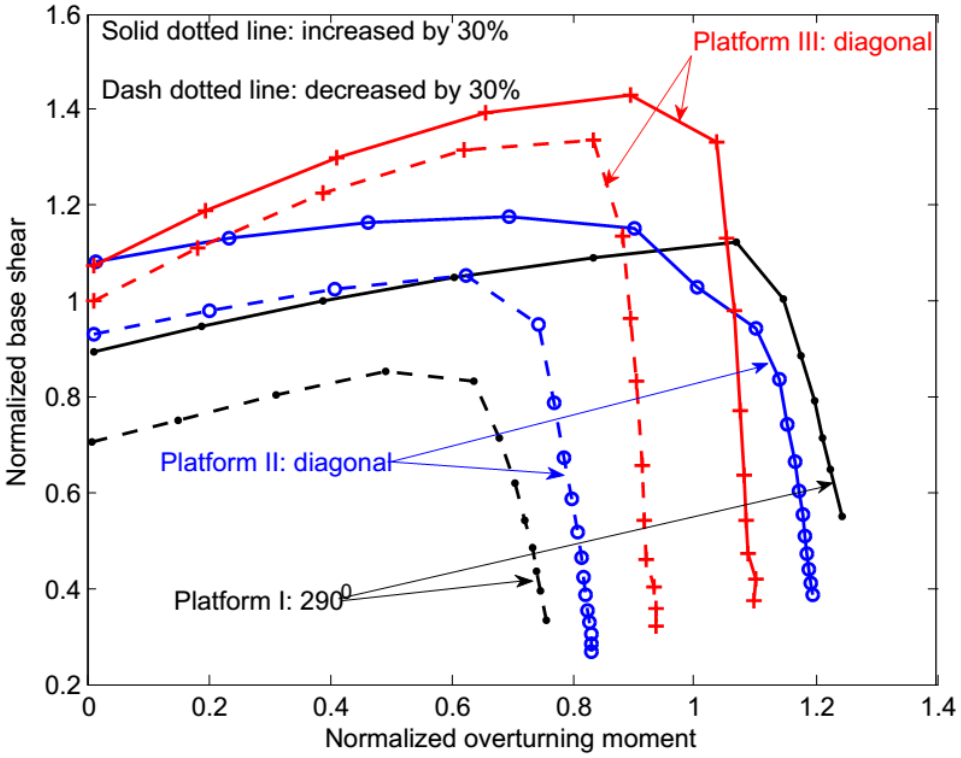

Figure 5.16 Comparison of pile system robustness - diagonal

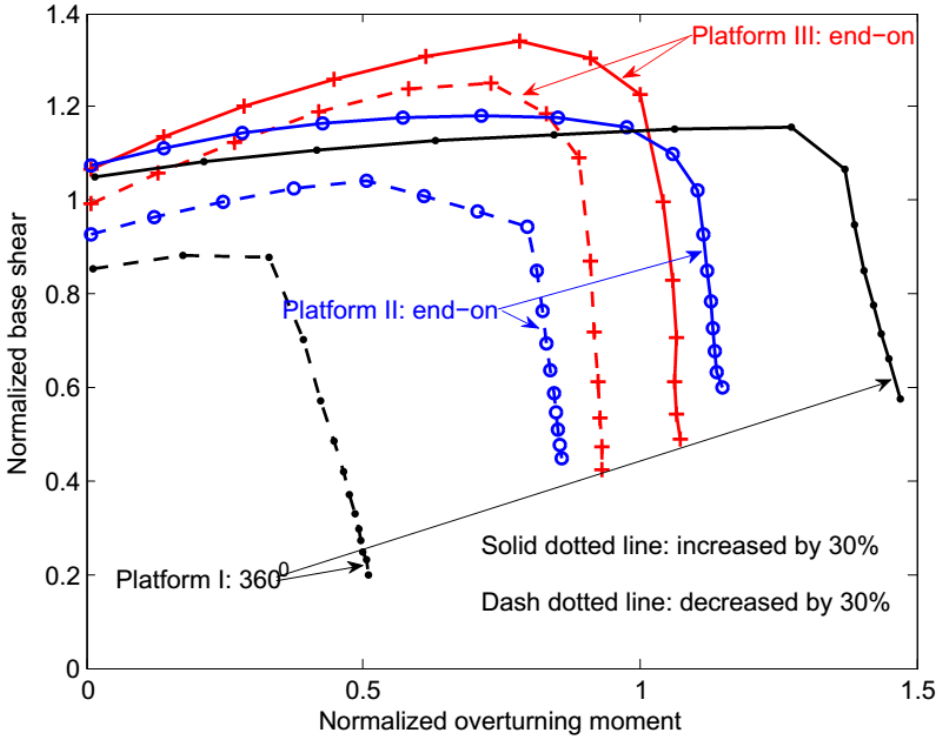

Figure 5.17 Comparison of pile system robustness – end-on

5.3 Conclusions

This chapter presents deterministic redundancy and robustness analyses of pile systems. Based on the study of 3-leg, 4-leg, and 8-leg pile systems, the pile system redundancy is found to depend on the failure mode, pile geometry and layout, and loading directions. In the base shear region, the pile system is close to the ultimate failure after the lateral failure of the most critical pile; however, the pile system capacity is about 40 to 60% higher than the first damage capacity. In the overturning failure region, for the 3-leg platform, little redundancy is observed; for the 4-leg platform, little redundancy is observed in the broadside and end-on directions; for the 8-leg platform, little redundancy is observed in the broadside, but the system capacity is about 15% and 25 to 30% higher than the first failure capacity in the end-on direction and close to the diagonal direction, respectively.

For the system robustness, in the base shear region, the sensitivity of the system capacity is roughly proportional to the inverse of the number of piles, and is insensitive to the loading directions and torsional loading. In the overturning region, the sensitivity decreases with the number of piles. Hence, the 8-leg pile system is more robust than that of the 3-leg and 4-leg pile system. In general, the pile system is more robust in the base shear failure region than that in the overturning failure region, and the system symmetry increases the robustness of a pile system.

6 Calibration of Biases in API Recipe

This chapter aims to calibrate the model bias factors in the API load and resistance design recipes for offshore jacket platforms. Analytically predicted performance of eighteen platforms will be compared to the observed performance in recent Gulf of Mexico hurricanes, and the model bias factors will be updated using Bayes' Theorem. A back analysis of a failed platform will also be conducted based on Bayes' Theorem and the Monte Carlo simulation.

6.1 Background on calibration

Hurricanes Andrew (1992), Lili (2002), Ivan (2004), Katrina (2005), Rita (2005), Gustav (2008) and Ike (2008) passed thousands of offshore platforms in the Gulf of Mexico in the past two decades, and caused damages/failures to hundreds of offshore platforms. Observed offshore platform performance in these major hurricanes is valuable in understanding the safety margin of the current design practice for offshore platforms. Through case studies conducted on the survived, damaged, and failed platforms, it is possible to improve the knowledge of platform performance under full scale conditions.

A joint industry project (JIP) was carried out to assess overall platform structure and foundation performance in Hurricane Andrew (PMB Engineering, 1993). Thirteen platforms (six survived, three were damaged, and four failed) were selected for detailed analyses and were used in Bayesian updating to evaluate the overall conservatism in the structural design recipes, i.e., the API design guideline. Six platforms (three jackets and three caissons) with detailed foundation information were further selected in the Phase II of the JIP (PMB Engineering, 1996) to focus on the foundation conservatism of the API design method. Similar projects were conducted

after major hurricanes and the conservatisms in the API guideline were updated and synthesized (ABS, 2004, Energo Engineering, 2005, Energo Engineering, 2007).

Within the same framework, this study calibrates the model bias factors for the API recipes by comparing the analytically predicted with the actually observed performance of eighteen offshore platforms in recent Gulf of Mexico hurricanes. The uncertainties in wave loads, jacket structural resistance and foundation capacities are integrated, and the model bias factors are updated through Bayes' Theorem.

Compared to the previous studies, the current study improves the Bayesian updating by (i) compiling more platforms (in total 18 platforms) in the database for Bayesian updating, especially one platform failed in foundation is incorporated, (ii) using the updated statistics on the hindcast data based on recent hurricanes, and (iii) separating the biases in the load and resistance.

6.2 Study platforms

6.2.1 Platform characteristics

In total, performance information on 18 platforms has been synthesized based on previous studies (Chen *et al.*, 2010, PMB Engineering, 1993, PMB Engineering, 1996) (Tables 6.1). The platforms are numbered from B1 to B18 as shown in the first column of Table 6.1. The original name of the platform is shown in the second column for the convenience of further references.

The compiled offshore platforms span typical practice in the Gulf of Mexico: 3-, 4-, 6- and 8-leg platforms. Seven platforms experienced Hurricane Andrew, three experienced Hurricane Lili, four experienced Hurricane Katrina, three experienced

Hurricane Rita, and one experienced Hurricane Ike. Platform B1 and B3 are at the same site. Platform B12 and B17 are at the same site.

The geotechnical site conditions, as shown in Table 6.2, are simplistically characterized by the primary type of soil providing lateral soil resistance (i.e., the predominant soil type between 10 to 20 pile diameters below the mudline) and that providing axial soil resistance (i.e., the predominant soil type in the lower third of the pile length). Based on the availability of geotechnical information, the distance of the boring location to the platform site, and the complexity of the soil layers, the foundation performance of Platform B2, B4, B7 to B10, B13, B15, and B16 is excluded in the Bayesian calibration.

Based on post-hurricane investigations, the platforms are grouped into six categories as shown in Table 6.1:

(1) Survival: No damage occurred in the jacket structure and foundation, or only minor non-structural damage is identified;
(2) Damage I: Known damage to the jacket, but the foundation is intact;
(3) Damage II: Known damage, but not attributed specifically to the jacket or foundation;
(4) Failure I: Known failure of the jacket, the foundation is intact;
(5) Failure II: Known failure, but not attributed specifically to the jacket or foundation;
(6) Failure III, Known failure of the foundation, the jacket is intact.

Table 6.1 Summary of candidate platforms

Current Platform No.	Original Platform Name or No.	Hurricane & Year	Observed Event	Installation Year	Water Depth (ft)	Wave Height Hitting Deck (ft)	Number of Piles	Pile Diameter (ft)	Length of Piles (ft)
B1	ST151K[1]	Andrew-1992	Survival	1963	137	52.5	8	2.5	175
B2	ST130Q[1]	Andrew-1992	Survival	1964	170	60	4	2.5	210
B3	ST151H[1]	Andrew-1992	Failure I	1964	137	55	8	2.5	180
B4	ST130A[1]	Andrew-1992	Failure I	1958	180	72.5	8	2.5	175
B5	ST177B[1]	Andrew-1992	Damage I	1965	142	42.5	8	2.5	187
B6	T25[1]	Andrew-1992	Damage II	1969	62	50.6	4	3	165
B7	T21[1]	Andrew-1992	Failure II	1969	61	54.6	4	3	170
B8	El231CA[2]	Lili-2002	Damage I	1968	111	-	-	-	-
B9	El252C/L[2]	Lili-2002	Survival	-	-	45	-	-	-
B10	SS269A[2]	Lili-2002	Damage I	1965	170	34	-	-	-
B11	A (30)[3]	Katrina-2005	Damage I	1973	150	74	6	4	210
B12	B (1)[3]	Katrina-2005	Survival	1965	140	63	8	2.75	135
B13	C (28)[3]	Rita-2005	Damage I	1981	60	53	8	-	-
B14	D (12)[3]	Rita-2005	Damage I	1972	190	79	4	4	255
B15	E (25)[3]	Katrina-2005	Damage I	1967	90	76	4	3	169
B16	F (22)[3]	Rita-2005	Damage I	1976	110	68	4	3.5	290
B17	2[4]	Katrina-2005	Survival	1966	140	-	6	3	140
B18	10[4]	Ike-2008	Failure III	2001	360	-	3	4	220/265

[1] Platforms are obtained from PMB Engineering (1993);

[2] Platforms are obtained from ABS (2004);

[3]Platforms are obtained from Energo Engineering (2007). The number in the parenthesis is the platform number in Chen *et al.* (2010);

[4] Platforms are obtained from Chen *et al.* (2010)

Table 6.2 Soil boring information and platforms used in foundation calibration

Current Platform No.	Original Platform Name or No.	Boring log location	Brief boring information	Overturning resistance soil type	Lateral resistance soil type	Foundation included
B1	ST151K	Same block	Clay	Clay	Clay	✓
B2	ST130Q	Close to ST134 borelog	-	-	-	×
B3	ST151H	Same block	Clay	Clay	Clay	✓
B4	ST130A	farther away from ST134 borelog	-	-	-	×
B5	ST177B	Same block	Tipped in clays, 20ft sand layer contributes to the shaft friction	Clay	Clay	✓
B6	T25	Same block	Tipped in sands for 5ft, underlying sand layer is 14ft	Clay	Clay	✓
B7	T21	Same block	-	-	-	×
B8	El231CA	-	-	-	-	×
B9	El252C/L	-	-	-	-	×
B10	SS269A	-	-	-	-	×
B11	A (30)	Same block	Top 78ft is clay, rest is dense sand	Sand	Clay	✓
B12	B (1)	0.3 miles away	Top 87ft is clay, rest is dense sand	Sand	Clay	✓
B13	C (28)	-	top 25ft is stiff clay, the rest is dominated by medium dense sand	Sand	Clay	×
B14	D (12)	Same block	Tipped in sands for about 30ft, but was expected to fail by pulling out	Clay	Clay	✓
B15	E (25)	Same block	contributions of clays and sand are equal	Clay&Sand	Clay	×
B16	F (22)	Same block	clay contributes 60%, sand contributes 40%	Clay&Sand	Clay	×
B17	2	0.3 miles away	Top 87ft is clay, rest is dense sand	Sand	Clay	✓
B18	10	Same block	Clay	Clay	Clay	✓

6.2.2 Predicted load

The predicted maximum base shear loads at the mudline were established based on the current state of practice using the 3-hour hindcast data from the peak sea state in the primary hurricane wave direction (ABS, 2004, Chen *et al.*, 2010, Energo Engineering, 2007, PMB Engineering, 1993, PMB Engineering, 1996). The global base shear (BS) acting on the jacket in the hindcast primary wave direction is expressed as follows (ABS, 2004, Energo Engineering, 2007):

$$BS = C_1\left(h + C_2 u\right)^{C_3} \qquad h \le h_d \qquad \text{6.1 (a)}$$

$$BS = \left[C_1 + C_4\left(h - h_d\right)\right]\left(h + C_2 u\right)^{C_3} \qquad h > h_d \qquad \text{6.1 (b)}$$

where h is the wave height in feet, u is the surface current velocity in knots, h_d is the minimum wave height hitting the platform deck. C_1, C_2, C_3, C_4 are load coefficients. C_3 is dimensional less while the remaining are unit-dependent. For Platform B1-B16, C_1, C_2, C_3, C_4 were determined from comprehensive simulations with different combinations of wave heights, wave periods, wind velocities, and current velocities following the API loading recipe using the state of practice design software (ABS, 2004, Energo Engineering, 2007, PMB Engineering, 1993, PMB Engineering, 1996). However, for Platform B17 and B18, such detailed simulations are not available. Hence C_4 is assumed to be zeros (i.e., no wave-in-deck), and C_1, C_2, C_3 are estimated from the loads under the design, re-assessment and hindcast situations. Nevertheless, the errors in Equation 6.1 for Platform B17 and B18 are expected to be smaller since the expected hindcast loads are well captured. Table 6.3 summarizes the hindcast data at the peak sea state in the corresponding hurricanes at the platform sites pertinent to

the current study, where h_s and T_p are significant wave height and spectral peak wave period, respectively. Table 6.4 summarizes C_1, C_2, C_3, C_4 for the 18 platforms. The expected maximum wave base shear from the 3-hour sea state is shown in Table 6.5.

Table 6.3 Three-hour peak sea state hindcast data

Current Platform No.	Hindcast Hour 1			Hindcast Hour 2			Hindcast Hour 3		
	h_s (ft)	Current (knots)	T_p (s)	h_s (ft)	Current (knots)	T_p (s)	h_s (ft)	Current (knots)	T_p (s)
B1	34.7	2.0	13.1	34.6	2.0	13.0	31.8	1.8	12.8
B2	33.3	1.9	13.0	33.7	1.8	12.9	32.0	1.6	12.1
B3	34.7	2.0	13.1	34.6	2.0	13.0	31.8	1.8	12.8
B4	31.7	1.8	12.8	32.4	1.8	12.8	30.9	1.6	11.7
B5	35.9	2.5	13.3	32.2	2.4	13.0	31.1	2.3	12.7
B6	21.1	2.6	13.9	26.0	2.6	13.0	24.5	2.5	12.8
B7	27.9	2.4	13.1	27.5	2.3	12.8	24.8	2.1	11.7
B8	28.9	3.3	12.8	26.1	3.7	11.7	23.4	3.4	11.4
B9	29.5	2.3	12.9	26.7	1.7	12.1	23.3	1.7	11.4
B10	33.2	2.2	13.2	30.4	2.2	12.7	26.9	2.0	11.6
B11	34.8	1.6	16.2	35.8	1.9	15.9	34.6	2.2	15.5
B12	33.0	1.6	16.5	34.1	1.9	16.1	33.3	2.3	15.7
B13	24.5	4.1	13.2	26.1	4.3	13.0	26.1	4.2	12.4
B14	36.8	2.9	14.5	36.8	3.2	14.2	36.0	3.6	13.4
B15	24.3	1.8	12.7	25.0	2.0	13.0	24.6	2.1	13.0
B16	31.6	3.2	14.2	32.0	3.2	14.1	31.7	3.0	13.9
B17	33.0	1.6	16.5	34.1	1.9	16.1	33.3	2.3	15.7
B18	38.6	2.7	14.3	39.0	3.0	14.0	38.0	3.3	13.9

Table 6.4 Loading coefficients

Current Platform Number	Wave Force Parameters			
	C1	C2	C3	C4
B1	0.233	6.521	2.258	1.00E-03
B2	0.035	6.770	2.414	1.00E-03
B3	0.522	7.284	2.031	1.30E-02
B4	0.131	6.646	2.326	1.00E-04
B5	0.364	7.136	2.166	1.00E-04
B6	0.655	2.106	1.935	1.00E-04
B7	1.117	2.569	1.788	1.00E-04
B8	0.218	6.245	2.059	0.00E+00
B9	0.806	8.502	2.070	9.81E-03
B10	0.308	8.601	2.108	2.54E-03
B11	0.585	5.975	2.058	1.30E-02
B12	0.653	4.717	2.071	1.10E-02
B13	3.993	4.261	1.656	7.03E-01
B14	0.441	5.667	2.042	5.24E-03
B15	0.381	5.124	1.958	4.60E-02
B16	0.960	3.990	1.853	5.40E-02
B17	0.595	2.100	2.088	0.00E+00
B18	0.102	6.500	2.081	0.00E+00

6.2.3 Predicted resistance

The predicted platform resistance was established based on the current state of practice (ABS, 2004, Chen *et al.*, 2015, Chen *et al.*, 2016, Chen *et al.*, 2010, Energo Engineering, 2007, PMB Engineering, 1993, PMB Engineering, 1996). For the jacket structure capacity, the known conservatisms in design were removed, e.g., use the mean yield strength of 42 ksi instead of the nominal one of 36ksi for A36 steels to acknowledge the mean value and the loading effect in storms. For the foundation capacity, static p-y curves were used since static p-y curves were judged to be more representative in the ultimate condition than cyclic p-y curves used in the design situations (Hamilton and Murff, 1995, Jeanjean, 2009, Senanayake *et al.*, 2015). The strength parameters for the pile axial capacity were assessed based on the boring logs, sample obtaining methods, and engineering judgments.

The three platform failure modes are considered: the jacket failure, the foundation lateral failure, and the foundation overturning failure. The failure capacity in one failure mode was obtained by restricting the other two failure modes. For Platform B11, B12 and B14-B18, the foundation capacities were determined from the 3D lower bound model described in Chapter 3. The contributions from the well conductors were considered. For Platform B12 and B17, as discussed in Chapter 4, the nearby geotechnical report obtained from a site 0.3 miles away from the platform site. Hence, the soil parameters were re-interpreted, i.e., the loose sand layer 110 ft below the mudline was changed to dense sand based on the discussion in Chapter 4.

Table 6.5 summarizes the presented capacities corresponding to three different failure modes for the 18 platforms. The expected maximum wave base shear for each platform is also shown.

Table 6.5 Summary on platform capacities

Current Platform No.	Expected Maximum Wave Base Shear (kip)	Jacket Damage Resistance (kip)	Jacket Ultimate Resistance (kip)	Foundation Base Shear Resistance (kip)	Foundation Overturning Resistance (kip)
B1	3757	2900	3800	4230	4000
B2	1032	1380	1410	1470	1860
B3	3551	2680	3250	3970	3580
B4	2322	2000	2930	1800	2860
B5	4496	3900	5210	4700	3700
B6	1224	1250	1640	2240	2665
B7	1349	1260	1610	3250	2700
B8	1345	669	1102	1196	1244
B9	5516	6264	8412	8770	9307
B10	3250	2666	3998	4165	3449
B11	4230	2825	3650	6643	7920
B12	4240	-	4661	4950	4650
B13	3956	4804	5638	-	-
B14	3715	2531	4181	5812	6110
B15	999	1337	2554	3350	3500
B16	2533	2300	3220	4679	3481
B17	3452	-	4025	5750	3710
B18	1200	1426	-	3199	1218

6.2.4 Observed versus predicted performance

Table 6.6 shows a comparison of the predicted and observed platform performance in hurricanes. The platform ultimate system capacity is the minimum of the ultimate capacities of the three modes (i.e., the jacket failure, foundation lateral failure and foundation overturning failure). Consequently, the factor of safety (FS) is defined as the ratio of the platform ultimate system capacity to the best estimate of the wave base shear. As shown, the predicted performance of Platform B2, B3, B9, B10, B14, B16, B18 is consistent with the observed platform performance in the corresponding hurricanes.

Platform B1 and B3 are at the same site. Platform B1 was installed in 1963, while Platform B2 was installed in 1964. The soil boring was obtained at the same block where the two platforms are located. Both platforms are 8-leg structures. Platform B1 was predicted to fail in the jacket structure (the FS is slightly larger than 1.0 as shown in Table 6.6) but Platform B1 survived Hurricane Andrew. Platform B3 was predicted to fail and did fail in Hurricane Andrew. Therefore, the performance of Platform B1 and B3 reflects the uncertainties in the predicted load and resistance.

Platforms B12 (the same platform as Platform 1 in Chapter 4) and B17 (the same platform as Platform 2 in Chapter 4) both survived Hurricane Katrina even though the predicted safety margins are slightly less than one. As discussed in Chapter 4, there is more than typical uncertainty in the predicted foundation capacity because the geotechnical information comes from a soil boring drilled 0.3 miles away from the platform site for another project. Since the geological setting is a complex and variable alluvial deposit with interbedded layers of clay and sand, it is difficult to extrapolate conditions to the site of Platforms B12 and B17 (Gilbert *et al.*, 2010). Similarly, there is added uncertainty in the foundation capacity for Platform B6 because the nearest soil boring was about 1 mile away from the platform location (PMB Engineering, 1996, PMB Engineering, 1993).

Platform B18 failed during Hurricane Ike by pull-out of the pile loaded in tension (Chen *et al.*, 2013, Gilbert *et al.*, 2010). The post-hurricane study indicated that the strain-softening in the pile axial capacity was not considered in sizing the length of the pile, which effectively reduced the design FS from 1.5 to 1.35. The predicted FS is slightly larger than 1.0 (1.02 as shown in Table 6.6) and the platform is predicted and judged to fail in foundation overturning.

Table 6.6 Comparison of predicted and observed performance

Current Platform No.	Predicted Base Shear (kip)	Platform Ultimate Capacity (kip)	Predicted Factor of Safety	Predicted performance	Observed performance
B1	3757	3800	1.01	Failure I	Survival
B2	1032	1410	1.37	Survival	Survival
B3	3551	3250	0.92	Failure I	Failure I
B4	2322	1800	0.78	Failure III	Failure I
B5	4496	3700	0.82	Failure III	Damage I
B6	1224	1640	1.34	Survival	Damage II
B7	1349	1610	1.19	Damage I	Failure II
B8	1345	1102	0.82	Failure II	Damage I
B9	5516	8412	1.53	Survival	Survival
B10	3250	3449	1.06	Damage I	Damage I
B11	4230	3650	0.86	Failure I	Damage I
B12	4240	4180	0.99	Failure III	Survival
B13	3956	5638	1.43	Survival	Damage I
B14	3715	4181	1.13	Damage I	Damage I
B15	999	2554	2.56	Survival	Damage I
B16	2533	3220	1.27	Damage I	Damage I
B17	3452	3371	0.98	Failure III	Survival
B18	1200	1218	1.02	Failure III	Failure III

6.3 Reliability model

The Bayesian calibration of model biases is conducted through the comparison of the analytically predicted foundation performance with the actually observed responses. A bias factor is defined as the ratio of the true value to the predicted value in this study. A reliability model based on the platform global load and resistance is then expressed as follows:

$$g = B_R \xi_R r_{predicted} - B_s S \qquad 6.2$$

where g is the value of the limit state function with $g > 0$ indicating the safe region and $g \leq 0$ indicating the failure region; B_R and B_s are random variables representing the epistemic uncertainty in the model bias factors for the resistance and load, respectively; ξ_R is the random variable representing the aleatory variabilities (i.e., spatial and temporal variations) in the predicted resistance; $r_{predicted}$ is the predicted deterministic resistance as shown in Table 6.5. S represents the random wave base shear load and reflects the aleaotry uncertainties.

Depending on the expected failure mechanisms of the jacket structure and foundation system, B_R is divided into a model bias factor for the jacket structural capacity B_j, for the pile system base shear (i.e., lateral) capacity in clay[2], B_{fl}^c, and bias factors for the pile system overturning (i.e., axial) capacities in clay B_{fa}^c and in sand B_{fa}^s, respectively. Correspondingly, the random variable ξ_R is divided into individual variables for the different failure mechanisms, ξ_j, ξ_{fl}^c, ξ_{fa}^c and ξ_{fa}^s. Since only one bias factor B_j is introduced for the jacket structural capacity, it is implicitly assumed that the bias factors for predicting the jacket damage load and the jacket ultimate capacity are the same and perfectly correlated.

6.3.1 Model uncertainty

The uncertainty in the model bias factor (i.e., B_s, B_j, B_{fl}^c, B_{fa}^c and B_{fa}^s) is epistemic due to limited data in calibrating the design methods. This epistemic model uncertainty can generally be reduced with additional data and will be calibrated through Bayes' Theorem in this study.

[2] Note that there are no available case study platforms to provide information about lateral capacity in sand.

For wave loading, epistemic uncertainty is due to estimating the base shear from the wave height (Haring *et al.*, 1979, Puskar *et al.*, 1994, Heideman and Weaver, 1992, Efthymiou *et al.*, 1997), which includes the systematic errors in calculating of wave particle kinematics in three dimensions and in estimating the hydrodynamic coefficients. Based on previous work (ABS, 2004, Energo Engineering, 2005, Haring *et al.*, 1979), the prior distribution for the wave load model bias factor B_s is assumed to be log-normal with a mean of 0.93 and a c.o.v. of 0.2.

For the jacket structure, the epistemic uncertainty comes from the modeling of an actual platform in computer programs (e.g., initial imperfections, inaccuracies in platform geometries), the strength and connections of individual components, and the system behavior of a jacket structure. The prior distribution for B_j is assumed to be log-normal with a mean of 1.0 and a c.o.v. of 0.2 based on literature review (ABS, 2004, Energo Engineering, 2007, PMB Engineering, 1996).

For pile capacities, epistemic uncertainty comes from (i) limited data in the pile load testing databases, e.g., Lacasse *et al.* (2013); (ii) extrapolation from small scale load tests to actual piles used in offshore platforms, e.g., Chen *et al.* (2013) and (iii) differences between the actual environmental loading condition (rapid and cyclic after years after pile installation) and the pile test loading condition (slower, static and within weeks of pile installation). The effects of rapid loading, cyclic degradation and ageing depend on the soil properties, the pile geometry and the level and rate of cyclic loading (API RP 2GEO, 2011). All these effects are lumped into the model bias factors. The epistemic uncertainty due to the extrapolation from small scale piles to actual piles cannot be reduced with additional data from small scale pile load testing; hence, engineering judgments play a key role in establishing the statistics on the prior

distributions of the pile model biases. Based on the literature review and the writer's experience, the prior distributions for the model bias factors for the pile system capacities are taken to be log-normal with means of 1.0, 1.3, 1.3, and c.o.v. values of 0.3, 0.3, 0.5 for B_{fl}^{c}, B_{fa}^{c} and B_{fa}^{s}, respectively.

Statistical independence is assumed between any two model bias factors for the prior distribution. A summary on the statistics on the model bias factors for the prior distributions is shown in Table 6.7.

Table 6.7 Prior probability distributions of model bias factors

Bias Factor	Prior distribution		
	Type	mean	c.o.v.
B_s	Log-normal	0.93	0.2
B_j	Log-normal	1.0	0.2
B_{fl}^{c}	Log-normal	1.0	0.3
B_{fa}^{c}	Log-normal	1.3	0.3
B_{fa}^{s}	Log-normal	1.3	0.5

6.3.2 Aleatory variability

There is aleatory variability in the predicted load and resistance (i.e., S, ξ_j, ξ_{fl}^{c}, ξ_{fa}^{c} and ξ_{fa}^{s}) that cannot be reduced without improving the prediction models for load and resistance.

6.3.2.1 Aleatory variability in wave load

For wave loads, this variability consists of three parts as follows: (i) the temporal variations in waves, winds and currents during a sea state (Forristall, 1978), (ii) the variation of wave loads (according to Equation 6.1) given the wave height and current

velocity in each wave cycle due to the random sea state (ABS, 2004, PMB Engineering, 1996, Jonathan and Taylor, 1996), and (iii) the temporal and spatial variations between estimated wave heights and currents from the hindcast model and the actual wave heights and currents (Forristall, 2007).

For the first part of wave load aleatory variability, the effect of currents is relatively small to the wave height. Hence, the current velocity is treated to be deterministic. The wind load is implicitly included in Equation 6.1 since the wind load is usually small for jacket type offshore platforms. The variation of the wave height in each wave cycle is usually modeled by the Weibull type empirical Forristall's distribution (Forristall, 1978) conditioned on the significant wave height h_s in a specific duration as follows:

$$PDF\left(h \mid h_s\right) = \frac{a4^a}{bh_s}\left(\frac{h}{h_s}\right)^{a-1} \exp\left[-\frac{4^a}{b}\left(\frac{h}{h_s}\right)^a\right] \qquad 6.3\text{ (a)}$$

$$CDF\left(h \mid h_s\right) = 1 - \exp\left[-\frac{1}{b}\left(\frac{4h}{h_s}\right)^a\right] \qquad 6.3\text{ (b)}$$

where $PDF\left(h \mid h_s\right)$ and $CDF\left(h \mid h_s\right)$ are respectively the probability density function (PDF) and the cumulative distribution function (CDF) of the wave height conditioned on h_s; h is the wave height in a specific wave cycle; a and b are respectively the shape and scaling parameters, i.e., $a = 2.126$ and $b = 8.42$ in the Forristall's distribution.

For the second part of wave load aleatory variability, the wave load calculated from Equation 6.1 is assumed to be log-normal, and is independent from wave cycles to wave cycles (ABS, 2004, Energo Engineering, 2007, PMB Engineering, 1996). Hence,

a multiplicative error term ε_0 is introduced to the wave load calculated from Equation 6.1, given the wave height *h* and the current velocity *u* in each wave cycle.

For the third part of wave load aleatory variability, the errors introduced by the hindcast model is usually assessed by comparing the hindcast data to the observed wave data in the Gulf of Mexico. Hence, these errors cannot be reduced without improving the hindcast model. Therefore, the hindcast errors will not be updated through Bayes' Theorem in this study. The hindcast errors are reflected in the hindcast significant wave height h_s and the hindcast current velocity *u*. Therefore, multiplicative error terms $\varepsilon_1, \varepsilon_2$ are respectively introduced for the hindcast h_s and u.

Table 6.8 summarizes the statistics on the random variables contributing to the aleatory variability in the wave load. These statistics are based on the literature review (ABS, 2004, Energo Engineering, 2007, PMB Engineering, 1996). The statistics for ε_1 are based on the measured data in recent hurricanes as will be presented in the following sections. Note that ε_0 is assumed to be independent from wave cycles to wave cycles. However, ε_1 is assumed to be perfectly correlated throughout the whole sea state, i.e., the ratio between the two significant wave heights at different intervals (or the significant wave height profile) is deterministic for a given storm, but is assumed to be independent for different storms. The same assumption as ε_1 is made for ε_2 for simplicity. The reasons for this assumption are as follows: (i) the hindcast h_s is typically obtained from 20-min wave samples, and is presented by running a 3-hour box-car filter through the hourly time series to remove the sampling variability (Oceanweather, 2006). Hence, the hourly time series of h_s is inherently correlated. (ii) the current study focuses on the 3-hour peak sea state. From the data presented in

Forristall (2007), the hindcast model consistently over-predicts or under-predicts the actual h_s during the peak sea state (3-hour) in a given storm; however, in different storms, ε_1 tends to be independent.

Table 6.8 Wave loading aleatory random variables

	Distribution Type	Mean	c.o.v.
Individual wave height h	Forristal	per formula	per formula
Wave to wave error ε_0 -Non wave-in-deck	Log-normal	1.0	0.2
Wave to wave error ε_0 - wave-in-deck	Log-normal	1.0	0.25
Hindcast model error ε_1 for h_s	Log-normal	1.0	0.15
Hindcast model error ε_2 for u	Log-normal	1.0	0.15

6.3.2.1.1 Wave-by-wave analysis of wave load

The wave-by-wave analysis establishes the maximum wave base shear based on the distribution of the wave force in a single wave cycle and the number of wave cycles in a sea state. The wave-by-wave analysis considers all the three parts of the aleatory variability. In a single wave cycle, the wave height *h* is given by the Forristall's distribution (Equation 6.3). Hence, in a single wave cycle, the CDF of the global wave base shear (BS) CDF_{BS} conditioned on h and u is obtained as follows:

$$CDF_{BS}\left(x \mid h,u\right) = CDF_{LN,\varepsilon_0}\left[\frac{x}{BS\left(h,u\right)}\right] \qquad 6.4$$

where $BS\left(h,u\right)$ is determined from Equation 6.1 given *h* and *u*; CDF_{LN,ε_0} is the CDF of log-normally distributed ε_0.

The CDF of the maximum *BS* in a given sea interval, $CDF_{MBS}(x)$, conditioned on h_s and u is obtained as follows:

$$CDF_{MBS}(x \mid h_s, u, N) = \left[\int_0^{\infty} \left[CDF_{BS}(x \mid h, u) PDF(h \mid h_s) \right] dh \right]^N \quad 6.5$$

where *N* is the number of wave cycles in a given sea state interval.

If the sea state is divided into *n* intervals with each interval governed by $h_{s,i}$, the duration T_i (where *i* indicates the *ith* interval), and the current velocity u_i, $CDF_{MBS}(x)$ in a sea state is calculated as

$$CDF_{MBS}(x \mid h_{s,i}, u_i, T_i, T_{z,i}, n) = \prod_{i=1}^{n} CDF_{MBS,i}(x \mid h_{s,i}, u_i, N_i) \quad 6.6$$

where $N_i = T_i / T_{z,i}$; T_z is the mean zero-crossing period and is assumed to be deterministic.

Considering the hindcast errors in $h_{s,i}, u_i$ $CDF_{MBS}(x)$ in a given sea state is obtained as follows:

$$CDF_{MBS}(x \mid h_{s,i}, u_i, T_i, T_{z,i}, n) = \int_0^{\infty} \int_0^{\infty} \left[\prod_{i=1}^{n} CDF_{MBS,i}(x \mid h_{s,i}, u_i, N_i) PDF_{LN}(\varepsilon_1) PDF_{LN}(\varepsilon_2) \right] d\varepsilon_1 d\varepsilon_2 \quad 6.7$$

where $h_{s,i}$ should be interpreted as the multiplication of a realization of ε_1 with the hindcast significant wave height in the *ith* interval. The same interpretation applies to u_i.

6.3.2.1.2 Sea state analysis of wave load

The sea state-by-sea state analysis establishes the maximum wave base shear based on the maximum wave height in a sea state. Using the Forristall's distribution for the wave height, and assuming the wave height is independent from waves to waves (Anderson *et al.*, 1982), the distribution of the maximum wave height can be determined asymptotically from as follows:

$$CDF_{h_{\max}}\left(h \mid h_{s,i}, T_i, T_{z,i}, n\right) = \prod_{i=1}^{n}\left\{1-\exp\left[-\frac{1}{b}\left(\frac{4h}{h_{s,i}}\right)^{a}\right]\right\}^{N_i} \tag{6.8}$$

Following Tromans and Vandersohuren (1995), Equation 6.8 converges to an asymptotic form, and the CDF of $h_{\max}$ is shown to be

$$CDF_{h_{\max}}\left(h \mid h_{mp}\right) = \exp\left\{-\exp\left[\lambda\left(\frac{h^2}{h_{mp}^2}-1\right)\right]\right\} \tag{6.9}$$

where λ is a parameter related to the number of wave cycles in a sea state and is calibrated by comparing Equation 6.8 and 6.9. h_{mp} is the so-called most probable maximum wave height, which is determined from $CDF_{h_{\max}}\left(h \mid h_{s,i}, T_i, T_{z,i}, n\right) = \exp(-1)$ in Equation 6.8 as a consequence of Equation 6.9.

Since the effect of the current is relatively small when compared to the effect of the wave height, and typically the mean value of the current velocity in the 3-hour peak sea state remains relatively uniform in each time interval (i.e., 1-hour), it is assumed the hindcast current velocity in the 3-hour sea state is uniform with a value taken to be the maximum value in the hindcast 3-hour sea state. The same as the wave-by-wave analysis, log-normally distributed multiplication factors $\varepsilon_1, \varepsilon_2$ are respectively

introduced for the hindcast significant wave height and the hindcast current velocity. Combining Equation 6.1, 6.9, and the hindcast errors $\varepsilon_1, \varepsilon_2$, the distribution of the maximum wave base shear from the sea state-by-sea state approach is obtained as follows:

$$CDF_{MBS}\left(x \mid h_{s,i}, u_{\max}, T_i, T_{z,i}, n\right) = \int_0^{\infty}\int_0^{\infty}\left\{\int_0^{\infty} BS(h,u)\, d\left[CDF_{h_{\max}}\left(h \mid h_{mp}\right)\right] PDF_{LN}\left(\varepsilon_1\right) PDF_{LN}\left(\varepsilon_2\right)\right\} d\varepsilon_1 d\varepsilon_2 \quad 6.10$$

where $u_{\max}$ represents the maximum hindcast current velocity.

6.3.2.2 Aleatory variability in capacity

For the jacket structural capacity, the aleatory variability ξ_j is assumed to be log-normal with a mean of 1.0 and a c.o.v. of 0.15 (PMB Engineering, 1996). For pile capacities, the aleatory variability accounts for variations between piles due to variations in local and depth-averaged soil properties and in installation effects. In this dissertation, it is assumed that the lateral capacities of individual piles within the foundation system are perfectly correlated. The same assumption applies to the axial capacities of individual piles. Based on available information from pile load data bases and judgment in extrapolating that data to platform performance (e.g., Tang 1988, Tang and Gilbert 1990, LaCasse et al. 2013 and Gilbert et al. 2014), ξ_{fl}^{c}, ξ_{fa}^{c} and ξ_{fa}^{s} are taken to be log-normal with the same mean of 1.0 and c.o.v. values of 0.1, 0.1 and 0.2, respectively. These distributions apply to the case where a modern soil boring (e.g., pushed sampling) is available at the site of the platform. These c.o.v. values are increased to 0.15, 0.2 and 0.3 for ξ_{fl}^{c}, ξ_{fa}^{c} and ξ_{fa}^{s}, respectively, where the site-specific boring is based on an out-of-date method (e.g., driven penetration method). These c.o.v. values are increased to 0.2, 0.3 and 0.5 where a site-specific boring is not available (note that the definition of site-specific captures the distance

between the boring and the platform relative to the distance of lateral variations in soil properties in a particular geologic setting). The probability distributions for S, ξ_j, ξ_{fl}^c, ξ_{fa}^c and ξ_{fa}^s are summarized in Table 6.9.

Table 6.9 Probability distributions for S, ξ_j, ξ_{fl}^c, ξ_{fa}^c and ξ_{fa}^s

Platform No.	S		ξ_j -Log-normal		ξ_{fl}^c -Log-normal		ξ_{fa}^c & ξ_{fa}^s - Log-normal	
	Mean	c.o.v.	Mean	c.o.v.	Mean	c.o.v.	Mean	c.o.v.
B1	Per Equation 6.7 or 6.10		1.0	0.15	1.0	0.15	1.0	0.2
B2			1.0	0.15	-	-	-	-
B3			1.0	0.15	1.0	0.15	1.0	0.2
B4			1.0	0.15	-	-	-	-
B5			1.0	0.15	1.0	0.2	1.0	0.3
B6			1.0	0.15	1.0	0.15	1.0	0.2
B7			1.0	0.15	-	-	-	-
B8			1.0	0.15	-	-	-	-
B9			1.0	0.15	-	-	-	-
B10			1.0	0.15	-0	-	-	-
B11			1.0	0.15	1.0	0.1	1.0	0.3
B12			1.0	0.15	1.0	0.2	1.0	0.5
B13			1.0	0.15	-	-	-	-
B14			1.0	0.15	1.0	0.15	1.0	0.2
B15			1.0	0.15	-	-	-	-
B16			1.0	0.15	-	-	-	-
B17			1.0	0.15	1.0	0.2	1.0	0.5
B18			1.0	0.15	1.0	0.1	1.0	0.1

6.4 Bayesian calibration process

6.4.1 Bayes' Theorem

The probability distributions of the model bias factors are updated with the observed platform performance using Bayes' Theorem as follows (Ang and Tang, 1975):

$$PDF''(\mathbf{B}=\mathbf{b}\,|\,\text{Performance}) = \frac{LH\left(\text{Performance}|\mathbf{B}=\mathbf{b}\right)PDF'(\mathbf{B}=\mathbf{b})}{\int_{-\infty}^{\infty} LH\left(\text{Performance}|\mathbf{B}=\mathbf{b}\right)PDF'(\mathbf{B}=\mathbf{b})d\mathbf{b}} \qquad 6.11$$

where $PDF'(\mathbf{B})$ and $PDF''(\mathbf{B})$ are respectively the prior and updated joint PDFs of $\mathbf{B}$. $\mathbf{B}$ is a vector containing all the model bias factors to be updated, i.e., $\mathbf{B}=\left[B_s, B_j, B_{fl}^c, B_{fa}^c, B_{fa}^s\right]$, and $\mathbf{b}$ is a specific realization of $\mathbf{B}$. $LH\left(\text{Performance}|\mathbf{B}=\mathbf{b}\right)$ is the probability of occurrence of the observed performance conditioned on the given bias vector $\mathbf{B}=\mathbf{b}$, and termed likelihood function. The $PDF'(\mathbf{B})$ represents the best estimate for $\mathbf{B}$ based on past information and accumulated knowledge, and the statistics are presented in Table 6.7. The $PDF''(\mathbf{B})$ represents the improved understanding of $\mathbf{B}$ based on the current observed foundation performance.

6.4.2 Likelihood function

6.4.2.1 Likelihood function definition

The likelihood function conveys information implied by the observed platform performance during hurricanes, and improves the understanding of the platform bias factors through the Bayesian process. The likelihood function of performance is the probability of occurrence of the observed platform performance in a specific hurricane. This probability of occurrence is a conditional probability that the model bias factors are given specific values, i.e., $\mathbf{B}=\mathbf{b}$ is given. Hence, this probability of occurrence or the likelihood function depends only on the aleatory variability for specific $\mathbf{B}=\mathbf{b}$.

Based on the observed performance category in Section 6.2.1, the likelihood function of the observed performance is evaluated as follows:

(1) Survival: $LH\left(\text{Survival}\,|\mathbf{B}=\mathbf{b}\right)$ =*P*(*BS*<jacket first damage resistance AND *BS* <foundation lateral resistance AND *BS* <foundation overturning resistance)

(2) Damage I: $LH\left(\text{Damage I}\,|\mathbf{B}=\mathbf{b}\right)$=*P*(jacket first damage resistance< *BS* <jacket ultimate resistance AND *BS* <foundation lateral resistance AND *BS* <foundation overturning resistance)

(3) Damage II: $LH\left(\text{Damage II}\,|\mathbf{B}=\mathbf{b}\right)$ =*P*(jacket first damage resistance< *BS* OR foundation lateral resistance< *BS* OR foundation overturning resistance< *BS*)

(4) Failure I: $LH\left(\text{Failure I}\,|\mathbf{B}=\mathbf{b}\right)$ =*P*(jacket ultimate resistance< *BS* AND jacket ultimate resistance <foundation lateral resistance AND jacket ultimate resistance <foundation overturning resistance)

(5) Failure II: $LH\left(\text{Failure II}\,|\mathbf{B}=\mathbf{b}\right)$=*P*(jacket ultimate resistance< *BS* OR foundation lateral resistance<*BS* OR foundation overturning resistance<*BS*)

(6) Failure III: $LH\left(\text{Failure III}\,|\mathbf{B}=\mathbf{b}\right)$ =*P*(jacket ultimate resistance>*BS* AND foundation lateral resistance <*BS* OR foundation overturning resistance<*BS*)

where $P(\cdot)$ is the probability of an event.

The calculation of $P(\cdot)$ is based on Equation 6.2, i.e., $g = B_R \xi_R r_{predicted} - B_s S$. Note that B_R and B_s are given by $\mathbf{B}=\mathbf{b}$, and the only random variables are ξ_R and S. Depending on the different approaches in modeling the wave base shear (wave-by-wave approach vs. sea state approach), there are two methods to calculate $P(\cdot)$.

6.4.2.2 Wave-by-wave approach

In essence, the calculation of the $P(\cdot)$ using the wave-by-wave approach is the integration of a time variant problem, and can be calculated as follows (Wen and Chen, 1987):

$$P(\cdot) = \int_{\mathbf{x}} P(\cdot \mid \mathbf{x}) PDF_{\mathbf{X}}(\mathbf{x})\, d\mathbf{x} \qquad 6.12$$

where $\mathbf{x}$ a time-invariant random vector, $PDF_{\mathbf{X}}(\mathbf{x})$ is the joint PDF of $\mathbf{x}$ and $P(\cdot \mid \mathbf{x})$ is the $P(\cdot)$ of a time variant problem conditioned on the realization of $\mathbf{x}$.

Direct integration of Equation 6.12 is not efficient, and the result is sensitive to the integration resolution based on the preliminary study. This sensitivity is because that the calculation of $P(\cdot \mid \mathbf{x})$ involves a large number of wave cycles (around 1000 cycles in a 3-hour sea state).

Wen and Chen (1987) demonstrated that the $P(\cdot)$ in Equation 6.12 is equivalent to the failure probability with a limit state function as

$$g(U, \mathbf{x}) = U - \Phi^{-1}\left[P(\cdot \mid \mathbf{x})\right] \qquad 6.13$$

where U is an auxiliary standard normal variate, and Φ is the CDF of a standard normal distribution.

Using the first order reliability method (FORM) (Ang and Tang, 1984), Equation 6.13 can be solved using inner and outer loops (FORM/FORM) calculation (ABS, 2004, PMB Engineering, 1996), with the inner loop to calculate $P(\cdot \mid \mathbf{x})$ and the outer loop to calculate $P(\cdot)$ with the limit state function expressed in Equation 6.13.

(i) Inner loop: conditioned on the realizations of the significant wave height, the current velocity and the random resistance, the FORM is performed to find $P(\cdot|\mathbf{x})$. The random variables in this loop are the wave height *h* and the wave-to-wave error base shear ε_0;

(ii) Outer loop: the FORM is performed to find $P(\cdot)$. The random variables in this loop are $\varepsilon_1, \varepsilon_2$, and the random platform capacities.

6.4.2.3 Sea state approach

Since a deterministic significant wave height profile (the ratio of the two significant wave heights at different intervals is deterministic) is assumed in a given sea state, and the total number of wave cycles in the 3-hour sea state is deterministic, the wave number parameter λ and the ratio of most probable wave height to the maximum significant wave height $h_{mp}/h_{s,\max}$ are deterministic (see Equation 6.8 and 6.9). Therefore, the FORM can be used directly to estimate $P(\cdot)$, and the calculation is greatly simplified when compared to the wave-by-wave analysis.

6.4.2.4 Discussion on wave-by-wave and sea state approaches

In general, the wave-by-wave approach is more elegant since it captures the variation of the wave base shear from waves to waves; however, the approach is time-consuming to calculate the $P(\cdot)$ because both inner and outer loops involve iterations. Besides, sometimes it is difficult to reach convergence, especially when the $P(\cdot)$ is very large or very small or the limit state is expected to occur in the transition region where the wave-in-deck load starts to occur.

The sea state approach, which establishes the maximum wave force based on the maximum wave height, is more relevant to the practice since the design of offshore platforms is based on the maximum wave height, and the reliabilities of offshore structures are often estimated based on the distribution of the maximum wave height (Energo Engineering, 2009, Moses, 1986). In addition, the sea state approach is more efficient because the direction FORM is used. Figure 6.1 shows the comparison of the maximum *BS* distributions obtained by the wave-by-wave approach and the sea state approach for Platform B1 using the FORM for the statistics of ε_0 presented in Table 6.8. The maximum *BS* from the uncorrected sea state approach (i.e., directly follows Equation 6.10) is smaller than that from the wave-by-wave approach at the same percentile. The reason for this difference between the two approaches is that the variation of the base shear from waves to waves (i.e., ε_0) is neglected in the sea state approach, which implicitly assumes that the maximum wave force occurs at the maximum wave height if the epistemic model bias factor is given. Consequently, the sea state approach assumes that the uncertainty in the wave force is perfectly correlated throughout the whole sea state for a specific platform given the wave height.

Therefore, a multiplication correction factor B_{ws}, which reflects the variability of the base shear in a single wave cycle (i.e., ε_0), is introduced to match the distribution of the maximum *BS* obtained from the sea state approach to that from the wave-by-wave approach, i.e., the maximum *BS* obtained from the sea state approach is multiplied by B_{ws}. Theoretically, all the factors affecting the distribution of the maximum *BS* will affect the value of B_{ws}, and B_{ws} is unlikely to be deterministic. Nevertheless, in a typical 3-hour sea state with about 1000 wave cycles, B_{ws} can be well approximated by a deterministic value which is only a function of ε_0. The reason

for this approximation is that the large number of wave cycles averages the variability from a single wave cycle.

The corrected sea state approach (i.e., $B_{ws}=1.17$) yields almost the same distribution for the maximum *BS* as that from the wave-by-wave approach for Platform B1 (see Figure 6.1). The mean value of B_{ws} calibrated from the metocean data at the sites of 18 platforms is shown in Figure 6.2 as a function of the c.o.v. of ε_0 for the none wave-in-deck case (the mean of ε_0 is 1.0). The c.o.v. for the wave-in-deck case is implicitly assumed to be 0.05 higher than that for the none wave-in-deck case, except for the case of c.o.v.=0 where ε_0 is deterministic for both none wave-in-deck and wave-in-deck cases. The variation of B_{ws} across the 18 platforms is small, and the c.o.v. of the mean of B_{ws} obtained from 18 platform sites is less than 0.01, which justifies using a deterministic value of B_{ws}.

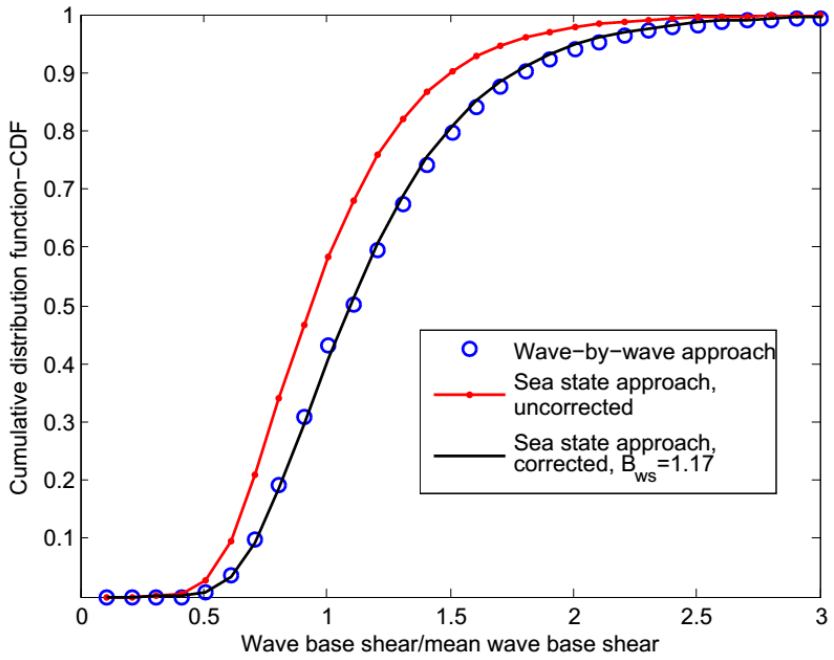

(a) Linear scale

Figure 6.1 continues next page

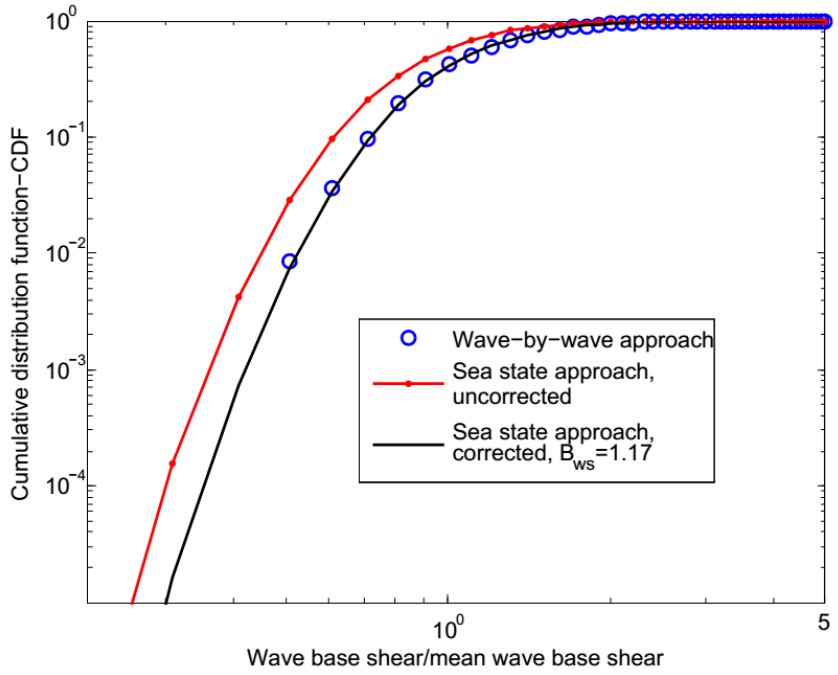

(b) Logarithmic scale

Figure 6.1 Wave-by-wave approach and sea state approach comparison

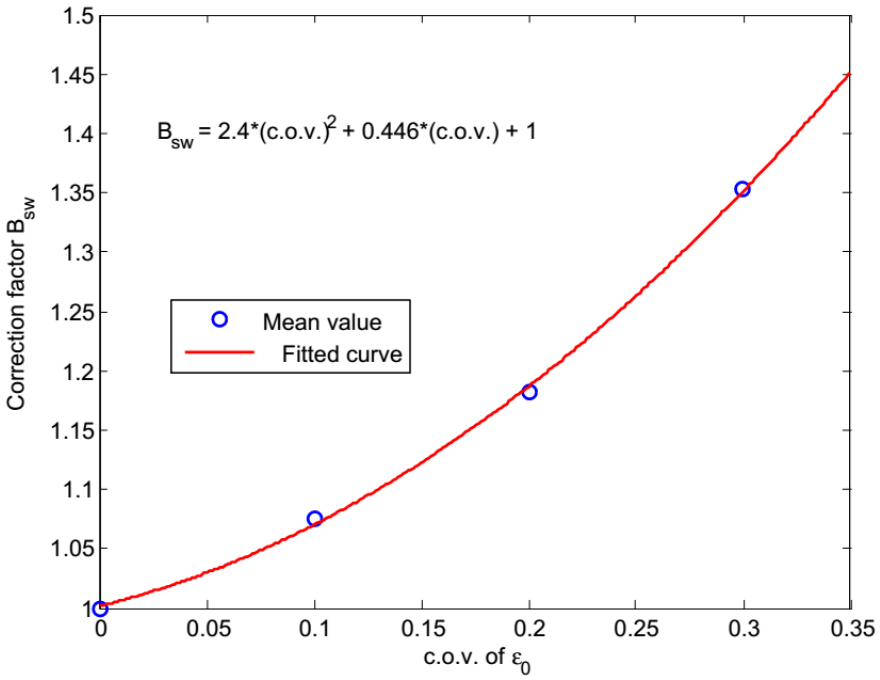

Figure 6.2 Variation of B_{ws} with c.o.v. of ε_0

6.4.2.5 Probability of union and intersection

In general, the observed performance reveals information on the three failure modes (i.e., the jacket structure, foundation lateral and overturning behaviors). Hence, the likelihood function involves the union and intersection of multiple events. In this dissertation, the probability of the intersection of multiple events is calculated by the De Morgan's laws as follows:

$$P\left[\bigcap_{all\ i}\left(g_i>0\right)\right]=1-P\left[\bigcup_{all\ i}\left(g_i\le 0\right)\right] \tag{6.14}$$

where $\bigcap$ and $\bigcup$ respectively indicate the intersection and union of multiple events.

The correlation coefficient is estimated from the most probable failure point within the framework of the FORM (Ditlevsen, 1979). The probability of the intersection of two events is calculated from the bivariate lognormal distribution (Thoft-Christensen and Murotsu, 1986) as follows:

$$P\left[\left(g_i>0\right)\bigcap\left(g_j>0\right)\right]=\Phi\left(\beta_i\right)\Phi\left(\beta_j\right)+\int_0^{\rho_{ij}} PDF_{N,2}\left(\beta_i,\beta_j,z\right)dz \tag{6.15}$$

where β is the reliability index corresponding to $g>0$. ρ_{ij} is the correlation coefficient of the two events.

The union of several events is estimated from the Ditlevsen bounds (Ditlevsen, 1979) as follows:

$$P\left(\bigcup_{all\ i} g_i\le 0\right)\ge P\left(g_1\le 0\right)+\sum_{i=2}^{m}\max\left[P\left(g_i\le 0\right)-\sum_{j=1}^{i-1}P\left(g_i\le 0\bigcap g_j\le 0\right),0\right] \tag{6.16 (a)}$$

$$P\left(\bigcup_{all\ i} g_i< 0\right)\le \sum_{i=1}^{m}P\left(g_i<0\right)-\sum_{i=2}^{m}\max_{j<i}\left[P\left(g_i<0\bigcap g_j<0\right)\right] \tag{6.16 (b)}$$

where m is the number of events. The geometric mean of the upper and lower bound probabilities is used in this study.

6.4.2.6 Verification of FORM and sea state approach

The Monte Carlo simulation is performed to verify the accuracy of the FORM in estimating the probability of the observed performance. The result from the Monte Carlo simulation is the mean from 10 simulations. The number of realizations in each Monte Carlo simulation is chosen to keep the c.o.v. of the mean from the 10 simulations less than 0.02. Figure 6.3 shows the variation of the probability of the occurrence of the damage in the structure with the jacket resistance model bias for Platform B15 (B_s is fixed to be 1.0). As can be seen, two conclusions can be reached: (i) the sea state approach with a deterministic correction factor can give similar results to the wave-by-wave analysis, and (ii) the FORM is appropriate to estimating the probability of the problem under investigation since the results from the FORM are in good agreement with the results from the Monte Carlo simulation. Therefore, for all the following analyses, the FORM combined with the sea state approach will be used.

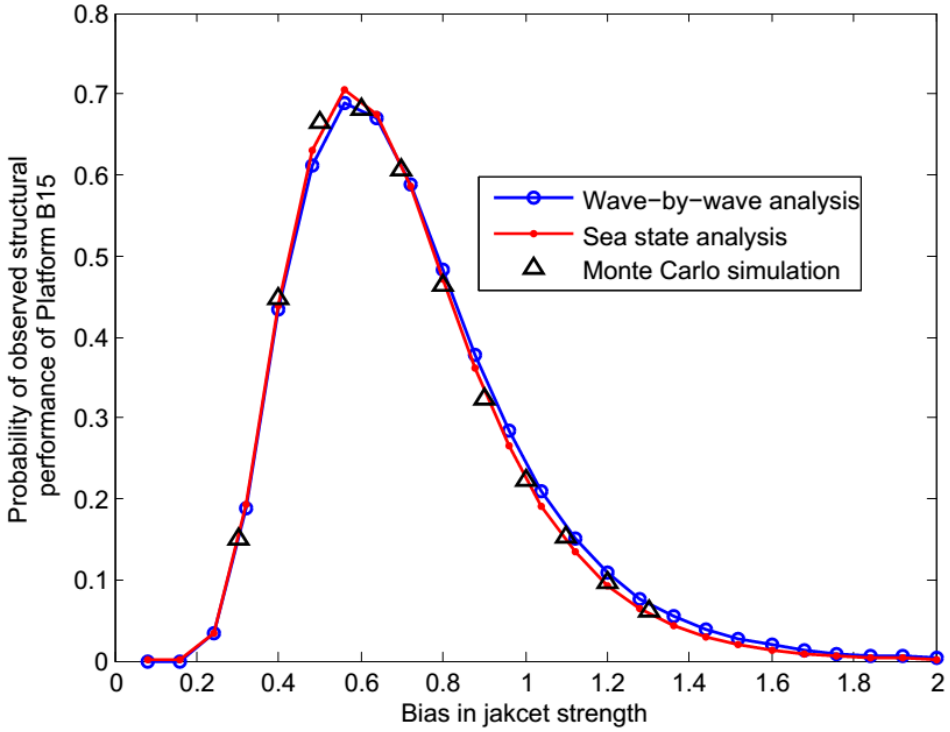

Figure 6.3 Validation of FORM and sea state approach

6.4.2.7 Likelihood functions of multiple observations

For platforms at different sites (i.e., in different geological settings), or platforms subjected to different hurricanes, it is expected that the platform performances will be statistically independent. Therefore, the likelihood function of multiple platforms can be calculated as follows:

$$LH\left(\text{Performance}|\mathbf{B}=\mathbf{b}\right)=\left[\prod_{all\ i\ failures}P\left(\text{Failures}\,|\,\mathbf{B}=\mathbf{b}\right)\right]\times\left[\prod_{all\ \text{j}\ damages}P\left(\text{Damages}\,|\,\mathbf{B}=\mathbf{b}\right)\right]\times\left[\prod_{all\ k\ survivals}P\left(\text{Survivals}\,|\,\mathbf{B}=\mathbf{b}\right)\right] \quad 6.17$$

where "*i*", "*j*", and "*k*" represent *ith*, *jth*, and *kth* platforms in Table 6.1, respectively.

For platforms at the same site subjected to the same hurricane, the wave loads are correlated since the metocean conditions and the model errors in the hindcast model

are the same. This correlation is captured in the FORM through the hindcast significant wave height error ε_1 and current velocity error ε_2. In addition, while the foundation capacities are also positively correlated, this effect is relatively small compared to the wave loading due to the random variability induced by pile driving; hence it is reasonable to neglect it. Therefore, for two platforms at the same site subjected to the same hurricane, the likelihood of the observed performance is estimated from six failure mechanisms (i.e., two jacket failure mechanisms, two base shear failure mechanisms, and two overturning failure mechanisms) with correlated wave loads, where the correlation in wave loads is calculated from the most probable failure point through the hindcast errors ε_1 and ε_2.

6.4.2.8 Example likelihood functions

Figure 6.4 shows the variation of the likelihood functions of selected platforms with the bias factor in the structural resistance B_j (all the other biases are fixed to 1.0). Since Platform B1 survived Hurricane Andrew, the likelihood increases with B_j for $B_j \leq 1.6$ after which the likelihood remains essentially the same since the survival of the platform will be governed by the foundation capacity for the large value of B_j. Opposite to the trend of Platform B1, the likelihood of Platform B3 remains almost the same for small value of B_j and decreases with B_j for large B_j since it failed in the jacket structure but the foundation was intact. For Platform B14, the likelihood function is bounded since the platform structure was damaged but not collapsed during Hurricane Rita.

Figure 6.5 shows the variation of the likelihood functions of selected platforms with the bias factor in the foundation overturning resistance in clay B_{fa}^c (all the other biases

are fixed to 1.0). The likelihood function of Platform B1 and B14 increase with B_{fa}^{c} since Platform B1 survived the hurricane, while Platform B14 was damaged but the foundation was intact. The likelihood of Platform B18 decreases with B_{fa}^{c} since it failed in foundation overturning, but the jacket structure was intact.

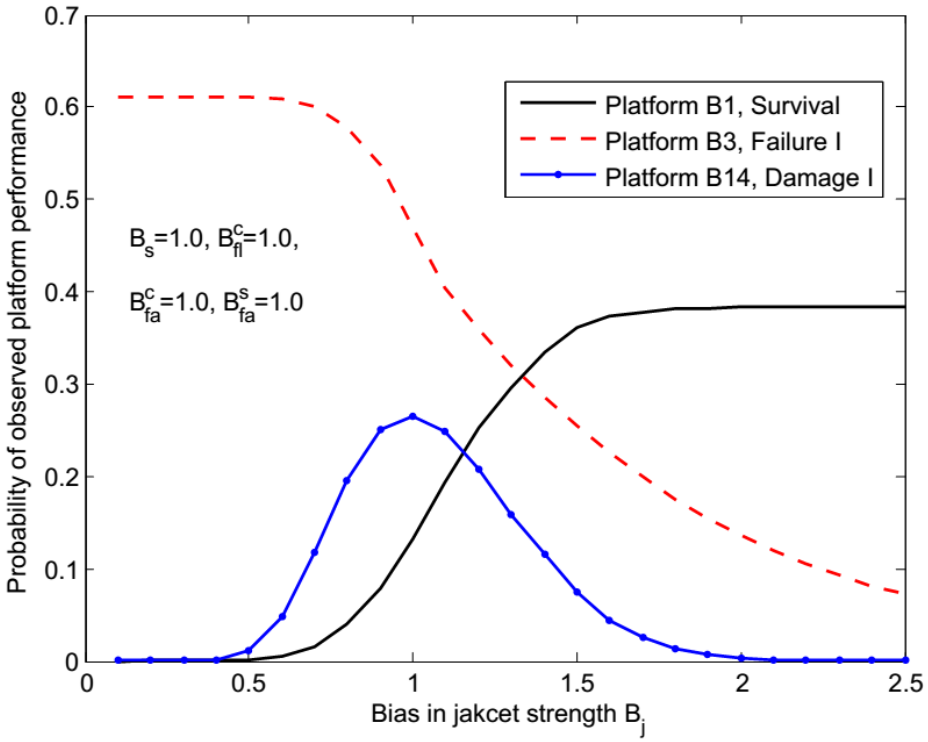

Figure 6.4 Likelihood functions of selected platforms- B_j varies

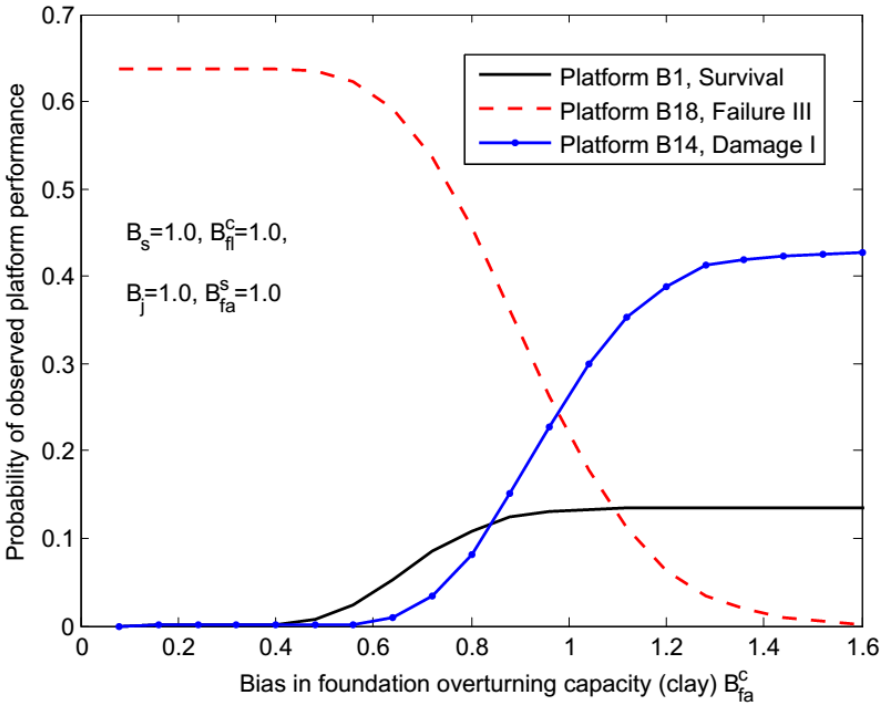

Figure 6.5 Likelihood functions of selected platforms- B_{fa}^{c} varies

6.5 Model improvements over previous studies

This study uses the same Bayesian calibration framework as the previous studies (ABS, 2004, Energo Engineering, 2007, PMB Engineering, 1993, PMB Engineering, 1996), but improves the model from the following aspects:

(1) The error in the hindcast significant wave height ε_1 is assumed to be log-normal with a c.o.v. of 0.15, instead of 0.1 in the previous studies. The c.o.v. of 0.1 used in the previous studies was primarily based on the hindcast data from Hurricane Andrew in 1992, and only three data points were used for the estimation of the c.o.v. (see Figure 6.6). More observations are available from recent Gulf of Mexico hurricanes. Figure 6.6 shows the predicted and measured (3-hour averaged) maximum hindcast significant wave height in the peak sea state in recent Gulf of Mexico hurricanes (Forristall, 2007, Oceanweather, 2006, PMB

Engineering, 1993, Oceanweather, 2003). For all the data points presented the Figure 6.6, the mean of ε_1 is 1.03 and the c.o.v. is 0.14; for the significant wave height of engineering significance (i.e., $h_s \geq 20$ ft), the mean is 1.01 and the c.o.v. is 0.15. This finding is consistent with the conclusions of Forristall (2007) which were obtained from the comparison of the predicted and measured significant wave height in the whole sea state (not just the peak sea state) in recent Gulf of Mexico hurricanes (sampling variability excluded).

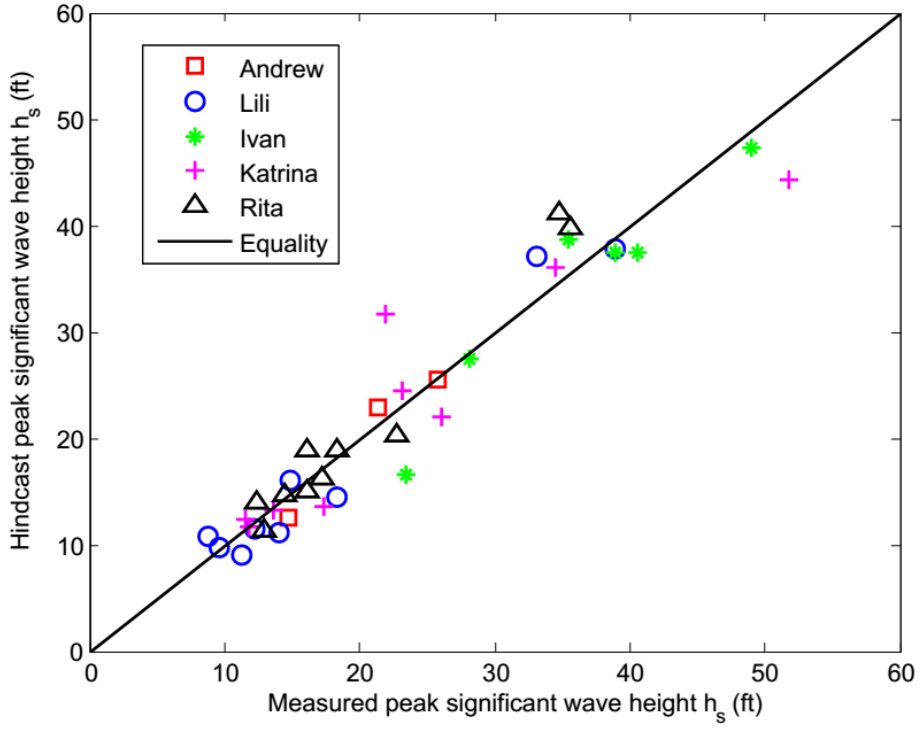

Figure 6.6 Comparison of predicted and measured h_s

(2) The mean zero-crossing wave period T_z is used in the current study for the calculation of wave cycles, instead of the spectral peak period T_p in the previous studies. In the Gulf of Mexico hurricane conditions, T_z can be approximated as $0.74T_p$ (Chakrabarti, 2005). The use of T_z is consistent with the original derivation of the Forristall's distribution (Forristall, 1978), and is consistent with

the industry practice of the wave statistics (Anderson *et al.*, 1982, Tromans and Vandersohuren, 1995, API RP 2A-WSD, 2014, Chakrabarti, 2005).

(3) The current study uses more platforms (in total, 18 platforms from recent five Gulf of Mexico hurricanes) than the previous studies in the Bayesian updating. In particular, a foundation failure case (Platform B18) is incorporated. In addition, best estimates of the soil parameters are made in determining the foundation capacity (e.g., Platform B12 and B17) and the jacket structural capacity (e.g., Platform B12).

(4) For platforms at the same site subjected to the same hurricane (i.e., Platform B1 and B3 subjected to Hurricane Andrew, Platform B12 and B17 subjected to Hurricane Katrina), the wave statistics for the two platforms are similar. Hence, the correlation of the platforms in evaluating the likelihood function through the hindcast errors (i.e., $\varepsilon_1, \varepsilon_2$) is explicitly considered in the FORM.

(5) A consistent logic for Damage I platforms (i.e., the jacket structure is known to be damaged, but the foundation is intact) is used in the current study. In the previous studies (ABS, 2004, Energo Engineering, 2007, PMB Engineering, 1993, PMB Engineering, 1996), the calculation of the likelihood function of a Damage I platform is based on the logic that the wave base shear force is in between the jacket first damage resistance and the jacket ultimate resistance, and the jacket first damage resistance is less than the foundation resistance. However, this logic does not preclude the possibility that the wave base shear force exceeds the foundation resistance which will fail the foundation. Hence, a more consistent logic in evaluating the likelihood function of a Damage I platform is shown in Section 6.4.2, i.e., $LH\left(\text{Damage I}\,|\mathbf{B}=\mathbf{b}\right)$=*P*(jacket first damage resistance< *BS*

<jacket ultimate resistance AND *BS* <foundation lateral resistance AND *BS* <foundation overturning resistance).

(6) In the previous studies, the model bias factor is defined as the ratio of the resistance bias to the load bias. This approach captures the global safety margin in offshore platform designs, and three global safety bias factors respectively for jacket structure, foundation lateral, and foundation axial behaviors were introduced. An implicit assumption made in the calibration is that the three global safety bias factors are statistically independent for the prior distributions. Theoretically, this statistical independence assumption is not correct because the global safety bias factors are correlated as all the three failure modes subject to the same wave loading. The approach used in this study breaks the global safety bias factor into the separate load and resistance bias factors which overcome the above shortcoming theoretically. In addition, the current approach classifies the pile in clay and sand, which provides more insights into the bias in the pile axial capacity prediction model.

(7) In addition to the wave-by-wave analysis, a sea state approach is also used in this study, which greatly increases the efficiency and convergence of the model.

6.6 Calibration results

The updated distributions for the epistemic model bias factors are shown in Figure 6.7 to 6.11 and the updated statistics are listed in Table 6.10. The mean is calibrated from 0.93 to 0.92 for B_s; from 1.0 to 0.95 for B_j; from 1.0 to 1.17 for B_{fl}^c; from 1.3 to 1.05 for B_{fa}^c, and from 1.3 to 1.44 for B_{fa}^s. The c.o.v. is calibrated from 0.2 to 0.13 for B_s; from 0.2 to 0.13 for B_j; from 0.3 to 0.24 for B_{fl}^c; from 0.3 to 0.19 for B_{fa}^c, and from 0.5 to 0.37 for B_{fa}^s.

The mean values for the wave load and jacket structural capacity are lower than 1.0, which indicates that the current method following the API recipe both over-predicts the wave load and the jacket structural capacity on average. The mean of the updated bias factor for lateral capacity, B_{fl}^{c}, increases because all of the case study platforms survived hurricane loading in this failure mechanism. The mean of the updated bias factor for an overturning failure in clay, B_{fa}^{c}, decreases because there are both survivals and failures for this failure mechanism in the case study platforms. Similarly, the updated c.o.v. value for this bias factor reduces significantly because the combination of survivals and failures effectively limits the possibilities of both large and small values for B_{fa}^{c}. The mean of the updated bias factor for an overturning failure in sand increases because all of the case study platforms survived hurricane loading in this failure mechanism and several of the survivals were unexpected. The updated c.o.v. value for this failure mechanism is the largest because there tends to be greater aleatory variability in these cases due to lack of site-specific soil borings.

Table 6.10 Comparison of prior and updated statistics on bias factors

	Prior			Updated		
	Mean	c.o.v.	Correlation Coefficient	Mean	c.o.v.	Correlation Coefficient
B_s	0.93	0.2	-	0.92	0.13	-
B_j	1.0	0.2		0.95	0.13	
B_{fl}^{c}	1.0	0.3	-	1.17	0.24	-
B_{fa}^{c}	1.3	0.3	-	1.05	0.19	-
B_{fa}^{s}	1.3	0.5	-	1.46	0.37	-
B_s, B_j			0			0.79
B_s, B_{fl}^{c}	-	-	0	-	-	0.19
B_s, B_{fa}^{c}	-	-	0	-	-	0.40
B_s, B_{fa}^{s}	-	-	0	-	-	0.07

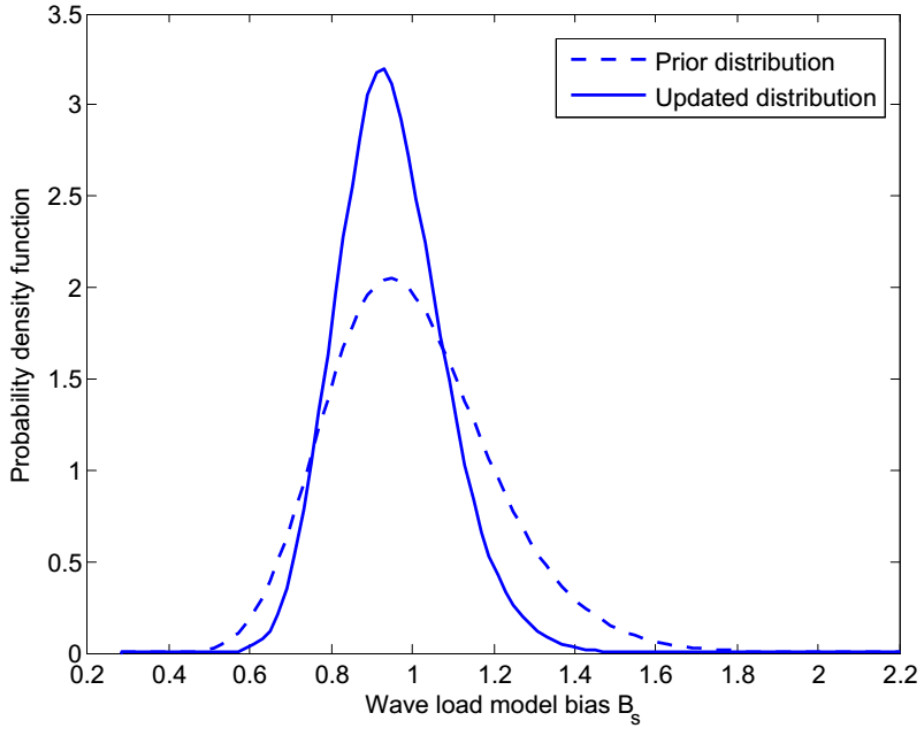

Figure 6.7 Comparison of prior and updated probability distributions for B_s

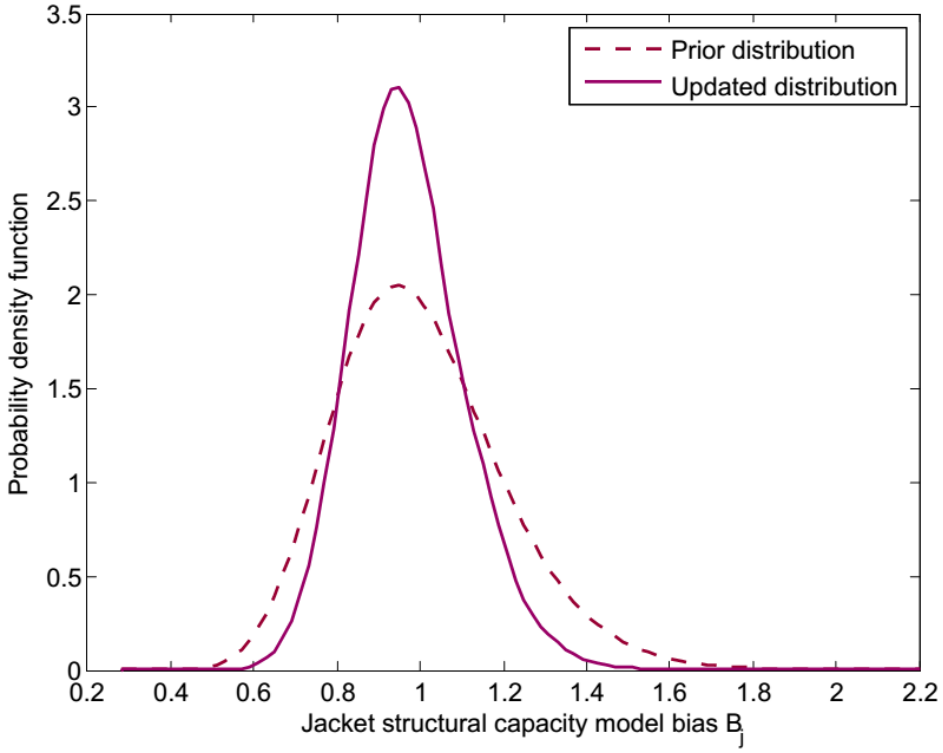

Figure 6.8 Comparison of prior and updated probability distributions for B_j

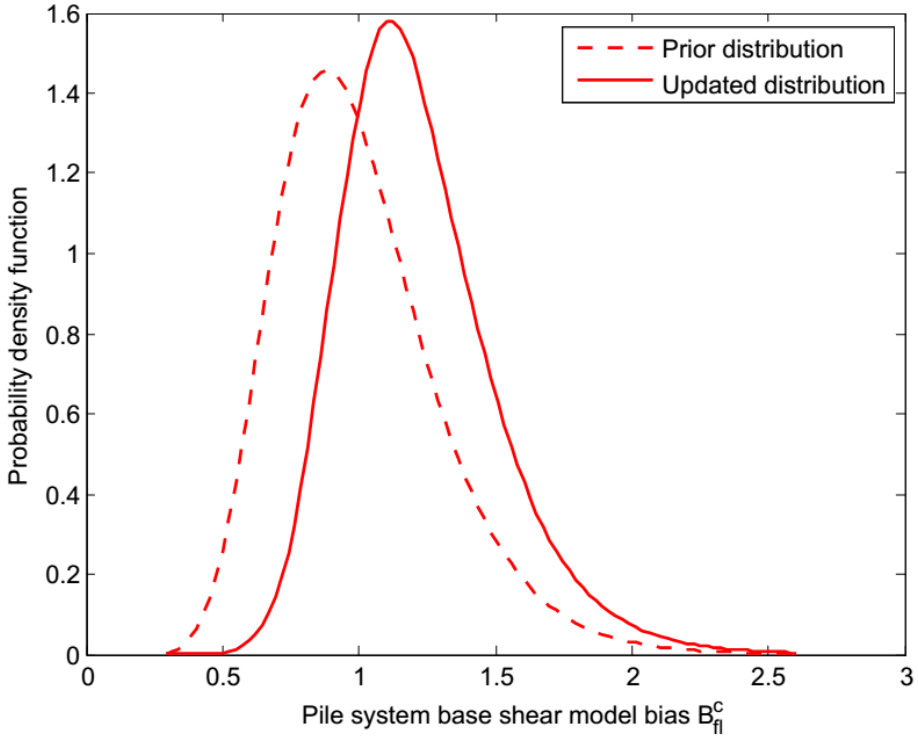

Figure 6.9 Comparison of prior and updated probability distributions for B_{fl}^c

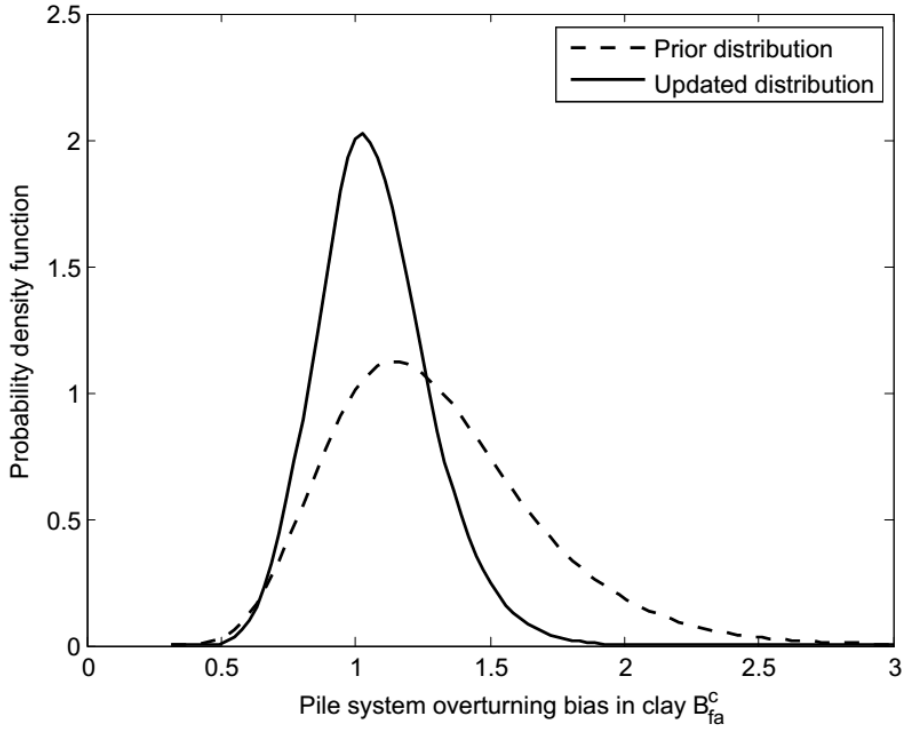

Figure 6.10 Comparison of prior and updated probability distributions for B_{fa}^c

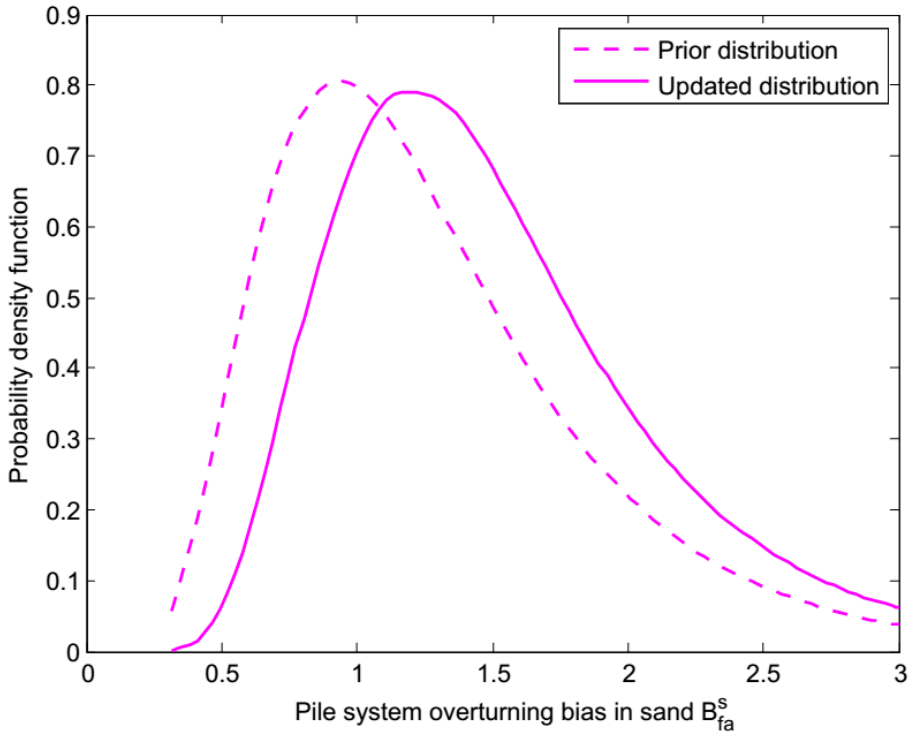

Figure 6.11 Comparison of prior and updated probability distributions for B^s_{fa}

It is useful to introduce a safety bias factor that captures the combined effects of updating the loads and the capacities, defined as

$$\text{Safety bias} = \frac{B_R}{B_s} \tag{6.18}$$

The safety bias measures the bias in the predicted performance accounting both for the load and resistance.

Table 6.11 lists the mean and c.o.v. for the safety bias before and after the calibration by a log-normal approximation (the correlation between the variables in the updated bias factor is considered). As shown, the updated mean of B_j/B_s is 1.04, and is smaller than that in the prior distribution. Besides, the c.o.v. of B_j/B_s is reduced significantly. This indicates that the prediction of jacket performance following the API recipe using the current state-of-practice modeling skills are almost

unbiased, and the uncertainty in predicting the safety margin is low (i.e., c.o.v.=0.08). The updated safety bias factor an overturning failure in clay B^c_{fa}/B_s is decreased from 1.45 in the prior distribution to 1.16, and the c.o.v. is reduced significantly, from 0.37 in the prior distribution to 0.18 in the updated distribution. Since no foundations fail laterally or fail in an overturning in sand, the updated means for B^c_{fl}/B_s and B^s_{fa}/B_s increase when compared to the prior means; however, the c.o.v. reduces. Therefore, the API load and resistance recipe is slightly conservative for predicting a foundation overturning failure in clay, and is conservative for predicting a lateral failure in clay and a foundation overturning failure in sand.

Table 6.11 Comparison of prior and updated moments for safety bias factors

	Prior		Updated	
	Mean	c.o.v.	Mean	c.o.v.
B_j/B_s	1.12	0.29	1.05	0.08
B^c_{fl}/B_s	1.12	0.37	1.29	0.25
B^c_{fa}/B_s	1.45	0.37	1.16	0.18
B^s_{fa}/B_s	1.45	0.55	1.61	0.39

6.7 Hypothetical case calibration

The updated distribution for the wave load model bias factor has a low c.o.v. value of about 0.13, which may imply that the wave load prediction is consistent with the actual wave load in general. To further check that whether the low c.o.v. value calibrated from the Bayesian updating implies the consistent wave load prediction, two hypothetical platforms, Platform A and B, are tested in the Bayesian updating. Only the jacket performance of Platform A and B is considered. The wave load model and the hindcast data for Platform A are exactly the same as Platform B1 in Table 6.1. Hence, the mean wave load is 3757 kips, and the capacity is 2900 kips. Hypothetically,

Platform A is observed to survive the hurricane. The wave load model and the hindcast data for Platform B are exactly the same as Platform B3 in Table 6.1. Hence, the mean wave load is 3551 kips; however, the jacket capacity of Platform B is assumed to be 4500 kips. Hypothetically, Platform B failed in the hurricane. Based on the above assumptions, the predicted platform performance is inconsistent with the observed platform performance (see Table 6.12).

Based on these two hypothetical platforms, the mean is calibrated from 0.93 to 0.87 for the wave load bias factor B_s; from 1.0 to 1.06 for the jacket resistance model bias factor B_j. The c.o.v. is calibrated from 0.2 to 0.176 for B_s; from 0.2 to 0.177 for B_j. Therefore, the updated distributions have lower variability when compared to the prior distributions (Figure 6.12 and 6.13). These results reveal that based on the current mathematical model for the likelihood function and the prior distribution, even when the predicted platform performance is inconsistent with the observed performance, the updated distribution will still have lower variability. This finding directly challenges the claim that the updated low c.o.v. value of 0.13 for the wave load model bias factor implies that the wave load prediction is consistent with the actual wave force. Therefore, further research is required to improve the mathematical model for the likelihood function and the prior distribution so that the variability in the updated distribution may increase when the prediction is inconsistent with the observation.

Table 6.12 Predicted and observed performance of hypothetical platforms

Platform	Expected Maximum Wave Base Shear (kip)	Jacket Resistance (kip)	Predicted Performance	Observed Performance
A	3757	2900	Failure	Survival
B	3551	4500	Survival	Failure

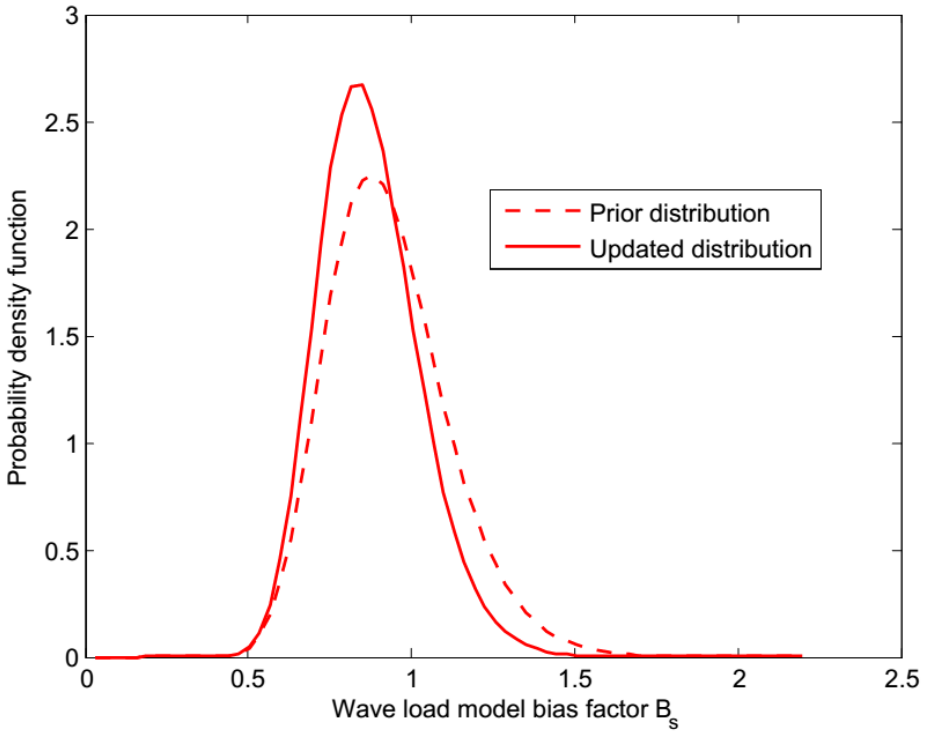

Figure 6.12 Updated wave load model bias from hypothetical platforms

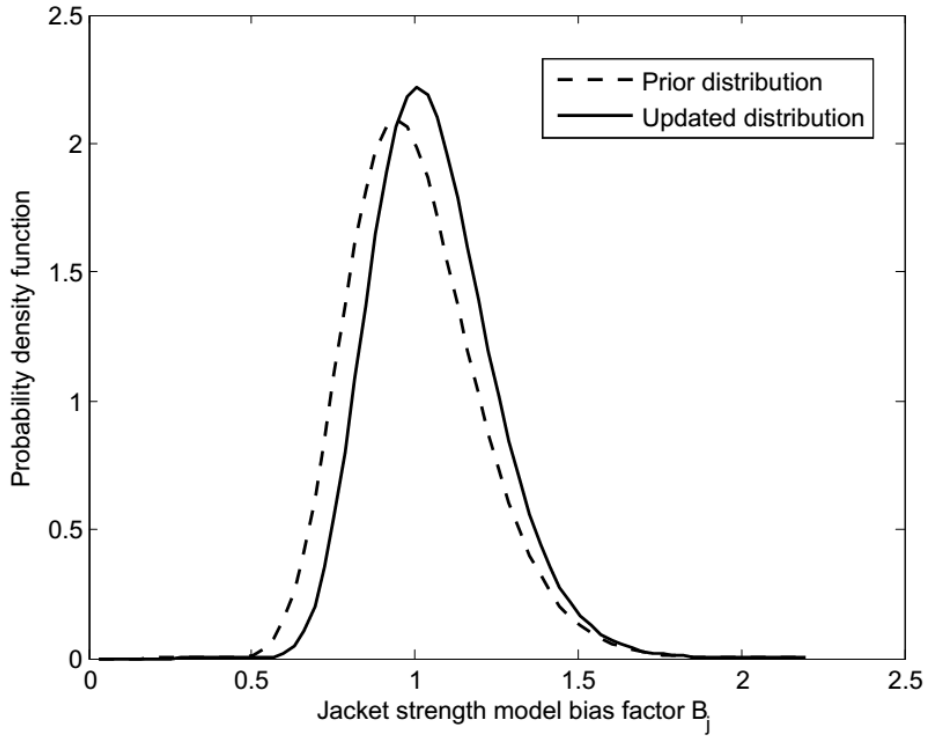

Figure 6.13 Updated jacket resistance model bias from hypothetical platforms

6.8 Back analysis of Platform B18

Platform B18 is the first comprehensively documented case of foundation failure for a jacket platform in a hurricane, where the foundation system was loaded beyond its design capacity and failed (Chen *et al.*, 2013). Hence, the overturning failure of Platform B18 provides a valuable full-scale pile load test under actual extreme environmental conditions. The current practice can be improved from the comparison of the predicted and observed pile axial capacities. However, significant uncertainty exists in the observed pile axial capacity due to the uncertain hindcast model, uncertain wave loading recipe, and the inherent variability in waves and currents. Chen *et al.* (2013) analyzed the distribution of the pile axial load based on a simplified wave loading model and the hindcast model uncertainty was primary based on the observations in Hurricane Andrew in 1992. The uncertainties in the pile axial load and capacity can be reduced by observing the platform structure response in Hurricane Ike since the structure was intact in the hurricane. This structural response information and the failure of Platform B18 are incorporated the Bayesian calibration to update the distributions of the pile axial load and capacity.

The prior distribution of the pile axial load is established through the detailed analysis of the metocean data in the 3-hour sea state, the hindcast model uncertainty based on recent hurricanes (Figure 6.6), and the wave force model (Equation 6.1) using the FORM. The prior distribution of the wave loading model bias factor is used, i.e., the mean is 0.93 and the c.o.v. is 0.2. The prior distribution of the pile axial capacity is established by considering the prior distribution of the model bias factor for the pile system overturning (i.e., axial) capacities in clay B_{fa}^{c} (i.e., the mean is 1.3 and the c.o.v. is 0.3) and considering the aleatory uncertainty (i.e., the c.o.v. is 0.1).

The prior distributions for the axial load on Pile C and the axial resistance of Pile C are shown in Figure 6.14.

The pile head axial load and the pile axial capacity can be updated from the observed performance of Platform B18 (i.e., the platform failed in overturning) as well as the observed performance of the remaining 17 platforms in Table 6.1. Hence, Bayes' Theorem is used to update the axial load and resistance. To learn from the observed platform performance presented in the previous sections, in the Bayesian updating, the updated epistemic wave loading model bias B_s, calibrated from 17 platforms (i.e., Platform B1 to B17 in order to avoid the repetitive use of Platform B18 in the Bayesian updating), is used. Similarly, the updated epistemic model biases which are calibrated from Platform B1 to B17 are used for the jacket strength and the pile axial capacity.

As shown in Figure 6.14, the mean of the maximum axial load on the most critical pile (denote Pile C) is updated from 3631 kips to 3858 kips. While the mean of the maximum axial load increases slightly, the c.o.v. is reduced significantly from 0.35 in the prior distribution to 0.16 in the updated distribution. The mean of the axial capacity of Pile C is updated from 4584 kips to 3424 kips, the corresponding c.o.v. is reduced from 0.32 to 0.17. The 70% confidence bounds of the maximum axial load and the capacity of Pile C are updated from 2430-4930 kips to 3170-4460 kips, and from 3283-6243 kips to 2830-4025 kips, respectively.

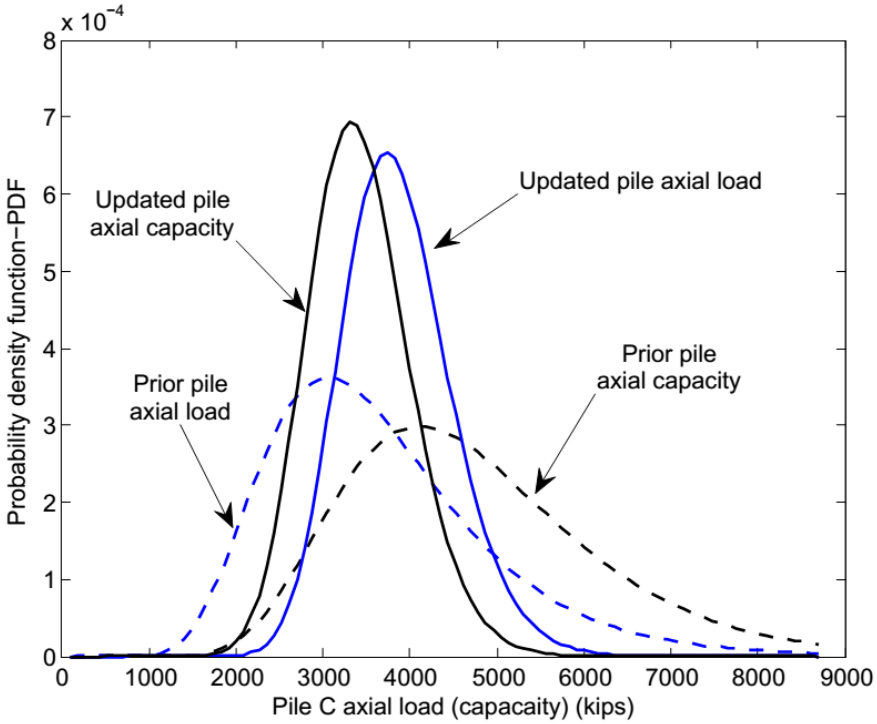

Figure 6.14 Distributions of pile axial load/capacity

It is meaningful to estimate the number of wave cycles exceeding a specific load level. The prior estimation is based on the prior model bias factors before the Bayesian calibration, and hence does not contain observed platform performance. The updated results are obtained from the Monte Carlos simulation and incorporate the observed platform performance through the Bayesian updating (i.e., the platform fails in overturning, but the jacket is intact) and the updated model bias factors from 17 platforms. The sea state approach is used in the Monte Carlo simulation.

The direct Monte Carlo simulation with the wave-by-wave analysis is almost impossible to perform the above task when the Monte Carlo simulation is combined with Bayesian updating. The reason is that, as discussed above, the wave-by-wave analysis involves two loops: (i) the inner loop which essentially simulates the Forristall's distribution and has about 1000 wave cycles in a 3-hour peak sea state, and (ii) the outer loop which simulates the hindcast errors and random capacities. Each loop has to be conducted by the Monte Carlo simulation. With the combination

of the Bayesian updating, the wave force from the inner loop must be consistent with the observed platform performance, e.g., the wave force from the inner loop must exceed the overturning capacity, but be less than the pile system lateral capacity and the jacket system capacity of Platform B18. If in the outer loop, the realized significant wave height is small but the realized pile system overturning capacity is high, the computational effort will be extremely high in the inner loop since the small significant wave height is difficult to produce a large wave load to fail the platform and each realization of the outer loop causes about 1000 realizations in the inner loop.

Figure 6.15 shows the expected number of wave cycles for different levels of loading (fraction of the updated mean Pile C axial capacity). Since all the epistemic and aleatory uncertainties considered, the result is expected to be more representative than that in Chen *et al.* (2013). The number of cycles is doubled if the loading level is decreased by 10% of the mean axial capacity, e.g., it is expect that 2 cycles of waves causing axial loads exceeding the mean axial capacity of Pile C, and 8 cycles exceeding 80% of the mean axial capacity of Pile C based on the updated results.

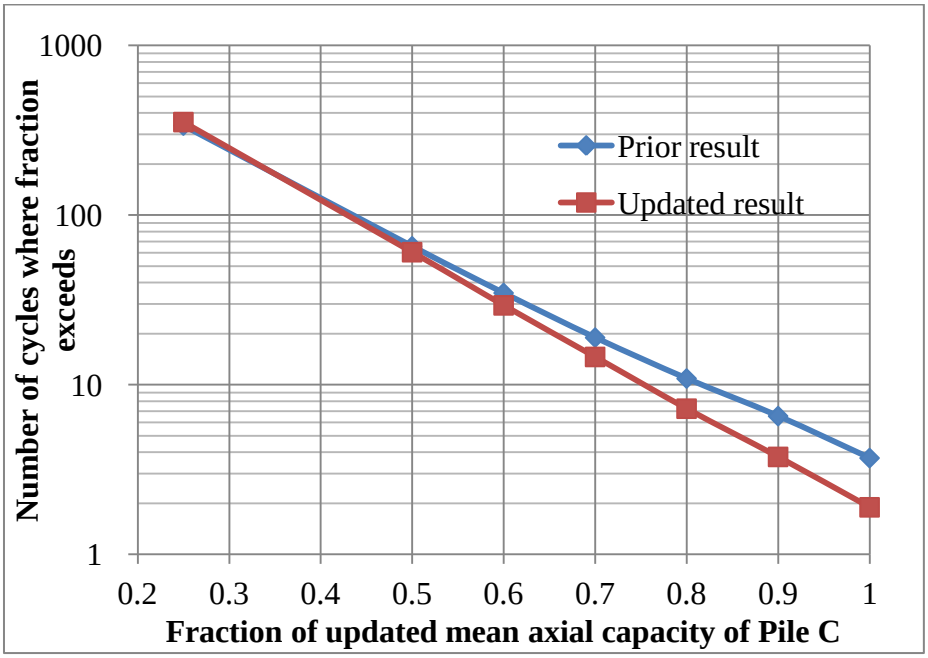

Figure 6.15 Expected number of cycles for different levels of axial load on Pile C

6.9 Conclusions

This chapter calibrates the model biases in the API load and resistance recipes by comparing analytically predicted with actually observed offshore platform performance in recent Gulf of Mexico hurricanes using Bayes' Theorem. Platform performance is divided into damage/collapse in the jacket structure, lateral base shear and overturning failures of the foundation. Both wave-by-wave and sea state approaches are used to capture the wave loading uncertainty. The calibration reveals that the API load and resistance recipe is close to be unbiased for predicting the jacket system performance; is slightly conservative for predicting a foundation overturning failure in clay; and is conservative for predicting a lateral failure in clay and a foundation overturning failure in sand.

A back analysis of a failed tripod (Platform B18) is conducted. With the updated model bias factors and the observed failure of the tripod, the uncertainties in the pile head load and the pile capacity reduced. The Monte Carlo simulation reveals that about two wave cycles produce a pile head load exceeding the updated mean axial capacity of the most critical pile.

7 Offshore Platform Reliability

This chapter aims to present reliability evaluations for generic platforms and specific case study platforms. The proposed lower bound method for the pile system capacity will be combined with reliability methods to evaluate the pile system reliability. The first order reliability method (FORM) will be used in all the reliability calculations.

7.1 Lifetime reliability model

Comparing to the short-term 3-hour peak sea state analysis, additional uncertainty exists in the reliability of a pile system over its design life due to the unknown number, strength and location of future hurricanes at the site (Gilbert *et al.*, 2014). In the current study, this additional uncertainty is accounted for by introducing the long term distribution of the maximum wave height $H_{\max}$. Hence, the reliability calculation is based on $H_{\max}$ and a sea state approach is used. By combining the simple wave force model (Equation 6.1) and the reliability model (Equation 6.2), the limit state function for the lifetime reliability can be simplified as

$$g = B_R \xi_R r_{predicted} - B_s B_{sw} C_1 \left(H_{\max,life} \right)^{C3} \tag{7.1}$$

where $H_{\max,life}$ represents the lifetime maximum wave height. Note that in Equation 7.1, the current velocity is neglected due to the relatively small effect when compared to the effect of the wave height. The resistance model bias factor B_R and the load model bias factor B_s are random variables, and can be correlated. B_{sw} is deterministic and reflects the difference between the wave-by-wave analysis and the sea state analysis, i.e., the sea state approach implicitly assumes that the uncertainty in the

wave force for a given platform under the given wave height, is perfectly correlated and independent of sea states and platform durations; hence, the sea state approach tends to under-predict the maximum wave force in general. $B_{sw} = 1.18$ is used based on Figure 6.2.

The distribution of $H_{\max,life}$ is calculated from the annual distribution of maximum wave height as follows:

$$CDF\left(H_{\max,life}\right) = \left[CDF\left(H_{\max,annual}\right)\right]^{N} \quad 7.2$$

where $H_{\max,annual}$ represents the annual maximum wave height; *N* is the platform design life in years. Hence, statistical independence of the maximum wave height from years to years is assumed in Equation 7.2.

The upper tail of the distribution of $H_{\max,annual}$ usually governs the reliability of an offshore pile system. Hence, $CDF\left(H_{\max,annual}\right)$ is directly interpolated from the return period curve for $H_{\max,annual}$ from API RP 2MET (2014) for return period between 10 to 1000 years. For a return period less than 10 years or greater than 1000 years, $CDF\left(H_{\max,annual}\right)$ is extrapolated by two-parameter Weibull distributions fitted at the return period of 10 to 15 years, and 500 to 1000 years, respectively. Figure 7.1 shows the example distribution of $H_{\max,annual}$ at different water depths in different regions of the Gulf of Mexico.

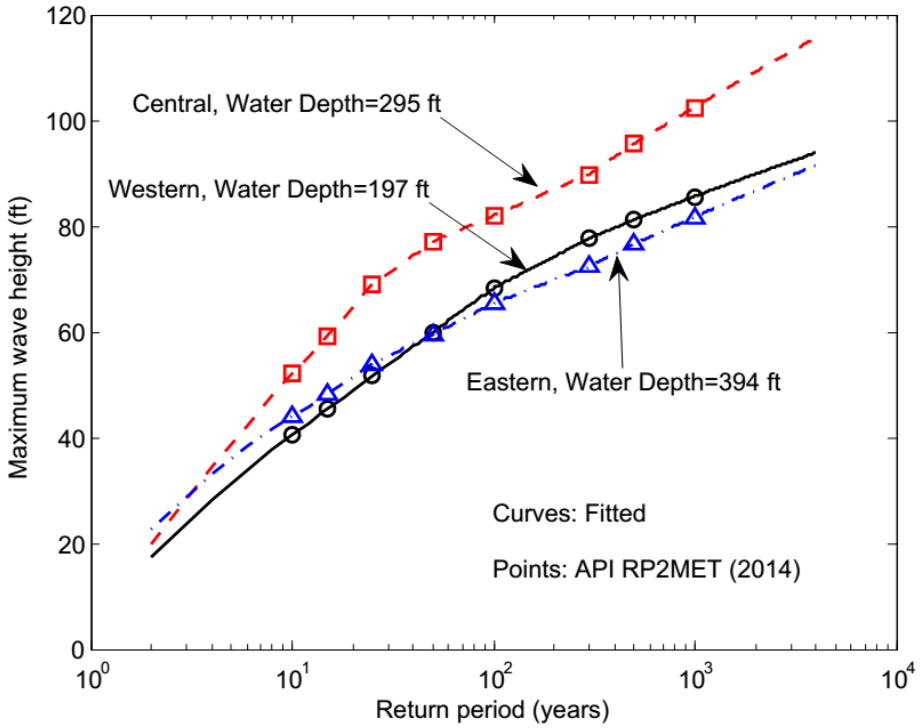

Figure 7.1 Example distributions of $H_{\max,annual}$ in Gulf of Mexico

7.2 Simplified reliabilities of generic offshore platforms

For the simplified analysis of a generic jacket structural system, the concept of the reserve strength ratio (RSR) (Krieger *et al.*, 1994) is used, which is defined as the ratio of the system ultimate capacity to the 100-year environmental load. Both the system ultimate capacity and 100-year environmental load are expressed in terms of the global base shear force at the mudline.

The prior and updated model bias factors used in the reliability calculation are based on Chapter 6. For the aleatory uncertainty in the pile system, it is assumed that a site-specific soil boring using the modern technique is available.

7.2.1 Reliability of a jacket structural system

Figure 7.2 shows the variation of the 20-year reliability index β_{20} of a generic jacket structural system with the RSR, at the water depth of 200 ft in the western region of the Gulf of Mexico. In the wave force model, C3=2.0 is used which represents the drag dominant platforms. The design wave height is based on 100-year return period, and hence represents the newly designed L1 structure. As shown, the reliability of the jacket increases with the updated model bias factors, the increment of β_{20} is about 0.1 at RSR=1.5, and is about 0.35 at RSR=2.5. For newly designed offshore jackets, the RSR is typically in the range of 1.85 to 2.2. In this range, the reduction of the failure probability using the updated model bias factors is around 2 when compared to that obtained from the prior model bias factors.

Figure 7.3 shows the variation of β_{20} of a generic jacket structural system with water depths and locations in the Gulf of Mexico (RSR=2.0). The updated model bias factors and C3=2.0 are used. As shown, the reliability is insensitive to the water depths and the locations, except for the central Gulf of Mexico at water depth less than 150 ft, where the reliability is the highest. Figure 7.4 shows the variation of β_{20} with the wave force model parameter C3 at the water depth of 200 ft in western region the Gulf of Mexico based on the updated model bias factors. For platforms dominated by the inertia force, C3 is close to 1.0; for platforms dominated by the drag force, C3 is around 2.0. When platforms subject to a wave-in-deck force, C3 will be greater than 2.0. As shown, the reliability decreases with the increase C3 due to the increase of the variability in the wave force when C3 increases. For RSR=1.85 to 2.2, β_{20} ranges from 2.43 to 3.13 when C3=1.0; ranges from 1.88 to 2.31 when C3=2.0.

The system β_{20} from Figure 7.3 is around 2.1, and is less than the average β_{20} of 2.7 to 2.8 for offshore tubular components in the API RP 2A-LRFD 1st edition (API RP 2A-LRFD, 1993). The reduction of the reliability index in this study when compared to the previous studies (Moses, 1986) are due to (i) the variation of the base shear from waves to waves is considered, i.e., $B_{sw} = 1.18$ is introduced in Equation 7.1, and (ii) the variability in the maximum wave height is higher than that used in the calibration of the API RP 2A-LRFD 1st edition.

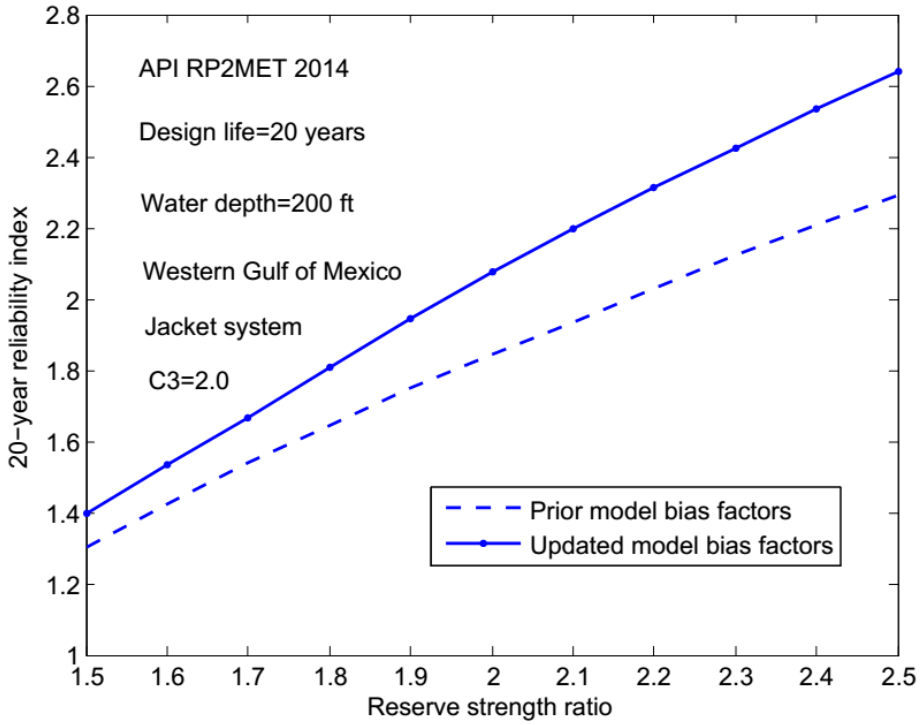

Figure 7.2 Variation of β_{20} with RSR - jacket

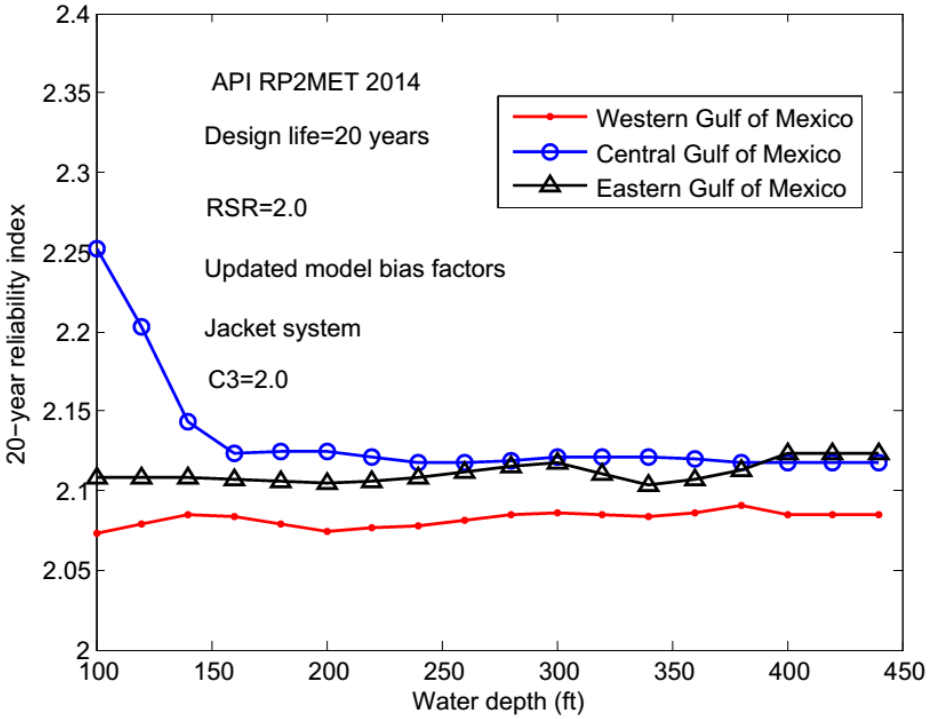

Figure 7.3 Variation of β_{20} with water depth – jacket

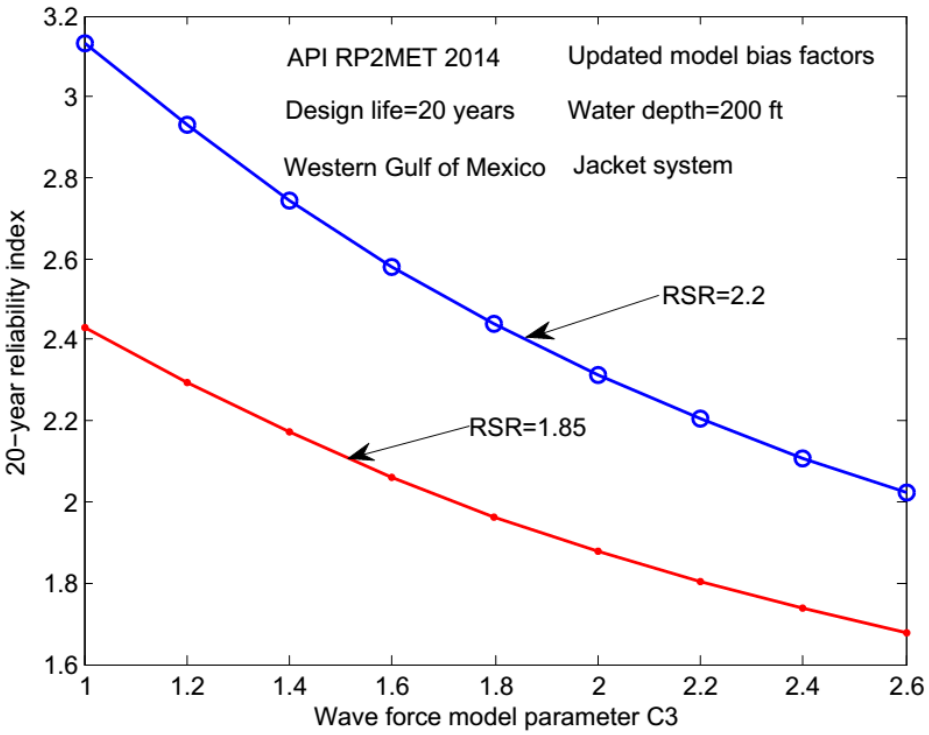

Figure 7.4 Variation of β_{20} with C3 – jacket

7.2.2 Reliability of pile system against a lateral failure

Figure 7.5 shows the variation of the 20-year reliability index β_{20} of the pile system against a lateral failure with the RSR, at the water depth of 200 ft in the western region of the Gulf of Mexico. C3=2.0 is used. The design wave height is based on 100-year return period, and hence represents the newly designed L1 structure. Similar results as the jacket structural system are observed. The increment of β_{20} is about 0.5 to 0.7 for RSR=1.5 to 2.5.

The design of laterally loaded piles is based on the model of a beam-column on nonlinear springs. The current design practice in the Gulf of Mexico is based on the working stress design, e.g., API RP 2A-WSD (2014). The design criterion is to limit the maximum stress in the pile wall to the allowable stress. In the design check equations for beam-columns, the allowable axial stress for compression is $0.6F_y$, where F_y is the yield strength of the pile steel, and allowable bending stress is usually $0.75F_y$ since the diameter-to-thickness ratio of the pile is typically less than 60. Considering the one-third increase in the steel yield strength in the extreme environmental conditions, the load causing the outmost fiber yield in the pile to the 100-year design load is about 1.0 to 1.25. Typically, column buckling in the pile is not usual due to the lateral resistance of the soil. Hence, the lateral failure of the pile will usually form plastic hinges. For tubular members, the ratio of the plastic section modulus to the elastic section modulus is about 1.3. Therefore, the ratio of the load causing the first plastic hinge in the most critical pile in a pile system to the 100-year load is about 1.3 to 1.625. Based on the redundancy analysis in Chapter 5, the pile system lateral capacity is about 40 to 60% higher than the load causing the first plastic hinge. Therefore, the RSR for the pile system lateral behavior is about 1.82 to 2.6.

The lower limit of RSR corresponds to the case with no axial load on the pile. Hence, a reasonable RSR for the pile system lateral behavior will be about 2.2. This RSR of 2.2 will generally be higher than the RSR for the jacket structural system, and it is expected that the reliability of the pile system against a lateral failure will be higher. As shown in Figure 7.6, the reliability is insensitive to the water depths and the locations, except for the central Gulf of Mexico at water depth less than 150 ft. The β_{20} is about 2.55 to 2.60 at RSR=2.2 in general.

Figure 7.7 shows the variation of β_{20} with the wave force model parameter C3 at the water depth of 200 ft in western region the Gulf of Mexico based on the updated model bias factors. Similarly, the reliability decreases with the increase C3. For RSR=1.82 to 2.6, β_{20} ranges from 2.58 to 3.70 when C3=1.0; ranges from 1.94 to 2.61 when C3=2.0.

The above analysis of the RSR for the pile system lateral behavior implicitly assumes that all the loads acting on the pile are caused by environmental loads. The presence of gravity load increases the reliability of the pile system against a lateral failure. This increased reliability is due to (i) gravity loads in general have less variability than the environmental loads, and (ii) the gravity loads generally cause axial stress on the piles, while the design factor of safety for axial compression (1.25 when one-third increase of the yield strength is considered) is higher than that for the bending stress (1.0 when one-third increase of the yield strength is considered for the diameter-to-thickness ratio less than 60) following API RP 2A-WSD (2014). Therefore, in reality, the reliability of the offshore pile system against a lateral failure is expected to be higher than that evaluated here.

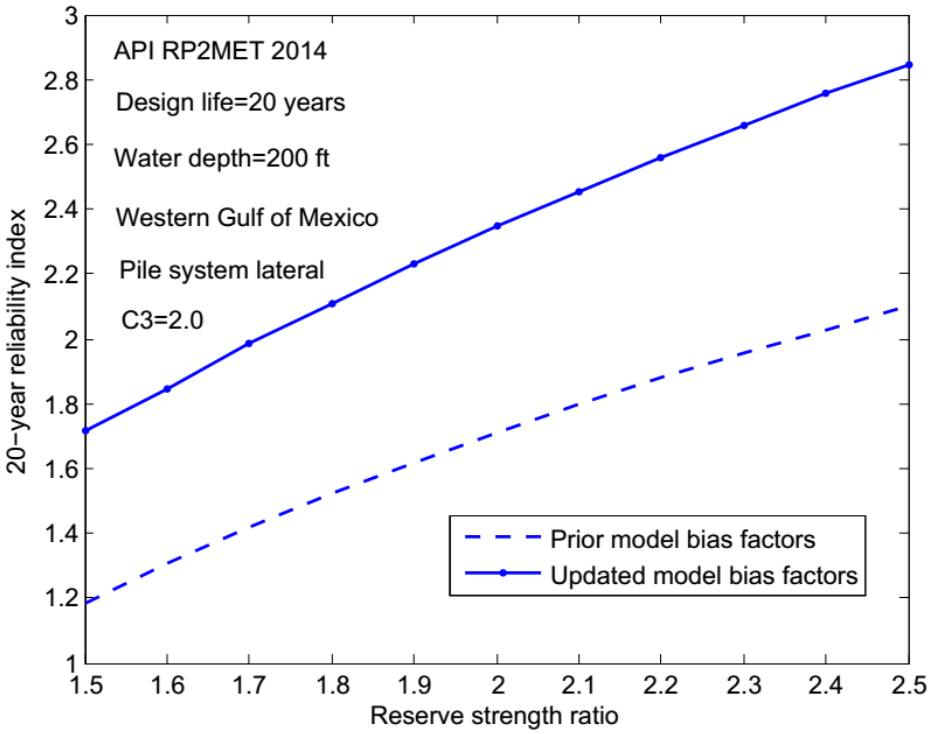

Figure 7.5 Variation of β_{20} with RSR – foundation lateral

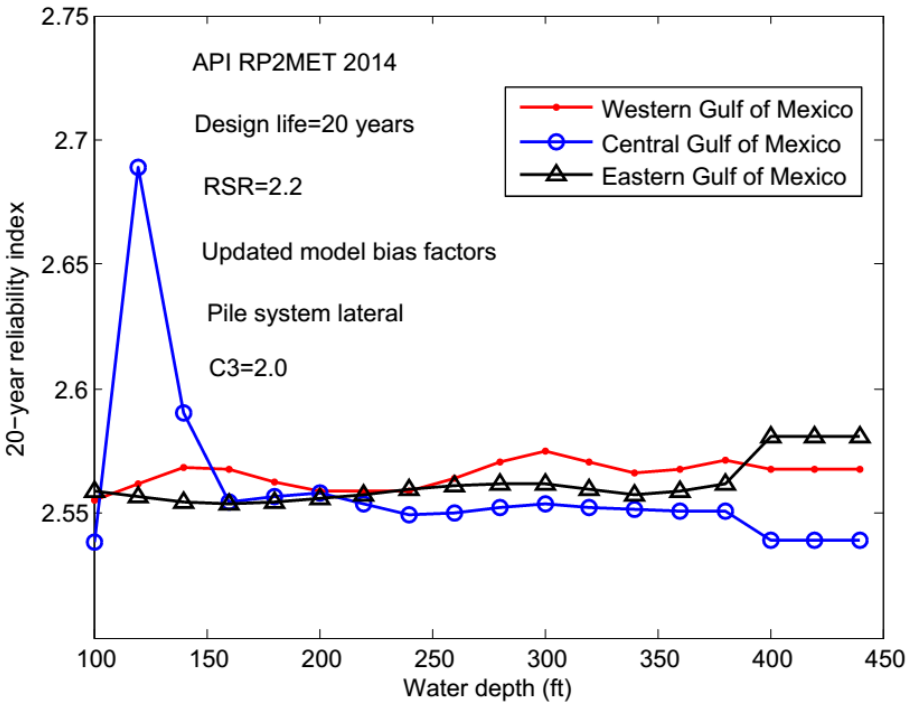

Figure 7.6 Variation of β_{20} with water depth – foundation lateral

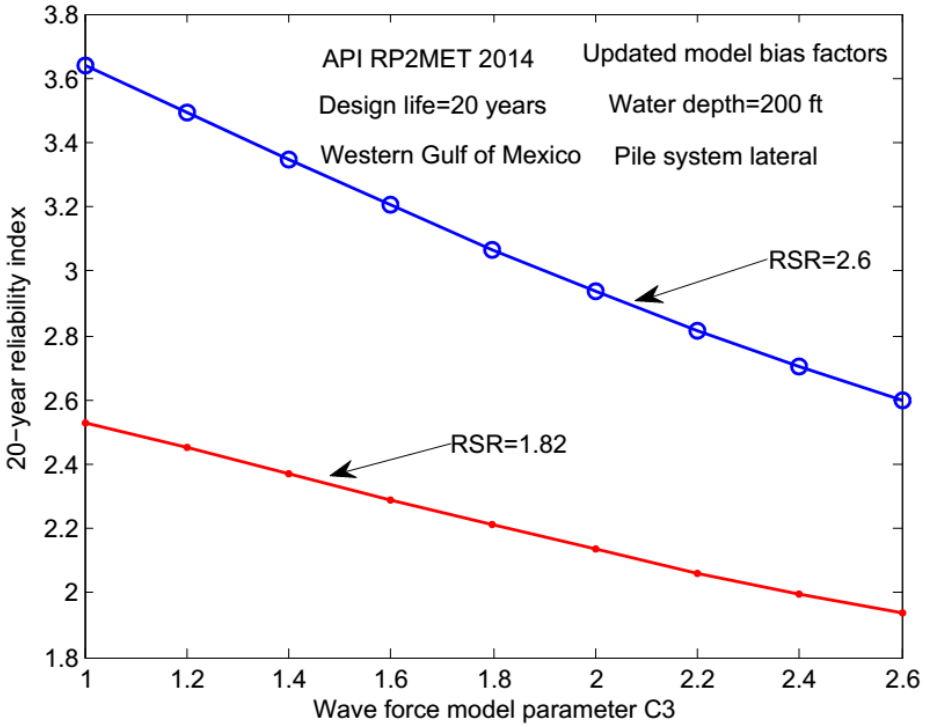

Figure 7.7 Variation of β_{20} with C3 – foundation lateral

7.2.3 Reliability of pile system against an overturning failure

The current state of practice in the Gulf of Mexico for the design of axially loaded piles uses a FS=1.5 based on the most heavily loaded pile in a pile system. The design environmental to gravity load ratio is typically in the range of $0.5 \sim 3.0$ based on platform surveys (Moses, 1986). Since the RSR is defined based on the 100-year environmental load and the gravity load on a pile is comparable to that caused by the environmental loads, the gravity load must be considered in relating the RSR to the FS. Using a FS=1.5 and assuming the nonlinear effect is not significant before the first axial failure of the most critical pile, the following relation can be obtained:

$$\frac{W_{first}}{W_n} = \frac{(G_n + W_n) \times FS - G_n}{W_n} = FS + (FS - 1)\frac{G_n}{W_n} \tag{7.3}$$

where W_{first}, W_n, and G_n represents the environmental load causing the first axial failure of the most critical pile, 100-year design environmental load, and design gravity load, respectively.

Using the concept of the deterministic system redundancy factor (DSRF) proposed in Chapter 5, the RSR can be expressed as follows:

$$RSR = \left[FS + (FS - 1) \times \frac{G_n}{W_n} \right] \times DSRF \qquad 7.4$$

Using a FS=1.5, $W_n / G_n = 0.5 \sim 3.0$, the RSR is in the range of 1.67 to 2.5 if the DSRF=1.0; in the range of 2.0 to 3.0 if the DSRF=1.2.

Figure 7.8 shows the variation of the 20-year reliability index β_{20} of the pile system against an overturning failure with the DSRF, at the water depth of 200 ft in the western region of the Gulf of Mexico. FS=1.5 and C3=2.0 are used. The design wave height is based on 100-year return period, and hence represents the newly designed L1 structure. As shown, the reliability of a pile system in clay against an overturning failure increases slightly using the updated model bias factors when compared to that using the prior model bias factors. However, the reliability of a pile system in sand against an overturning failure increases significantly using the updated model bias factors when compared to that using the prior model bias factors due to the fact that no pile systems in sand fail in overturning in the Bayesian calibration in Chapter 6.

Figure 7.8 also shows that the value of the environmental to gravity load ratio, W_n / G_n, has a large effect on the pile system reliability. Based on the updated model bias factors, $W_n / G_n = 0.5 \sim 3.0$, β_{20} against an overturning failure ranges from 1.8 to 2.8, and 1.9 to 2.6 for a pile system in clay and in sand, respectively, for the

DSRF=1.0; ranges from 2.3 to 3.2, and 2.2 to 2.9 for a pile system in clay and in sand, respectively, for the DSRF=1.2.

Similar to the previous discussions, the reliability against an overturning failure is insensitive to the water depths and the locations as shown in Figure 7.9. For the FS=1.5, $W_n/G_n = 2.0$, and DSRF=1.0, the β_{20} against an overturning failure is around 2.0 for both a pile system in clay and in sand. Figure 7.10 shows the variation of β_{20} with the wave force model parameter C3 at the water depth of 200 ft in western region the Gulf of Mexico based on the updated model bias factors at $W_n/G_n = 2.0$. For pile systems in clay, for DSRF=1.0 to 1.2, β_{20} ranges from 2.5 to 3.1 when C3=1.0; ranges from 1.8 to 2.1 when C3=2.0. For pile systems in sand, for DSRF=1.0 to 1.2, β_{20} ranges from 2.1 to 2.5 when C3=1.0; ranges from 2.0 to 2.2 when C3=2.0. The decrease of β_{20} is minor with the increase of C3, especially when C3 is less than 2.0. The reason for this minor variation is due to the relative high variability in the model bias factor for pile systems in sand.

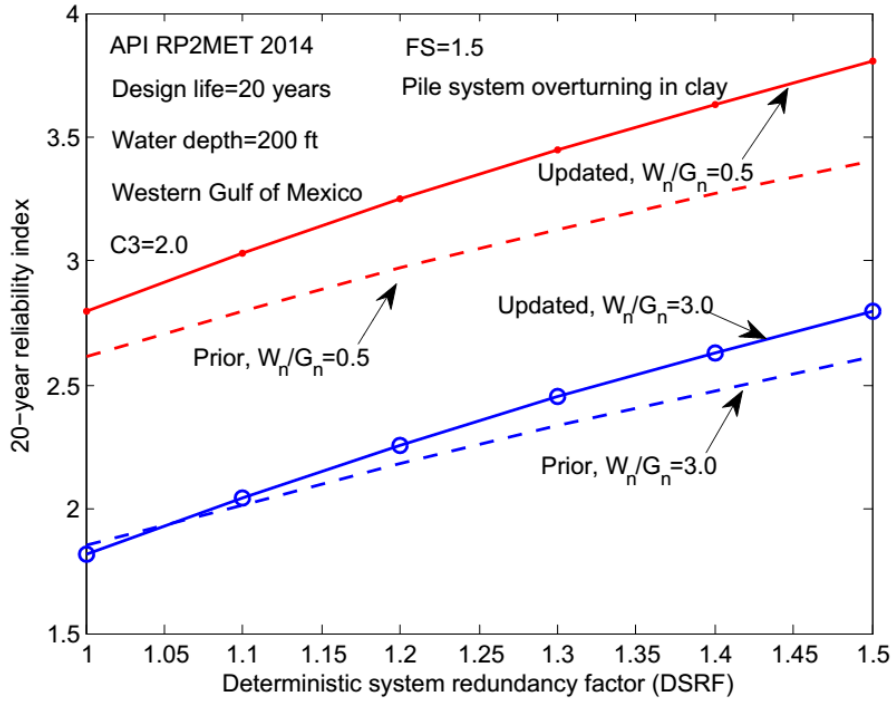

(a) Clay

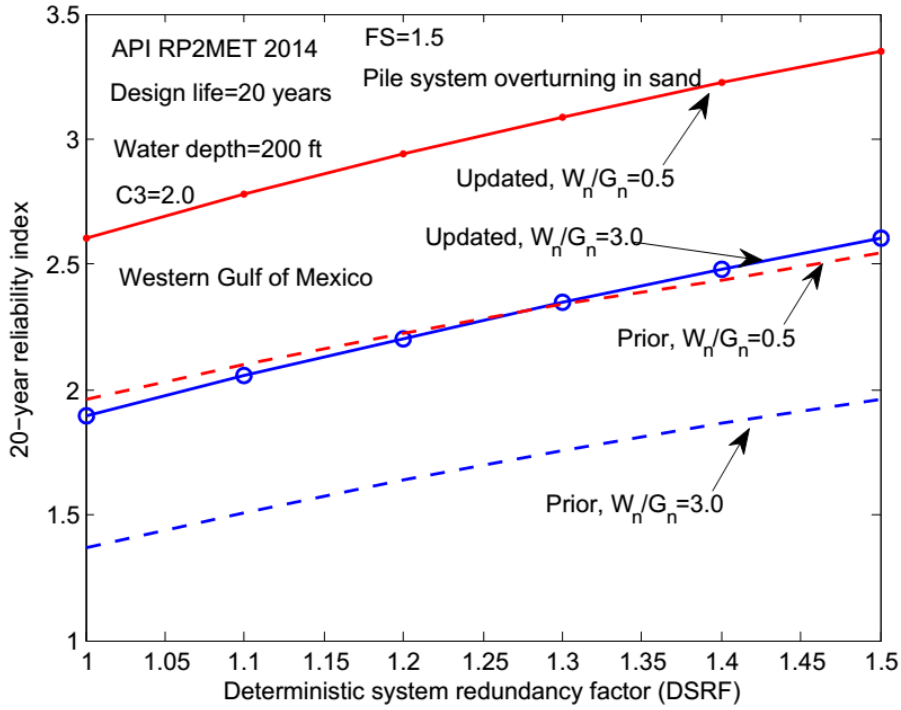

(b) Sand

Figure 7.8 Variation of β_{20} with DSRF

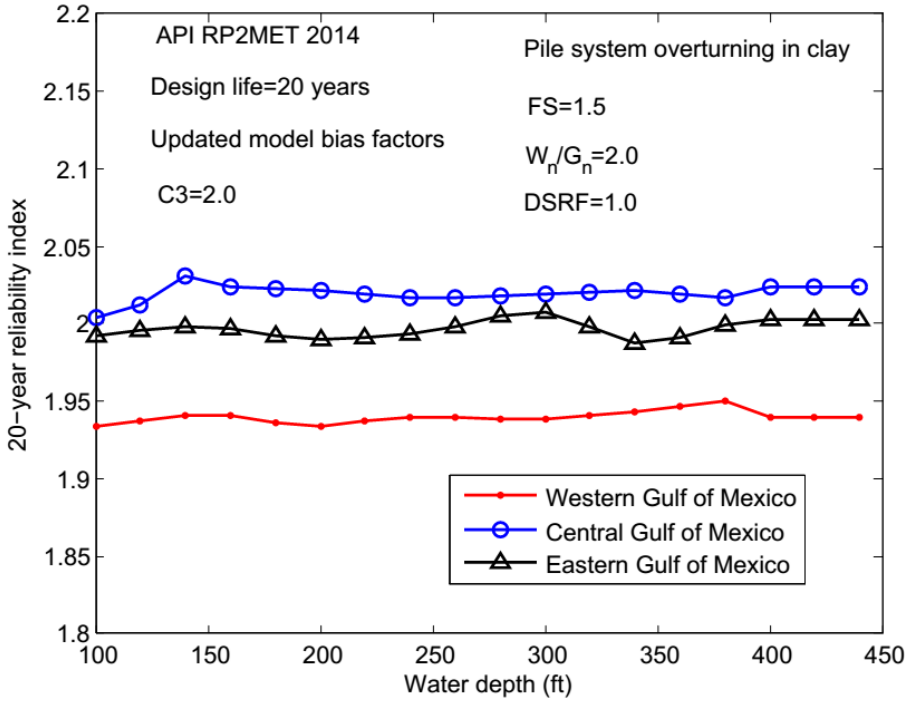

(a) Clay

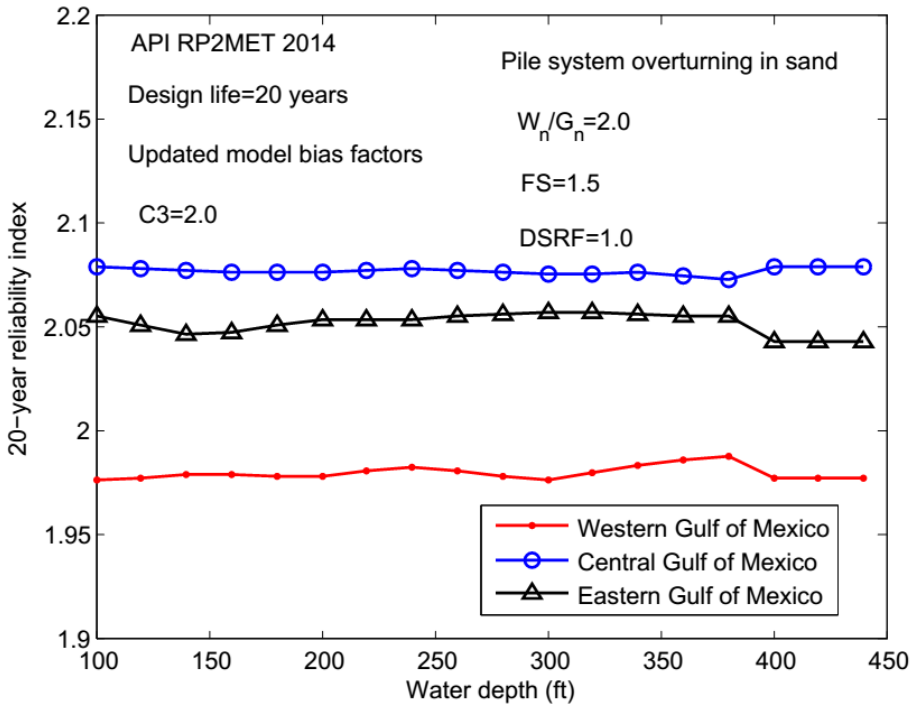

(a) Sand

Figure 7.9 Variation of β_{20} with water depth – foundation overturning

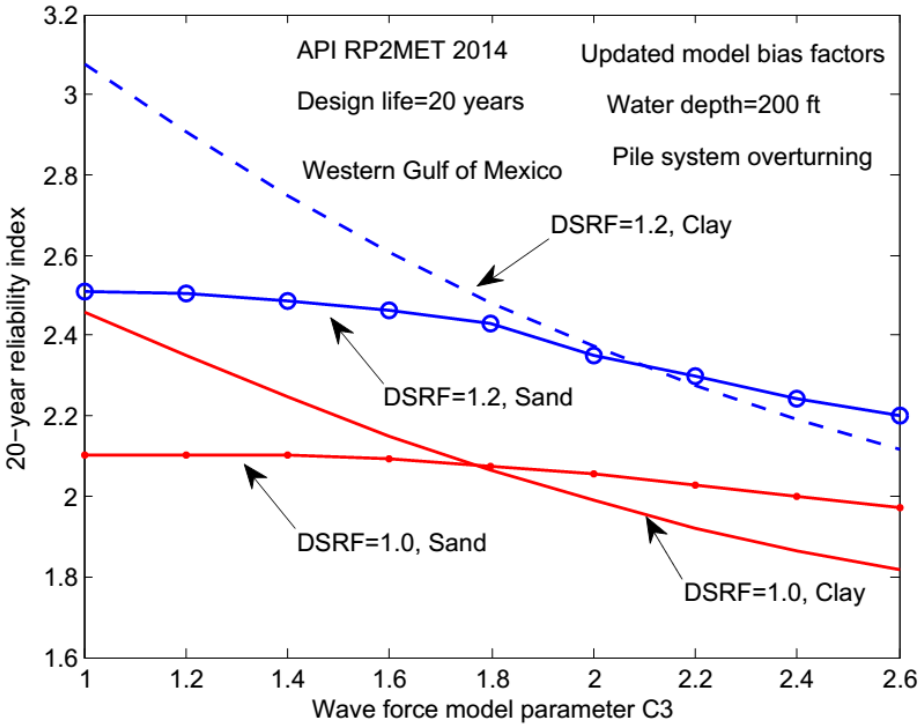

Figure 7.10 Variation of β_{20} with C3 – foundation overturning

7.2.4 Probabilistic system redundancy

The system redundancy of a pile system is studied deterministically in Chapter 5, a probabilistic system redundancy factor (PSRF) is introduced to measure the system redundancy probabilistically. Following Cornell (1987) and Tang and Gilbert (1992), the PSRF is defined as the ratio of the damage/failure probability of any pile to the probability of the failure of the pile system (i.e., approximately the inverse of the conditional probability of system failure given first damage/failure).

For the simplified reliability analysis of a generic platform, it is implicitly assume that the damage/failure probability of any pile is equal to that of the most critical pile, and different failure modes and failures in different piles are neglected. Therefore, the PSRF can be directly related to the DSRF using the reliability model in Equation 7.1.

Figure 7.11 shows the relation between the PSRF and the DSRF for the pile system against lateral and overturning failures at the water depth of 200 ft in the western

region of the Gulf of Mexico. The PSRF and DSRF are defined based on the system capacity and the first damage load. For the pile system against a lateral failure, the ratio of the load causing the first plastic hinge in the most critical pile in a pile system to the 100-year load is assumed to be 1.46, which is obtained using the average FS for the axial stress and bending stress based on the analysis in Section 7.23. For the pile system against an overturning failure, the FS=1.5 and $W_n/G_n = 2.0$ are used. The updated model bias factors in Chapter 6 and C3=2.0 are used. As shown, the PSRF approximately increases exponentially with the DSRF. For the DSRF=1.5, the PSRF is close to 10 for the lateral failure of a pile system, which means that the probability of a pile system fails laterally is about an order to magnitude less than the probability of occurring a plastic hinge in the pile system. For the DSRF=1.3, the PSRFs are respectively close to 5 and 3 for the overturning failure of a pile system in clay and in sand, which mean that the probability of a pile system fails in overturning is about one-fifth and one-third of the probability of a single pile fails in a system. This DSRF=1.3 represents the redundancy in the diagonal direction of an 8-leg platform based on Chapter 5.

Also shown in Figure 7.11 is that the PSRF depends on the uncertainty in the resistance. The PSRF decreases with the increase of the uncertainty in the resistance. Hence, the PSRF for a pile system in clay fails in overturning is higher than that in sand. The PSRF depends also on the uncertainty in the load as shown in Figure 7.12. The uncertainty in the wave load increases with the wave force model parameter C3, and consequently, the PSRF decreases with C3. The effect of the platform exposure time on the PSRF is shown in Figure 7.13. Comparing to the effects of the uncertainties in the load and resistance, the effect of the platform exposure time on the PSRF is minor. Hence, it is reasonable to state that the PSRF is approximately

independent of the platform exposure time, i.e., the PSRF is approximately the same whether the failure probability is annual-based or design life-based.

Therefore, the PSRF complements the DSRF and measures the conditional system failure probability upon the first damage and/or failure.

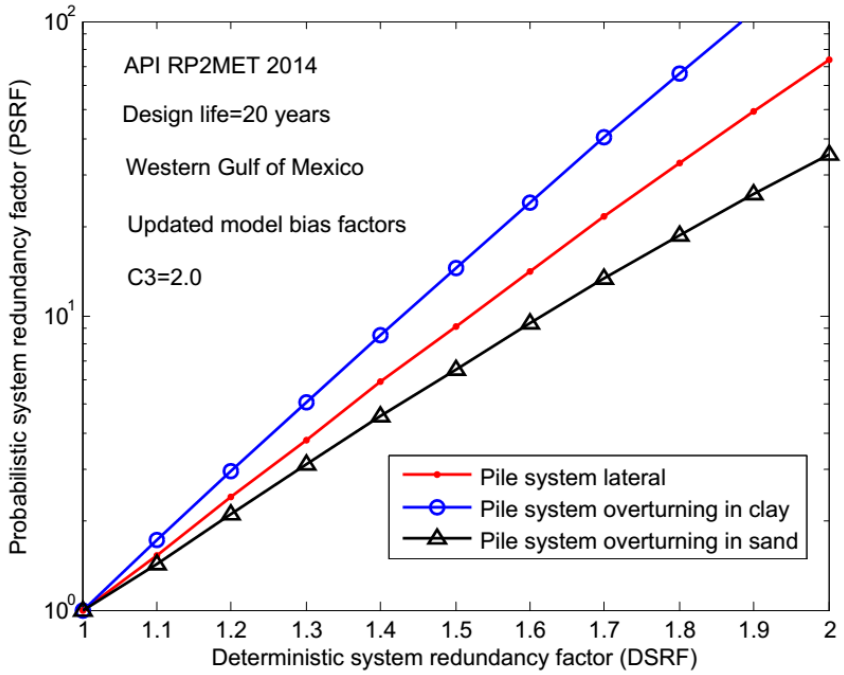

Figure 7.11 Variation of PSRF with DSRF

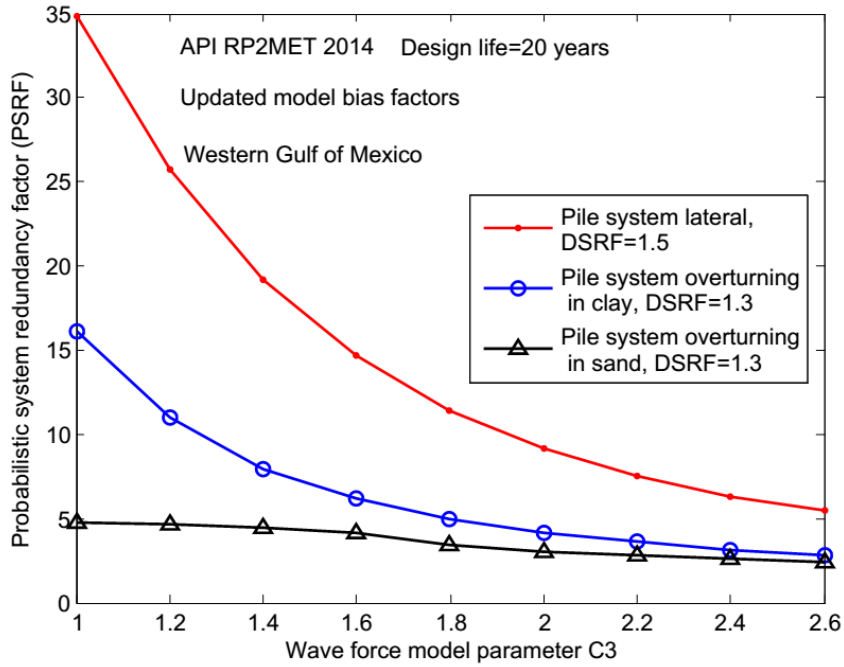

Figure 7.12 Variation of PSRF with C3

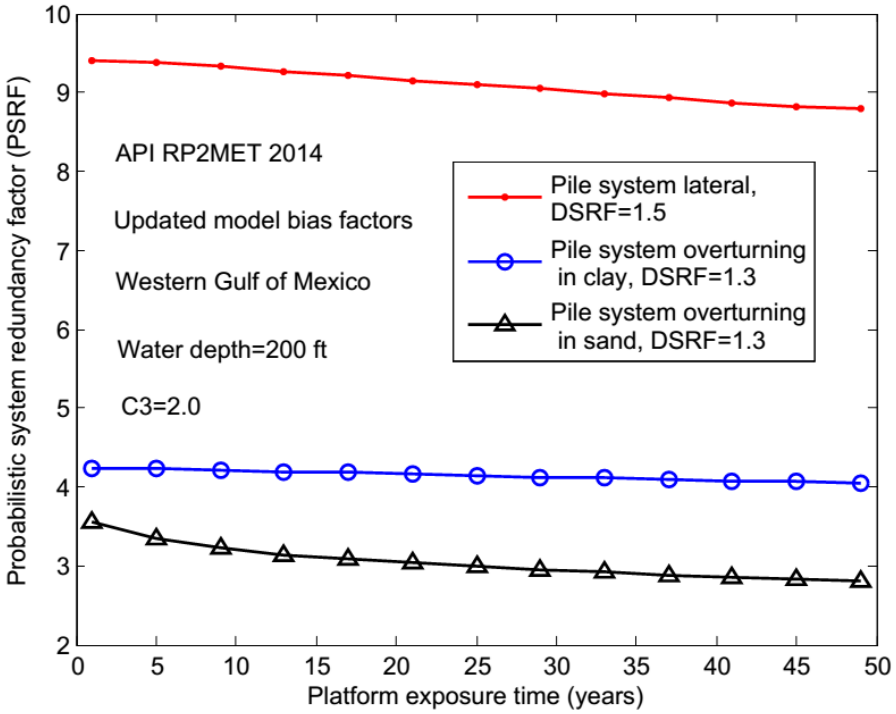

Figure 7.13 Variation of PSRF with platform exposure time

7.2.5 Discussion and summary on reliability analysis of generic platforms

A discussion and summary on the reliability analysis of generic platforms are provided as follows:

1. The reliability of a generic offshore platform is insensitive to water depths in the Gulf of Mexico. Although relatively larger variation in the 20-year reliability index β_{20} is observed for platforms in the Central region of the Gulf of Mexico at a water depth less than 150 ft when compared other cases, the variation in the β_{20} is not significant.
2. The reliability of a generic offshore platform is insensitive to locations in the Gulf of Mexico. Based on Figure 7.3, 7.6, and 7.9, the β_{20} in the western region is in general slightly less than that in the central and eastern regions.
3. With a typical value of RSR=2.0, the β_{20} is about 2.10 for the jacket structural system for drag dominated platforms. With an estimated RSR=2.2, β_{20} is around

2.57 for the pile system against a lateral failure for drag dominated platforms. Therefore, in general, the reliability of the pile system against a lateral failure is higher than that of the jacket structural system.

4. The β_{20} for the pile system against an overturning failure depends highly on the environmental to gravity load ratio. The β_{20} increases with the increase of the gravity load following the state-of-practice design procedure. With $W_n/G_n = 2.0$, the β_{20} is around 2.0 for both pile systems in clay and in sand for drag dominated platforms with no redundancy. This reliability is similar to the reliability of the jacket structural system. However, with the redundancy in the pile system and a smaller value of environmental load, the reliability of the pile system against an overturning failure is expected to increase.
5. The reliability of an offshore platform decreases with the wave force model parameter C3. Hence, the reliability of an inertia dominated platform is expected to higher than that of a drag dominated platform. For a pile system in sand against an overturning failure, the reliability is relatively insensitive to C3 due to the relatively large variability in the pile axial model bias factor. This insensitivity of the pile system in sand to C3 can be further explained from Figure 7.14. As shown, the contributions of the maximum wave height to the total system uncertainty are less than 15% and 40% for inertia dominated and drag dominated platforms, respectively. However, for the jacket structure and the pile system lateral reliability, the variability in the maximum wave height constitutes about 80% of the total uncertainty for a drag dominated platform; hence, the reliability of the jacket structure and the pile system lateral behavior will be mainly governed by the long term distribution of the maximum wave height.

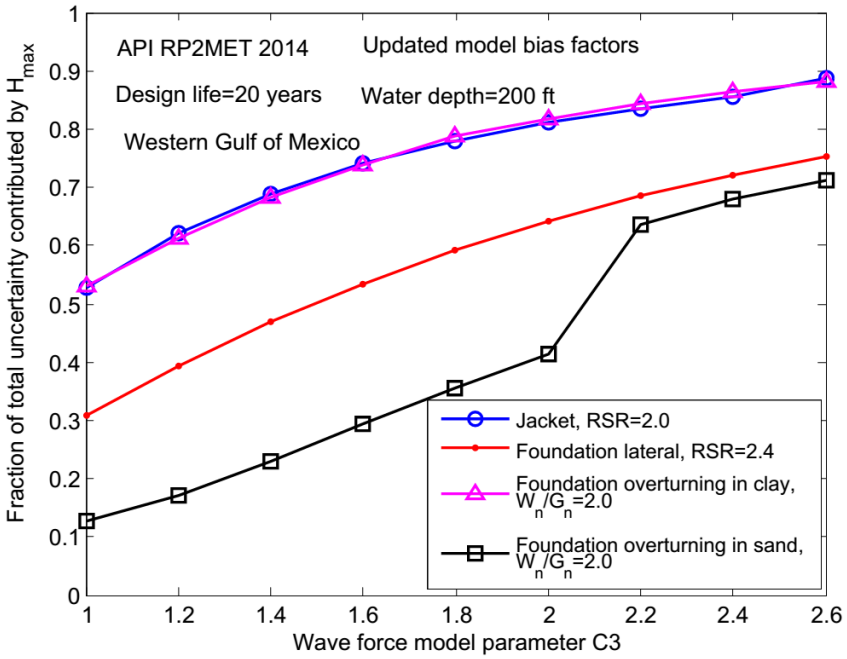

Figure 7.14 Contribution of maximum wave height variability

6. In general, all the reliabilities depend on the environmental to gravity load ratio. For a jacket structural system, the RSR is a good indicator widely accepted by the offshore industry (Krieger *et al.*, 1994). For a pile system against a lateral failure, the estimated RSR tends to be lower since it is assumed that all the loads on the pile are caused by environmental loads. Consequently, the β_{20} for a pile system against a lateral failure tends to be lower due to (i) the estimated lower RSR, (ii) the lower variability of gravity loads, and (iii) the higher FS for axial stress than the bending stress (API RP 2A-WSD, 2014). For a pile system against an overturning failure, the gravity load is comparable to the environmental load. The effect of the gravity load is considered in determining the RSR in this study, but the variability of the gravity load is neglected. Hence, the simplified reliability analysis presented here tends to overestimate the reliability of a pile system against an overturning failure.

7. The β_{20} for a jacket structural system of about 2.10 estimated here is less than the average β_{20} of 2.7 to 2.8 for offshore tubular components in the API RP 2A-

LRFD 1st edition. The reasons for this difference are (i) the variation of the base shear from waves to waves is considered in this study, i.e., $B_{sw}=1.18$ is introduced in Equation 7.1, and (ii) the variability in the maximum wave height in API RP 2MET (2014) is higher than that used in the calibration of the API RP-2A-LRFD 1st edition.

8. For a typical value of DSRF=1.5, the PSRF (with respect to the first plastic hinge) is close to 10 for the lateral failure of a pile system. For a value of DSRF=1.3, the PSRFs (with respect to the first axial failure of a single pile) are close to 5 and 3 for the overturning failure of a pile system in clay and in sand.

9. The PSRF complements the DSRF by considering the uncertainties in the load and resistance, and measures the conditional system failure probability upon the first damage and/or failure.

7.3 Reliability of case study pile systems

The previous sections provide simplified reliability analyses of generic offshore platforms based on the concept of the reserve strength ratio. This section estimates the reliabilities of the pile systems of three case study platforms, i.e., Platform I, II, and III described in Chapter 5. The metocean criteria in API RP 2MET (2014) are used in the reliability analysis. Since these three platforms were designed according to previous API metocean criteria, the reliabilities of these platforms estimated here represent the reliabilities of existing offshore pile systems, but not the reliabilities of newly design offshore pile systems.

7.3.1 Load and resistance random variables

Instead of modeling the pile system capacity as a log-normal random variable, a number of random variables are introduced for each single pile in a pile system. The

limit state function is similar to that used in the simplified reliability analysis of generic offshore platforms as follows:

$$g = R - B_s B_{sw} C_1 \left(H_{\max,annual} \right)^{C3} \tag{7.5}$$

where B_{sw} is a deterministic value of 1.18 based on Chapter 6. Given the random variables for each single pile and the uncertainty in the gravity load, the random resistance R is obtained based on the lower bound model proposed in Chapter 3 for the pile system capacity, and is based on the FE procedure proposed in Chapter 5 for the first damage/failure capacity.

The load/resistance variables and the corresponding distribution types used in this section are summarized as follows:

Loading variables:

- $H_{\max,annual}$ - annual maximum wave height which directly interpreted from API RP 2MET (2014) based on the platform location and site water depth.
- B_s - multiplication wave load model bias factor, log-normal.
- $B_{gravity}$ - multiplication gravity bias factor for the platform gravity load, normal.

Resistance variables:

- B_{yield} - multiplication bias factor for the pile steel, normal. For the same pile, B_{yield} is assumed to be perfectly correlated along the pile length. B_{yield} is assigned to each pile. The correlation coefficient of B_{yield}, ρ_{yield}, for any two different piles is assumed to be same.

- B_{py} - multiplication bias factor for the p-y curves, log-normal. For the same pile, B_{py} is assumed to be perfectly correlated along the soil depth; hence, the variation of the B_{py} for different soil depths is neglected. B_{py} is assigned to each pile. The correlation coefficient of B_{py}, ρ_{py}, for any two different piles is assumed to be same.
- B_{axial} - multiplication bias factor for the single pile axial capacity, log-normal. B_{axial} is assigned to each pile. The correlation coefficient of B_{axial}, ρ_{axial}, for any two different piles is assumed to be same.
- D_{scour} - scouring depth, log-normal. The scour is assumed to cover the whole platform site. The scour is modeled by removing the soil weight and assigning zero lateral resistance in the p-y curves within the scour depth.
- B_{system} - multiplication bias factor for the pile system capacity, log-normal.

In all the following reliability calculations, $B_{gravity}$ is assumed to be normal with a mean of 1.0 and a c.o.v. of 0.15, B_{yield} is assumed to be normal with a mean of 1.15 and a c.o.v. of 0.1, and D_{scour} is assumed to be log-normal with a mean of 5 ft and a c.o.v. of 0.4. For the pile system failure, the pile system capacity is based on limit analysis and hence B_{system} is assumed to be log-normal with a mean of 0.95 and a c.o.v. of 0.1 (PMB Engineering, 1996, PMB Engineering, 1993, Tang and Gilbert, 1992, Tang and Gilbert, 1990). For the first damage/failure load, an FE procedure is used and hence B_{system} is assumed to be log-normal with a mean of 1.0 and a c.o.v. of 0.1.

The Bayesian updating in Chapter 6 calibrates the model bias factors for the pile system lateral and overturning capacities. Although those updated model bias factors are not strictly applicable to single piles, it is believed that the updated model bias

factors for pile systems reveal important information on the single pile model bias factors. Based on the Bayesian calibration in Chapter 6, literature reviews (Lacasse and Goulois, 1989, Lacasse *et al.*, 2013, Tang, 1988), and engineering judgment, it is reasonable to assume that the updated mean and c.o.v. values for the pile system overturning capacity model bias factors, B_{fa}^{c} and B_{fa}^{s}, are also applicable to the axial capacities of single piles. Hence, the mean and c.o.v. for B_{axial} are established based on the model bias and aleatory uncertainty.

Since both the pile steel yield strength and the soil affect the pile system lateral capacity, based on the relative contribution of the pile steel yield strength and the soil lateral resistance, and the theoretical plastic limit analysis of pile lateral resistance (Randolph and Houlsby, 1984), it is reasonable to assume that B_{py} has a mean of 1.3 and a c.o.v. of 0.3 for the lateral limiting pressure acting on the pile in clay. Because the soil type at the Platform I site is exclusively clay, and the soil type in the upper 260 ft below the mudline is also clay at the Platform III site, the mean of 1.3 and the c.o.v. of 0.3 for B_{py} are appropriate. However, there is a thin sand layer of about 8 ft immediately below the mudline at the Platform II site which complicates the estimation of the statistics on B_{py}. Considering the expected scouring, the lateral capacity of the pile in Platform II system will still be governed by the clay layer. Hence, it is reasonable to use a mean of 1.3 and a c.o.v. of 0.3 for B_{py} for Platform II.

The correlation coefficient of the yield strength of any two piles, ρ_{yield}, is assumed to be the same with a value of 0.5 due to the similar manufacture process (Tang and Gilbert, 1992). The correlation coefficient of the axial capacities of any two piles, ρ_{axial}, and the correlation coefficient of the limiting lateral resistance of any two piles,

ρ_{py}, are difficult to estimate due to the random variability induced during pile driving. For simplicity, it is assumed that $\rho_{axial} = 0.5$ and $\rho_{py} = 0.5$.

The statistics on the random variables used in the reliability analyses of case study pile systems are summarized in Table 7.1.

Table 7.1 Statistics of random variables used in case study pile systems

Random variable	Type	Platform I		Platform II		Platform III	
		mean	c.o.v.	mean	c.o.v.	mean	c.o.v.
$H_{\max,annual}$	per API RP2MET (2014)	per API RP2MET (2014)		per API RP2MET (2014)		per API RP2MET (2014)	
B_s	Log-normal	0.92	0.13	0.92	0.13	0.92	0.13
$B_{gravity}$	Normal	1.00	0.15	1.00	0.15	1.00	0.15
B_{yield}	Normal	1.15	0.10	1.15	0.10	1.15	0.10
B_{py}	Log-normal	1.30	0.30	1.30	0.30	1.30	0.30
B_{axial} - Clay	Log-normal	1.05	0.21	1.05	0.21	1.05	0.21
B_{axial} - Sand	Log-normal			1.46	0.41	1.46	0.41
D_{scour}	Log-normal	4 ft	0.50	4 ft	0.50	4 ft	0.50
B_{system} - System capacity	Log-normal	0.95	0.10	0.95	0.10	0.95	0.10
B_{system} - first damage/failure capacity	Log-normal	1.00	0.10	1.00	0.10	1.00	0.10

7.3.2 Failure probability calculation

The FORM is used in all the reliability calculations presented here. For the pile system failure probability, the pile system capacity is calculated from the lower bound model proposed in Chapter 3 based on the specific realizations of random variables for single piles in each iteration in the FORM. For the pile first damage/failure probability, the FE procedure proposed in Chapter 5 is combined with the FORM in

the calculation. These methods, which combine the pile system lower bound method with the FORM, or combine the FE procedure with the FORM, are more robust than the simplified analyses using the concept of the reserve strength ratio.

For a single pile, two distinct modes are identified, i.e., the two-plastic-hinge lateral failure (or one-plastic-hinge for the damage) and the axial failure. Thus the failure probability of a single pile is the probability of the union of the lateral and axial failures. For the damage/failure of any pile, 2N modes are identified, where N is the number of piles in a pile system. Hence, the probability of the damage/failure of any pile is the probability of the union of any single pile damages/fails.

For a pile system, as shown in Chapter 4 and 5, the pile system may fail in base shear (piles fail laterally), or in overturning (piles fail axially), or in a combination of base shear and overturning (some piles fail laterally, and some fail axially). For simplicity, two failure modes are considered in the reliability calculation, i.e., the base shear failure and the overturning failure. Similar to the single pile analysis, the failure probability of a pile system is the probability of the union of the base shear and overturning failures.

The union and intersection of different failure modes are manipulated through the De Morgan's law. The probability of the intersection of two failure modes is calculated using the bivariate lognormal distribution (Thoft-Christensen and Murotsu, 1986). Ditlevsen probability bounds (Ditlevsen, 1979) is then used to estimate the probability of the union of all the failure modes.

The challenge is to calculate the reliability index of each individual failure mode and the correlation coefficient between any two failure modes. Within the framework of the FORM, the correlation coefficient between any two failure modes is calculated

as the inner product of the unit outward normal direction to the limit state surface at the most probable failure points (i.e., the β-point in the FORM) in the standard normal space (Ditlevsen, 1979). Several different methods exist to estimate the reliability index of each failure mode:

(1) The FORM calculates the reliability index in terms of the shortest distance from the origin to the limit state surface in the standard normal space. This calculation is based on the first order approximation, i.e., the local linearization of the limit state surface. Hence, if multiple modes contribute to the failure of a pile or a pile system, different reliability indices can be obtained depending on the curvature of the limit state surface and the starting point (which represents the normalized random variables in the standard normal space) in the iteration (Sørensen, 2004). Hence, theoretically, the reliability indices corresponding to all the potential failure modes can be obtained by choosing different starting points in the iteration. However, the shortcoming of this method is that it is difficult to know exactly which starting point to be chosen to reach a reliability index corresponding to a specific failure mode. The common outcome of this method is that the obtained reliability indices from different starting points are the same and the correlation coefficient between the two "assumed" different failure modes is close to 1.0, i.e., the failure mode is the same. Hence, this method tends to underestimate the failure probability. Nevertheless, this method captures the dominant failure modes, and any other failure modes missed may not have a significant impact on the calculated probability. Therefore, this study uses this method.

(2) The reliability index corresponding to one specific failure mode is calculated by restricting the other failure modes by arbitrarily increasing the strength against other failure modes, e.g., the reliability index of a single pile against a lateral

failure is calculated by increasing the axial capacity of that pile, and both the axial and lateral capacities of all the other piles. However, this method is sensitive to the increment of the capacities in restricting the failures of other piles due to the interactions among piles in the pile system, and it seems that there is no general guidelines for presenting other failure modes.

(3) The loads acting on a single pile are established through an elastic analysis for all the single piles. Then the reliability index for each single pile is calculated by combining the resistance uncertainty and the established loads. This method was used by Tang and Gilbert (1992). However, this method neglects the nonlinear effect of the piles and the possible load redistribution within the pile system when a single pile approaches failure.

7.3.3 Annual failure probability

Annual first damage probability (which is the annual damage probability of any piles), annual first probability (which is the annual failure probability of any single piles), and the annual failure probability of a pile system are calculated in this section.

Figure 7.15 shows the annual failure probabilities of the pile foundation of Platform I for various failure events. Since the pile system of Platform I is expected to fail in overturning, the first damage probability is essentially the same as the first failure probability. The first failure probability is close to the system failure probability due to the little redundancy of a 3-pile system failing in overturning. The annual failure probability of the pile system various from 4.5×10^{-3} to 4.0×10^{-2} for the loading direction in 180^{o} to 360^{o}, and the failure probability in 360^{o} is about an order of magnitude larger than that in the 180^{o}. Hence, the specific layout of the piles in a pile system plays an important role in the reliability of a pile system.

For convenience, the broadside and end-on directions of Platform II in Figure 5.4 are re-defined to be 0^o and 90^o, respectively. Figure 7.16 shows the annual failure probabilities of the pile foundation of Platform II for various failure events. As shown, the pile system failure probability varies from 3.3×10^{-3} to 1.2×10^{-2} for the loading direction in 0^o to 90^o, and is slightly less than those for the first damage and first failure for the loading direction less than 90^o. For loading in 90^o, the first damage and first failure probabilities are the same, and is relatively much higher than the pile system failure probability. The identical first damage and first failure probabilities imply that the most probability damage mode for the critical pile is the axial failure. Detailed investigation into the probabilistic results reveals that plunge-in of Pile 2 (the shorter pile) governs the failure probability. However, from the deterministic analysis as shown in Figure 5.6, for 90^o, the first failure load is about 20% higher than the first damage load, which implies that the first damage of the critical pile is forming a plastic hinge, rather than an axial failure. Hence, although the deterministic analysis provides a direct measurement of the reserve strength of the pile system upon first damage/failure, but may miss the most probable failure mode. The probabilistic analysis complements that by considering the uncertainties in loads and capacities.

Similar to Platform II, the broadside and end-on directions of Platform III in Figure 5.8 are re-defined to be 0^o and 90^o, respectively. Figure 7.17 shows the annual failure probabilities of the pile foundation of Platform III for various failure events. As shown, the pile system failure probability is insensitive to the loading direction and is about 1.0×10^{-4} to 2.0×10^{-4}. The system failure probability is about an order of magnitude less than that of the first damage. The first failure probability is in between the first damage probability and system failure probability.

The pile system annual failure probability increases with the correlation among the piles (see Figure 7.18). For simplicity, it is assumed that $\rho_{axial} = \rho_{py} = \rho_{yield}$ in the parametric study, and the system annual failure probability is normalized by the annual failure probability with the zero correlation case in Figure 7.18. For the 3-leg pile system, the system failure probability is almost independent of the correlation because the pile system is expected to fail in overturning and the axial capacity of Pile 2 (see Figure 4.2) governs the system capacity. For the 8-leg pile system, the system failure probability increases about 50% for the fully correlated case when compared to the fully independent case because the pile system is expected to fail in the base shear and all the eight piles contribute to the system ultimate capacity. For the 4-leg pile system, the effect of correlation lies between the 3-leg and 8-leg pile system. Therefore, the effect of the correlation among the piles on the pile system annual failure probability depends on the pile number and the expected system failure mode. However, in general, the effect of the correlation among the piles on the system failure probability is not significant since the variability in the wave load dominates the total uncertainty of the system, e.g., for these three case study pile systems, the maximum wave height uncertainty contributes around 80% of the total uncertainty in the system based on the results of FORM.

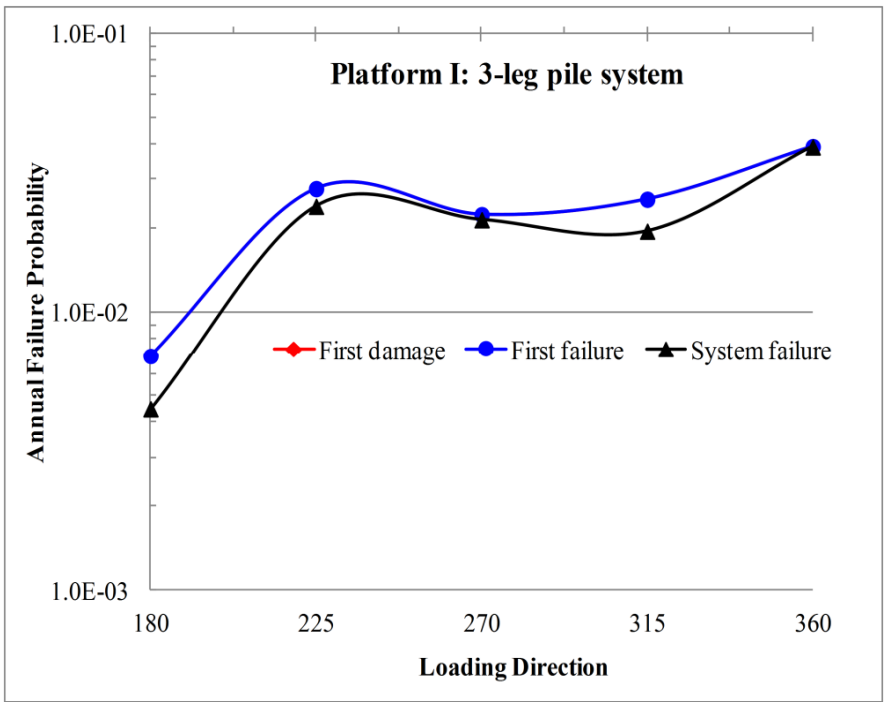

Figure 7.15 Failure probabilities of Platform I pile system

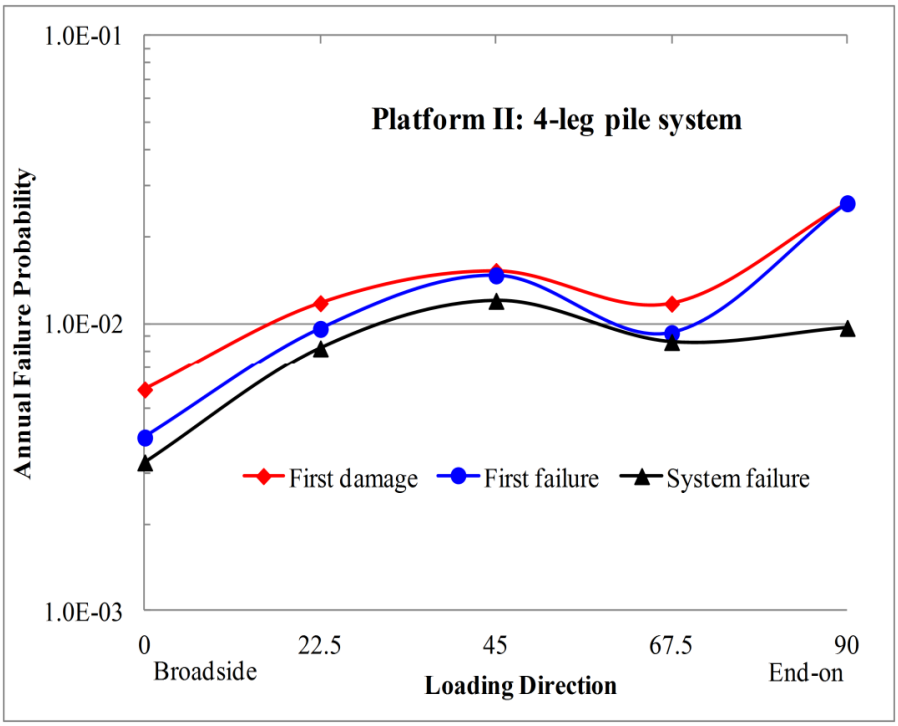

Figure 7.16 Failure probabilities of Platform II pile system

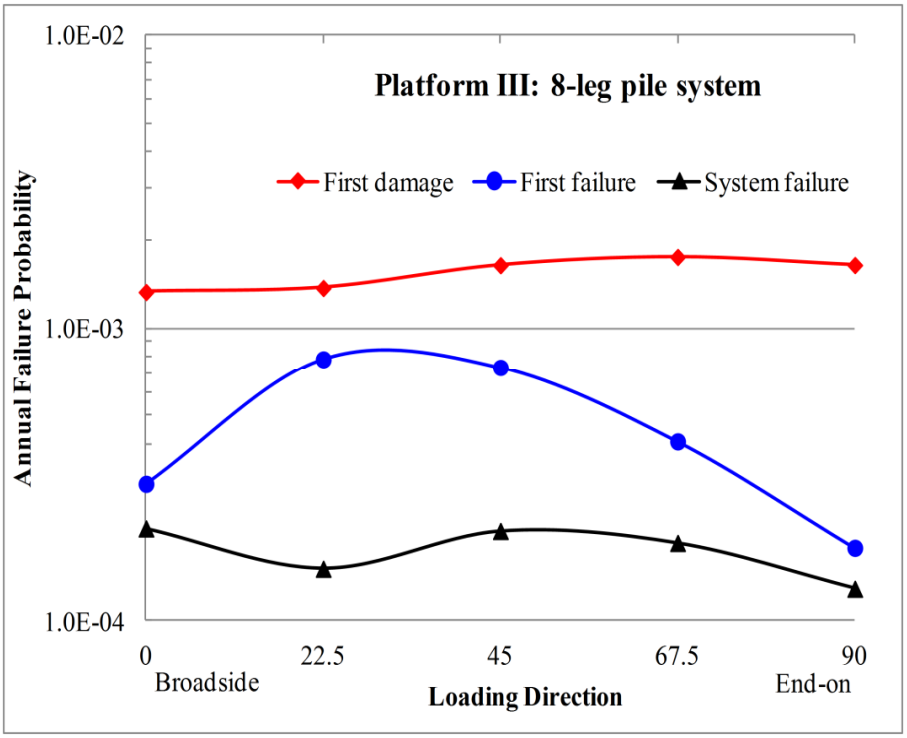

Figure 7.17 Failure probabilities of Platform III pile system

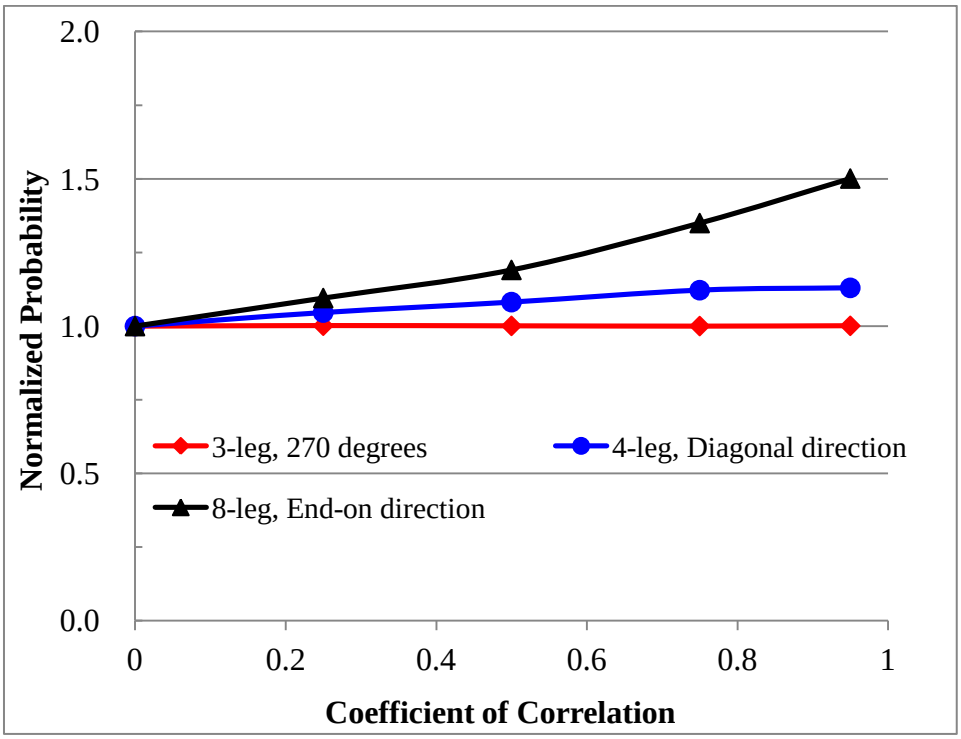

Figure 7.18 Effect of correlation coefficient on system failure probability

7.3.4 Probabilistic system redundancy

Figure 7.19 shows the PSRFs of the three case study platforms based on the pile system failure and first damage probabilities. As shown, the PSRF of Platform III is about 7 to 13 depending on the loading direction, and is much higher than those of Platform I and II. For Platform II, the PSRF is close to 3 in the 90^o direction, and is greater than that in other loading direction. The reason for a larger PSRF in the 90^o direction is that Pile 2 (see Figure 5.5) is the weakest component and has a relatively large plunge-in probability. For Platform I, the PSRF is close to 1.0 due to the little redundancy of the pile system.

Figure 7.20 shows the PSRFs of the three case study platforms based on the pile system failure and first failure probabilities. As shown, the PSRFs decrease when compared to those based on the first damage probability. For Platform III, the PSRF is close to 1.0 since the pile system tends to fail in a base shear mechanism (see Figure 5.12 and 5.14); is relatively large (a value of close to 6) close to the diagonal direction since the pile system tends to fail in a combination of base shear and overturning (see Figure 5.13) and the both the axial failure and lateral failure contribute to the single pile failure probability. For Platform I and II, the PSRFs are similar to those based on the first damage probability.

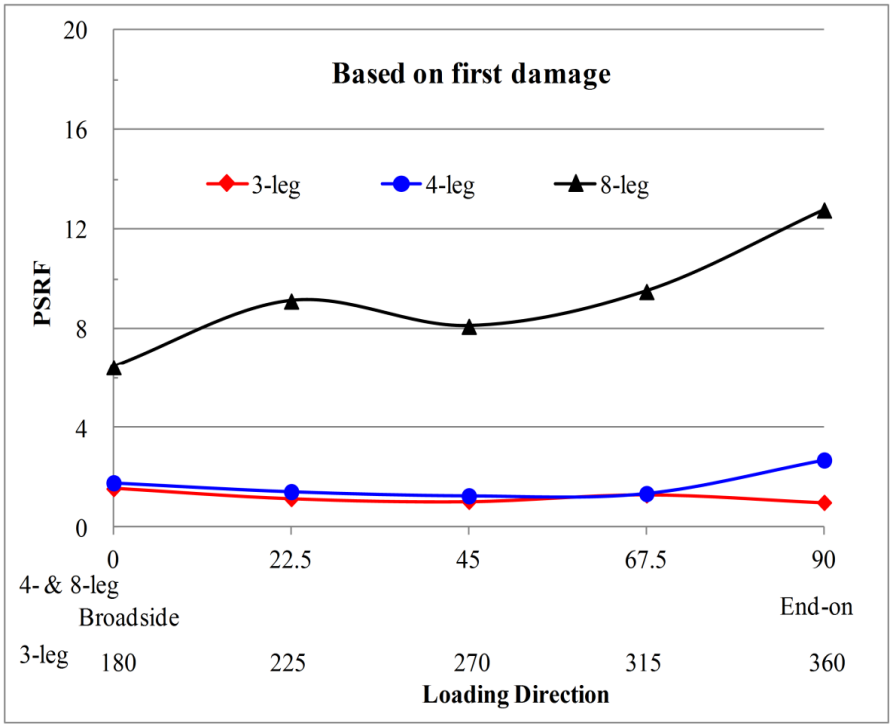

Figure 7.19 PSRF of three pile systems – first damage

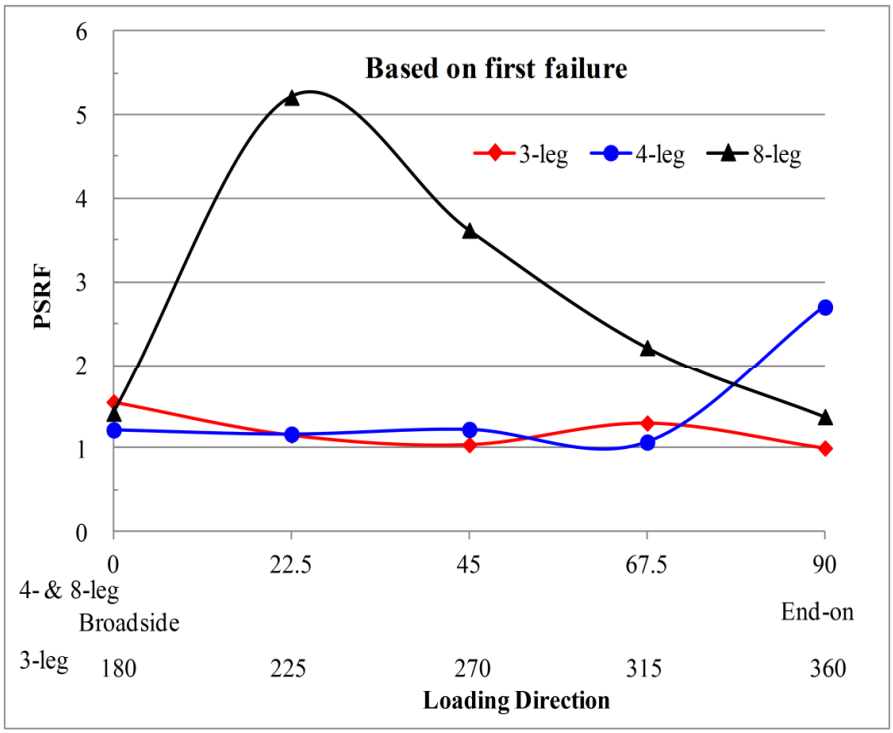

Figure 7.20 PSRF of three pile systems – first failure

7.3.5 Probabilistic system robustness

Using Nordal *et al.* (1988) as a guide, the probabilistic system sensitivity factor studied here is defined as the ratio of the percentage change of the pile system reliability index to the percentage change of the capacity of the most critical pile. The axial and lateral capacities of the most critical pile in a system are reduced by 30% to determine the probabilistic system sensitivity factor. Therefore, the probabilistic system sensitivity factor defined here approximately measures the gradient of the pile system reliability index with respect to the capacity of the most critical pile. A higher probabilistic system sensitivity factor indicates that the system reliability index is more sensitive to the single pile capacity, and thus implies a less robustness level; on the other hand, a lower probabilistic system sensitivity factor indicates that the system reliability index is less sensitive to the single pile capacity, and thus implies a high robustness level.

The probabilistic system sensitivity factors for the three pile systems are shown in Figure 7.21. The annual reliability index is used in the calculation. For the 3-leg pile system, the probabilistic system sensitivity factor is around 0.6; however, for in the 360^{o}, the probabilistic system sensitivity factor is much higher than that in other directions because the gravity load center is close to the most critical pile (Pile 3 in Figure 4.2) that makes the pile system sensitive to the axial capacity of the most critical pile. For the 4-leg pile system, the probabilistic system sensitivity factor ranges from about 0.2 to 0.6, and is not very sensitive to the loading direction. Hence, in general, the 4-leg pile system in this study is more robust that the 3-leg pile system. For the 8-leg pile system, the probabilistic system sensitivity factor is much lower than those for the 3-leg and 4-leg pile systems, and is less than 0.1 in general.

Therefore, consistent with the deterministic robustness findings in Chapter 5, the 8-leg pile system is more robust than the 3-leg and 4-leg pile systems.

Note that the sensitivity factor defined here is based on the capacity reduction of the most critical pile, while the capacities of the remaining piles remain the same, even when all the piles are perfectly correlated. Hence, the system sensitivity factor studied here represent the case where one pile is undersized in a pile system. In general, the pile system sensitivity factor decreases with the increase of the correlation among the piles (see Figure 7.21); however, the dependence is weak, e.g., the maximum decrease of the pile system sensitivity factor is about 25% for the 8-leg pile system when the correlation coefficient increases from zero to 1.0. Therefore, a pile system with higher correlation of piles tends to be more robust than the one with lower correlation of piles with respect to the undersize of the most critical pile.

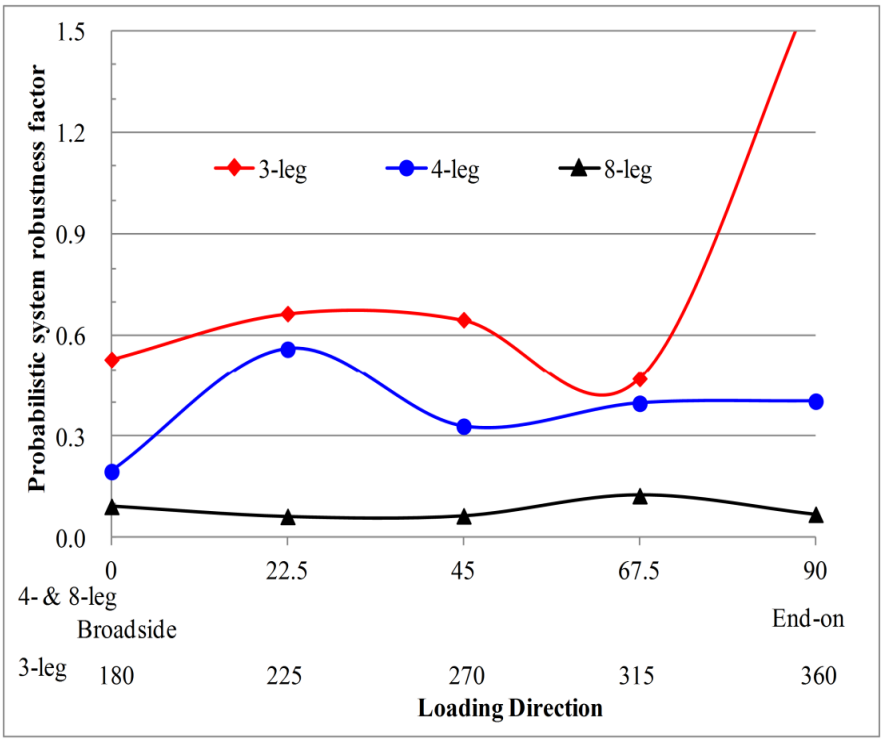

Figure 7.21 Probabilistic system sensitivity factors

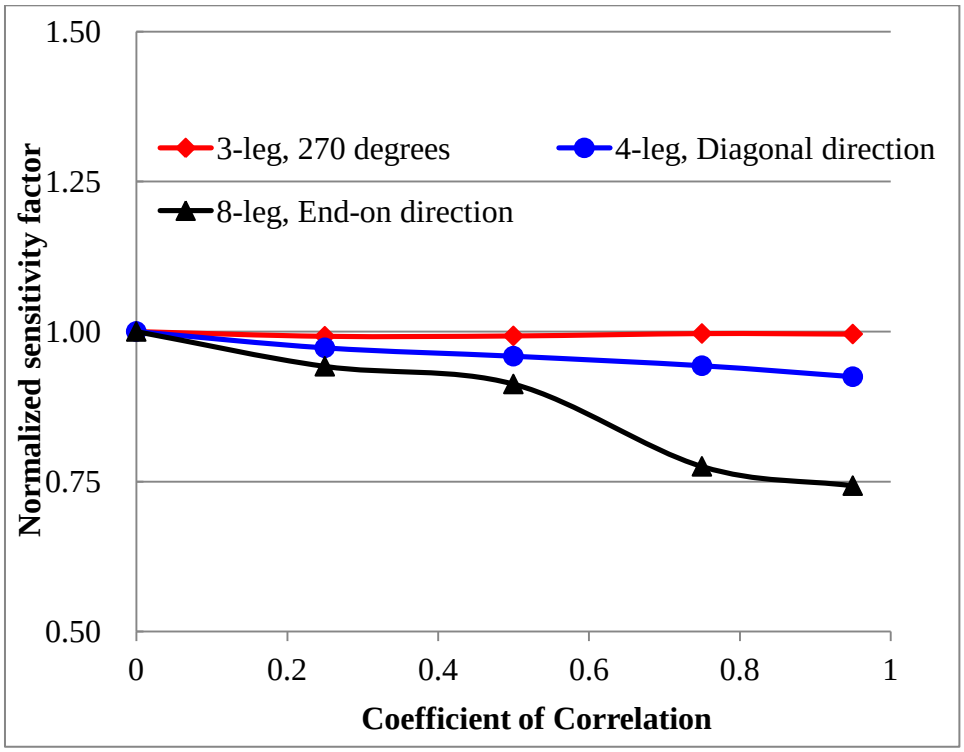

Figure 7.22 Effect of correlation coefficient on system sensitivity factor

7.3.6 Complexity factor

The complexity factor represents an inverse measure of the dominance of one failure mode relative to the failure of any piles. Based on Cornell (1987) and Tang and Gilbert (1992), in this study, the complexity factor for first damage is defined as the ratio of the first damage probability of any piles to the first damage probability of the most critical pile.

Figure 7.23 and 7.24 show the two complexity factors under different loading directions. As shown, the complexity factor is generally small (less than 1.6), which is consistent with the findings from three case study platforms (Tang and Gilbert, 1992). This means that the failure probability of the most critical pile can well represent the failure probability of any piles. The complexity factor varies with the loading

direction and hence the layout of the piles. Besides, the complexity factor depends on the expected failure mode of a single pile. If a pile is likely to fail in both the axial and lateral direction, the complexity factor will be larger. Hence, the complexity factor depends on the expected failure mode of the most critical pile. In addition, the weakest component in a pile system has a large effect on the complexity factor. As shown in Figure 7.24, the complexity factor for Platform II is 1.0 if the loading direction deviates from the broadside direction. This is because the failure of Pile 1 (the shorter pile and is expected to fail in tension) governs the failure probability for loading close to the diagonal, while Pile 2 (the shorter pile and is expected to fail in plunge-in) governs the failure probability for loading close to the end-on direction.

The pile system complexity factor for the single pile failure decreases with the increase of the correlation among the piles (see Figure 7.25). The complexity factor is expected to reach 1.0 when all the piles are fully correlated, and there is no direct relation between the complexity factor and the pile number. Instead, the complexity factor depends highly on the pile failure mode and the uncertainty in the pile capacity. For the 3-leg pile system under the 315^{o} direction, the failure probabilities of Pile 2 (in tension) and Pile 3 (in compression) are close to each other and the c.o.v. of the pile axial capacity is 0.22 which result in a complexity factor of about 1.4 when all the piles are independent. For the 8-leg pile system, Pile 2 and 3 (see Figure 5.10) are the most critical pile in the end-on direction, and the complexity factor is about 1.2 since the c.o.v. of the pile lateral capacity (about 0.15) is lower than the c.o.v. of the pile axial capacity. For the 4-leg pile system, the complexity factor is 1.0 and independent of the correlation coefficient in the diagonal direction, which demonstrates that when weakest component (Pile 1 in tension in Figure 5.5) dominates the first failure probability of the pile system.

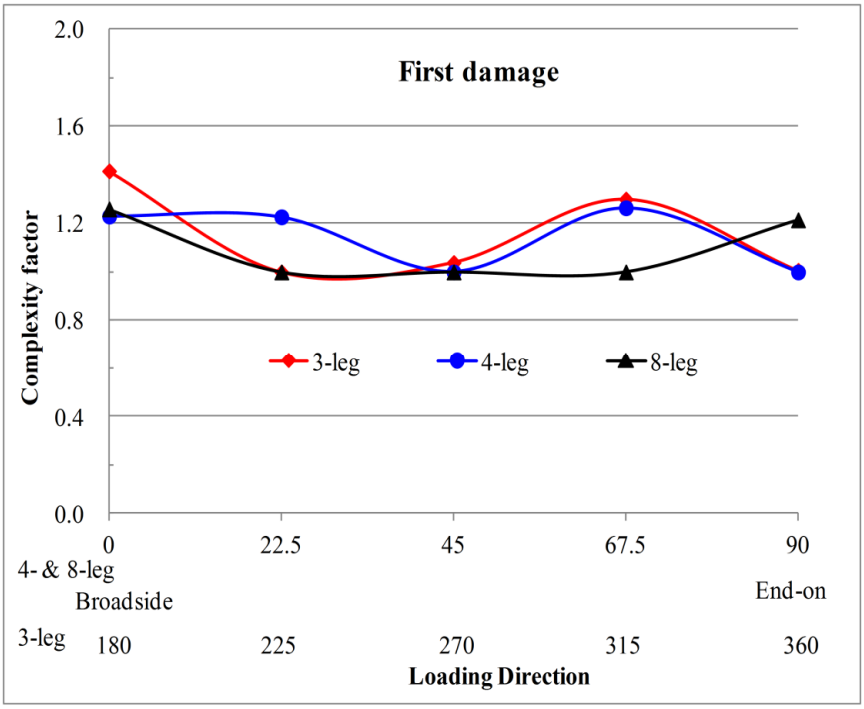

Figure 7.23 Complexity factor – first damage

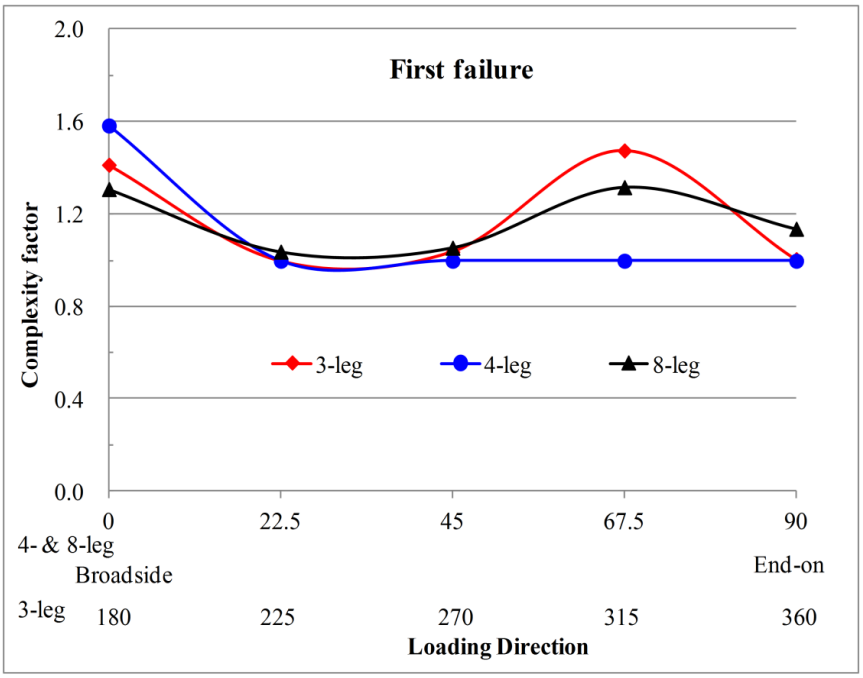

Figure 7.24 Complexity factor – first failure

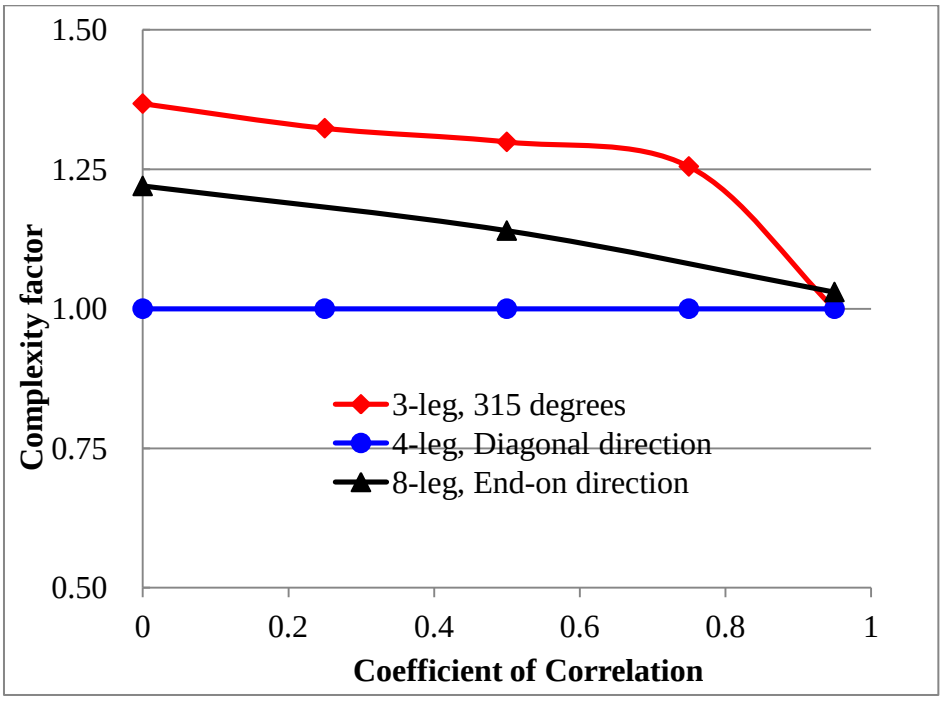

Figure 7.25 Effect of correlation coefficient on complexity factor

7.4 Conclusions

This chapter presents reliability analyses of generic offshore platforms and selected cast study offshore pile system using the first order reliability method (FORM). The reliability of a generic offshore platform is found to be insensitive to water depths and locations in the Gulf of Mexico. In general, the reliability of the pile system against a lateral failure is higher than that of the jacket structural system. With an environmental to gravity load ratio of 2.0, the reliabilities of both pile systems in clay and in sand for drag dominated platforms with no redundancy is similar to the reliability of the jacket structural system.

The failure probability of a pile system depends on the pile layout, the number of piles, the loading direction, and the expected failure mode, and increases slightly with the correlations among the piles. The probabilistic system redundancy factor (PSRF) is an inverse measure of the conditional system probability given the failure/damage

of any pile. For the 3-leg pile system, the PSRF is close to 1.0 (the same based on first damage or first failure) which implies that the 3-leg pile system has little redundancy. For the 4-leg pile system, the PSRF is similar based on the first damage or first failure, and is close to 1.0 except in the end-on direction where the PSRF is about 3.0 due to the plunge-in of the shorter pile based on the probabilistic analysis. For the 8-leg pile system, , the PSRF is about 7 to 13 based on the first damage, and about 1 to 6 based on the first failure depending on the loading direction. Hence, in general, the 8-leg pile system is more redundant than the 3-leg and 4-leg pile systems.

The probabilistic system sensitivity factor measures the gradient of the pile system reliability index with respect to the capacity of the most critical pile, and is insensitive to the correlations among the piles. The system robustness factor for the 3-leg pile system is around 0.6, but depends highly on the loading direction; ranges from 0.2 to 0.6 for the 4-leg pile system, and is less than 0.1 for the 8-leg pile system in general. Therefore, the 8-leg pile system is more robust than the 3-leg and 4-leg pile systems.

The complexity factor is defined as the ratio of the first damage/failure probability of any piles to the first damage/failure probability of the most critical pile, and represents an inverse measure of the dominance of one failure mode relative to the failure of any piles. The complexity factor depends on the layout of the piles, the expected failure mode of a single pile and the pile capacity uncertainty. From the three case study pile system, there is no direct relation between the complexity factor and the number of piles. In general, the complexity factors from the three platforms are small (in the range of 1.0 to 1.6), which implies that the failure probability of the most critical pile can well represent the failure probability of any piles.

8 Conclusions and Future Work

This dissertation presents deterministic and probabilistic studies on offshore pile systems. The objectives of this research are to improve understanding of pile system performance under three dimensional loading, to determine the relation between the component-based design and the pile system behavior, to calibrate the bias factors in the offshore pile foundation design, and to provide a basis for the load and resistance factors design. The conclusions and the suggested future work are provided below.

8.1 Conclusions

1. Analytical lower and upper bound solutions based on the plastic limit theorems are derived for a single pile under pile head three dimensional loads (excluding torsion). The two bounding solutions are shown to be close, and a simplified failure surface for a single pile is proposed in terms of pile head loads based on the lower bound solution. The simplified single pile failure surface is verified through case studies using optimized upper bound and finite element analyses.
2. Numerical lower and upper bound models are proposed for the ultimate capacity of a pile system against a catastrophic failure. The lower bound model uses the proposed simplified single pile failure surface, and is optimized by systematically adjusting the stiffness of each pile in each elastic iteration. The upper bound model uses the failure mechanism determined from the elastic solution in the lower bound analysis. The two bounding solutions are shown to be close, and are efficient because the lower bound model is based on an elastic analysis and the searching for the optimized failure mechanism is avoided in the upper bound model.
3. The proposed bounding models for the pile system capacity can effectively capture the effects of global torsion on the jacket and the global out-of-plane

failure of a pile system. The evidence from the survival of offshore platforms indicates that (1) well conductors should be included in assessing the pile system ultimate capacity; (2) static p-y curves should be used in the assessment which increases the pile system base shear capacity by about 10 to 20% and the actual performance in several case studies can only be explained if static p-y curves are assumed; (3) the mean value of the steel yield strength should be used to acknowledge the rapid loading effect and the difference between the mean value and nominal yield strength of the steel; (4) jacket leg stubs should be included which essentially increases the pile cross-sectional bending capacity; and (5) site-specific geotechnical information is important – when a soil boring at the platform site is not available, the soil conditions can at least be inferred approximately based on the design practice (e.g., the design wave height, the stress in the pile wall) at the time the platform was designed.

4. The model bias factors in the API load and resistance design recipe are calibrated through Bayes' Theorem. The Bayesian calibration is conducted by comparing the analytically predicted and actually observed performance of eighteen offshore platforms in recent Gulf of Mexico hurricanes. The mean and c.o.v. for the wave load model bias factor are updated from 0.93 to 0.92 and 0.20 to 0.13, respectively. The mean and c.o.v. for the jacket structural resistance model bias factor are updated from 1.0 to 0.95 and 0.20 to 0.13, respectively. The mean and c.o.v. for the pile system lateral capacity in clay model bias factor are updated from 1.0 to 1.17 and 0.30 to 0.24, respectively. The mean and c.o.v. for the pile system overturning capacity in clay model bias factor are updated from 1.3 to 1.05 and 0.30 to 0.19, respectively. The mean and c.o.v. for the pile system overturning capacity in sand model bias factor are updated from 1.3 to 1.46 and 0.50 to 0.37, respectively. Therefore, the API load and resistance design recipe is close to be

unbiased for predicting the jacket system performance; is slightly conservative for predicting a foundation overturning failure in clay; and is conservative for predicting a lateral failure in clay and a foundation overturning failure in sand.

5. For a generic offshore platform, the reliability is insensitive to water depths and locations in the Gulf of Mexico. In general, the pile system reliability against a lateral failure is higher than that against a jacket structure failure. The pile system lateral failure probability is about an order of magnitude less than that of forming a plastic hinge. The 20-year reliability index β_{20} for a pile system against an overturning failure depends highly on the environmental to gravity load ratio, W_n/G_n. With $W_n/G_n = 2.0$, the β_{20} is around 2.0 for both pile systems in clay and in sand against an overturning failure for drag dominated platforms with no redundancy. This reliability is similar to the reliability of a jacket structural system against a catastrophic failure. The β_{20} for a jacket structural system is estimated to be about 2.10 which is less than the average β_{20} of 2.7 to 2.8 for offshore tubular components obtained in calibration work for the API RP 2A-LRFD 1st edition. The reasons for this difference are: (i) the variation of the base shear from waves to waves is considered in this study which results in a higher wave load given a specific wave height, and (ii) the variability in the maximum wave height in API RP 2MET (2014) is higher than that in the calibration of the API RP 2A-LRFD 1st edition.

6. For the three case study offshore pile systems (i.e., 3-leg, 4-leg, and 8-leg pile systems), the failure probability depends on the pile layout, the number of piles, the loading direction, the expected failure mode, and increases slightly with the correlation among the piles. The annual failure probabilities vary from 4.5×10^{-3} to 4.0×10^{-2} for the 3-leg pile system; from 3.3×10^{-3} to 1.2×10^{-2} for the 4-leg

pile system; and from 1.0×10^{-4} to 2.0×10^{-4} for the 8-leg pile system under different loading directions. Therefore, the 3-leg pile system is sensitive to the loading direction, and the failure probability differs approximately by an order of magnitude, while the 8-leg pile system is relatively insensitive to the loading direction. These failure probabilities may imply the reliabilities of existing offshore pile systems, but do not represent newly designed pile systems.

7. The pile system redundancy is analyzed both deterministically and probabilistically based on three case study offshore pile systems. From a deterministic aspect, in the base shear failure region, the pile system is close to the ultimate failure after the lateral failure of the most critical pile; however, the pile system capacity is about 40 to 60% higher than the load causing the first plastic hinge. In the overturning failure region, little redundancy is observed for the 3-leg, 4-leg pile systems and the broadside direction of the 8-leg pile system, while the system capacity is about 15% and 25 to 30% higher than the load causing the first axial failure of a pile in the end-on and close to the diagonal directions, respectively. From a probabilistic aspect, for the 3-leg platform, the first damage, first failure, and system failure probabilities of the pile foundation are similar, which implies little redundancy. For the 4-leg platform, little redundancy is observed except in the end-on direction, where the shorter pile is the weakest component in the system and the system failure probability is about one-third of the failure probability of a single pile. For the 8-leg platform, the system failure probability is about an order of magnitude less than the first damage probability.
8. The pile system robustness is analyzed both deterministically and probabilistically based on three case study offshore pile systems. From a deterministic aspect, in the base shear failure region, the sensitivity of the system capacity is roughly

proportional to the inverse of the number of piles, and is insensitive to the loading directions and global torsional loads on the jacket. In the overturning region, the sensitivity decreases with the number of piles. In general, the pile system is more robust in the base shear failure region than in the overturning failure region, and increasing symmetry increases the robustness of a pile system. From a probabilistic aspect, the gradient of the reliability index with respect to the capacity of the most critical pile depends on the loading direction, and is insensitive to the correlation among the piles. This gradient is relatively high for the 3-leg pile system and relatively low for the 8-leg pile system.

9. The deterministic redundancy and robustness analyses provide a direct measurement of the reserve strength of the pile system upon first damage/failure and the sensitivity of the pile system to the single pile capacity. The probabilistic analyses complements the deterministic analyses by considering the uncertainties in the load and resistance, by measuring the conditional system failure probability upon the first damage and/or failure, and by providing the gradient of the reliability index with respect to the single pile capacity.
10. The complexity factor depends on the layout of the piles, the expected failure mode of a single pile and the pile capacity uncertainty. If a pile is likely to fail in both the axial and lateral direction, the complexity factor will be larger. From the three case study pile systems, there is no direct relation between the complexity factor and the number of piles. In general, the complexity factors from the three platforms are small, which means that the failure probability of the most critical pile can well represent the failure probability of any piles.

8.2 Future Work

A list of future work is suggested here in order to better understand the pile system behavior and to better guide the engineering practice:

1. The proposed single pile failure surface can be extended to concrete piles and steel H-piles. For concrete piles, the interaction between the axial load and bending moment should be considered. For H-piles, the local buckling effect should be taken into account. Then, the proposed lower bound method can be applied to concrete pile systems for bridges, and to H-pile systems for levee systems.
2. Based on the proposed lower bound model for the pile system capacity and the finite element procedure for the first damage and first failure loads, the pile system redundancy of 3-,4-,6-,8-leg platforms can be analyzed. The findings from this redundancy analysis will be helpful in improving the offshore pile design practice, e.g., to use different safety factors for different pile systems.
3. This study shows that the 8-leg pile system is more robust than the 3- and 4-leg pile systems deterministically and probabilistically. However, more research is required to include this robustness in a reliability based design.
4. This study treats the c.o.v. for the aleatory uncertainty in the pile system capacity as deterministic, and the specific value is based on the availability of site-specific geotechnical information, testing technique, and judgments. If more platform performance data can be obtained, this c.o.v. can also be modeled as a random variable and can be updated through Bayes' Theorem.
5. The difference between the wave-by-wave approach and the sea state approach results from the variability in the base shear force from wave cycles to wave cycles. The wave-by-wave analysis tends to give a higher wave force becasue the variation of the base shear from waves to waves is considered. If a c.o.v. of 0.2 is

used for the variation of the base shear from waves to waves, the wave-by-wave approach gives a base shear force about 18% higher than that from the sea state approach at the same percentile. Although the c.o.v. value of 0.2 used here is based on the previous studies (ABS, 2004, Energo Engineering, 2005, PMB Engineering, 1996), more research is required to justify this assumption.

6. More research is required to balance the reliability of a pile system to that of a jacket structure system in order to result in an economical design.

Appendix I Derivation of single pile failure surfaces

3D upper bound analysis of single piles

To determine the lateral capacity, the axial failure of the pile is not considered, which requires $|V| < |V_m|$. Without a loss of generality, the pile is assumed to be vertical, the pile head is assumed to be at the same level as the soil surface, the positive *x*-direction is taken to be in the direction of the lateral load *F* as shown in Figure 2.1. Thus the *y*-component of the pile head lateral load is zero and the moment component M_x represents the out-of-plane moment. The cross-sectional axial load-moment interaction relation for steel pipe piles is shown in Equation A1 following Chen and Han (1985)

$$\frac{|M|}{M_p} - \cos\left(\frac{\pi}{2}\frac{V}{V_p}\right) = 0 \qquad \text{A1}$$

where M_p and V_p are the pile cross-sectional plastic moment capacity (pure bending) and steel yield capacity (pure axial loading), respectively. Neglecting the $P-\Delta$ effect, referring to Figure 2.1 and assuming the pile section between *a* and *b* is rigid, the energy dissipation rate consists of three parts: the dissipation due to the soil axial and lateral resistance (respectively $\dot{D}_{sa}$ and $\dot{D}_{sl}$) in the section between *a* and *b*, and the dissipation of the plastic hinge at *b* $\dot{D}_{pile}$ as follows

$$\dot{D} = \dot{D}_{sa} + \dot{D}_{sl} + \dot{D}_{pile} \qquad \text{A2}$$

where $\dot{D}$ is the dissipation rate; the '$\cdot$' indicates the plastic virtual terms and will be used throughout this report; $\dot{D}_{sa}$, $\dot{D}_{sl}$ and $\dot{D}_{pile}$ are calculated as follows

$$\dot{D}_{sa} = \int_0^{l_{ab}} \dot{\delta}_v T(z) dz \qquad \text{A3 (a)}$$

$$\dot{D}_{sl} = \int_0^{l_{ab}} P(z)\left(1 - \frac{z}{l_{ab}}\right)\sqrt{\dot{\delta}_{hx}^2 + \dot{\delta}_{hy}^2}\, dz \qquad \text{A3 (b)}$$

$$\dot{D}_{pile} = M_b \dot{\theta}_b + V_b \dot{\delta}_v \qquad \text{A3(c)}$$

where δ_v, δ_{hx} and δ_{hy} are respectively the plastic axial, x-direction lateral and y-direction lateral displacements at the pile head. For the convenience of the derivation, δ_v, δ_{hx} and δ_{hy} are assumed to be positive, which will not affect the final result. The subscripts *'x'* and *'y'* respectively refer to the x and y directions and will be used throughout this study. The subscript '*b*' indicates the position is at *b* and will be used throughout this study. θ_b, the axial load V_b and the bending moment M_b at *b* are calculated from the pile geometry and the associated flow rule as shown in Equation A4.

$$|\theta_b| = \frac{\sqrt{\delta_{hx}^2 + \delta_{hy}^2}}{l_{ab}} \qquad \text{A4 (a)}$$

$$V_b = \frac{2V_{pb}}{\pi} \sin^{-1}\left(\frac{2V_{pb}}{\pi M_{pb}} \frac{\dot{\delta}_v}{|\dot{\theta}_b|}\right) \qquad \text{A4 (b)}$$

$$M_b = M_{pb} \cos\left(\frac{\pi}{2} \frac{V_b}{V_{pb}}\right) \mathrm{sgn}(\dot{\theta}_b) \qquad \text{A4 (c)}$$

The input work rate $\dot{E}$ can be calculated as

$$\dot{E} = F\dot{\delta}_{hx} + V\dot{\delta}_v + M_x\dot{\delta}_{\theta x} + M_y\dot{\delta}_{\theta y} \qquad \text{A5}$$

where $\delta_{\theta x}$ and $\delta_{\theta y}$ are respectively the plastic angular displacement at the pile head *a*. Since the pile section between *a* and *b* is rigid, $\delta_{\theta x} = \delta_{hy} / l_{ab}$ and $\delta_{\theta y} = -\delta_{hx} / l_{ab}$.

Introducing $\eta = \delta_v / \delta_{hx}$ and $\xi = \delta_{hy} / \delta_{hx}$, and equating the energy dissipation rate $\dot{D}$ to the input work rate $\dot{E}$ yields F as

$$F = \sqrt{1+\xi^2} \int_0^{l_{ab}} P(z)\left(1 - \frac{z}{l_{ab}}\right) dz + \eta \int_0^{l_{ab}} T(z) dz + \eta V_b + \frac{M_b \sqrt{1+\xi^2}}{l_{ab}} - \eta V - \frac{\xi M_x}{l_{ab}} + \frac{M_y}{l_{ab}} \quad \text{A6}$$

Taking *V* at the pile head as a constant, *F* is maximized when $\frac{\partial F}{\partial \eta} = 0$, $\frac{\partial F}{\partial l_{ab}} = 0$ and $\frac{\partial F}{\partial \xi} = 0$. Combining $\frac{\partial F}{\partial \eta} = 0$, $\frac{\partial F}{\partial l_{ab}} = 0$ and Equation A4 (c), the following equations are obtained:

$$\int_0^{l_{ab}} T(z) dz + V_b - V = 0 \quad \text{A7 (a)}$$

$$\eta T(L) + \frac{\sqrt{1+\xi^2}}{l_{ab}^2} \int_0^{l_{ab}} P(z) z dz - \frac{\sqrt{1+\xi^2}}{l_{ab}^2} M_{pb} \cos\left(\frac{\pi}{2} \frac{V_b}{V_{pb}}\right) + \frac{\xi M_x}{l_{ab}^2} - \frac{M_y}{l_{ab}^2} = 0 \quad \text{A7 (b)}$$

Noting δ_v, δ_{hx} and δ_{hy} are positive, from Equation A4 (b), η can be expressed as

$$\eta = \sqrt{1+\xi^2} \frac{\pi M_{pb}}{2 V_{pb} l_{ab}} \sin\left(\frac{\pi}{2} \frac{V_b}{V_{pb}}\right) \quad \text{A8}$$

Introducing $\varphi = \sin^{-1}\left(\xi / \sqrt{1+\xi^2}\right)$, Equation 2.1 (c) is obtained from Equation A7 (a). Substituting Equation A7 (a) and A8 into Equation A6, Equation 2.1 (a) is obtained. Substituting Equation A8 into Equation A7 (b), Equation 2.1 (b) is obtained.

To check the pile section interfaces, the distance l_{ab} is set to be the same as the depth of the pile section interface under consideration. In this case, the only variables in Equation A6 are η and ξ since l_{ab} is fixed. Equation A6 (a) still holds in this case. Substituting Equation A7 (a) into Equation A6 and noting $\varphi = \sin^{-1}\left(\xi \Big/ \sqrt{1+\xi^2}\right)$ gives

$$F = \frac{1}{\cos(\varphi)}\left[\int_0^{l_{ab}} P(z)\left(1-\frac{z}{l_{ab}}\right)dz + \frac{M_{pb}}{l_{ab}}\cos\left(\frac{\pi}{2}\frac{V_b}{V_{pb}}\right) + \frac{M\sin(\theta-\varphi)}{l_{ab}}\right] \quad \text{A9}$$

where θ is the angle between the direction of the head moment *M* and the direction of head lateral load *F*.

3D single pile lower bound analysis

The same assumption is made here as in the upper bound analysis, i.e., $|V| < |V_m|$ holds, the $P-\Delta$ effect is neglected, and the lateral load is aligned with the positive x-direction. Referring to Figure 2.1, the bending moment M_b at the pile cross-section at a depth l_{ab} below the pile head can be calculated as

$$M_{bx} = M_x - \int_0^{l_{ab}} P_y(z)(l_{ab}-z)\,dz \quad \text{A10 (a)}$$

$$M_{by} = -Fl_{ab} + M_y + \int_0^{l_{ab}} P_x(z)(l_{ab}-z)\,dz \quad \text{A10 (b)}$$

Considering vertical equilibrium, Equation 2.2 (c) can be obtained. For a lower bound solution to be valid, the yield criteria cannot be violated. Using Equation A1 as the yield surface for the pile cross-section gives

$$\sqrt{M_{bx}^2+M_{by}^2} \le M_{pb}\cos\left[\frac{\pi}{2V_{pb}}\left(V-\int_0^{l_{ab}} T(z)\,dz\right)\right] \quad \text{A11}$$

Denoting $f=\sqrt{M_{bx}^2+M_{by}^2}-M_{pb}\cos\left[\frac{\pi}{2V_{pb}}\left(V-\int_0^{l_{ab}} T(z)\,dz\right)\right]$, and setting $\frac{df}{dl_{ab}}=0$ yields

$$M_{by}\left[-H+\int_0^{l_{ab}} P_x(z)dz\right]+M_{bx}\left[-\int_0^{l_{ab}} P_y(z)dz\right]=\frac{\pi M_{pb}^2 T(l_{ab})}{4V_{pb}}\sin\left(\pi\frac{V_b}{V_{pb}}\right) \quad \text{A12}$$

For the exact solution, $P_x(z)$ and $P_y(z)$ depend on both *F* and the out-of-plane moment M_x. To get an explicit solution, $P(z)$ is assumed to be aligned with the direction of *F*, i.e., $P_x(z)=P(z)$ and $P_y(z)=0$. It is safe to neglect the strength of a part of the system in the lower bound analysis. This can also be seen from Equation A12 by noting M_{by} will be negative based on the right-hand coordinate system since in the limiting case, the lateral failure of a pile is driven by *F*. Thus the shaft resistance of the soil within the depth l_{ab} below the pile head is neglected, resulting in Equation 2.2 (a) from Equation A12. Then substituting Equation A12 and A10 into Equation A11, and setting $f=0$, gives a quadratic equation with the unknown $\int_0^{l_{ab}} P(z)z\,dz$ as follows:

$$\left[\int_0^{l_{ab}} P(z)z\,dz\right]^2-2M_y\int_0^{l_{ab}} P(z)z\,dz+M_x^2+M_y^2-\left[M_{pb}\cos\left(\frac{\pi}{2V_{pb}}\left(V-\int_0^{l_{ab}} T(z)\,dz\right)\right)\right]^2=0 \quad \text{A13}$$

Solving the above quadratic equation, Equation 2.2 (b) can be obtained.

To check the pile section interfaces, substituting Equation A10 into Equation A11 to check whether the inequality is satisfied since l_{ab} is fixed. The above derivation implicitly assumes an equilibrium force field can be constructed below l_{ab}, which is true for typical long offshore piles. However, if a balanced force field cannot be found as in the case for relatively short piles, the method described here is not appropriate.

Appendix II Derivation of Upper Bound Solution for Pile Systems

Following the right-hand coordinate system as defined in Figure 3.1, the virtual velocity vector at the jacket origin $\dot{\mathbf{\Delta}} = \left[\dot{\Delta}_x, \dot{\Delta}_y, \dot{\Delta}_z, \dot{\Delta}_{\theta x}, \dot{\Delta}_{\theta y}, \dot{\Delta}_{\theta z}\right]^T$, where $\dot{\Delta}_x, \dot{\Delta}_y, \dot{\Delta}_z$ respectively represent the jacket virtual translational velocity in the *x*, *y* and *z* directions; $\dot{\Delta}_{\theta x}, \dot{\Delta}_{\theta y}, \dot{\Delta}_{\theta z}$ respectively represent the jacket virtual angular velocity around the *x*, *y* and *z* axes. Due to the compatibility requirement, the virtual velocity at the head of the *ith* pile imposed by the jacket structure in the jacket global system $\dot{\boldsymbol{\delta}}_i$ is given by

$$\dot{\boldsymbol{\delta}}_i = \left[\left(\dot{\Delta}_x - y_i \cdot \dot{\Delta}_{\theta z}\right), \left(\dot{\Delta}_y + x_i \cdot \dot{\Delta}_{\theta z}\right), \left(\dot{\Delta}_z + y_i \cdot \dot{\Delta}_{\theta x} - x_i \cdot \dot{\Delta}_{\theta y}\right), \dot{\Delta}_{\theta x}, \dot{\Delta}_{\theta y}, \dot{\Delta}_{\theta z}\right]^T \qquad \text{A14}$$

where x_i and y_i are the coordinates of the head of the *ith* pile in the global coordinate system, respectively. The virtual velocity at the head of the *ith* pile imposed by the jacket structure in the *ith* pile local coordinate system $\dot{\boldsymbol{\delta}}'_i$ is then determined to be $\dot{\boldsymbol{\delta}}'_i = \mathbf{B}_i \dot{\boldsymbol{\delta}}_i$, where $\mathbf{B}_i$ is the transformation matrix from the jacket global coordinate system to the *ith* pile local coordinate system and the prime indicates that the variable is defined in the pile local coordinate system. The following analysis is similar to the existing upper bound methods (Murff and Wesselink, 1986, Tang and Gilbert, 1992). The analysis focuses on a specific *ith* pile since the analyses for other piles are similar. For the convenience of the presentation, $\dot{\boldsymbol{\delta}}'_i$ is represented as $\dot{\boldsymbol{\delta}}'_i = \left[\dot{\delta}'_x, \dot{\delta}'_y, \dot{\delta}'_z, \dot{\delta}'_{\theta x}, \dot{\delta}'_{\theta y}, \dot{\delta}'_{\theta z}\right]^T$. $\dot{\delta}'_x, \dot{\delta}'_y, \dot{\delta}'_z$ respectively represent the virtual translational velocity in the *x*, *y* and *z* directions in the *ith* pile local coordinate system; $\dot{\delta}'_{\theta x}, \dot{\delta}'_{\theta y}, \dot{\delta}'_{\theta z}$ respectively represent the virtual angular velocity around the *x*, *y* and *z* axes in the *ith* pile local coordinate system. The subscript "*i*" indicate the *ith* pile is

neglected for simplicity whenever confusions will not be caused. Let l'_{ab} be the distance between the pile head *a* and the lower plastic hinge *b* along the pile axis. By assuming the pile material is rigid perfectly plastic, the total virtual angular velocities at the *ith* pile head $\dot{\Theta}'_a$ and at the lower plastic hinge $\dot{\Theta}'_b$ in the pile local coordinate system can be expressed as

$$\dot{\Theta}'_a = \sqrt{\left(\frac{\dot{\delta}'_x}{l'_{ab}} + \dot{\delta}'_{\theta y}\right)^2 + \left(\frac{\dot{\delta}'_y}{l'_{ab}} - \dot{\delta}'_{\theta x}\right)^2} \qquad \text{A15 (a)}$$

$$\dot{\Theta}'_b = \frac{\sqrt{\dot{\delta}'^2_{\theta x} + \dot{\delta}'^2_{\theta y}}}{l'_{ab}} \qquad \text{A15 (b)}$$

Note that $\dot{\Theta}'_a$ and $\dot{\Theta}'_b$ consider the virtual angular velocities imposed by the jacket structure and those caused by the pile rotation about the lower plastic hinge. Let $\omega\dot{\delta}'_z$ be the virtual axial velocity caused by the yielding at the pile head *a*, then the virtual axial velocity caused by the yielding at *b* is given by $(1-\omega)\dot{\delta}'_z$. The energy dissipation rate of the *ith* pile $\dot{D}_i = \dot{D}_{i,s} + \dot{D}_{i,p}$, where $\dot{D}_{i,s}$ and $\dot{D}_{i,p}$ are respectively the dissipation due to the soil within the range of l'_{ab} and the dissipation due to the yielding of the pile at *a* and *b*. $\dot{D}_{i,s}$ and $\dot{D}_{i,p}$ are calculated as follows

$$\dot{D}_{i,s} = \int_0^{l'_{ab}} (1-\omega)\dot{\delta}'_z T(z')dz' + \int_0^{l'_{ab}} P(z')\left(1-\frac{z'}{l'_{ab}}\right)\sqrt{\dot{\delta}'^2_{\theta x} + \dot{\delta}'^2_{\theta y}}\,dz' \qquad \text{A16 (a)}$$

$$\dot{D}_{i,p} = \left|V'_a \omega \dot{\delta}'_z\right| + \left|M_{pa}\cos\left(\frac{\pi}{2}\frac{V'_a}{V_{pa}}\right)\dot{\Theta}'_a\right| + \left|V'_b(1-\omega)\dot{\delta}'_z\right| + \left|M_{pb}\cos\left(\frac{\pi}{2}\frac{V'_b}{V_{pb}}\right)\dot{\Theta}'_b\right| \qquad \text{A16 (b)}$$

where V_a' and V_b' are the axial loads at yielding at *a* and *b*, respectively. The integration in Equation A16 (a) is carried out along the pile axis in the pile local coordinate system (*z'* is used to avoid confusions). V_a' and V_b' are calculated from the associated flow rule and Equation A1 as follows

$$V_a' = \frac{2V_{pa}}{\pi}\sin^{-1}\left(\frac{2V_{pa}}{\pi M_{pa}}\frac{\omega\dot{\delta}_z'}{\dot{\Theta}_a'}\right) \quad \text{A17 (a)}$$

$$V_b' = \frac{2V_{pb}}{\pi}\sin^{-1}\left[\frac{2V_{pb}}{\pi M_{pb}}\frac{(1-\omega)\dot{\delta}_z'}{\dot{\Theta}_b'}\right] \quad \text{A17 (b)}$$

To be noted, V_a' and V_b' in Equation A17 should be limited to the pile geotechnical axial capacity at *a* and *b*, respectively. Following the current definition of the coordinate system, a positive (negative) virtual axial velocity corresponds to a compressive (tensile) axial load, and hence V_a' and V_b' should be limited to the compressive (tensile) axial capacity at *a* and *b*, respectively.

The total energy dissipation rate within the pile system $\dot{D}$ is the sum of the energy dissipation rate in each individual pile as follows

$$\dot{D} = \sum_{all\ i}\dot{D}_i = \sum_{all\ i}\left(\dot{D}_{i,s} + \dot{D}_{i,p}\right) \quad \text{A18}$$

The input work rate to the jacket system $\dot{E}$ can be calculated as

$$\dot{E} = \left(\mathbf{P_c} + \lambda_{upp}\tilde{\mathbf{p}}\right)\bullet\dot{\mathbf{\Delta}} \quad \text{A19}$$

Equation 3.3 is obtained from $\dot{D} = \dot{E}$. The upper bound solution is then optimized by considering different failure mechanisms. For a given failure mechanism $\dot{\mathbf{\Delta}}$, for each

pile, there are two independent optimizing parameters ω and l'_{ab}. Hence, $\dot{D}_i$ should be minimized with respect to ω and l'_{ab} in order to get an optimized upper bound solution. For different piles, the combination of ω and l'_{ab} generally may not necessarily be the same. Thus generally the minimization of $\dot{D}$ involves 2N independent optimizing parameters for a given failure mechanism $\dot{\boldsymbol{\Delta}}$, where N is the number of piles in the pile system.

References

ABS, C. (2004) *Hurricane Lili's Impact on Fixed Platforms*: Final Report Prepared for Minerals Management Service, MMS Order No.: 0103PO72325.

Aggarwal, R., Litton, R., Cornell, C., Tang, W., Chen, J. and Murff, J. (1996) Development of pile foundation bias factors using observed behavior of platforms during Hurricane Andrew. *Offshore Technology Conference*, Houston, Texas.

Anderson, W. D., Silbert, M. N. and Lloyd, J. R. (1982) Reliability procedure for fixed offshore platforms, *Journal of the Structural Division*, 108(11), pp. 2517-2538.

Ang, A. H. S. and Tang, W. H. (1975) *Probability concepts in engineering planning and design, Vol. I, Basic Principles, New York, John Wiley & Sons.*

Ang, A. H. S. and Tang, W. H. (1984) Probability concepts in engineering planning and design, *Vol. II, Decision, Risk and Reliability, John Wiky and Sons, New York.*

API RP 2A-LRFD (1993) *Recommended Practice for Planning, Designing and Constructing Fixed Offshore Platforms - Load and Resistance Factor Design, 1st Edition*: American Petroleum Institute, Washington, D.C.

API RP 2A-WSD (2014) *Recommended Practice for Planning, Designing and Constructing Fixed Offshore Platforms-Working Stress Design*: American Petroleum Institute, Washington, D.C.

API RP 2GEO (2011) *Geotechnical and Foundation Design Considerations, Washington, D.C., American Petroleum Institute*.

API RP 2MET (2014) *Derivation of Metocean Design and Operating Conditions, RP 2MET First Edition*: American Petroleum Institute.

Bea, R. (1983) Characterization of the reliability of offshore piles subjected to axial loadings. *Proceedings of the ASCE Structures Congress*.

Bea, R., Jin, Z., Valle, C. and Ramos, R. (1999) Evaluation of reliability of platform pile foundations, *Journal of Geotechnical and Geoenvironmental Engineering*, 125(8), pp. 696-704.

Bea, R. G. (1974) Gulf of Mexico hurricane wave heights. *Offshore Technology Conference*, Houston, Texas.

Chakrabarti, S. (2005) *Handbook of Offshore Engineering (2-volume set).* Elsevier.

Chen, J. B., Gilbert, R. B., Choo, Y. S., Marshall, P. W. and Murff, J. D. (2015) Two dimensional lower bound analysis of offshore pile foundation systems, *INT J NUMER ANAL MET, doi: 10.1002/nag.2488.*

Chen, J. B., Gilbert, R. B., Murff, J. D. and Marshall, P. W. (2016) Three dimensional lower and upper bounds analyses of pile foundation systems, *INT J NUMER ANAL MET,* Under Review.

Chen, J. Y., Gilbert, R. B., Puskar, F. J. and Verret, S. (2013) Case study of offshore pile system failure in Hurricane Ike, *Journal of Geotechnical and Geoenvironmental Engineering*, 139(10), pp. 1699-1708.

Chen, J. Y., Materek, B., Carpenter, J. F., Gilbert, R. B., Verret, S. and Puskar, F. J. (2010) *Analysis of potential conservatism in foundation design for offshore platform assessment*, Final Project Report Prepared for the American Petroleum Institute, Contract No. 2007-103130.

Chen, W. F. and Han, D. J. (1985) *Tubular members in offshore structures.* Pitman.

Cornell, C. A. (1987) *Offshore structural systems reliability*, A Report to Amoco Production Company for the JIP Participants.

Ditlevsen, O. (1979) Narrow reliability bounds for structural systems, *Journal of structural mechanics,* 7(4), pp. 453-472.

Efthymiou, M., van de Graaf, J. W., Tromans, P. S. and Hines, I. M. (1997) Reliability-based criteria for fixed steel offshore platforms, *Journal of Offshore Mechanics and Arctic Engineering,* 119(2), pp. 120-124.

Energo Engineering (2005) *Assessment of Fixed Offshore Platform Performance in Hurricanes Andew, Lili and Ivan*: Final Report Prepared for Minerals Management Service, MMS Project Number 549.

Energo Engineering (2007) *Assessment of Fixed Offshore Platform Performance in Hurricanes Katrina and Rita*: Final Report Prepared for Minerals Management Service, MMS Project Number 578.

Energo Engineering (2009) *Reliability vs. Consequence of Failure for API RP 2A Fixed Platforms Using API Bulletin 2INT-MET*: Final Report Prepared for Minerals Management Service, MMS Project Number 609.

Energo Engineering (2010) *Assessment of damage and failure mechanisms for offshore structures and pipelines in Hurricanes Gustav and Ike*: Rep. MMS TAR Project No. 642, Minerals Management Service, U.S. Dept. of Interior, Herndon, VA.

FMMG (2001) *Geotechnical Investigation, Platform I Location, Gulf of Mexico,* : Report to Confidential Client.

Forristall, G. Z. (1978) On the statistical distribution of wave heights in a storm, *Journal of Geophysical Research: Oceans (1978–2012)*, 83(C5), pp. 2353-2358.

Forristall, G. Z. (2007) Comparing Hindcasts With Wave Measurements From Hurricanes Lili, Ivan, Katrina and Rita. *Proc. 10th International Workshop on Wave Hindcasting and Forecasting and Coastal Hazards Symposium, North Shore, Oahu, HI, Nov*, 11-16.

Gilbert, R. B., Chen, J. Y., Chen, J. B. and Puskar, F. (2014) Lessons learned about performance reliability of jacket foundation systems in Gulf of Mexico Hurricanes. *Second Offshore Structural Reliability Conference*, Houston, Texas, Sept. 16-18.

Gilbert, R. B., Chen, J. Y., Materek, B., Puskar, F., Verret, S., Carpenter, J., Young, A. and Murff, J. (2010) Comparison of observed and predicted performance for jacket pile foundations in hurricanes. *Proceedings of Offshore Technology Conference*, Houston, Texas.

Hamilton, J. and Murff, J. (1995) Ultimate lateral capacity of piles in clay. *Proceedings of Offshore Technology Conference*, Houston, Texas.

Hamilton, J. M. and Murff, J. D. (1988) Probabilistic Assessment of the Foundation Collapse Strength of Pile Offshore Platforms. *Proceedings of International Conference on the Behaviour of OffShore Structures (BOSS)*.

Hamilton, J. M. and Murff, J. D. (1992) Selection of LRFD resistance factors for pile foundation design. *Proceedings Structures Congress' 92*.

Haring, R. E., Johansson, P. I. and Olsen, O. A. (1979) Total wave force and moment vs. design practice. *Civil Engineering in the Oceans IV*: ASCE, 805-819.

Heideman, J. C. and Weaver, T. O. (1992) Static wave force procedure for platform design. *Civil Engineering in the Oceans V*: ASCE, 496-517.

Jeanjean, P. (2009) Re-assessment of py curves for soft clays from centrifuge testing and finite element modeling. *Proceedings of Offshore Technology Conference*, Houston, Texas.

Jonathan, P. and Taylor, P. H. (1996) *Wave-induced loads on fixed offshore structures: An assessment of``wave-by-wave``load variability and bias*: American Society of Mechanical Engineers, New York, NY (United States).

Krieger, W., Banon, H., Lloyd, J., De, R., Digre, K., Nair, D., Irick, J. and Guynes, S. (1994) Process for assessment of existing platforms to determine their fitness for purpose. *Offshore Technology Conference*: Offshore Technology Conference.

Lacasse, S. and Goulois, A. (1989) Uncertainty in API parameters for prediction of axial capacity of driven piles in sand. *Offshore Technology Conference*, Houston, Texas.

Lacasse, S. and Nadim, F. (1996) Model uncertainty in pile axial capacity calculations. *Offshore Technology Conference*, Houston, Texas.

Lacasse, S., Nadim, F., Guttormsen, T. R., Eide, A., Knudsen, S., Yetginer, G. L. and Langford, T. (2013) Model Uncertainty in Axial Pile Capacity Design Methods. *Offshore Technology Conference*.

Lloyd, J. and Clawson, W. (1984) Reserve and residual strength of pile founded offshore platforms, *The Role of Design, Inspection and Redundancy in Marine Structural Reliability*, pp. 157-198.

Marshall, P. W. (2015) Personal discussions.

Marshall, P. W. and Bea, R. G. (1976) Failure modes of offshore platforms. *First International Conference on Behavior of Offshore Structures*, Trondheim, Norway.

Martin, J. (1975) *Plasticity: fundamentals and general results.* MIT Press, Cambridge, MA.

Moses, F. (1986) Development of preliminary load and resistance design document for fixed offshore platforms, *final report, API-PRAC*, pp. 85-22.

Murff, J. (1987) Plastic collapse of long piles under inclined loading, *International Journal for Numerical and Analytical Methods in Geomechanics,* 11(2), pp. 185-192.

Murff, J. D. (1999) The mechanics of pile foundation collapse. *Proceedings of the Offshore Technology Research Center Conference*, Austin, Texas: Analysis, Design, Construction, and Testing of Deep Foundations, Geotechnical Special Publications 88, 76-95.

Murff, J. D. (2000) 'Limit analysis of foundation systems with offshore applications', in Booker, R., Gioda, G. & Zaman, M. (eds.) *Modeling in geomechanics*. New York: John Wiley & Sons, pp. 359-388.

Murff, J. D. (2012) Estimating capacity of offshore foundations. *7th International Conference in Offshore Site Investigation: Integrated Geotechnologies-Present and Future*, London, UK.

Murff, J. D., Lacasse, S. and Young, A. G. (1993) Discussion and summary on foundation elements, system and analysis. *Int. Workshop on Assessment and Requalification of Offshore Production Structures*, Offshore Technology Research Center, College Station, TX, and the Univ. of California at Berkeley, Berkeley, CA, 151-165.

Murff, J. D. and Wesselink, B. D. (1986) Collapse analysis of pile foundations. *Proceedings of the 3rd International Conference on Numerical Methods in Offshore Piling*, 445-459.

Nordal, H., Cornell, C. A. and Karamchandani, A. (1988) *A system reliability case study of an eight-leg jacket platform*, Department of Civil Engineering, Stanford University. Report No. RMS-3.

O'Neill, M. W. and Murchison, J. M. (1983) *An evaluation of p-y relationships in sands*: Rsearch Report to American Petroleum Institute for Project PRAC 82-41-1, University of Houston.

O'Neill, M. W. and Gazioglu, S. M. (1984) *Evaluation of p-y relationships in clays*: Rsearch Report to American Petroleum Institute for Project PRAC 82-41-2, University of Houston.

Oceanweather (2003) *MMS Hindcast Study of Hurricane Lili (2002)-Offshore Northern Gulf of Mexico*: Report Submitted to US Department of the Interior Minerals Management Service.

Oceanweather (2006) *Hindcast Data on Winds, Waves, and Currents in Northern Gulf of Mexico in Hurricanes Katrina and Rita*: Report Submitted to US Department of the Interior Minerals Management Service.

Olsen, R. E. (1984) *Analysis of Pile Response under Axial Loads*: Final report on Project 83-42B, American Petroleum Institute.

PMB Engineering (1993) *Hurricane Andrew-Effects on offshore platforms*: Final Report to Joint Industry Porject.

PMB Engineering (1996) *Hurricane Andrew-Effects on offshore platforms, Phase II*: Final Report to Joint Industry Porject.

Ponter, A. and Carter, K. (1997) Limit state solutions, based upon linear elastic solutions with a spatially varying elastic modulus, *Computer methods in applied mechanics and engineering*, 140(3), pp. 237-258.

Ponter, A. R., Fuschi, P. and Engelhardt, M. (2000) Limit analysis for a general class of yield conditions, *European Journal of Mechanics-A/Solids*, 19(3), pp. 401-421.

Puskar, F. J., Aggarwal, R. K., Cornell, C. A., Moses, F. and Petrauskas, C. (1994) A comparison of analytically predicted platform damage to actual platform damage during Hurricane Andrew. *Offshore Technology Conference*: Offshore Technology Conference.

Randolph, M. F. and Houlsby, G. (1984) The limiting pressure on a circular pile loaded laterally in cohesive soil, *Geotechnique*, 34(4), pp. 613-623.

Sørensen, J. D. (2004) Notes in structural reliability theory and risk analysis, *Aalborg University*.

Senanayake, A., Rendon, E., Wang, S.-T., Gerkus, H., Stevens, R. F. and Gilbert, R. B. (2015) Design of large diameter monopiles under lateral loads in normally to moderately overconsolidated clay. *Proceedings of Offshore Technology Conference*, Houston, Texas.

Tang, W. H. (1988) *Offshore axial pile design reliability*: Rsearch Report to American Petroleum Institute for Project PRAC 86-29B.

Tang, W. H. and Gilbert, R. B. (1990) *Offshore Lateral Pile Design Reliability*: Research Report American Petroleum Institute for Project PRAC 87-29.

Tang, W. H. and Gilbert, R. B. (1992) *Offshore pile system reliability*, Final Report to American Petroleum Institute (Project PRAC 89-29).

Thoft-Christensen, P. and Murotsu, Y. (1986) *Application of structural systems reliability theory*. Springer-Verlag Berlin, Heidelberg.

Tromans, P. S. and Vandersohuren, L. (1995) Response based design conditions in the North Sea: Application of a new method. *Proceedings of Offshore Technology Conference*, Houston, Texas.

Wen, Y. and Chen, H.-C. (1987) 'On fast integration for time variant structural reliability', *Stochastic Approaches in Earthquake Engineering*: Springer, pp. 428-454.

Vita

Jinbo Chen was born in Xiujuan Wang and Caiyao Chen's family in Zhejiang Province, the People's Republic of China. After finishing his high school study at Chun Hui High School in 2005, he joined the Department of Civil Engineering at Tongji University at the same year. In 2009, he received the Bachelor of Engineering from Tongji University with the highest honor in Shanghai before joining the Geotechnical Engineering for graduate study at Zhejiang University. In 2010, he terminated his study in Zhejiang University and joined the Centre for Offshore Research and Engineering at the National University of Singapore as a full time Research Engineer focusing on the re-assessment of offshore platforms for life extension. In 2011, he began his part time Master's study and received his part time degree of Master of Engineering (by research) in 2013 for his research on cyclic constitutive modeling of clays. In August 2013, he joined the Ph.D. program in Geotechnical Engineering at The University of Texas at Austin.

Permanent email: cvechenjinbo@utexas.edu

This dissertation was typed by Jinbo Chen.